UNIVERSITY OF SOUTHAMPTON

FACULTY OF ENGINEERING, SCIENCE & MATHEMATICS

School of Engineering Sciences

NEOIMPACTOR - A TOOL FOR ASSESSING EARTH'S VULNERABILITY TO THE NEO IMPACT HAZARD

by

Nicholas James Bailey MEng

thesis for the degree of Doctor of Philosophy

June, 2009

UNIVERSITY OF SOUTHAMPTON

ABSTRACT

FACULTY OF ENGINEERING, SCIENCE & MATHEMATICS
SCHOOL OF ENGINEERING SCIENCES

Doctor of Philosophy

NEOIMPACTOR - A TOOL FOR ASSESSING EARTH'S VULNERABILITY TO THE NEO IMPACT HAZARD

by Nicholas James Bailey MEng

The Earth's surface bears the scars of 4.5 billion years of bombardment by asteroids, despite most having been erased by tectonic activity and erosion. Asteroids predominantly orbit the Sun in the asteroid belt between Mars and Jupiter, but a large number occupy orbits close to the Earth's. These bodies are termed Near Earth Objects (NEOs) and they present a very real impact threat to the Earth. In 1998 NASA inaugurated the 'Spaceguard Survey' to catalogue 90% of NEOs greater than 1 km in diameter. The smaller bodies, meanwhile, remain undetected and far more numerous.

In order to understand the NEO hazard, the consequences resulting from an asteroid impact require modelling. While the atmospheric entry of asteroids is a critical part of the impact process, it is the surface impact which is most important, both onto land and into the oceans. It is the impact generated effects (IGEs) that are hazardous to human populations on the Earth and the infrastructure they occupy. By modelling these IGEs and the consequences they present for humans and infrastructure, an understanding of the global vulnerability to the hazard is developed.

'NEOimpactor' is the software solution built to investigate the global vulnerability to NEO impacts. By combining existing mathematical models which describe the impact and effects, a unified impact simulator tool has been developed with the capacity to model the real consequences of any terrestrial impact.

By comparing the consequences of multiple impact events, a complete vulnerability assessment of the global NEO hazard is derived. The result maps are designed for ease of dissemination to explain the impact risk to a non-specialist audience. The system has identified China, US, India, Japan and Brazil as facing the greatest overall risk, as well as indicating the various factors influencing vulnerability. The results can be used for informing the international decision making processes regarding the NEO hazard and potential mitigation strategies.

Contents

List of Figures

List of Tables

Acknowledgements

First, I offer my humblest thanks to my supervisor, Graham, for his leadership over the course of the project. Not only did he offer me the opportunity for such an adventure, but has nurtured my skills along the way and enabled me to achieve what at times seemed impossible. He faced a difficult task getting me through this thesis, but his skill and tireless efforts have found in me something I am truly proud of.

Secondly I would like to thank my family, for the inspiration to reach out for this goal and the support to finally achieve it. To my parents, Elaine and Peter, for their continuous support and encouragement throughout my PhD study. Without my mother's visits, phone calls and unfailing love I fear I would have given up long ago. Peter's sensitive assessment of my early draft gave me the confidence I needed to know I had this thesis in me. I would also like to extend my thanks to my brother, Chris, who has kept a watchful eye on my progress and nurtured my research skills throughout the past four years over coffee and long walks in the countryside. To Anne Rawlinson, John Dixon, Aunty Mavis and Dave Viggars who have, each in their own way, been looking out for me, I thank you. My dear Suyeon has also been an unfailing support over this past year. Her ability to keep up my mental strength has been invaluable.

My advisor, Hugh, has been a continual aid throughout, with much technical assistance and personal support as I learnt the art of programming. Stories from his research experience have helped maintain not only my morale, but also that of my research group. It is to them that I also owe a huge debt of gratitude. Not only has the group been a joy to work with, but also to share four years of my life with. My thanks then to Aim, Andrew, Cheryl, Dave, Jaye, Nick, Rebecca, Riaz and Tarek. I extend particular thanks to Angela, Sam, John, François, Luke, Christelle, and James for both the high and low times spent together. I especially thank Piers, who has continued to surprise me with his love, friendship and excellent advice.

Finally I dedicate this thesis to my father David, the original Dr Bailey, who I miss terribly and without whom I would not be. Through this experience I feel I have come to know him closer than I ever expected; a very precious gift. I have felt his pain and the difficulty he faced during his PhD, and I know now that I am my father's son.

Acknowledgement of Sponsors

The author gratefully acknowledges the financial support of the Science and Technology Facilities Council (STFC), UK and the School of Engineering Sciences, University of Southampton, UK. Without this sponsorship, the research presented in this thesis would not have been possible.

List of Acronyms

APL	Applied Physics Laboratory
ESA	European Space Agency
CIA	Criminal Intelligence Agency
IGE	Impact Generated Effect
ISRO	Indian Space Research Organisation
JAXA	Japan Aerospace Exploration Agency
JPL	Jet Propulsion Laboratory
KE	Kinetic Energy
KT	Kilotons (of TNT)
LPL	Lunar and Planetary Laboratory
LPSTI	Light Pollution Science and Technology Institute
LOV	Line Of Variance
MFC	Microsoft Foundation Class
MIT	Massachusetts Institute of Technology
MOID	Mean Orbit Intersection Distance
MSFC	Marshall Space Flight Center
MT	Megatons (of TNT)
NASA	National Aersonautical and Space Administration
NEA	Near Earth Asteroid
NEAR	Near Earth Asteroid Rendezvous
NEO	Near Earth Object
NIU	NEOimpactor Infrastructure Unit
NOAA	National Oceanic and Atmospheric Administration
OM	Operational Modules
PHO	Potentially Hazardous Object
SA	Simulation Applications
UI	User Interface
UNOOSA	United Nations Office for Outer Space Affairs
USGS	United States Geological Survey
Web	World Wide Web

Nomenclature

a	Semi-major axis
A_{cell}	Area of the database cell
A_{crit}	Critical wave amplitude
A_{deep}	Deep water wave amplitude
A_{neo}	NEO area incident on atmosphere
$A_{shallow}$	Deep water wave amplitude
c_0	Speed of sound
c_d	NEO drag coefficient
c_h	NEO Heat transfer coeficient
d_{cavity}	Ocean cavity depth
d_{cavity}^{eff}	Effective cavity depth
D_{cavity}	Ocean cavity diameter
d_{crit}	Critical crater depth
D_{crit}	Critical crater diameter
D_{ejecta}	Ejecta diameter
d_{final}	Final crater depth
D_{final}	Final crater diameter
D_{neo}	NEO diameter
d_{trans}	Transient crater depth
D_{trans}	Transient crater diameter
E_{imp}	Impact energy of NEO
E_{ke}	Kinetic energy of NEO
E_{kt}	Impact energy equivalent in kilotons (TNT)
f	Fireball visible ratio
F_a	Force of acceleration
F_d	Force of drag
g	Local gravitational acceleration
g_0	Gravitational acceleration at sea level
h	Altitude
H	Absolute magnitude of orbital asteroid
h_{crit}	Critical ocean depth

h_{deep}	Ocean depth at impact location
h_{fr}	Rim height around final crater
h_{half}	Half energy height
h_{imp}	Ocean depth at impact location
h_{in}	Tsunami inundation run-in distance
$h_{shallow}$	Ocean depth at coastal location
h_{up}	Tsunami inundation run-up distance
I_{cell}	Calculated infrastructure value of cell
I_{real}	Real world infrastructure value estimate
L_{neo}	NEO length of cylindrical section
M_{imp}	Earthquake magnitude at impact site
M_{neo}	NEO mass
M_r	Earthquake magnitude at distance r
$M_{\rho_{dataset}}$	Scaling density factor for the dataset
N	Number of asteroids in the orbital population
P_0	Atmospheric pressure at sea level
P_{atm}	Local atmospheric pressure
P_{cell}	Calculated population of cell
$P_{dataset}$	Population summation for the dataset
P_{peak}	Peak blast wave overpressure
P_{real}	Real world population estimate
p_x	Blast wave pressure at the transition point
q	Perihelion
Q	Aphelion
Q_{neo}	NEO heat of ablation
r	Distance from impact site
r_1	Distance from a 1 kt explosion
R_{cavity}	Ocean cavity radius
r_{crit}	Distance at which the critical height is reached
R_{crit}	Critical crater radius
R_{earth}	Radius of the earth
R_{final}	Final crater radius
R_{neo}	NEO radius
R_{trans}	Transient crater radius
r_x	Distance of transition point from a 1 kt explosion
S_{neo}	Internal Strength of the NEO
t	Time since impact
t_{br}	Thickness of the breccia lens

t_{ejecta}	Ejecta thickness
$t_{recurrence}$	Impact recurrence interval time
u_{peak}	Peak wind velocity
V_{deep}	Deep water wave velocity
V_{ejecta}	Ejecta velocity
V_{neo}	NEO velocity
δ_f	Fireball half angle
Δ	Geocentric angle between impact site and r
ε_{ir}	Thermal irradiation flux
η	Fireball energy ratio
Θ	Nadir point longitude
τ_{ir}	Duration of irradiation exposure
ρ_{atm}	atmospheric density
$\rho_{dataset}$	Density value from dataset
ρ_{earth}	impact target density
ρ_{neo}	NEO density
ρ_{water}	Density of water
σ_a	Ablation coefficient
ϕ	Angle between astronomical horizon and trajectory
Φ	Nadir point latitude
ψ	Wave amplitude power term
Ψ	Angle subtended down from astronomical horizon
Ω	Velocity bearing (from North)

For David

Thank you for the Maltesers

Chapter 1

Introduction

Beginning with the sun's accretion disk, 4.5 billion years ago, the solar system has been composed of many rocky lumps of all sizes. Through collision and adhesion of these bodies, protoplanets grew gradually into the eight[1] planets of the solar system we observe today. While we may want to believe this process has ceased, the reality is that asteroids are still present in the solar system and continue to collide with each other and with the planets, including our own Earth. Evidence for the continued threat from Near Earth Objects (NEOs) abounds, from spectacular annual meteor showers through to geological records of massive impact structures in the Earth's crust. To think humanity is safe simply because no deaths have been recorded is to stick our collective head in the sand. The frequently quoted adage rings true:

"It's not a question of if but when."

Asteroid research has a long history. Ceres was the first asteroid discovered in 1801 by Giuseppe Piazzi, although it was not initially understood as such [Foderà Serio et al., 2002]. But it took nearly two hundred years before the first asteroid with a close proximity to the Earth was discovered by Scotti et al. [1991]. Since then the catalogue of Near Earth Asteroids (NEAs) has continued to grow, helped to a large degree by amateur astronomers. In 1998 NASA begun a ten year effort to catalogue 90% of the NEO population larger than one kilometre in diameter. This is scheduled to conclude in 2008, which is also the centenary of the Tunguska explosion, arguably the event that first alerted humanity to the threat from extra-terrestrial objects.

1.1 Focus of Current NEO Research

The majority of expenditure on the NEO threat is currently in the detection and cataloguing of the orbiting populations. Before such systematic surveying began, asteroids were discovered by chance as a side effect of other observations. This meant

[1] Following the downgrading of Pluto from its status as planet to 'minor body' [IAU, 2006]

that asteroids were occasionally spotted only as they passed very close to Earth. Such experiences are unnerving as they suggest the possibility of a scenario in which an asteroid on collision course is detected just prior to impact. Indeed, for the first time on the 7^{th} of October 2008 an object on collision course was detected just prior to atmospheric entry over northern Sudan [NASA - JPL, 2008b].

Naturally the consequences of impact from a large, super-kilometre, asteroid is severe. Such an event could generate a vast number of casualties across the world - in the region of hundreds of millions - or potentially lead to mass extinction [Courtillot and McClinton, 2002]. The geological record details a number of extinction periods in Earth's history, of which some coincide with impact events, the most famous and contentious being the Chixulub impact 65 million years ago [Raup, 1986]. Furthermore, the secondary impact effects, such as heat, dust and water vapour injected into the upper atmosphere, would have significant consequences for the global climate, requiring requiring complex atmospheric modelling to account for. From estimates of the orbital population, 1 km objects are 'expected' to impact every 1 million years or so (see Figure 2.1). As such, the probability of one impacting in the near future is very small. However, despite this infrequency, the potential consequences from such an impact averaged over the impact interval, remains higher than that of other natural disasters (see Section 2.1.3) [Chapman and Morrison, 1994].

It is this large impact scenario which NASA's Spaceguard Survey aims to eliminate. By cataloguing all but a tiny fraction of this super-kilometre asteroid population, the unknown threat is reduced to this small percentage of the undiscovered population. This works on the assumption that a known 'threat' is preferable to the unknown 'hazard' - the reason being that something can be done to mitigate the threat. Thus the secondary aim of the catalogue is to locate any potential impact threats many decades prior to collision to provide the greatest 'lead time' possible to eliminate the threat.

It is in this field that the second major research investment is undertaken - mitigation mission studies. Many proposals have been put forward for ways of mitigating an asteroid threat including mass drives, solar sails and nuclear detonation. Their aim is to either move the body away from the collision course, or break up the asteroid in to small fragments. In recent years space agencies have launched specific asteroid rendezvous missions. These have helped enhance our understanding of these bodies, while also revealing how vast the range of types and properties can be. Mitigation mission investigations often fail to consider the possibility of a mission failure and in particular, the knock on consequences resulting from the partially attempted mitigation procedure. The resultant probability that a mitigated asteroid might still impact Earth is overlooked. Avoidance in studying this failure possibility is natural to assume, but even with engineered redundancy, space missions are never fail-safe.

Furthermore more, these proposals assume that discovery occurs many years prior to impact, affording enough time to launch a mitigation attempt.

1.1.1 Target Asteroid Population

One limitation of current NEO initiatives is their focus on the large 'killer' asteroids. Clearly, these present a potential threat of human extinction, making their detection critical to our safety. However, the small population of these object combined with the completeness of the catalogue (approximately 80%) leads to a low chance that a threatening object will be discovered. On the other hand, the population of small sub-kilometre bodies far outnumbers larger ones, resulting in a much higher impact frequency of the order of centuries or less, see Figure 2.1.

With the Spaceguard Survey nearing completion, a NASA Science Definition team report by Stokes and Yeomans [2003] assessed the feasibility of cataloguing all NEAs above 140 m diameter. The problem with this population is that they are difficult to detect. Smaller bodies reflect less light and require more powerful telescopes to locate. The report suggests a number of telescopic proposals including space based platforms at the L1 point to improve observations of the Aten bodies, those with orbits inside the Earth's (see Table 2.3). The size-frequency relationship identified in the report predicts a far larger population to catalogue. Until such a survey is underway, our estimation of the population will remain vague, and until completion the unidentified objects will represent a significant threat to Earth. Objects in the order of a few metres impact Earth without detection on a yearly basis, such as the recent Peruvian meteorite fall [Hecht, 2007].

1.2 Asteroid Impact Risk Assessment

1.2.1 Definition of Risk Analysis Terminology

An internal review paper of the journal *Disasters* by Alexander [1997] describes the difficulty in determining both a definition of a natural disaster, and the severity of such an event. The multidisciplinary nature of the field leads to many terms being re-defined based on a number of different factors. With no internationally accepted working model of disaster scaling model, it remains largely left to the individual to develop their own risk scale. Furthermore, there remains general confusion over the terms 'hazard', 'risk' and 'disaster', with the more recent idea of 'vulnerability' attempting to incorporate these three terms.

Even risk analysis studies typically use a range of terminology. As this project is multidisciplinary it is especially important to define these terms for consistent use

within this project. The following definitions will be implemented:

Hazard - a possible situation or event which has the potential to generate damage or injury on a large scale.

Natural Hazard - a hazard which is not man made. Asteroids represent the most significant natural hazard. If the characteristics of an asteroid is altered by man prior to impact in order to mitigate the threat, it could be argued that the hazard is no longer natural.

Threat - a hazard event which is about to happen. An asteroid on collision course is a particular threat.

Impact - used here to indicate the actual collision event and associated processes of the asteroid hitting the surface of the Earth.

Consequences - the subsequent effects of the asteroid impact on the Earth's global community. In particular the injury and damage to humans and infrastructure.

Risk - is a function of the probability that an asteroid will impact a location, and the consequences from that impact.

Vulnerability - the ability of a particular impact event to generate casualties and damage. One country is more vulnerable than another if it suffers greater consequences from the same event. Low vulnerability describes how well protected a location is to an impact threat.

Exposure - is the range of impact events or effects to which a particular country is vulnerable.

Resilience - is the ability for a location to return to normality following an impact. The shorter the period required, the more resilient is the community. Resilience is a multi-faceted function considering many inter-dependent systems.

1.2.2 The Need for Asteroid Impact Vulnerability Assessment

It is the uneasy scenario of an asteroid impacting the Earth which this study chooses to focus upon. Such a scenario is rarely covered as it suggests that either an undetected threat suddenly appears, or that a mitigation mission on a known threat has failed. However, not studying this impact outcome leaves a large gap in our understanding of Earth's vulnerability to the asteroid hazard. It also limits the planning and preparedness which governments need to improve resilience to the hazard. Without knowing the likely consequences from a particular or generic impact event, it is not possible to

fully understand the potential outcomes of a mitigation mission which might alter the predicted impact site. Furthermore, without understanding who is most vulnerable, the international community has no means of assessing where the responsibility for mitigation lies.

In the event of an impact, predictions of who is most vulnerable are required to co-ordinate both pre-evacuation and post-disaster relief efforts. This understanding of vulnerability leads to improvements in community preparedness and resilience. Assessment of impact vulnerability is required at both a national and international level. The assessment will be based on two consequence indicators: human casualty figures and infrastructure damage.

At a national level it will identify the communities most vulnerable to the effects of an asteroid impact through direct loss of life and loss of infrastructure. Both these losses will affect a community in different ways. Direct population loss will impact on a social level, reducing morale, reducing the skilled workforce and hindering the return to normality. Lost infrastructure will require re-building, impacting the local economy while also leading to displacement of communities from affected homes. At an international level, it is important to identify those countries with the greatest exposure. This is both the risk a country is exposed to by a random impact event, and the vulnerability of each country (i.e. the lost population and infrastructure if an impact occurs within or local to the country).

1.2.3 Project Aims and Objectives

In order to provide this risk assessment, a global study of the threat must be undertaken, as called for by Gálvez et al. [2003]. This will involve investigating the threat from ocean and land impacting asteroids and their associated Impact Generated Effects (IGEs). In the case of land impacts, the IGEs of small asteroids will be relatively localised, whereas the ocean impact generated tsunami will have the capability to propagate the energy and cause damage across the globe. For this reason the study must be performed at a global level.

Vulnerability will be assessed by considering the level of destruction each country is likely to experience due to an impact. Destruction will be measured in terms of the population lost (casualty estimate) and the cost of the infrastructure loss (damage estimate).

The principle aim of this project is:

> *to investigate the global asteroid impact vulnerability through the development of a new software tool (NEOimpactor), which will be used to derive a global risk assessment based on the threat to human populations worldwide and their associated infrastructure.*

It is vital countries understand that they are at risk from a NEO impact and that the risk could be greater than other, more common natural disasters. [Crowther et al., 2005] reports from the Global Science Forum meeting in 2003 the identification of the need for OECD countries to develop a NEO policy similar to those already in place for extreme weather events. In order to disseminate such information, the risk data needs to be displayed in an accessible format. By the use of the familiar parallel Earth cartographic projection, the regions and countries at highest risk can be identified by the use of colour shading. A comparable system would be the use of shading in climate maps to indicate temperature distributions world wide. The familiarity of such climate maps will enable an otherwise complex dataset to be grasped by a non-specialist audience.

The objectives of this project are:

- **Impact Modelling** - incorporate the full range of asteroid parameters into a coherent impact simulator. This will require separate studies of the atmospheric entry including the associated aerodynamic drag effects, the land impact effects, and the ocean impact effects. Each of these effects must be implemented at a global level so the consequences from every impact on each country can be plotted to ensure a combined understanding of the risk is achieved.

- **Population & Infrastructure Interactions** - an assessment of the impact consequences will be achieved through an examination of each IGE, and the influence it has on the local human populations and infrastructure. The severity of the consequence will depend on the magnitude of the IGE. The risk assessment will be based on the summations of the casualties and damage.

- **Understandable Outputs** - the nature of the NEO hazard, unlike other natural disasters, is its widespread threat to all people on Earth. Simultaneously, the infrequency of the impact events leads to general disregard for the hazard. Simulation results that are understandable by a wide section of society are vital for successful knowledge dissemination. This knowledge of an individual country's vulnerability is important to help improve resilience.

- **Development of a Global Vulnerability Assessment** - at an international level each country will have a relative vulnerability associated with the NEO hazard. Understanding the impact consequences on a global scale across multiple countries will identify particularly vulnerable countries. Such information is required to inform the decision making processes so that resilience can be maximised. These decisions are most powerful and influential when made through intergovernmental co-operation and organisations such as the United Nations.

Chapter 2

Literature Review

No corroborated historical evidence exists in the literature to suggest that anyone has died as a result of an asteroid impact (though Yau et al. [1994] study some cases in China where asteroid impacts have been given as an explanation for large casualty events). Furthermore, until 1891 and the discovery of the Arizona crater, there was no evidence to suggest that an asteroid had ever impacted the Earth. In July 1908 a small object entered the Earth's atmosphere and exploded over the Russian tundra near the Tunguska river, first alerting us to the possibility of NEO impacts and their devastating consequences. Thus, only in the last one hundred years has anyone begun to consider NEOs as a natural hazard.

The result of our limited human experience of terrestrial impacts is that we simply do not understand, nor can we predict with any certainty, the events leading to, and the consequences of an asteroid impact. The literature available concerning the three phases of an asteroid impact event - atmospheric entry (as discussed in Section 2.3), land impact and ocean impact (discussed in Section 2.4) - is neither conclusive nor clearly defined, with much still unknown and debated (such as fragmentation, see Section 2.3.1). Furthermore, these three phases of an impact event are currently studied in isolation, meaning that there is no common interface between the models. Thus the task of compiling a unified impact simulator is particularly difficult.

Finally, with the majority of research time and money being spent on object discovery (a large and important task detailed in Section 2.2), the trend of current research is to focus on pre-impact mitigation. These investigations, while worthwhile in terms of providing 'planetary defence', are mostly in preparation for the cataclysmic and highly improbable multi-kilometre 'killer' asteroid. Such research grabs media attention, but diverts the focus away from the real threat of the more probable small impact event. However, the close approach of the asteroid 99942 Apophis has generated a great deal of research interest, particularly in the mitigation prospects for this body or one of a similar scale ($\approx$300 m diameter).

2.1 Historical Background to Asteroid Impact Research

The background to the current field of asteroid impact research stems from the study firstly of impact craters on the moon and other solar system bodies, and subsequently those scars discovered on Earth. The first of these confirmed impact scars was Barringer Crater in Arizona, USA (Section 2.1.1). The largest event in the geological record, the Chicxulub impact in Mexico, is discussed in Section 2.1.1. Of great significance to the field as a whole is the Tunguska event of 1908 - the largest observed impact event in recent times. However, debate continues as to the object's characteristics.

2.1.1 The Earth's Geological Impact Record

Originally, categorisation of each newly discovered crater was based on the probability that it was generated by an asteroid impact [Shoemaker and Eggleton, 196l]. Modern investigations of terrestrial impact structures, however, rely on a number of corroboration factors to prove their extra-terrestrial origin. The primary geological evidence for impact craters is the presence of shatter cones. Shatter cones are formed by high pressure, high velocity shock waves that emanate from the impact which shatter rock layers into conical structures. The conical formations are aligned radially from the crater and enable geologists, such as Dietz [1964], to locate new impact craters. Other indicators are impact metamorphism of the target rock and spherules - small spheres of metal or glass generated by atmospheric ablation of the asteroid's surface [Borovijcka et al., 1998]. Ancient legends, passed on verbally, also suggest evidence for ancient observed impact events. For example the Argentinean 'Campo Del Cielo' craters have the aboriginal name 'Piguem Nonralta' meaning 'Field of the Sky'. These were only recently confirmed as having extraterrestrial origin by Hodge [1994]. Presently 176 impact structures have been identified on Earth [Spray, 2008]. The most recent meteorite, at the time of this writing, impacted Peru on the 15^{th} September 2007 generating a crater measuring 7.8 m in diameter [Hecht, 2007].

Not all structures resemble the classic round crater shape. The Sudbury structure in Ontario, Canada, is an elongated oval-shaped depression 30 by 10 km. Investigations by Boerner et al. [2000] and Morris [2002] have attempted to resolve the entanglement of geological processes which contributed to the crater's odd morphology. The importance of this particular impact is in the evidence that the impact fissure created remained molten for over 1,000 years. Similar magma pool events are hypothesised as evidence for mass-extinction events [Nordt et al., 2002]. Evidence also supports a late Triassic multiple impact event consisting of up to five separate craters, with one in excess of 100 km in diameter, spread over a ground range of 4,450 km [Spray et al., 1998].

Meteor Crater

Meteor Crater in Arizona is widely regarded as the Earth's archetypal impact crater and was the first to be categorised as such. However, in 1891 Grove Karl Gilbert, the head geologist of the US National Geological Survey, visited Arizona to study the crater and proposed that the crater was the result of a volcanic venting phenomena, along the lines of a geyser, as no immediate evidence of material deposit of extra-terrestrial origin was found. The discovery of small iron particles surrounding the site was thought to be coincidental. However, in 1902 it was these iron particles that led Daniel Moreau Barringer to conclude that an iron meteorite had excavated the crater due to the huge energy of impact required. Despite the lack of evidence of the original iron body [Hoyt, 1987], this hypothesis was accepted and the crater was subsequently named after him.

This well preserved and accessible impact crater has been studied in depth to develop understanding of the complex cratering processes. It is believed to have been formed by a 40 m diameter iron asteroid. The publication '*Benchmark Papers in Geology*' by McCall [1977] demonstrates the thrust of terrestrial crater studies undertaken in the 1930s and then the 1960s. The publication also demonstrates the progression in our understanding of impacts as unlikely events to common occurrences and, more recently, a real threat.

Chicxulub Impact, Yucatan Peninsula, Mexico

The largest crater identified in the geological record is the Chicxulub crater on the Yucatan Peninsular, Mexico. In this instance the event was known prior to the discovery of the crater, due to an iodine-rich deposit delineating the Cretaceous and Tertiary rock strata of 65 million years ago. Evidence of ancient tsunami deposits were also identified surrounding the Gulf of Mexico [Smit et al., 2002]. The source crater was eventually identified in 1990 by drilling core samples which probed the structure buried under nearly 1 km of sediment [Urrutia-Fucugauchi et al., 1996].

The media attention given to this particular event over the past two decades has arguably been the greatest driving force behind the field of NEO research. Public awareness has been enhanced regarding the event and its suggested connection with the dinosaur mass-extinction event, though this remains a contentious issue [Smit, 1999; Glikson, 1999, 2005; Kerr, 1997; Pope, 2002]. This high level of interest regarding super-kilometre impacts leaves a gulf in the focus on small objects. Furthermore, the very low impact frequency of these large objects results in a near-zero probability that one will impact within our lifetime. Therefore objects of this super-kilometre scale are not considered further in this study.

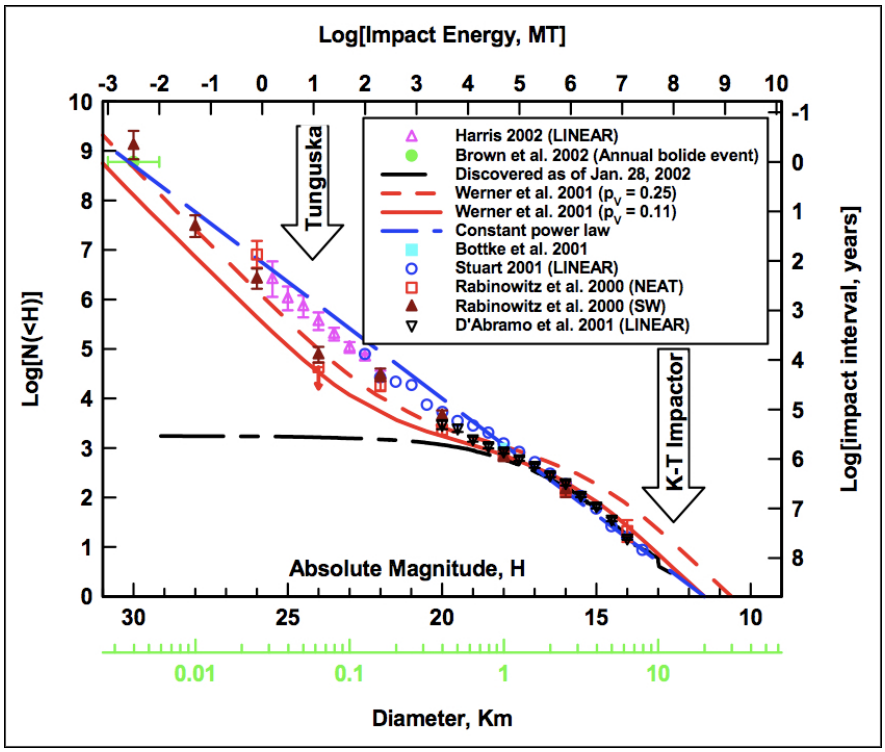

Figure 2.1: Graph by Alan Harris plotting various models to predict the relationship between asteroid size (diameter) and impact frequency. The main axis is the observed absolute magnitude of the body in orbit. N is the population count of asteroids below that magnitude and impact energy is given in the equivalent megatons (MT) of TNT. Originally Figure 2.3 in [Stokes and Yeomans, 2003]

2.1.2 The Tunguska Airburst Event of 1908

The geological record is not a complete account of the Earth's impact history. Very little evidence of small impact events remains, which skews our perception of the threat to focus on large impact events. This missing information is significant due to the inverse size-frequency distribution observed in the NEO population, Figure 2.1. While the very small bodies suffer complete attenuation by atmospheric ablation (seen as shooting stars or bolides [Bland and Artemieva, 2003]), those of the order of a few metres will reach the ground as meteorites.

The Tunguska event of June 30^{th} 1908 provides the only living memory record of an airburst event. The explosion devastated 20,000 km^2 of Siberian forest [Stulov, 2004], an area equivalent to that contained within the M25 motorway surrounding London, UK. Despite many extensive field expeditions no remains of the original object have been recovered, leading to the continued debate concerning the object's origins. Chyba et al. [1993] maintain that the object was asteroidal, whereas Hughes [1976] support the object being of cometary nature.

The cometary hypothesis was first proposed by Whipple [1934] due to the at-

mospheric dust (assumed to be from the comets tail) that reached Europe following the event. Bronshten [2000] notes that the date and radiant were close to that of the Taurid meteor shower, emanating from Comet 2P Encke [Zotkin, 1966], as further evidence pointing toward a cometary origin. Their calculated initial velocity of impact is between 25 and 40 km/s. Grigorian [1998] provides a mathematical model of atmospheric penetration to corroborate his earlier works which supports the cometary hypothesis [Grigorian, 1976, 1979].

Calculations by Lyne et al. [1996] suggest that for an asteroid to have exploded at the observed altitude (as recorded by eye witnesses) the atmospheric angle of attack (ϕ, the angle subtended between the trajectory and the local horizontal) would have been close to 90° (near vertical). Work by Hills and Goda [1993] concludes with a discussion on Tunguska, focusing on the analysis of the fire damage sustained by the forest, showing that the intensity of the thermal radiation was sufficient to ignite the forest below. However, this fire would have bee subsequently blown out by the pressure blast wave generated by the explosion. Cometary objects, they argue, explode higher in the atmosphere so that the generated blast wave would have dissipated and become too weak to extinguish the fire. In Hills and Goda [1998] the conclusion drawn is that the airburst was the result of the explosion of a 50 m diameter stony asteroid.

In their paper, Boslough and Crawford [2008] argue that the object was smaller than this, revising the estimate down to between 30 and 40 m in diameter. Their complex three-dimensional simulation predicts that most objects below 120 m in diameter break apart entirely before they reach the ground. However, their model take into account the momentum of the 'sticky' air surrounding the fragmented body, suggesting that this continues on path to impact the ground with the ability to excavate a crater.

Whatever the original composition of the Tunguska body, it was just large enough to be a significant event despite the object not impacting the ground. Objects smaller than this 50 m threshold will likely be disrupted higher in the atmosphere, becoming increasingly less of a threat. Figure 2.2 also places the lowest hazard limit at the same 50 m diameter threshold. Furthermore, the relative ablative mass-loss for smaller bodies becomes increasingly significant, leading to a greater error in predicting their atmospheric trajectory. Most studies suggest that the Tunguska body was at the lowest range of object densities, either low density ice or porous rock, contributing to its catastrophic breakup. By simulating with a denser stony-iron type asteroid, it seems reasonable to suggest that this 50 m diameter (25 m radius) can be taken as the lower limit for this study. While objects larger than this might still catastrophically fragment, the study will make the assumption that the object will penetrate the atmosphere intact. This accounts for the results by Boslough and Crawford [2008] which indicate the potential for damage on the ground, despite atmospheric break-up of an asteroid.

2.1.3 Asteroid Impact Annualised Casualty Figure

The NASA report on the NEO hazard by Stokes and Yeomans [2003] attempts to quantify the risk to humanity posed by NEO impacts. A basic assessment of the expected casualty figures produced by objects 1 km in diameter and larger combined with the predicted impact rate (using the size-population correlation of Figure 2.1) averaged over time for the unknown asteroid population provides a figure for the number of casualties killed each year by the undiscovered population. Prior to the NASA Spaceguard Survey, discussed in Section 2.2.1, this yearly figure was assessed to be approximately 3,000 deaths per year [Chapman et al., 2001], and the aim of the Survey was to reduce this to below 300 per year by 2008, the nominal value shown in Table 2.1. Large uncertainty remains due to the inherent uncertainty in knowledge of the orbital NEO populations.

RESIDUAL IMPACT HAZARD POST-SPACEGUARD

Casualties per Year	Land	Tsunami	Global
Minimum 81	34%	62%	4%
Nominal 293	17%	53%	30%
Maximum 1105	8%	29%	63%

Table 2.1: Summary of residual impact hazard, i.e. the anticipated annual casualty rate, following the expected conclusion of the Space Guard Survey in 2008. The breakdown on the right hand side indicate the percentages attributed to land impacts, ocean impacts and global scale events. Table 3-7 from Stokes and Yeomans [2003]

This figure of 300 casualties per year is a risk-based measurement of the NEO threat. It can be compared with other estimated risk factors, both natural and man-made, for a particular country. Table 2.2 reproduces such a comparison table from Chapman and Morrison [1994] for the USA. The most striking observation made from this list is that asteroid impacts present a greater risk to the individual than any other form of natural hazard. The reason for this high risk is the potential for a single impact event to cause a widespread disaster generating many millions of casualties. Despite averaging this estimated casualty figure over the low impact frequency, the annualised figure remains high.

However, the NEO threat is the only natural hazard that can be completely mitigated by human intervention. Section 2.5 discusses in more detail the research relating to mitigation. Nevertheless, funding into NEO research remains disproportionately low compared to other much lower risk factors. For example Gerrard [2000] highlights this discrepancy with a study investigating the risk and funding differences between the NEO impact threat and from the very low risk case of a nuclear waste leak induced death. The missing factor is the inability of the public at large to grasp the threat

CHANCE OF DEATH FOR A US CITIZEN

Cause of Death	Chances
Vehicle accident	1 in 100
Murder	1 in 300
Fire	1 in 800
Firearms Accident	1 in 2,500
Asteroid Impact (maximum)	1 in 3,000
Electrocution	1 in 5,000
Asteroid Impact (nominal)	1 in 20,000
Air-crash	1 in 20,000
Flood	1 in 30,000
Tornado	1 in 60,000
Venomous Sting	1 in 100,000
Asteroid Impact (minimum)	1 in 250,000
Fireworks Accident	1 in 1 million

Table 2.2: Chances of an average American citizen dying as a result of various causes [Chapman and Morrison, 1994]

of NEO impacts; it is simply not something that worries the public consciousness. Therefore, it is an important aspect of this project to develop indicators that can be understood easily by the general public, to increase awareness.

Figure 2.2 presents the residual risk of each diameter bin following the survey completion. Error on the super-kilometre size bins remains high and the greatest single hazard is still associated with these bodies. Peter et al. [2004] argues that these bodies remain the most pressing hazard. However, studying the nominal curve, the cumulative hazard for the sub-kilometre diameter bodies begins to out weigh that of the larger objects as an increasing proportion of the large diameter NEOs are discovered.

The frequency of this population is such that the probability of witnessing an impact becomes increasingly significant. An estimation of the time between impacts of an object with particular energy, the recurrence interval in years, $t_{recurrence}$, is given by Collins et al. [2004] as

$$t_{recurrence} = 110 E_{mt}^{0.77} \tag{2.1}$$

where E_{mt} is the kinetic energy of the body in MT. The difficulties of detecting these small bodies will decrease the likelihood of detecting an impacting body with enough time to mitigate the threat. It is this population, in particular, that the project will focus upon.

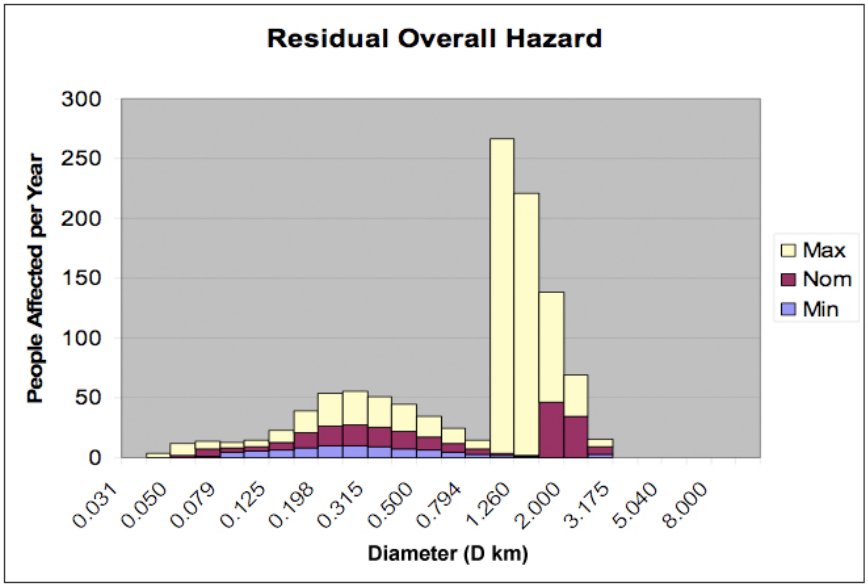

Figure 2.2: The remaining hazard following the Spaceguard Survey attributed to each size bin (diameter, D). The three colours relate to the same minimum, nominal and maximum asteroid population estimates as shown in Table 2.1. This residual hazard is that hazard presented by the undiscovered population. Originally Figure 3.11 in [Stokes and Yeomans, 2003]

2.2 Orbital Asteroid Surveys and Catalogues

The natural hazard exists due to the possibility that an asteroid could impact Earth. While there remain objects that have not been observed an catalogued there remains the potential hazard that an object may impact Earth. By detecting and cataloguing the orbital asteroid population the potential impact hazard is mitigated. Near Earth asteroid surveys are, therefore, the leading means for mitigating the hazard and NASA's Spaceguard Survey is the primary contributor. If, during the cataloguing, a threat is identified, then time is provided to act to mitigate that threat. The view being taken is that it is better to know about a threat than experience an impact unawares.

2.2.1 Telescopic Surveys

Originally Morrison [1992] proposed the establishment of a 25 year NEO survey to catalogue the entire population. This was followed by a report by Shoemaker [1995] which recommended the target of cataloguing 90% of the NEO population within fifteen years. Both of these proposals failed to gain funding, but lead to the Spaceguard Survey being established in 1998 by NASA as a worldwide co-ordinated effort to detect and catalogue 90% of all Near Earth Objects greater than 1 km in diameter within a ten year period. It was the first co-ordinated search effort of its kind. The 1 km diameter baseline was chosen by the threshold brightness (albedo) of these large

bodies. Based on existing observations of known asteroids of this size, the original limiting magnitude H = 18.0 was taken from the thesis of Stuart [2003]. Work by Stuart and Binzel [2004] has subsequently refined the measurements of asteroid albedo showing that they are 20% brighter than previously assumed, and so reducing the limiting magnitude to H = 17.75.

Figure 2.3 provides a graph of the number of NEOs catalogued every six months attributed to each observatory. The plot shows that the number of new observations is gradually tailing off despite new observatories coming online. This is an indication that the catalogue is nearing completion with fewer unobserved objects remaining. LINEAR has proven to be the most successful NEO observatory, with the recent Catalina observatory also making a significant contribution to the ongoing cataloguing process. The combined result of the Spaceguard Survey is, unfortunately, expected to fail to complete the 90% objective by 2008. Of the expected 990 large NEOs, 76% (752 bodies) had been discovered by the first half of 2008 [NASA - JPL, 2008a].

The NASA report by Stokes and Yeomans [2003] investigates the feasibility of extending Spaceguard to search for objects of smaller diameter. Multiple survey techniques are investigated, including ground telescopes and spaced-based observatories in low Earth orbit or at the Lagrangian points. The report suggests that a new target of cataloguing 90% of objects greater than 140 m in diameter within a 7-20 year time scale should be adopted. The report sets this lower limit, suggesting that below this, the impact consequences would be significantly reduced or eliminated by atmospheric attenuation. The report also mentions that comets will account for approximately 1% of the threat and so should not be searched for specifically due to their unpredictability and infrequency. This view has been adopted and the project will limit its investigation to NEOs of asteroidal origin.

2.2.2 Asteroid Discovery and Impact Event Prediction

Position information comprising a new observation are first cross-referenced with the existing catalogue of asteroids to identify whether it is a new discovery. If the object is new, the observational data is sent to the Minor Planet Center in Cambridge, Massachusetts [IAU, 2008], which uses the automated online 'Near Earth Orbit Dynamic System' (NEODyS) to make an initial assessment of the object's position and orbit and then publishes the data [Milani, 2005]. Publishing each new asteroid observation online allows astronomers across the world to make rapid follow up observations of the object, which are fed back into NEODyS to increase the accuracy of the orbit prediction. Three observations are required for the minimum orbit determination accuracy, followed by two further observations within seven days, and then a third within one month. The asteroid's future orbits are simulated to identify possible

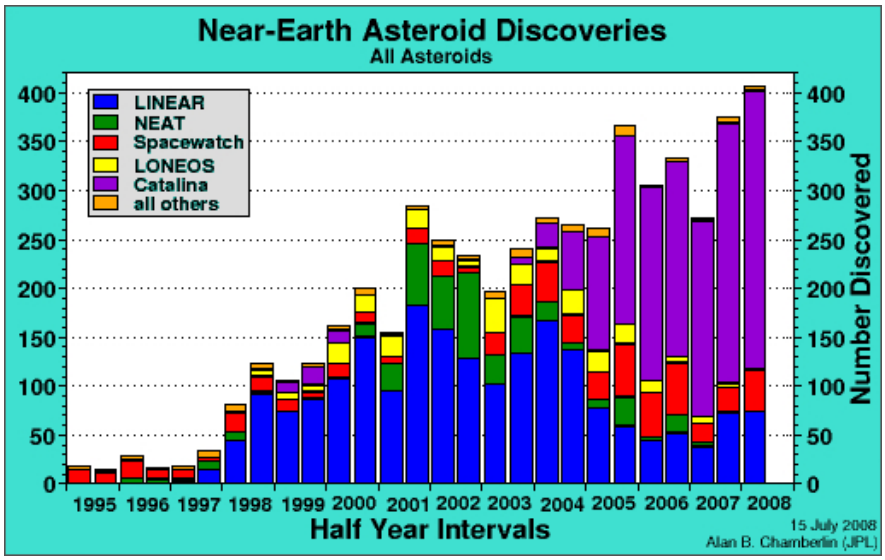

Figure 2.3: Rate of Near Earth Asteroid (NEA) detection in half yearly bins for the various survey telescope systems world wide as part of the NASA Spaceguard Survey. Taken from [NASA - JPL, 2008a]

planetary orbit intersections. The system also checks previous observational records, in case the object was previously discovered and lost. This function is particularly pertinent in the case of asteroid 99942 Apophis which, when first observed in late 2004, rose significantly on the Torino hazard scale due to an initially inaccurate orbit determination which suggested a significant impact risk in 2029. Subsequently, previously unidentified observations from March of that year were discovered which refined the orbit, and this significantly reduced the impact probability.

The ranging error inherent in optical observations (based on predictions of the asteroid's albedo) demands multiple observations to accurately define the orbit characteristics. Preliminary orbit determination from initial observations will provide some prediction of an object's impact probability. As new observations are made, the errors in the orbit determination will gradually reduce, narrowing the uncertainty region around the asteroid and refining the impact probability. For those objects identified with a potential impact point in the future, this uncertainty region can be projected onto this future orbit intersection plane as an ellipse in which the Earth lies. As the orbit is refined this ellipse is reduced in size. While the Earth remains within this ellipse, the reduction will act to increase the impact probability (and risk) [Chapman, 2004]. However, eventually as the ellipse is shrunk, the Earth will fall outside it, removing the impact risk entirely. The consequence of this is that any identified potential impacting object will experience this risk response as the orbit is refined. If the impact probability was plotted it would show a gradually rising curve, followed by a sudden drop.

The same effect will occur for objects with close approaches to Earth[1]. Asteroid 99942 Apophis presents such a keyhole opportunity during its close approach in 2029. When an asteroid passes a planet its orbit is deflected to an extent dependent on its proximity to the planet. At some points in particular, the orbit will be deflected to such an extent that the asteroid's subsequent orbit will be on collision course with the planet. These particular locations at the point of closest approach to the planet are called keyholes, see Figure 2.4. The region of orbit uncertainty at the point of closest approach (here represented as a line rather than ellipse) may cover one or more of these keyholes, resulting in a non-zero impact probability. Refining the orbit reduces the uncertainty region but increases the Impact Probability (IP). While a keyhole remains in the uncertainty region, decreasing the uncertainty will increase the impact probability until the keyhole is eventually falls out of the uncertainty region [Milani et al., 2002]. Public perception of this process will be affected by this IP curve. Multiple impact probability 'scares' will act to lower public trust in the surveying efforts by repeatedly predicting impacts that never happen. Chesley [2007] discusses the changing public perception of the NEO hazard and the consequences for mitigation missions.

2.2.3 Classification and Predictions of the Target Asteroid Populations

An object is classified as a Near Earth Object if the Minimum Orbit Intersection Distance (MOID) between the object's and Earth's orbit is 0.5 AU (Astronomical Units) with perihelion distances $q \leq 1.3$ AU and aphelion distances $Q \geq 0.983$ AU. The majority of NEOs are Near Earth Asteroid's (NEAs) with comets only accounting for less than 1% of the population. Three classes of NEA define the population in relation to their orbits relative to Earths, defined in Table 2.3. A subset of the NEO population are Potentially Hazardous Objects (PHO). While not a particular threat, an object is classed a PHO when its MOID is smaller than 0.05 AU [IAU, 2008].

Population estimates for NEA's assume a constant power law, with the number of objects, N, larger than a particular diameter D in km given by

$$N(> D) = 1148 D_{neo}^{-2.354}. \tag{2.2}$$

Assuming that PHOs account for only 21% of all NEOs, according to the observations [Stokes and Yeomans, 2003], the PHO population can be expressed as

$$N(> D) = 198 D_{neo}^{-2.354}. \tag{2.3}$$

[1]Which results in a deflection of the asteroid's trajectory so that an impact occurs on a subsequent orbit

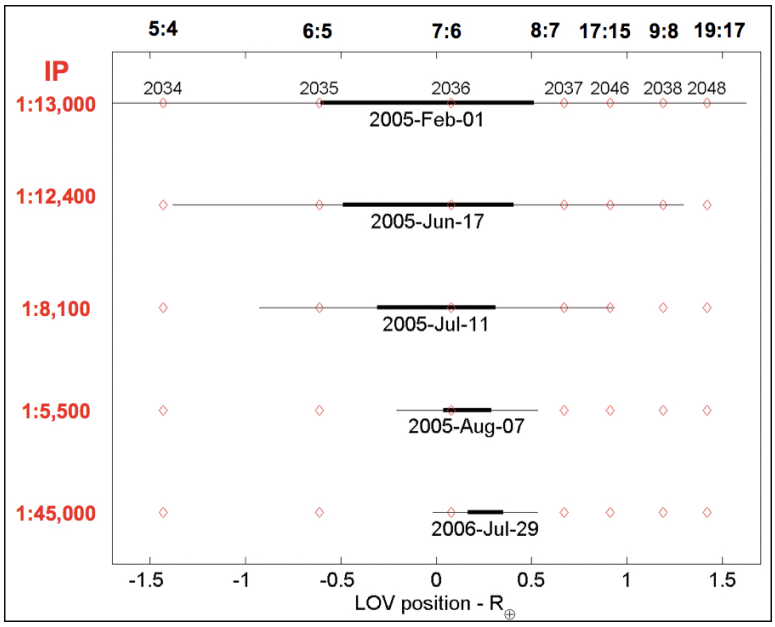

Figure 2.4: The black like is the plot of orbit uncertainty for asteroid 99942 Apophis at the point of closest approach in 2029. The impact probability (IP) is provided in red on the left hand side which is based on the probability that the asteroid's location coincides with a red circle. These small circles are the orbit solutions which will result in a subsequent impact., known as keyholes. As repeated observations improve the orbit definition the probability is seen to increase until the probability region is finally removed from the keyholes. The primary axis is the Line Of Variance (LOV) indicating the asteroid's orbit prediction accuracy, and the top scale identifies the resonance returns for the orbit keyholes. Page 8 in Chesley [2007]

Classification as a PHO does not imply that an asteroid *will* impact Earth, rather that it warrants continuous observation as orbital perturbations, for example gravity, could alter the orbit onto a collision course. Asteroid 99942 Apophis is a case in point, with the potential for it to pass through a keyhole in 2029. Other perturbing forces exist, such as the Yarkovsky effect described by Farinella et al. [1998], where the solar illumination and the resultant emitted thermal radiation act to thrust the body. The continuous nature of these minute perturbations demands regular repeat observations of all bodies in the catalogue, to maintain accurate orbital predictions and to update future impact possibilities. Here radar observations are critical, due to their unparalleled ranging accuracy; sensors such as the Arecibo dish in Puerto Rico remain a vital asset.

Asteroids are also classified by composition, Table 2.4 details the three primary categories of NEAs. Complete compositional classification of the asteroid population leads to over 20 types. Identification of an object's composition is based on its observed albedo and calculated distance from Earth, together with spectroscopic analysis of the reflected light. While compositional data is relatively simple to acquire, data concerning the internal structure remains more elusive.

NEA ORBIT CLASSIFICATION

Class	Orbit Description	Perihelion	Aphelion	Semi-major Axis
Aten	Earth orbit crossing (inside)		$Q \geq 0.983$ AU	$a \leq 1.0$ AU
Apollo	Earth orbit crossing (outside)	$q \geq 1.0167$ AU		$a \geq 1.0$ AU
Amor	entirely outside Earth's orbit	$1.0167 \text{ AU} < q \geq 1.3$ AU		

Table 2.3: Characteristics defining the three principle NEA populations based on their orbit classification.

NEA COMPOSITION

Type	Composition	Density	Population
C	carbonaceous chondrite	2,200 g/cm^3	75%
S	stony-iron	3,500 g/cm^3	15%
M	iron-nickel alloy	7,900 g/cm^3	8%

Table 2.4: The three primary classifications for NEAs based on their chemical composition. Density varies within the population but the value here represents the average and will be used henceforth.

2.2.4 Understanding an Asteroid's Internal Structure

Theories of asteroid formation through successive collision and cohesion of smaller bodies leads to the notion that not all asteroids will be single monolithic bodies. The other option is that the asteroids are weakly coalesced collections of smaller fragments, termed a 'rubble pile'. Only a handful of asteroids have been studied closely. NASA Applied Physics Laboratory's NEAR mission to the monolithic asteroid Eros [APL, 2002; Miller et al., 2002] and JAXA's Hayabusa mission to the rubble-pile asteroid Itokawa [JAXA, 2006; Fujiwara et al., 2006] are key examples. For rubble pile asteroids, such as Itokawa, accurate close-proximity analysis is key to our understanding of the internal structure. This analysis is vital to understanding and modelling the behaviour of the asteroid to potential mitigation strategies. Even after these expensive asteroid rendezvous missions, our understanding of the structure of the asteroid population remains limited. In order to address this, the number of visited NEOs must be significantly increased, possibly through the use of multiple micro-satellite launches [Wells et al., 2006].

Studies of asteroid spin rates have given credence to the rubble pile theory. Figure 2.5 presents the data by Pravec and Harris [2000] which indicates a so-called spin barrier. Larger objects (those above 150 m diameter) are largely confined to low rotational rates below the barrier, whilst small bodies are found with much higher spin rates. The conclusion is that as spin rate increases, the centripetal acceleration overcomes the internal cohesive force and the object breaks apart into its component monolithic

bodies [Pravec, 2006]. The relevance of this finding to the study undertaken in this thesis is in the investigation of the atmospheric passage, in particular fragmentation, discussed further in Section 2.3.1.

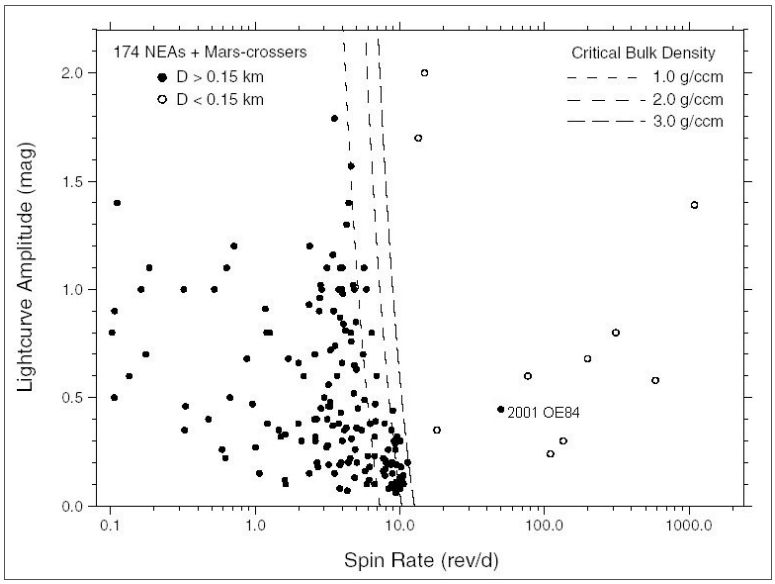

Figure 2.5: Orbital asteroids' spin rate data for two asteroid size ranges. The spin barrier is clearly demonstrated around 10 revolutions per day. The lightcurve amplitude is a measure of the variation in observed brightness of the asteroid as it rotates. Larger values indicate elongated asteroid shapes, while smaller values indicate spherical shaped bodies. Figure 8 in [Pravec and Harris, 2000]

2.3 Atmospheric Entry of the Body Prior to Impact

Bland et al. [1996] estimates that the yearly mass-flux of small meteorites into the Earth's atmosphere is between 2,900 kg and 7,800 kg. This does not account for the mass flux of dust sized particles which could contribute in the order of 80,000 kg per year. Larger objects which enter the atmosphere are seen as fireballs or 'bolides' as they burn up. Study of their fragmentation processes offers some insights into the aerodynamic processes acting during entry. Fragmentation and ablation theories constructed from these small diameter objects can be applied to larger asteroids.

2.3.1 Fragmentation of the Body

Australia's impact history is particularly well documented due to limited vegetation and tectonic activity, which usually act to obscure these features. The result being that even small impact scars remain visible. The Henbury formation is one such example with craters as small as 6 m in diameter clearly visible [Hodge, 1965]. The Sikhote-Alin impact event in the far East of Russia in 1947 is the only documented observed frag-

mentation event to produce impact craters [Ivanov and Ryzhanski, 1997; Grokhovsky et al., 2001]. The significance of both events is their evidence of fragmentation during atmospheric entry. Fragmentation is frequently observed in the re-entry of man made objects, for example MIR Space Station and the tragic event of the Columbia Space Shuttle [Langewiesche, 2003].

This large scale break-up is not a means of mass loss (such as the process of ablation, see Section 2.3.2), though through increasing the surface area, ablation will be increased. The most influential work on atmospheric fragmentation is by Hills and Goda [1993] and Bronshten [1995]. Their comprehensive results are presented in a series of figures plotting different aspects of asteroid fragmentation. Each figure in their paper presents the fragmentation response of different NEO types over a range of velocities. Two models dominate the literature, the Gross Fragmentation model proposed by [Hills and Goda, 1993] and the later Pancake Model by Lyne et al. [1996] based on the earlier work by Chyba et al. [1993]. A third model was proposed by Grigorian [1979, 1998], but this has gained little support. A full description of these models is available in the internal report by Bailey [2005].

The importance of fragmentation is critical to our understanding of the impact hazard and as such should be considered in this study. However, uncertainty in our understanding of the pre-entry structure, and the dominant influence this will have on the nature of the fragmentation, makes accurate fragmentation simulation impossible. As such, only a simple study will be attempted, investigating the difference between single and multiple impact events, (discussed in Section 6.3). The software system tool will be designed with an embedded fragmentation model which can be updated to enable proper consideration of these events at a later date (for example, if a particular threat is identified and its internal pre-fragemented structure known).

2.3.2 The Process of Mass-Loss During Ablation

Ablation is the mass-loss due to heating from friction as the object passes through the atmosphere. Erosion and vaporisation are the typical modes of ablation and occur as a gradual process during entry flight. Ablation is particularly significant for very small NEOs, where the mass lost becomes a significant proportion of the overall mass [Stulov, 2004]. The processes are typically neglected for NEOs above 1 km in diameter due the negligible impact on overall mass. Grigorian [1998] shows how ablation can alter the analysis of an impact event, while Kalashnikova et al. [2000] investigate the nucleation of mesospheric ice crystals around ablation particles linked to climate change.

Lyne et al. [1996] provide a concise review of the wide ranging ablation theories from the first work by Bronshten [1983]. Authors such as Svetsov et al. [1995] con-

clude that, for objects of the order of several metres in diameter, only the mechanical processes of fragmentation should be considered; others like Bland and Artemieva [2003] include an ablation term to calculate the change in mass as material is burnt off the surface. The most widely accepted system is the two-regime system by Chyba et al. [1993] and Chyba [1993], which takes 30 km as the transition between the high altitude, low ablation rate phase, and the high ablation rate phase through the lower atmosphere.

2.3.3 Airburst Explosions in the Atmosphere

Airbursts are the culmination of sudden fragmentation and complete ablation in an instantaneous explosion above the surface. A hypersonic blast wave is generated by the explosion, and it is this that impacts the Earth's surface, rather than the body itself. A thermal radiation flux is also generated by the exploding 'fireball'. The altitude of the break-up will determine the extent to which the blast energy is dissipated by the time it reaches the ground.

The Tunguska event of 1908 is the most famous airburst event recorded [Stulov, 2004]. It caused the destruction of over 2,200 km^2 of Siberian forest but left no observable impact crater [Jensen, 1998]. Calculations by Hills and Goda [1993] provide the rate of energy deposition as a function of the airburst altitude. This provides a means of identifying the characteristics of an object based on its observed or calculated break-up altitude. This point is termed the half energy height, h_{half}, and leads to the conclusion that the Tunguska body was about 50 m in diameter. As it was for fragmentation, so our understanding of an object's susceptibility to airburst is limited by our lack of knowledge of the original structure and composition. While we can study airburst events and predict the conditions prior to impact, it remains unclear how to predict whether or not a particular object will suffer airburst or not. Therefore, airburst events will not be studied further, and the assumption that all objects studied will reach landfall is adopted.

2.4 Effects and Consequences from Asteroids Impacting Earth

Following the ablative mass-loss and associated energy and trajectory alterations, the object will impact the Earth. At the point of impact, which can either be on land or in the ocean, a range of Impact Generated Effects (IGEs) are produced. These include an air blast wave and ground shock wave from land impacts and tsunami from ocean impacts. Each one will have an effect on human populations and infrastructure around the globe. These impact consequences are the primary factors for assessing the severity of an impact event.

2.4.1 Land Impacting Asteroids

Studies of asteroid impacts are limited. This is due to the absence of observational data from actual events. As no impacts have been predicted beforehand, none have been specifically monitored and scientifically recorded. Thus, most data stems from human witness observations and post-impact field research. Studies attempting to quantify the effects of impacts are limited to two fields: Nuclear weapon research, and the utilisation of complex hydrocode simulations to model crater formation. Pierazzo and Collins [2003] provides a detailed introduction to hydrocode simulation research and its application to asteroid impact studies. Ivanov et al. [1997] successfully applied hydrocode models to analyse extra-terrestrial craters, while Ailor [2007a] investigated their application to ocean impacts. However, these simulations are computer intensive and can only be used to model individual events.

The detonation of atomic devices represents humanity's largest explosive release of energy and, as such, they are our closest approximation to the energy released by an asteroid impact. Differences exist in the mode of energy generation (nuclear fission as opposed to kinetic energy) and the subsequent consequences from nuclear fallout. However, studies of subterranean detonations have led to models of the four principal IGEs: the pressure blast wave, the seismic shock wave, the fire ball radiation flux, and the ejecta excavated from the crater. Collins et al. [2002] utilises atomic test research (predominantly using data classified by the United States Military) to develop energy scaling models of the IGEs. These are detailed in Section 3.1.2. Ocean impacts have been investigated separately, with models for the initial cavitation derived from experimental tests by Ward and Asphaug [2000]. The subsequent tsunami model has been developed from models of tsunami generated by geological processes (such as landslides and sub-ocean earthquakes). Research on ocean impacts is discussed further in Section 2.4.2.

Terrestrial Crater Formation and Processes Associated with Land Impacts

At the point of impact, the object's kinetic energy is deposited into the rock strata beneath 'ground zero'. This energy will cause an explosion with part of the energy reflected into the atmosphere as a fireball and blast wave, and partly into the ground excavating a crater out of the rock and generating large seismic shock waves. The formation of the crater occurs in two stages. Firstly, a transient crater forms, which is shaped as material is initially excavated by the explosion. Secondly, the residual crater formation takes place, as the ground movements cease and the ejecta lands. The final crater morphology will depend on the size and trajectory of the impactor but also partly on the local geological conditions. Small objects produce 'simple' bowl-shaped

craters which are similar in form to the transient crater but slightly wider and with some in-filling by the ejecta. Larger impacts will generate 'complex' craters which have a single central uplift peak or a central uplift ring.

During the era of nuclear proliferation, the testing of nuclear devices, such as those at Los Alamos [Glasstone and Dolan, 1977], provided studies of high energy explosions. Parallels between nuclear detonations and meteorite impacts can be drawn, and impactor energy is often referred to in terms of megatons (MT) of TNT in the literature. This report will adopt the standard of using energy specifications in the SI unit of joules, with $4.185\text{x}10^{15}$ J equivalent to one megaton of explosive. The typical yield of nuclear tests only reach a few megaton, which is insignificant compared to the Chicxulub impactor $\approx 4\text{x}10^{23}$ J [Sagy et al., 2002]. High energy nuclear tests have produced shatter cones similar to those found around asteroid impact craters, as well as blasts waves, fireballs and shock waves that are assumed to parallel impact generated effects. However, the craters generated from nuclear tests are typically not congruent with NEO impact craters.

Land Impact Generated Effects

Collins et al. [2004] and Collins et al. [2005] provide an excellent overall view of the consequences of an asteroid impact for an observer located some distance, r, from the impact site. Four principle IGEs are assessed - ejecta material from the crater, an atmospheric blast wave, a seismic shock wave and the radiated thermal flux from the explosion fireball. These four effects, as well as the destruction caused by the crater formation, will be principle mechanisms modelled in the software system. Land craters are formed in two stages: the initial transient crater excavated by the impacting energy and then, following the settling of the excavated material and the dynamics of the rock strata, the final crater shape is attained [Wallis and McBride, 2002].

Ejecta is terrestrial material forced into the air during the excavation of the transient crater by the impact energy. This material is ejected from the impact site at varying velocities and trajectories, with a range of fragment sizes from fine dust to large boulders. Deposition of this material in the surrounding region forms the 'regolith', which will generate damage through collisions with humans and infrastructure. For larger ejecta, the fragment size can be determined based on an empirical law derived from ejecta patterns found on Venus by Korycansky and Zahnle [2004]. Pope [2002] suggests that smaller particles ejected could lead to climate change, an effect which increases in significance for larger scale impact events. Of the many meteorites discovered on Earth, more than ten have been assessed to be of Martian origin. The indication is that they are likely to be ejecta material from an asteroid impact on Mars. This prompted work concerning the velocity profiles of ejecta by Head et al. [2002] to

discover how material can be ejected at speeds greater than the planet escape velocity.

The impact explosion will generate a large fireball, similar to the mushroom cloud characteristic of nuclear explosions. Parallels can be drawn with the effects of the atomic devices dropped on Hiroshima and Nagasaki [Holdstock and Barnaby, 1995]. While the cloud will not be radioactive, a large flux of infra-red radiation will be released. This thermal radiation flux will cause further damage to the surrounding region, especially to humans. The fraction of the impact energy, E_{imp}, that generates the fireball is found to be $\eta = 0.0003$ [Nemtchinov et al., 1998]. As the fireball expands it also cools. In the initial phase the cloud is so hot that it appears opaque and the radiation is largely contained. However, as the cloud cools below the opaque transition temperature of $T_{trans} \approx 3,000\,\mathrm{K}$, the cloud becomes transparent to infra-red radiation, and the peak radiation is released causing the most damage.

As the blast develops, the extremes of heat and explosive pressure cause the surrounding air to expand sharply followed by a sudden contraction. This is transmitted from the impact site as the characteristic pressure blast wave typical of all explosive events. The pressure difference across the shockwave is called the peak overpressure P_{peak}, and can be manipulated to find the peak wind velocity behind the shock front. In the subsequent modelling process the magnitude of this wind velocity is used to assess the damage sustained, drawing on assessments of actual damage from measured wind speeds.

The final IGE modelled is a seismic shock wave. This is analogous to an earthquake generated through tectonic processes and is measured using the same Richter Scale. The decay of the shock strength with increasing distance will map a series of concentric rings around the impact site of equal Richter magnitude. Damage can then be assessed by studying the damage sustained from historical earthquakes of corresponding magnitude.

2.4.2 The Hazard from Ocean Impacting Asteroids

Geologically generated tsunami are more common than impact-generated events, and thus have been studied more widely [Hutchinson et al., 2000; Ward, 2001; Fritz et al., 2004]. The most famous historical tsunami event prior to Boxing Day Tsunami of 2004, was the result of the 1755 Lisbon earthquake. Fires ignited by the quake in the city caused people to flee to the coast for safety. However, the quake also generated a tsunami, which, a short time later, inundated the coastline and killed many of those fleeing the city [Chester, 2001]. Other notable geologically induced tsunamis include the 1883 eruption of Krakatoa, the 1960 Chilean earthquake and the Good Friday Tsunami of 1964, which struck the west coast of North America. The calculated peak wave amplitude of the tsunami generated by the 9.5 magnitude Chilean earthquake

(the largest ever recorded) was 10.7 m at a distance of 10,000 km. Fortunately it only killed 1,886 people, but it caused an estimated $ 675 million of damage to infrastructure [USGS, 2008c].

Recent endeavours to mitigate the tsunami threat depend on the development of early warning systems, such as the Pacific Tsunami Warning Center [NOAA, 2005]. By providing early warning of an approaching tsunami to coastal communities, they can be evacuated to mitigate the potential casualty numbers, though no system is in place to organise evacuations. The Sumatra tsunami on Boxing Day 2004 highlighted the devastating power that a tsunami can wreak. It generated the largest tsunami-induced casualty figure on record and one of the largest natural disasters in recorded history. Several factors contributed to the high casualty figure, predominantly the proximity to many highly populated coastal regions, the lack of a warning system, and the limited evacuation infrastructure. The consequences were felt most severely in the less developed countries such as Sumatra, whereas countries such as Thailand received the majority of the media attention [Smith et al., 2004].

Tsunami research is extremely relevant to the current study, as an asteroid impacting the ocean will generate a tsunami wave. However, the potential amplitude of an impact generated tsunami as it shoals onto the coastline exceeds that of geologically induced tsunami waves. The subsequent consequences for humans and infrastructure are equally increased. Recent research by Haslett and Bryant [2007, 2008] around the UK has identified the earliest human recorded evidence of tsunami inundation in 1014. This particular tsunami was witnessed along the Bristol Channel and is regarded as Britain's worst natural disaster. The particularly important factor in this event is the corroborating Arctic ice-core investigations by Baillie [2007] which suggest the tsunami was generated by a cometary fall into the Atlantic Ocean.

Ocean Impact Cratering - Cavitation

Much work on the modelling and simulation of tsunami events has been done by Steven Ward and Erik Asphaug at the Institute of Geophysics and Planetary Physics, University of California. Ward's research originally focused on geophysical processes, primarily plate tectonics and earthquakes which link with tsunami generation. More recent publications have specifically focused on asteroid impact generated tsunami [Ward and Asphaug, 2000]. Working together, Ward and Asphaug [2002] have investigated generation, propagation and the probabilistic hazard associated with an ocean impacting asteroid. The probabilistic hazard technique involves integrating over the entire asteroid size range the probabilities of a location being inundated by an impact tsunami wave in a particular time frame. The potential threat of a tsunami generated by the collapse of part of the La Palma volcano, in the Canary Islands, into the Atlantic

Ocean has also prompted recent simulation work by Ward and Day [2001].

Classical tsunami theory, as presented by Ward [2000], assumes that the ocean is incompressible, homogeneous, and a non-viscous fluid under a constant gravitational field. Ward applies eigenfunction analysis to the three modes of tsunami generation: Earthquake, landslide (surface or submarine) and asteroid impact. The impact solution assumes that an initial parabolic cavity is generated by the impact energy with a depth d_{cavity} m and radius R_{cavity} m. By modelling the ocean surface velocity conditions at various locations radiating out from the impact site, the tsunami wave can be modelled.

The predicted cavity depth is compared to the local ocean depth. Where the predicted depth is deeper than the ocean floor the cavity is said to have 'bottomed out' and, in such a scenario, some small excavation of the ocean floor is made. The lesser of the two depths is used as the effective cavity depth, d^{eff}_{cavity}, for subsequent calculations.

Tsunami Propagation Across the Ocean

Tsunami waves are propagated as the transient cavity rim collapses into the cavity. A central peak splash occurs and then continues to oscillate with successively reducing amplitude, issuing a wave train that radiates out from the impact site. The speed of tsunami waves is a function of ocean depth, but is approximately 0.2 km/s. This concentric radiating wave is diffracted by variations in ocean depth (with shallow water reducing wave speed and increasing deflection) and subsequently around continental land masses. Thus inundation may occur in areas that do not have a direct line of sight of the source.

In an ideal ocean, of open uniform-depth, the impact tsunami would radiate out as a series of concentric rings with the wave amplitude attenuated by distance from source. Real oceans vary in depth and have various land masses which interrupt the pattern. Differences in ocean depth will reduce the wave velocity and thus diffract the wave path, much as light is diffracted by dense media. Furthermore, interference of reflected or deflected waves result in an intricate pattern of peaks and troughs rather than simple concentric rings. The result is that the characteristics of the tsunami wave reaching landfall is far more complex than the original propagating splash. Accurate modelling of such complex waveforms, though possible, is expensive in terms of computing time, requiring a dedicated computer simulation [Ward and Asphaug, 2002].

Figure 2.6 presents a view of the real Indian Ocean Tsunami of 2004 with the wave height colour coded. The wave is a complex mix of peaks and troughs. Chesley and Ward [2003] limit their study to only the peak wave in the wave train and model

the effects of this wave as it reaches landfall - the process of shoaling. It is important to note that in open ocean, the wave amplitude is very small, typically below 1 m, whereas it is in the process of shoaling that the wave height increases dramatically and forms the expected large beaching waves, with heights in excess of 20 m.

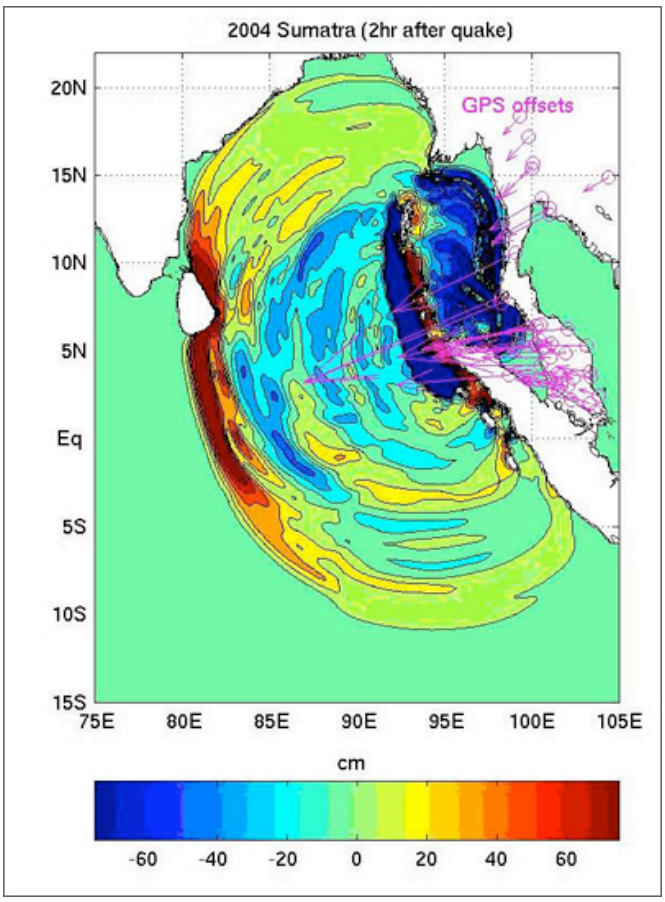

Figure 2.6: Displacement of the ocean surface two hours after the Sumatra earthquake of the 26th December 2004. The purple arrows indicate GPS data used to measure the surface displacement. Wave crests are shown in red with troughs in blue, demonstrating the complex makeup of a real tsunami wave. (Credit NASA/JPL)

Coastline Conditions for Tsunami Shoaling

As the tsunami approaches the continental shelf and shallower water, the characteristics change causing an increase in the wave amplitude and wavelength, as demonstrated in Figure 2.7. Run-up follows either an exponential build-up to the point where the tsunami breaks like a beach wave, or else the wave gradually rises up the beach, inundating it. Records and observations of tsunamis show both sequences can occur in close proximity due to a high dependance of the particular local bathymetry [Matsuyama et al., 1999]. For example, following the Sumatra earthquake two observers in the same ocean bay witnessed different inundation conditions [Siripong, 2006].

Typical shoaling wave heights from a geological induced tsunami are in the order of a few tens of meters [Chester, 2001]. Comparatively, expected shoaling wave heights from an ocean impacting asteroid 1 km in diameter are expected to be in the order of a hundred metres [Ward and Asphaug, 2003].

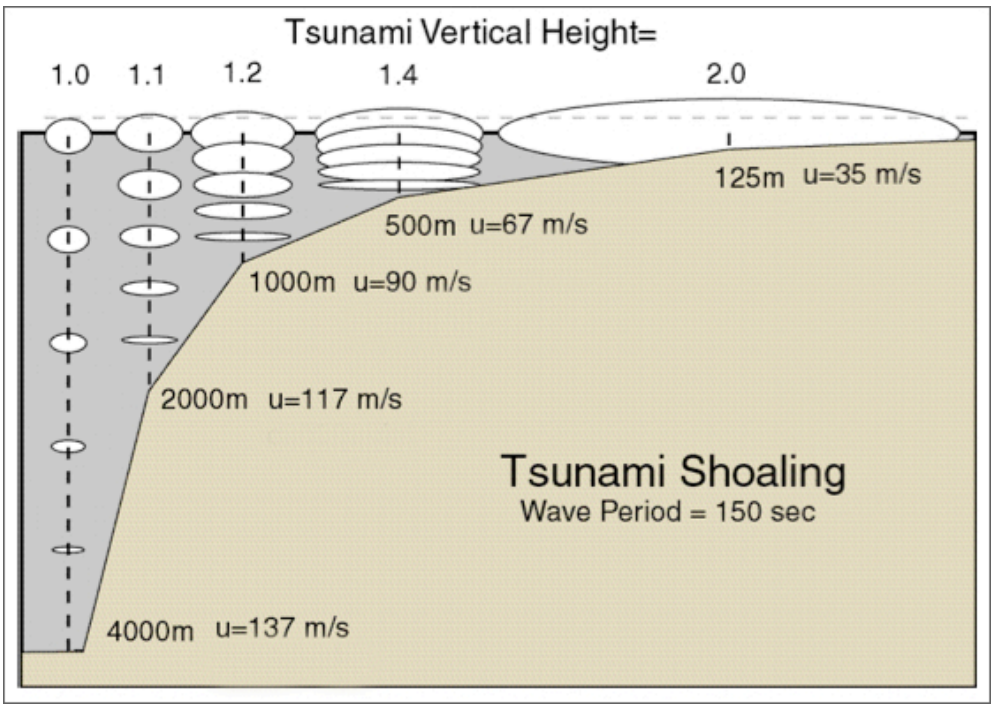

Figure 2.7: Cartoon of a shoaling tsunami wave from a generic source. As the ocean shallows close to landfall the wave is compressed into a smaller volume. As a result the amplitude increases in a process called shoaling. In this figure, 'u' is the wave speed. From Figure 11 in Ward [2000]

Consequences from Ocean Impacts

Coastal areas across the world are frequently the most densely populated region of a country, due to the natural resources the ocean offers, combined with its trading opportunities. Despite air travel, oceanic transportation remains the major system of world trade. This places high importance on a country's ports, frequently resulting in them becoming the capital city [Nicholls et al., 1999]. Recently coastal communities have been alerted to the threat of rising sea levels due to global warming. The low lying nature of many major coastal cities places a large global population at risk from this flooding and the tsunami hazard is a further risk factor.

Inundation of a coastline by a tsunami as it shoals is specified by two main properties of the wave: the run-up and run-in. Run-up, can be taken as a measure of tsunami severity - i.e. the height of the shoaling wave - while run-in predicts the inland reach of the wave, which can be many miles for large tsunamis. The

long wavelengths of tsunamis (of the order of kilometres), multiple wave peaks and the huge volume of water involved underlies the incredible power and potential for destruction of this hazard.

2.5 NEO Threat Mitigation - Opportunities and Risks

As detailed in Section 2.2.1, the mitigation of the NEO threat primarily relies on telescopic surveys eliminating the unknown hazard. This is a largely passive means of mitigation. However, should a particular threat be discovered, an active mitigation strategy would need to be implemented. This would be a space-based mission designed to physically manipulate the object's orbit to remove the threat of impact.

The primary mission objective would be to alter the object's orbit in order that it does not collide with Earth. The lowest energy procedure for achieving this is by providing a δV to the object along track. This orbit deflection essentially acts to alter the time at which the asteroid crosses Earth's orbit, making it either before or after the Earth occupies that crossing location. Uncertainties and errors in orbit prediction result in a persistent degree of uncertainty in the object's true position. Therefore, mitigation missions would likely require a rendezvous mission to place a transponder on or near the asteroid in order to accurately pinpoint the NEO's true location.

2.5.1 Space Based Mitigation Mission Options

Mitigation missions proposed fit into three categories: gravity tractor, kinetic impacts and nuclear detonations. Each mission type has its specific risks and advantages, which will determine the feasibility of implementation. Public perception of the mission risks will further influence the mission selection (see Section 2.5.2). Due to the international nature of the hazard, multinational co-operation would be imperative to any mitigation effort.

The gravity tractor proposed by Lu and Love [2005] takes advantage of the equal and opposite gravitational attraction between two bodies. By placing a probe in orbit a small distance from the NEO, the gravitational attraction will draw them together. By providing a continuous thrust, the probe counteracts this attraction causing the body to 'fall' towards the probe as it gradually thrusts away. This 'thrust' moves the NEO along its orbit, so avoiding a collision with the Earth. The advantage of this mode is the use of a continuous thrusting operation which would providing accurate control over the body's deflection. Its disadvantage is the long time frame required for deflection, perhaps in the order of years, as well as the associated political implications of a gradual mitigation procedure, see Section 6.4.1.

The second method is similar to NASAs flight proven 'Deep Impact' mission [Rountree-Brown, 2005], where a relatively massive impact-probe is released from satellite probe, impacting the asteroids surface at high velocity (and hence high kinetic energy). ESA is presently developing the Don Quijote mission as a 'NEO precursor mission' to test this kinetic-impact mitigation hypothesis [Gálvez and Carnelli, 2005]. The craft would consist of an impactor probe, released to impact the asteroid surface, and an orbital satellite which would accurately study the asteroid and monitor the impact's effect [González et al., 2004; Cartlidge, 2006]. Either the impactor itself, or the subsequent out-gassing, is used to act to thrust the body and achieve orbit deflection. The advantage of this impact technique is the shorter lead time required, as the impact is an instantaneous event. However, the mission presents a greater risk of failure due to the hit-or-miss approach. Potential complications might also arise from pre-existing internal fractures within the structure, which could result in the object breaking apart rather than altering the orbit.

The final mitigation methodology involves implementing some form of nuclear detonation on or near to the NEO. Either the detonation is used remotely to thrust the body, or it is buried into the NEO to cause a catastrophic fragmentation, [Patenaud, 2007]. Stand-off thrusting requires a probe satellite to deliver a nuclear payload close to the target object. This is then detonated exposing the object to extreme thermal radiation. δV is achieved through direct radiation pressure and the subsequent out-gassing of surface material heated by the radiation flux. Nuclear fragmentation requires complex drilling to position the device within the asteroid prior to detonation. The explosion would shatter the body into many small pieces. The nuclear option embodies the greatest mass to energy ratio, potentially delivering the greatest impulse. As such it can be used in scenarios with only a short lead time. However, public opinion is sensitive to the issue of using nuclear devices in space. Furthermore the consequences of the fragmented asteroid 'cloud' impacting the Earth are unknown and potentially more significant than a single event.

Figure 2.8 and Carusi et al. [2002] demonstrate that the required δV for successful deflection is lowest when implemented many years prior to impact. Clearly the sooner the mission is launched the easier the task of deflection. From this and much discussion regarding these three mitigation mission strategies the Planetary Defence Conference in 2007 suggested that, given time, a tractor-type mission would be launched. Closer to impact date, kinetic impacts would be attempted, with any nuclear mitigation means reserved as a last resort [Ailor, 2007b].

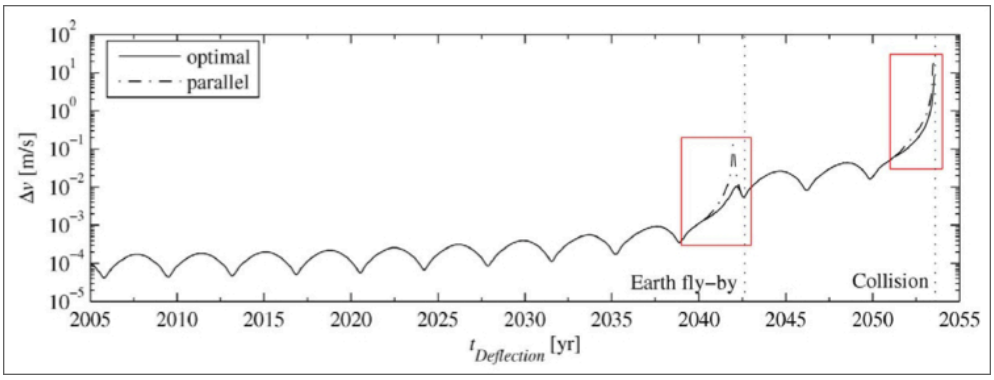

Figure 2.8: The increasing δV requirement as the Earth fly-by and predicted impact point approach. Figure 3 from Kahle et al. [2006].

2.5.2 Human Response to the Perceived NEO Hazard

Prior to the discovery of the Barringer crater, it was widely believed that the Earth was immune to extra terrestrial impact, or the scenario was simply not considered. However, as more terrestrial craters have been discovered the truth about our vulnerability has been gradually accepted. In 1998, two Hollywood films, *Deep Impact* and *Armageddon* [Leder, 1998; Bay, 1998], were released, portraying the consequences from a cometary impact into the ocean and an asteroid mitigation mission. While the science portrayed may not be accurate, the widespread media attention did raise awareness of the hazard in the public consciousness. It remains to be seen how the public would respond to the discovery of an impacting asteroid; the human response is critical to the method in which a threat is dealt with. Public perception of one mitigation option over another could have an impact on which is attempted.

Furthermore, upon discovery of an asteroid threat, the predicted impact location will be represented by a line of risk rather than a single point. This line relates to the orbit intersection and the uncertainty in orbit prediction. Populations lying along the line will immediately be placed at greatest risk with knock on consequences in many aspects of life such as housing prices, life insurance and reduced economic investment. As the predicted impact position is refined, and a mitigation mission strategy adopted, the decision must be made as to how to deflect the body (i.e. in which direction to thrust the body). This will dictate in which direction along the line of risk the asteroid's predicted impact location is translated. Any alteration of the impact position will immediately increase the risk for those populations along the line in the direction of movement. The associated decision making processes will become very complex and involved, requiring full international co-operation to chose the best direction of mitigation. Currently, the mechanisms to make such decisions are missing, but activists such as Schweickart [2006] have called for them to be in place in a timely manner.

2.6 Conclusions Drawn From the Literature Review

The following points are the key conclusions drawn from the literature. They place limits that refine the problem to one that is feasible to address. This will form the basis on which the subsequent computational solution is constructed.

- The Earth and its inhabitants are at real risk from the NEO hazard. The Earth has been hit multiple times in the past, continues to be hit on a daily basis and will be impacted in the future.
- Objects larger than 1 km in diameter are studied heavily due to their cataclysmic potential consequences from an impact. However, due to their low probability of impact, they will not be considered further here.
- Objects smaller than the Tunguska event are not expected to present a significant hazard. 50 m diameter (25 m radius) will be taken as the lower bound in terms of size.
- An order of magnitude larger than this will be taken as the upper bound - 500 m diameter (250 m radius).
- Comets represent approximately 1% of the NEO hazard and typically have very large diameters. As such the project will focus only on Asteroid impacts (i.e. NEAs).
- Fragmentation characteristics will be dominated by the pre-existing structural weaknesses. As these are unknown, asteroids will be modelled as monolithic bodies. The problem of fragmentation will be addressed, but only in its simplest form.
- The atmospheric passage of the asteroid will take into account the mass loss effect of ablation of surface material.
- Land impacts will model the terrestrial crater, pressure blast wave, seismic shock wave, fireball thermal flux and crater material ejecta.
- Ocean impacts will model the transient crater and generated tsunami. This wave will be propagated across the oceans and the run-up and run-in properties of the shoaling wave recorded for each coastal site.
- The study must provide a global vulnerability study due to the multinational nature of the hazard.
- Outputs from the study must be accessible to the public at large to encourage data dissemination as widely as possible to inform the global population.

Chapter 3

Methodology

The adoption of the conclusions drawn from the literature, detailed in Section 2.6, allows a computational model to be constructed to simulate terrestrial asteroid impact events. The asteroid is modelled from atmospheric entry to the ground, modelling both land and ocean impact scenarios. The various impact generated effects (IGEs) are also modelled, and their consequences upon the global human population and associated infrastructure are used to assess global vulnerability. This computer software package is called 'NEOimpactor'.

The shortage of experimental data related to the asteroid's atmospheric passage hampers efforts to understand the processes involved. The proposed model, detailed within this chapter, can only generate an approximation of the physical event. However, the structure of the software architecture allows each model to be altered easily, when experimental data becomes available to refine the simulation and improve model accuracy.

3.1 Mathematical Model Implementation

The role of the NEOimpactor system is to simulate the consequences of an asteroid impact on the Earth (either a known real threat or an example threat) and thus has not been tasked to perform orbit calculations which determine impact probability. The output of the system is thus a vulnerability study, rather than risk assessment, as the assumed probability of impact is unity. The reason for this is that present systems, such as NEODyS [Milani, 2005], are far more capable of providing such information. The simulation begins as the asteroid enters the Earth's atmosphere, and impact is thus a certainty.

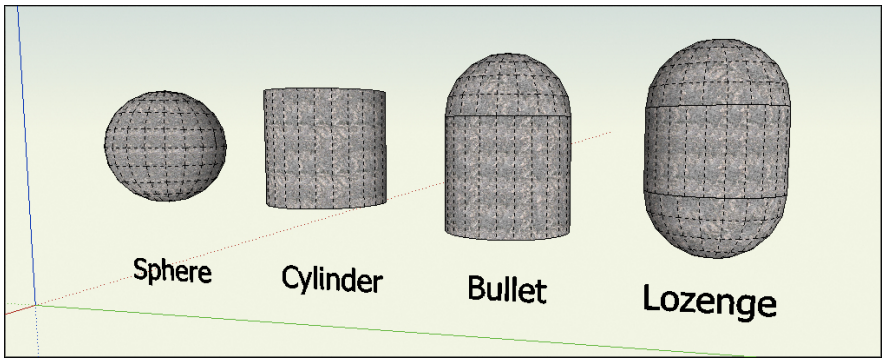

Figure 3.1: Diagram of the four simple geometrical asteroid shapes available in the NEOimpactor model. All shapes are composed of a combination of spherical hemispheres and cylindrical bodies. 'Radius' defines the hemisphere radius and 'Length' defines the length of the cylinder.

3.1.1 Asteroid Atmospheric Entry Model

The initial entry conditions of an asteroid are defined by six characteristics detailed in Table 3.1 and shown in Figure 3.2. Atmospheric passage is modelled by a force propagator that takes account of the Earth's gravitational acceleration and the opposing atmospheric drag. The force propagator works in Cartesian co-ordinates, using a small time step fourth order Runge-Kutta integrator to predict the object's path. The propagator calculates the asteroid position and component force, velocity and acceleration at each time step by determining the instantaneous gravitational acceleration, drag force and mass-loss over every time step. Gravitational acceleration force, F_a, is defined by the Newtonian equation:

$$F_a = gM_{neo} \ , \tag{3.1}$$

where M_{neo} is the asteroid mass and g is the local gravitational acceleration. Drag force, F_d, is proportional to the square of the object's velocity, V_{neo}, and determined by an equation analogous to that used in aeronautical analysis:

$$F_d = \frac{1}{2}\rho_{atm} V_{neo}^2 A_{neo} c_d \ . \tag{3.2}$$

Here ρ_{atm} is the current atmospheric density, A_{neo} the projected area seen by the atmosphere, and c_d is the drag coefficient. The latter describes the surface roughness of the asteroid, and is dependent on the shape of the asteroid Chyba et al. [1993]. The ISO Standard Atmosphere[1] model is used within the system, so that the local density and temperature is used at each time step.

Mass is lost by the process of ablation of the asteroid's surface material; a result of

[1] ISO 2533:1975, 1975

friction with the atmosphere. The frictional heating leads to out-gassing, combustion and vaporisation of the surface material over time, quantified as a rate of mass loss, σ_a. NEOimpactor implements the two-stage regime of Chyba [1993] as:

$$\begin{aligned} \text{for} \quad h > 30 \text{ km} \quad &: \quad \sigma_a = \frac{\frac{1}{2}\rho_{atm} A_{neo} V_{neo}^3 c_h}{Q} \\ \text{for} \quad h < 30 \text{ km} \quad &: \quad \sigma_a = \max \left\{ \begin{array}{l} \frac{\frac{1}{2}\rho_{atm} A_{neo} V_{neo}^3 c_h}{Q} \\ \frac{A_{neo} c_h T^4}{Q} \end{array} \right\} . \end{aligned} \tag{3.3}$$

Where c_h is the heat transfer coefficient, Q is the heat of ablation (both defined in Table 3.2), and T is the temperature of the compressed atmosphere bow-shock in front of the asteroid, taken from experiment to be assumed a constant 25,000 K [Chyba, 1993]. The ablation over each small time step is calculated by the Runge-Kutta integrator gradually reducing both M_{neo} and A_{neo}. This, then, continually alters the drag and acceleration forces, changing the asteroid's trajectory. However, in reality, the ablative mass loss will be most strongly influenced by coherence of the surface material, specific to each individual body.

The flight path integrator monitors the aerodynamic forces to check if they exceed the 'internal strength' parameter of the body. This internal strength, S_{neo}, is the yield strength of the asteroid's compositional material, assuming that no internal fractures are present. When the external drag force, applied over A_{neo}, exceeds this internal strength, a fragmentation event is flagged for later use. However, because the study contained within this thesis does not implement NEOimpactor's fragmentation model, this event is recorded but not acted upon.

THE SIX DEFINING ENTRY CHARACTERISTICS

Asteroid Position	symbol	**Asteroid Motion**	symbol
Altitude	h	Velocity	V_{neo}
Nadir point latitude	Φ	Velocity bearing (from North)	Ω
Nadir point longitude	Θ	Flight path angle	Ψ

Table 3.1: The six initial conditions to describe the asteroid's entry characteristics.

3.1.2 Land Impacts and Modelling of the Four IGEs

On identification that the impact site is situated on the land, NEOimpactor initially models the generation of the impact crater and subsequently the impact generated effects - ejecta material, thermal flux from the explosion fireball, the atmospheric blast

COMPOSITION OF THE THREE ASTEROID TYPES

	Soft Stone	**Hard Stone**	**Iron**
ρ_{neo} (kg/m^3)	2,200	3,500	7,870
S_{neo} (N/m^3)	1.0x10^6	1.0x10^7	1.0x10^8
Q_{neo} (J/kg)	5.0x10^6	8.0x10^6	8.0x10^6
c_h	0.09	0.09	0.09

Table 3.2: Composition of the three available asteroid types in NEOimpactor.

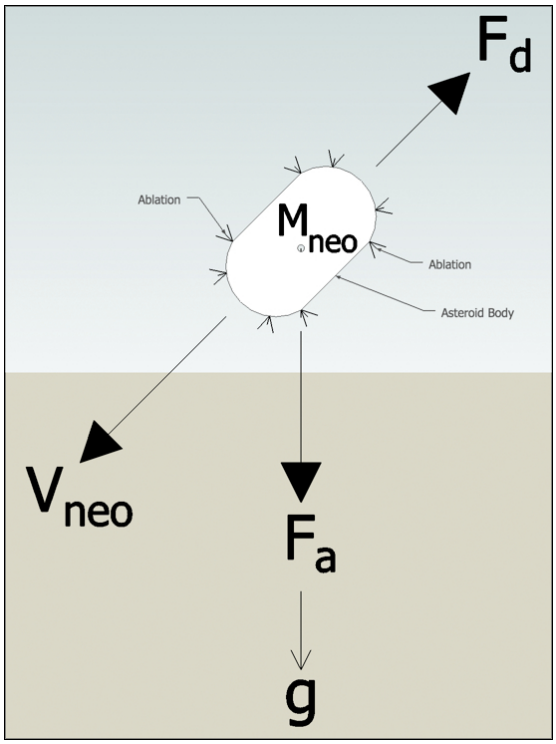

Figure 3.2: Diagram of the forces acting on the asteroid during atmospheric entry.

wave and the seismic shock wave. The models for these IGEs are largely based on the comprehensive work by Collins et al. [2004] and Collins et al. [2005] which predicts the magnitude of each effect at known distance from the impact site. This distance is defined as r km.

Calculation of the Land Crater Characteristics :

The impact crater is generated in two stages. The impacting energy initially excavates a 'transient' crater. This is a simple parabolic shape depression, the material from which is thrown into the air. As this excavated material lands, and the seismic energy dissipates, the final crater shape emerges. Collins et al. [2004] provide a simple calculation for the transient crater diameter in km, D_{trans}, based upon the object's pre-impact

characteristics as

$$D_{trans} = 1.161 \left(\frac{\rho_{neo}}{\rho_{earth}} \right)^{1/3} D_{neo}^{0.78} V_{neo}^{0.44} g_0^{-0.22} \sin(\Psi)^{1/3} , \tag{3.4}$$

where D_{neo} is the asteroid diameter, ρ_{neo} and ρ_{earth} are the asteroid and target densities respectively, and g_0 is Earth's surface gravitational acceleration. The development of the final crater form is dependant on the transient crater diameter. A critical diameter is identified, below which the crater form is classed as 'simple', and above which the crater is defined as 'complex'. From scaling law models, this critical diameter, D_{crit}, is found to be 3.2 km. The diameter of the final crater, D_{final}, is then given by

$$D_{final} = \begin{cases} 1.25 D_{trans} & \text{for} \quad D_{trans} \leq D_{crit} \\ \dfrac{1.17 D_{trans}^{1.13}}{D_{crit}^{0.13}} & \text{for} \quad D_{trans} > D_{crit} \end{cases} \tag{3.5}$$

The depth of the transient crater is defined as

$$d_{trans} = \frac{D_{trans}}{2\sqrt{2}} , \tag{3.6}$$

whereas the final crater depth for simple craters (typical for the NEO size range considered here) is given by

$$d_{final} = d_{trans} + h_{fr} - t_{br} . \tag{3.7}$$

Here h_{fr} is the height of the crater rim built up as the ejected material falls to the ground, and t_{br} determines the thickness of the breccia lens, defined respectively as

$$h_{fr} = 0.07 \left(\frac{D_{trans}^4}{D_{final}^3} \right) , \tag{3.8}$$

$$t_{br} = 0.0896 D_{final}^3 \left(\frac{d_{trans} + h_{fr}}{d_{trans} D_{final}^2} \right) . \tag{3.9}$$

The breccia lens is the region within the crater wall that consists of broken and fractured rock [Melosh and Ivanov, 1999]. Finally, the volume of the transient crater is calculated, based on the transient crater diameter as

$$V_{trans} = \pi \frac{D_{trans}^3}{16\sqrt{2}} , \tag{3.10}$$

Calculation of the Ejecta Material :

It is the material initially excavated by the impact energy that generates the ejecta, and as such the volume of ejecta is equal to the transient crater volume, V_{trans}. Much of the material falls to Earth within the boundary of the transient crater, forming the final crater. However, the remainder is thrown onto the surrounding terrain radially from the impact site as ejecta. The size distribution of this material around the impact site is related to the ejecta fragment size and mass. Collins et al. [2005] assume that at the crater rim the thickness of the ejecta layer is given by $t_{ejecta} = h_{fr}$. This thickness decays with distance r from the impact site according to the relationship

$$t_{ejecta} = \frac{D_{trans}^4}{112r^3} \ . \tag{3.11}$$

Assuming that all the material is ejected from the same point and at the optimum 45° angle, the ejection velocity can be determined. Due to the large distances involved, the range, r, is defined by the relationship

$$r = \Delta R_{earth} \ , \tag{3.12}$$

where Δ is the geocentric angle between the impact and point of interest, depicted in Figure 3.3. The ejection velocity of the ejecta is

$$V_{ejecta}^2 = \frac{2gR_{earth} \tan \Delta/2}{1 + \tan \Delta/2} \ . \tag{3.13}$$

Collins et al. [2002] calculate the diameter of the ejecta material, D_{ejecta} in meters, as a function of distance from the impact site, r_{km} in km, as

$$D_{ejecta} = 2400(\frac{D_{final}}{2})^{-1.62} \left(\frac{D_{final}}{2r_{km}} \right)^{2.65} \ . \tag{3.14}$$

This indicates the ability of smaller objects to travel further but it ignores the effect of wind transportation. The system only records the ejecta transportation up to 10,000 km from the impact site, corresponding to one quarter of the Earth's circumference.

Thermal Radiation Flux:

The impact explosion generates a fireball that expands and rises above the impact site. As it expands it cools. Initially the fireball temperature makes it appear opaque, and the thermal radiation is constrained within the fireball. Eventually the cooling drops below the opaque transition temperature, T_{trans} (found by Zeldovich and Raizer [1966] to be $\approx$ 3,000 K), at which point the peak level of radiation is released. Collins

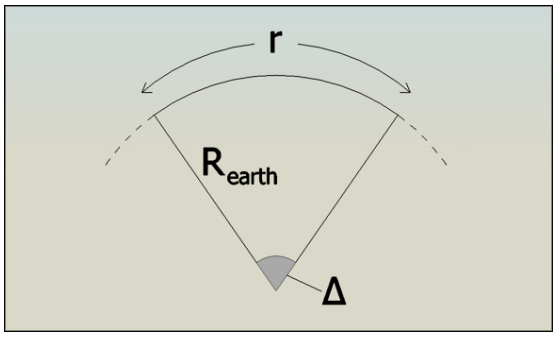

Figure 3.3: Diagram of the geocentric angle Δ used for large values of r.

et al. [2005] derive the following relationship between impactor energy in joules, E_{imp}, and fireball radius in meters:

$$R_{fireball} = 0.002 E_{imp}^{\frac{1}{3}} \,, \tag{3.15}$$

However, not all the kinetic energy of the asteroid goes into the generation of the fireball; a luminous efficiency fraction, η, is defined to account for the impact energy which forms the fireball. Numerical modelling suggests this fraction scales as some power law of impact velocity, and from the limited observational and experimental evidence is taken approximately as $\eta = 3x10^{-3}$ [Nemtchinov et al., 1998]. Between T_{trans} and the temperature at which the surface ceases to radiate is the irradiation duration, as approximated by Collins et al. [2004],

$$\tau_{ir} = \frac{\eta E_{imp}}{2\pi R_{fireball}^2 \sigma_B T_{trans}^4} \,, \tag{3.16}$$

where σ_B is the Stefan-Boltzmann constant (5.67x10^{-8}W/m^{2}K^4). The total thermal exposure ε_{ir} in J/m^2 at a distance r from the impact site is

$$\varepsilon_{ir} = \frac{\eta E_{imp}}{2\pi r^2} \,. \tag{3.17}$$

As distance from the impact site increases, the curvature of the Earth reduces the visible ratio of the fireball. The proportion of the fireball visible at a location is called the visible ratio, f, defined as

$$f = \frac{2}{\pi}\left(\delta - \frac{h_f}{R_{fireball}} \sin\delta_f\right) \,, \tag{3.18}$$

where

$$h_f = (1 - \cos\Delta) R_{Earth} \,, \tag{3.19}$$

$$\delta_f = \cos^{-1}\frac{h_f}{R_{fireball}} \,. \tag{3.20}$$

Here, h_f is the height of the fireball masked below the horizon (from the point of view of an observer at point r, see Figure 3.4), and $2\delta_f$ is the angle of the segment of fireball visible above the horizon. The actual thermal exposure experienced at point r is then

$$\varepsilon_{actual} = f\varepsilon_{ir} \ . \tag{3.21}$$

(3.22)

This thermal exposure value is taken by NEOimpactor as the measure of the magnitude of the radiation experienced on the ground This radiation generates casualties and damage through its interaction with the surrounding terrain.

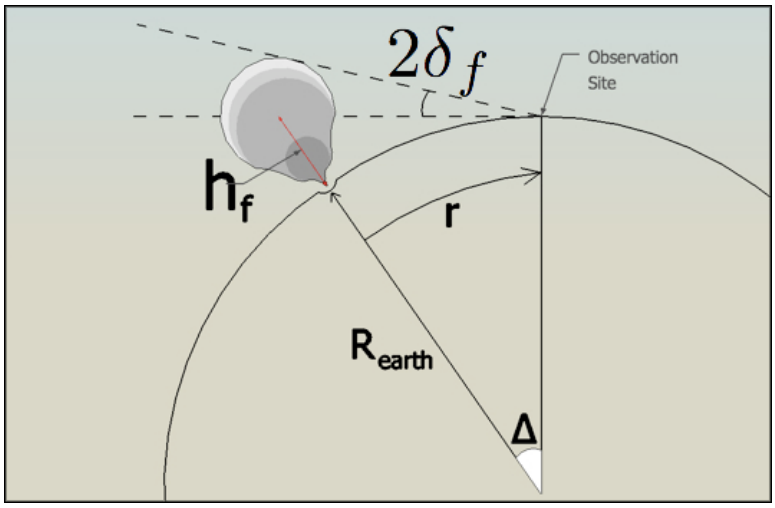

Figure 3.4: Diagram of the expanding fireball as observed from a distance r. Part of the fireball is obscured by the horizon (below the dotted line), which reduces the radiation received.

Modelling the Atmospheric Blast Wave:

The impact explosion generates a sudden expansion and compression of the local atmosphere. This is a pressure blast wave which radiates out from the impact site. The maximum pressure difference across the bast wave is the critical parameter, called the peak over-pressure, P_{peak}, measured in Pa. As the energy of an impact explosion is many orders of magnitude larger than those generated by explosives, Collins et al. [2005] use a scaling rule referenced to a 1 kiloton explosion. The peak overpressure at a distance r_1 from a 1 kiloton explosion is

$$P_{peak} = \frac{p_x r_x}{4r_1}\left(1 + 3\left[\frac{r_x}{r_1}\right]^{1.3}\right) , \tag{3.23}$$

where $r_x = 290$ m and $p_x = 75,000$ Pa. r_x is the distance at which the characteristics of the observed peak overpressure decay curve changes from a $\approx 1/r^{2.3}$ to a $\approx 1/r$ dependancy. P_x is the pressure at this transition point. To scale Equation 3.23 to a NEO impact blast scale, the following relationship is used

$$r_1 = r/E_{kt}^{1/3} \, . \tag{3.24}$$

This relationship links the overpressure experienced at a distance from an impact of 1 ktlotons of TNT. This is substituted into Equation 3.23. Here E_{kt} is the equivalent impact energy in kilotons of TNT. Collins et al. continue on to predict the peak wind velocity, u_{peak}, generated by this overpressure behind the shock front. This is calculated as

$$u_{peak} = \frac{5P_{peak}}{7P_0} \frac{c_0}{\left(1 + \frac{6P_{peak}}{7P_0}\right)^{0.5}} \, , \tag{3.25}$$

where P_0 is the ambient pressure at sea level and c_0 is the speed of sound [Glasstone and Dolan, 1977]. This peak wind velocity is used as the IGE magnitude to determine the wind damage generated by the impact.

Magnitude of the Seismic Shock Wave:

The impact event releases a significant amount of energy into the ground as seismic shock waves. These can be equated to typical geological earthquake events measured using the Richter Scale (a logarithmic intensity scale). Using the standard Gutenberg-Richter magnitude energy relation, Collins et al. [2005] specify the equivalent earthquake magnitude at the impact site as

$$M_{imp} = 0.67 \log_{10} E_{imp} - 5.87 \, . \tag{3.26}$$

The equivalent magnitude experienced at a distance r is described by three regimes depending on the distance from the impact site (in km) as

$$M_r = \begin{cases} M_{imp} - 0.0238r & r \leq 60 \text{ km} \\ M_{imp} - 0.0048r - 1.1644 & 60 \text{ km} < r \leq 700 \text{ km} \\ M_{imp} - 1.66 \log_{10} \Delta - 6.399 & r \geq 700 \text{ km} \end{cases} \tag{3.27}$$

This magnitude is used to assess the structural damage sustained at each point on the Earth's surface, referenced to the equivalent damage sustained by geological earthquakes.

3.1.3 Ocean Impacts: Cavitation, Tsunami Propagation and Shoaling

Ocean Cratering - Cavitation:

Collins et al. [2005] consider the modelling of ocean tsunamis as too complex and so the work by Ward [2000] is used as the basis for the tsunami model. The characteristics of the initial ocean crater are defined as follows. Due to the unstable nature of an ocean cavity, only the transient cavity can be defined. The dimensions of the cavity can be directly related to those of the impacting asteroid by

$$d_{cavity} = \frac{D_{cavity}}{3} = \frac{2}{3} R_{cavity} = \left(\frac{8 \epsilon \rho_{neo} V_{neo}^2}{9 \rho_{water} g_0} \right)^{1/4} R_{neo}^{\frac{3}{4}} , \tag{3.28}$$

where ρ_{neo}, V_{neo}, and R_{neo} are the asteroid's density, velocity and radius respectively, and ρ_{water} is the density of sea water (1,020 kg/m^3). d_{cavity} is the cavity depth and D_{cavity} and R_{cavity} is the cavity diameter and radius respectively. ϵ is a term to define the fraction of E_{imp} that goes into generating the tsunami wave. Ward suggests that $\epsilon \approx 0.15$. If d_{cavity} is larger than the local ocean depth, h_{imp} then $d_{cavity} = h_{imp}$.

Tsunami Propagation Algorithm:

Following the initial definition of the tsunami cavity, the wave is then propagated across the ocean. The ocean is modelled as a cellular grid with equal latitude and longitude bins (detailed in Section 3.2). These cells are rectangular and therefore the tsunami wave is only propagated across cell boundaries in the cardinal directions. The model algorithm systematically propagates the wave across these cell boundaries and every iteration radiates the wave out by one cell. During deep water propagation the algorithm uses linear theory calculations to record the current wave speed, travel time, amplitude and critical depth. From Ward and Asphaug [2002], the wave amplitude in deep water is based upon the dimensions of the initial cavity excavated in the ocean by the impact energy. It is the in-fill of this cavity, and subsequent central splash, which sets up the ocean oscillation which generate the tsunami wave. This initial amplitude is defined by

$$A_{deep} = d_{cavity} \left[\frac{1}{1 + \frac{2r}{D_{cavity}}} \right]^{\psi} , \tag{3.29}$$

where the wave amplitude power term, ψ, is defined as

$$\psi = \frac{1}{2} + 0.575^{\frac{-0.0175 D_{cavity}}{d_{cavity}}} . \tag{3.30}$$

Wave speed is calculated by

$$V_{wave} = g\frac{\tau_{wave}}{2\pi} \,, \tag{3.31}$$

where τ_{wave} is the tsunami period ($\approx$ 150 s). Wave travel time is therefore simply the cell distance travelled divided by V_{deep}. The critical amplitude is expressed by Ward and Asphaug [2003] as

$$A_{crit} = \psi^{0.2} A_{deep}^{0.8} d_{imp}^{0.2} \,. \tag{3.32}$$

Information about the present and following cell's ocean depth value determines whether the wave has a deep water wave characteristic or if it begins to shoal. This depth data is extracted from a global bathymetric dataset. The limitation of this algorithm is its inability for the wave to interact with itself to generate interference pattern's, as only the single peak wave amplitude is modelled. However, unlike ray-tracing methods, this algorithm successfully deflects the wave around complex coastline patterns to eventually shoal on every coastal shoreline to some extent to simulate real world diffraction.

Shoaling of the Tsunami Along Coastline Cells:

Deep water calculations of wave amplitude and speed using linear theory become anomalous in shallow water as it would predict an infinite shoaling wave height as ocean depth becomes zero. To prevent this, linear theory is implemented to predict wave amplitude, A_{deep}, until the shallow ocean of depth h_{shore} reaches a critical depth h_{crit} at distance r_{crit}. At this point the critical depth can be calculated as $h_{crit} = \frac{A_{crit}}{\psi}$. Figure 3.5 presents the methodology for modelling the transition between linear and non-linear aspects of the shoaling wave. Linear theory gives wave amplitude in shallow water as

$$A_{shallow} = A_{deep}\left[\frac{h_{deep}}{h_{shallow}}\right]^{1/4} \,, \tag{3.33}$$

where h_{deep} is the water depth out to sea and $h_{shallow}$ is the shallow water depth.

Eventually the wave reaches the very shallow water and begins to build in amplitude and break. The distance inland that the wave is able to reach is called the run-in distance. NEOimpactor uses this term to determine how much of the coastal cell is inundated by the incoming tsunami. The associated term run-up defines how far vertically the wave will reach. If the coastline is raised above this level then the location will be safe from inundagtion. Run-up is calculated directly from the model for the shoaling wave by Ward and Asphaug [2003]. It is found to be equal to the critical height, as

$$R = h_{up} = \psi h_{crit} \quad = \quad \psi^{1/5} A_{deep}^{4/5} h_{deep}^{1/5} \,. \tag{3.34}$$

Run-in is then calculated as

$$h_{in} \quad = \quad 10\sqrt{g_0 h_{up}} R_{cavity}^{0.375} \, . \tag{3.35}$$

As the system shoals the tsunami on each coastline cell, the inundation will only take place if the predicted run-up height is above the coastal cell's elevation. This check enables high altitude coastal sites to remain safe from tsunami inundation, as would be the case with communities situated on cliff or up steep slopes.

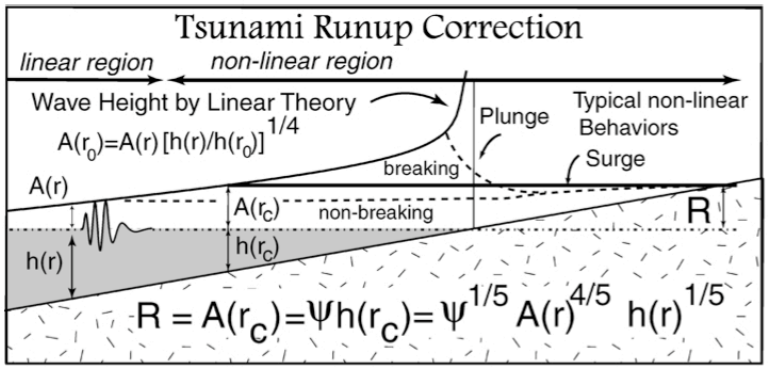

Figure 3.5: Diagram of the factors involved in calculating a waves shoaling characteristics, from Ward and Asphaug [2003]

3.2 Architectural Design

3.2.1 System Overview

NEOimpactor adopts a modular system architecture with three primary components:

- the User Interface (UI)
- Simulation Applications (SAs)
- and Operational Modules (OMs)

These are illustrated as a combined Venn Diagram in Figure 3.6. The entire C++ application was developed using the Microsoft Visual Studio software package, as this gave integral access to the Microsoft Foundation Class (MFC) environment. This MFC environment handles the creation of the familiar windows user interface systems, and this is how the NEOimpactor UI is organised. From the UI, the user is able to select and run one of the main simulation applications (SAs), or chose from a set of independent 'applets' (small exterior applications). It is the SAs that handle the operational modules (OMs) which contain the mathematical models, discussed in Section 3.1, to study the impact consequences. Data is based on a database model

of the Earth, from which output data can be extracted and saved to the user's hard disk.

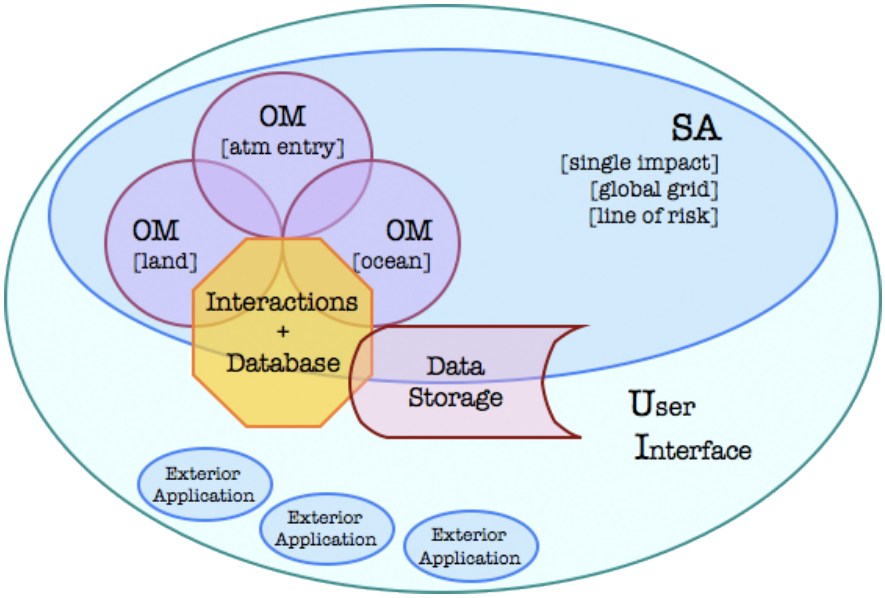

Figure 3.6: The NEOimpactor architecture simplified as a Venn Diagram. This view is taken from the perspective of a user, as everything is contained within the User Interface. Three Simulation Applications (SA) exist in parallel, each of which independently operate the three Operational Modules (OM). The database and data storage systems are accessed by both the SA and the UI. A small number of exterior applications exist to handle tertiary operations.

From the UI menu options, the user selects one of three SAs: 'Single Impact', 'Global Grid', or 'Line of Risk[2]'. Once launched, the SA runs independently of the user, handing the subsequent processes. Initially, the applications request starting conditions and simulation limits from the user using dialogue boxes. This data is passed to each OM in turn, as well as being stored as text files on the hard disk. Manipulation of the data defining the asteroid is performed by the OM, which are C++ 'objects' created and operated by the SA. Data is passed from the atmospheric flight analysis to the relevant impact OM which models the IGEs. Interaction of the IGEs with the Earth is then handled by the database module. Each SA is constructed differently but operates using the same three OMs. The structures of the three SAs are discussed and shown independently in Section 3.2.4.

At the heart of the software is the system database. Databases offer rapid access to layered data and enable cross referencing of layers to interrogate the results. Unlike the OMs, which work on a single flow of data (modelling the flow of kinetic energy through the impact event), the database OM stores and retrieves data and handles data queries. The database structure resembles a rectangular map of the Earth with

[2]The Line of Risk application is also referred to as the 'Line Impact' application.

each cell associated with a specific latitude-longitude bin. Each layer of the database records a single characteristic for that cell, such as ocean depth or population count. Queries access different layers to extract particular data sets, and entire layers can be extracted in raster form (pixel image) as a global map. The queries are largely the 'interactions' shown in Figure 3.6 and detailed in Section 3.2.3.

The final stage of an application is data storage. NEOimpactor constructs a directory tree for the data output, storing the results from each SA together in one directory. The results from each run of the SA are stored in sub-folders labelled by simulation name and date to distinguish them and to facilitate data retrieval. The output data is generated in three forms: as text files (for example, the characteristics of the asteroid chosen), raw data files (.csv format files listing the consequences for each cell of the database) and impact maps (using the 'parallel projection' cartographic projection).

3.2.2 Data Transfer within the NEOimpactor System

This overview is given from a user's perspective. However, the system itself is constructed in the opposite sense, with the OMs being the most critical aspect and the UI the least important. Figure 3.7 provides a system view of NEOimpactor from a perspective of the data flow within the system. Data transfer within NEOimpactor is handled by a number of variable arrays: one-dimensional 'vectors' and multi-dimensional 'arrays'.

Two data vectors are maintained throughout the simulation: the initial asteroid characteristics vector, and the impact characteristics vector. Using standardised data vectors across all OM allows the SA to keep track of the asteroid's changing characteristics and variables. The initial characteristics vector is filled with data extracted from the user dialogue 'pop-ups'. This is then implemented as the starting conditions for the atmospheric OM. On completion, this module outputs the impact conditions, which are stored in the impact characteristics vector. Both vectors remain active within the SA and are transferred to each operational module in turn. Finally the data is exported as a text file along with the simulation data outputs.

Multi-dimensional arrays are predominantly implemented within the database module for storing data-sets. Each layer of the database is a two-dimensional data array, with rows and columns related to longitude and latitude bins. Each layer is a flat representation of the real spherical cell structure of the Earth in terms of latitude and longitude. When considered as a whole, the database represents a very large three dimensional array - two dimensions account for the latitude and longitude cells and the 'vertical' axis represents each layer stacked on top of one another. Each database cell, representing a small region of the Earth's surface, comprises a stack of data points

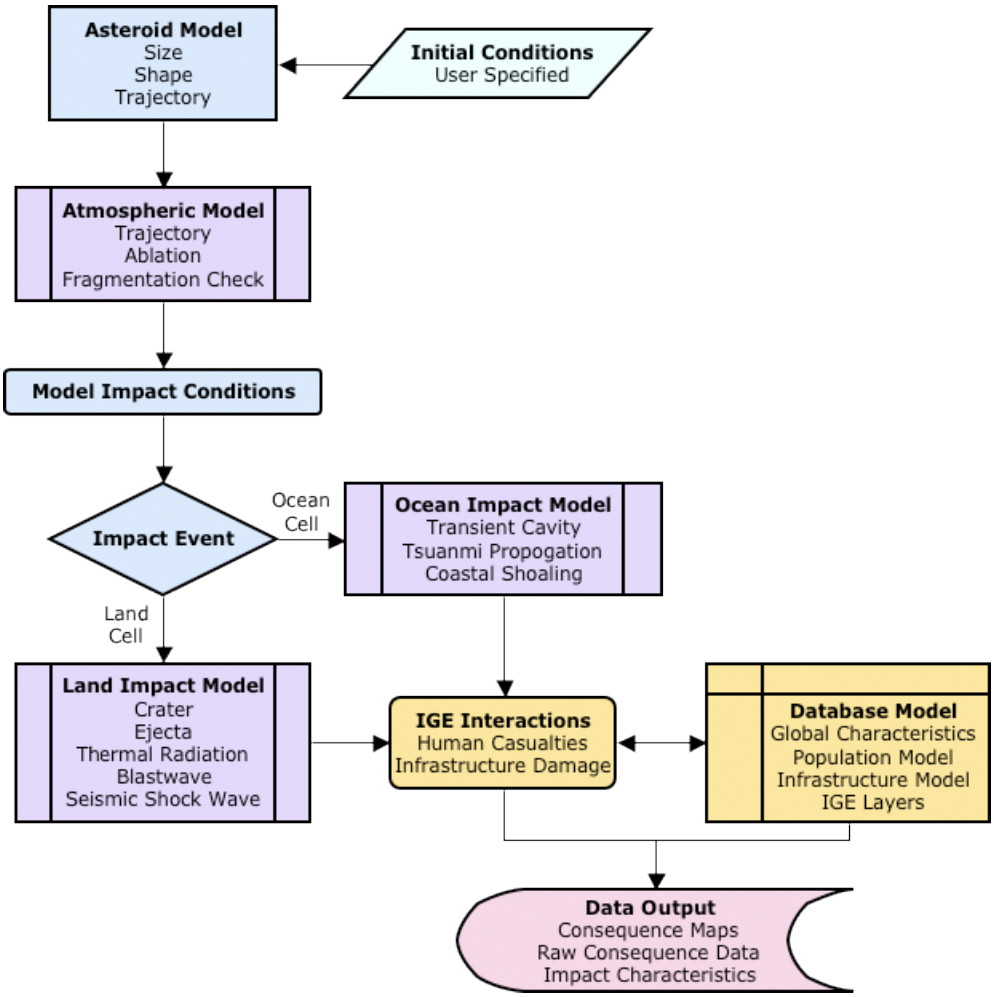

Figure 3.7: Overview of the data flow through the NEOimpactor system for a generic simulation application. The three operational modules are the primary means of data manipulation with the database and interactions modules producing the application outputs.

describing the averaged attributes of that region, such as population, altitude and land usage. A stack of many two-dimentional arrays are used rather than a single three-dimensional array due to the data handling requirement. A single array would generate over one gigabyte of data at the operating resolution (approximately two million cells). Separating the database arrays reduces the data transfer loads between the SA and the OMs, by allowing only relevant layers to be transferred rather than the whole database.

3.2.3 The Architecture of the Operational Modules

Operational modules (OM) handle the mathematical calculations of the simulation. They exist as independent C++ objects and are constructed and operated by each SA. The OM consists of a series of subroutines which perform the mathematical ma-

nipulations of the asteroid's properties. Their content can be easily updated as new research inputs become available. There are three OMs within NEOimpactor handling the atmospheric passage, land impact and ocean impact. Two other modules handle the database system, which stores the result data, and the interaction module, which draws together the database data and the simulated results to derive the impact consequences.

The Architecture of the Atmospheric Operational Module

The Atmospheric OM is the processed first by the system to model the initial atmospheric entry of the asteroid (see Figure 3.8). The key input is the initial entry conditions of the asteroid, which are defined by the user. Co-ordinate manipulation and other calculations using these parameters fully define the asteroid's physical characteristics, such as mass and kinetic energy, as well as the trajectory dynamics. The initial state vector (containing these fourteen parameters) is saved to disk, while the the starting conditions are passed to the Runge-Kutta integrator. The RK integrator uses a force propagator over a small time step to predict the asteroid's trajectory up to the point of impact. Ablative mass loss is taken into account at each step. The OM output defines the conditions at the point of impact, in particular the latitude and longitude of the impact site and the kinetic energy of the asteroid as it hits. The entire flight path profile at each time step is saved to disk for future reference.

The Architecture of the Land Impact Operational Module

If the atmospheric OM impact location output is on land, the land impact OM is launched (see Figure 3.9). It is constructed using the atmospheric OM's outputs and remains active while its subroutines are operated externally by the SA. Impact kinetic energy is used to determine the cratering characteristics and the four IGEs. Subroutines calculate the corresponding magnitude of each IGE at each database cell, based on the cell's distance from the impact location (r). The SA systematically works through the database, recording the IGE magnitude at each cell in specific database layers created for each IGE.

The Architecture of the Ocean Impact Operational Module

Similar to the land impact case, the ocean impact OM, detailed in Figure 3.10, initially defines the transient 'crater' excavated in the ocean by the energy of impact. It is the collapse of this cavity which develops the tsunami wave train through the oscillation of the surrounding ocean, caused by the in-filling of the cavity. The SA then calculates the propagation of the tsunami energy across the database's ocean layer. This involves

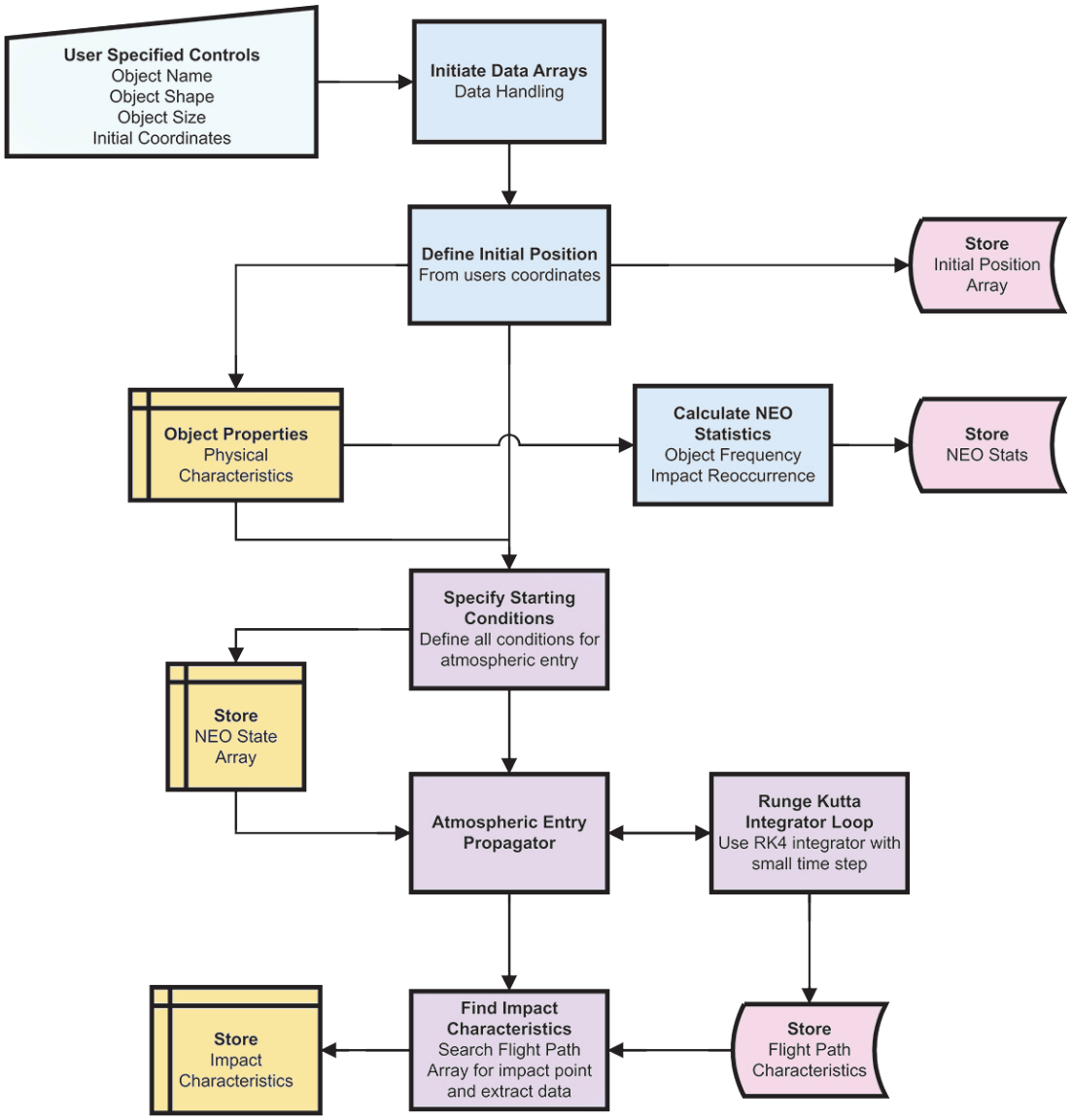

Figure 3.8: Flow diagram of the atmospheric Operational Module. The principle components are the flight propagator and Runge-Kutta integrator loop. The impact characteristics will detail the impact energy (used to derive the various IGE) and the impact location (to determine if the event is a land or ocean impact).

the use of large 'transient' arrays (deleted after use), which contain the parameters of the expanding wave front. The coastal database layer identifies coastal cells across the globe and initiates the wave shoaling algorithm. The shoaling tsunami's run-up and run-in characteristics determine the inundation predicted at each coastline cell. These characteristics are recorded in two separate database layers.

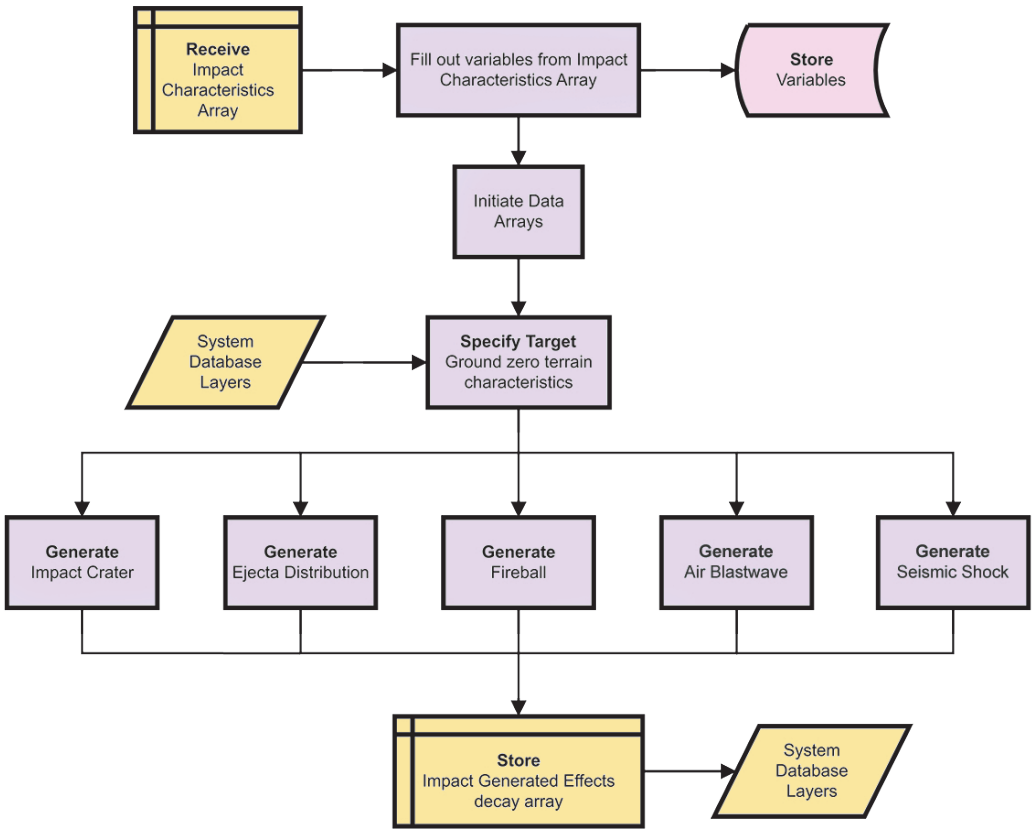

Figure 3.9: Architecture of the land impact Operational Module. Asteroids with impact locations on the ground initiate this OM to determine the severity of the IGE. The magnitude of these effects are recorded as specific database layers.

The Architecture of the Database Module

Figure 3.11 provides a graphical representation of the database OM. At its heart is a series of variable arrays, each containing data-sets of various characteristics of the Earth and its environment. Each layer has the same number of data points so that each cell on the Earth is represented throughout all layers of the database. The cell divisions are made uniformly across the Earth, with the same number of longitude divisions at the poles as there are along the equator. This results in cells away from the equator becoming increasingly exaggerated isosceles trapezium, eventually becoming triangular at the pole. This is a result of the Earth's poles being mathematical discontinuities. This change of shape and area is accounted for with layers that contain the effective cell area in km^2, as well the spherical co-ordinates of each corner. The resolution of the database can be altered to reduce the required data handling load (and hence processing time) or increased to improve data quality. However, the resolution of 2003x998 (1,998,994 cells) was chosen to match the resolution of the lowest quality data set available. Each cell has a unique ID number which allows the same cell location to be traced through every layer of the database.

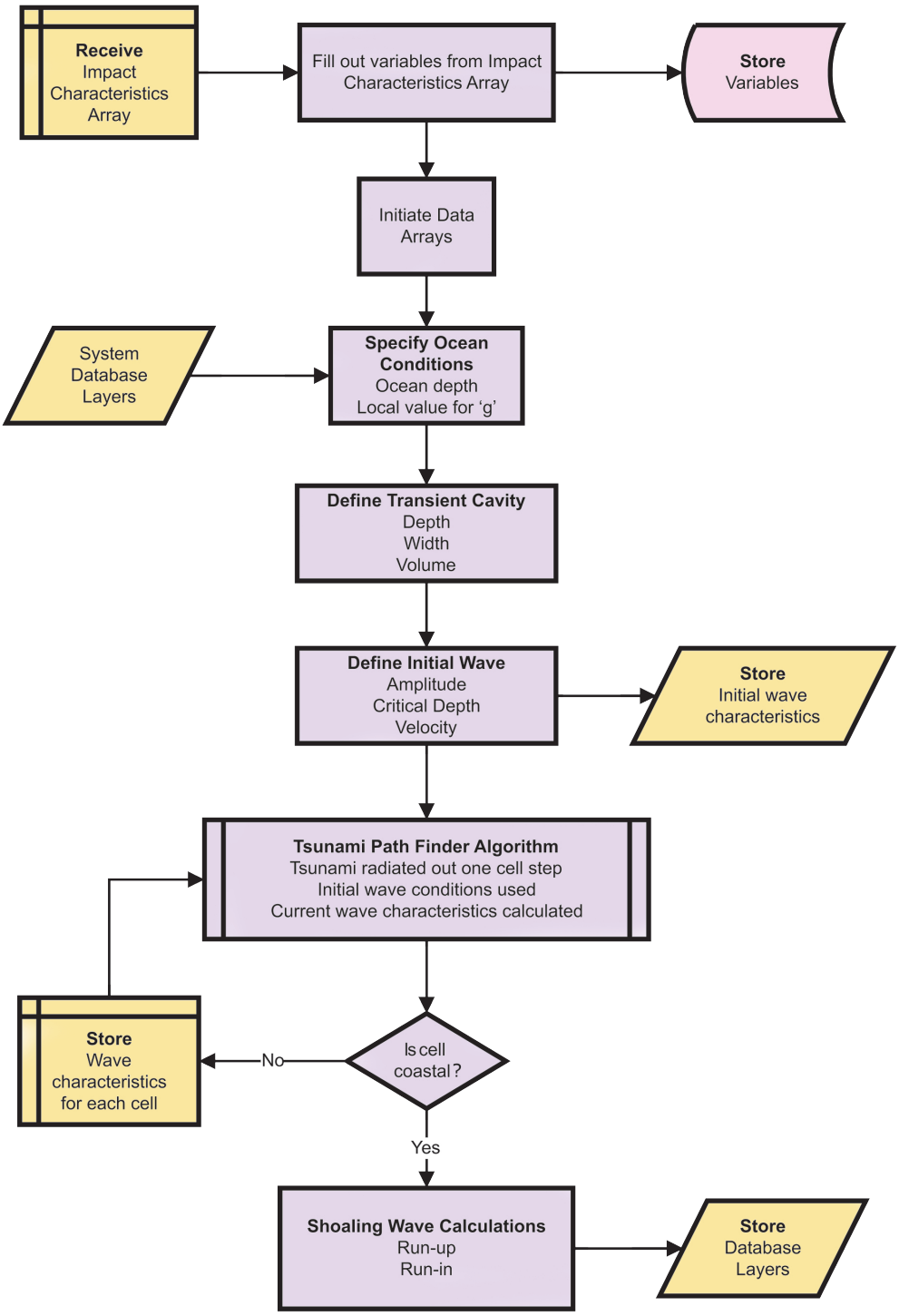

Figure 3.10: Flow diagram of the ocean impact Operational Module. This module is operated if the impact site is an ocean cell. The impact characteristics define the transient ocean cavity which determines the tsunami amplitude and subsequent coastal inundation.

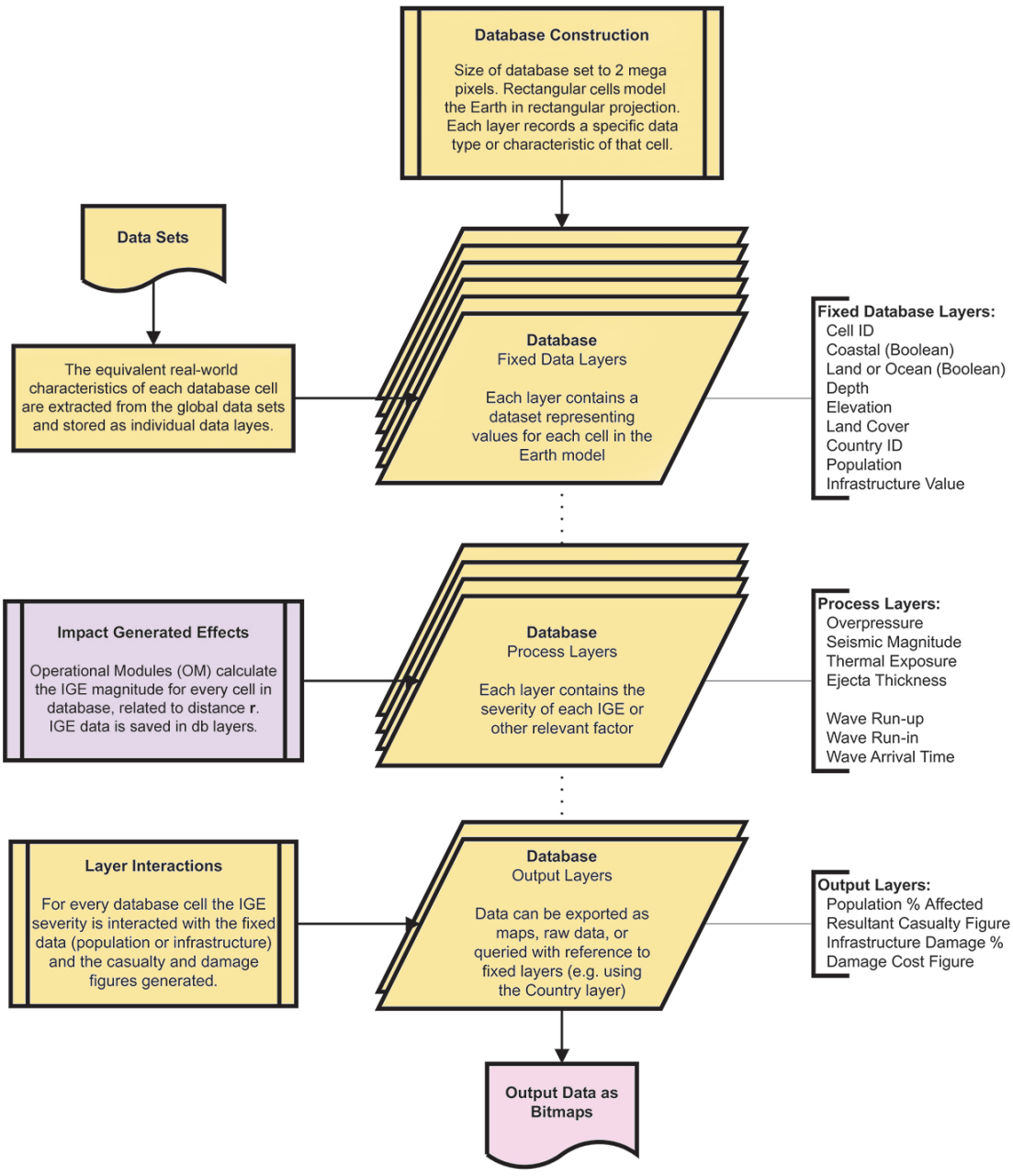

Figure 3.11: Diagram of the NEOimpactor system's database structure. Each layer has the same number of cells (1,998,994) which represent latitude-longitude regions of the Earth. Three types of layer exist in the system. The Fixed Data Layers describe characteristics of the Earth. The middle process layers are filled by the impact OMs, principally describing the IGEs. The Output Layers are then utilised by interactions of the fixed and process layers to predict the impact consequences.

The database system is created and handled by the SA, but remains accessible from the UI. The required variable arrays are created in system memory before being filled by data gathered from external data-sets, which are imported in the form of 'bitmap' file maps. The maps all conform to the parallel projection cartographic projection to match the database cell structure. A monochrome format was used for all data-sets as it is the lowest common format available, thus keeping all the data quality at an equitable level. A purpose built bitmap subroutine is utilised to disassemble the data-set images and extract the colour value for each cell. In monochrome (i.e. grayscale), the three colours (red, green and blue - 'rgb') have equal value and so only one colour channel needs extracting. This value represents the cell brightness and ranges from 0 (black) to 255 (white). The value for each cell is then multiplied by a scale factor (based on the original maps shading scale key) to represent the real world value for that cell. This scaled value is then stored in the database layer.

Further layers can then be extracted from within the database. For example, a subroutine is run which uses an edge-finding algorithm to identify each land cell that is part of the global coastline. These coastal cells are then highlighted in a specific database layer (using Boolean). This layer is used by the ocean OM to initiate the analysis of the tsunami shoaling on coastal cells. Other subroutines could be added that search the land layer to identify plains or deep valleys, which might enable more complex analysis of the impact explosion's interaction with local topography.

The Interaction Module to Derive the Impact Consequences

With the completed IGE data generated by the land and ocean OMs, and stored as layers in the database, the consequences can be assessed. Overall, the process is a loop that works through every land cell in the system. Figure 3.12 displays a flow diagram of the interaction module architecture. If the cell has no human population or is devoid of infrastructure, then no calculation is necessary. On the other hand, for all cells containing population and infrastructure, the system assesses the level of damage sustained by the IGEs incident on that cell. This is related to the magnitude of each IGE recorded for that cell in the relevant database layers. Cells within the crater are assumed to suffer 100% destruction.

For land impacts the relationship between each land IGE magnitude and the level of destruction generated is described by the four curves in Figure 3.14. These relationships have been derived by attributing a percentage loss value to the textual descriptions of damage listed for various effect magnitudes in the tables by Collins et al. [2005]. These four relationships are only approximations, but provide a quantitative means of calculating the damage to each cell. Below a particular threshold no damage is sustained. Between these extremes, the percentage population and infrastructure

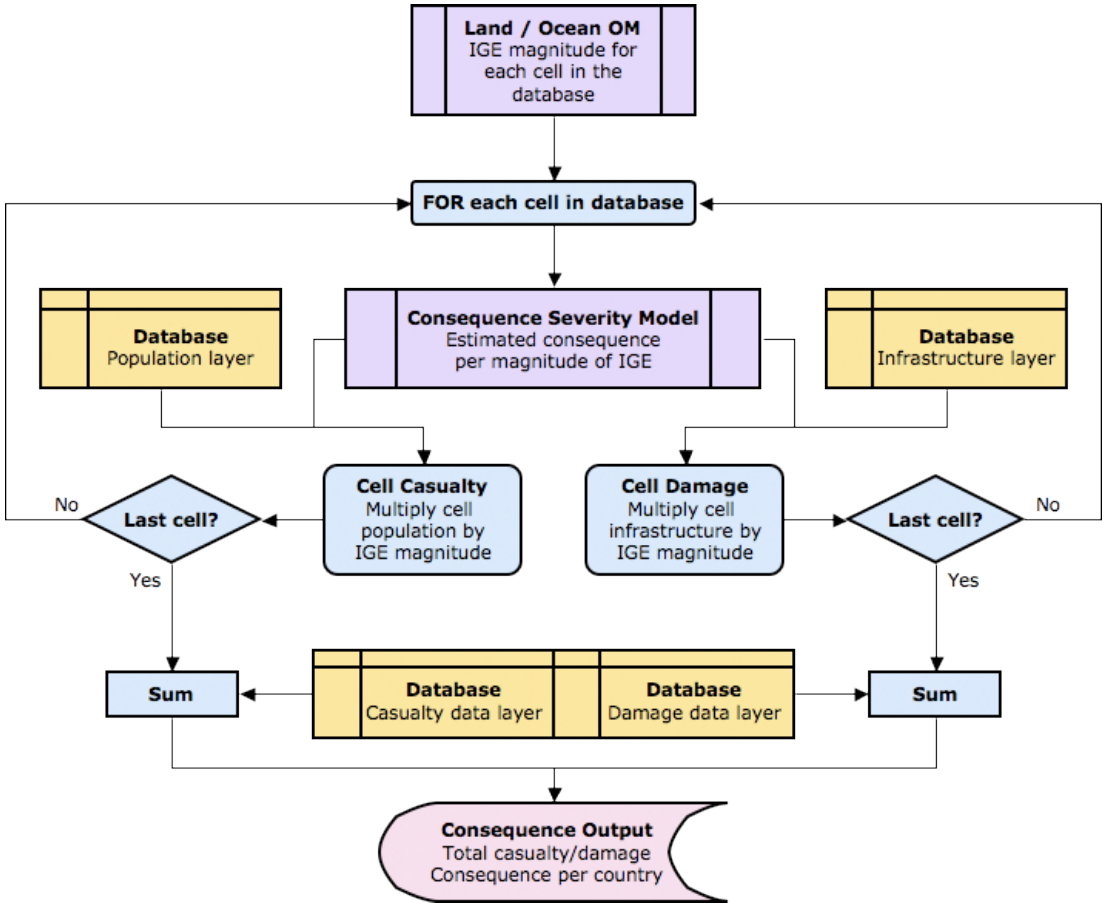

Figure 3.12: Flow diagram for the interaction module. This OM is a process loop which, for every cell in the database layer, calculates the human casualty or damage consequences as a result of the IGE magnitude. Summing up these values provides the total consequence for each impact event. Referencing the casualty and damage to the database layer specifying the country, the total consequences for each country can be assessed.

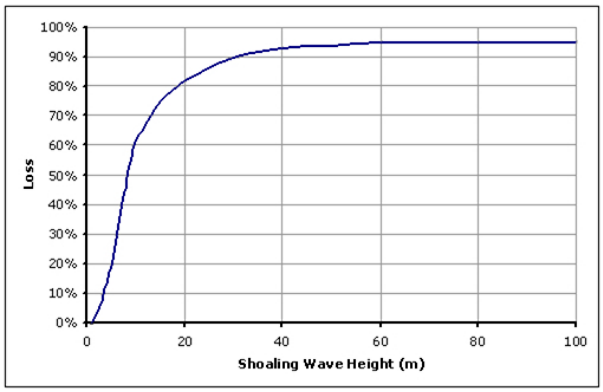

Figure 3.13: This plot shows the relationship used to associate the shoaling wave height with the level of destruction witnessed. A logarithmic form is adopted from the assumption that, above a particular wave size, no further destruction is expected, i.e. what withstands this particular wave will withstand any inundation.

loss is recorded for each cell, related to the IGE magnitudes it experiences. This percentage loss is multiplied by the cell's total population and infrastructure value (P_{cell} and I_{cell} respectively) to calculate the estimated casualty and damage totals.

Considering the tsunami generated by ocean impacts, a slightly different approach is taken. The two factors of the tsunami severity that are recorded are the run-up and run-in values (in metres). First the cell altitude is compared with the run-up value with no further calculation made if the cell altitude is greater (indicating that the cell is situated on a cliff and is therefore safe). The run-in distance determines the percentage of each coastal cell inundated by the wave. The shoaling wave height (run-up) then determines the severity of the wave's impact (larger waves being more destructive), using the approximate relationship displayed in Figure 3.13. This relationship has been adopted as a first stage approach to estimate the tsunami damage and casualty values which will need future refinement from external studies. The total casualty and damage figure is then recorded for each coastal cell.

These consequence values for each cell are recorded in specific database layers. Summing the cell values gives the total impact consequence. By referencing these consequence layers with another layer of the database, particular regional investigations can be made. In this research the country layer (which identifies the country to which each cell belongs) is used as the reference layer. This then allows the consequences for each country to be extracted. However, any database layer could be taken as the reference layer allowing investigations based on groupings other than national boundaries, for example ethnicity, wealth, geographic or environmental groupings.

3.2.4 Description of the Simulation Applications

The simulation applications (SA) are accessed from the UI menus by the user. Each application autonomously operates the independent OM to process the asteroid impact event. The separate nature of the three system components, and the fixed arrays for data transfer between OMs, allows new SAs to be constructed and embedded in the system without disturbing the existing SAs. They can then be incorporated easily into the UI with the addition of new menu options. The following subsections detail the operation of each SA presently contained within NEOimpactor.

Single Impact Simulation

The Single Impact simulation application begins by initiating the data-transfer variables required to handle the OM and sets any Boolean flags to default. These flags are used as a way of checking that each process has been completed and as a way of tracking data. The user is then requested to specify the asteroid trajectory and

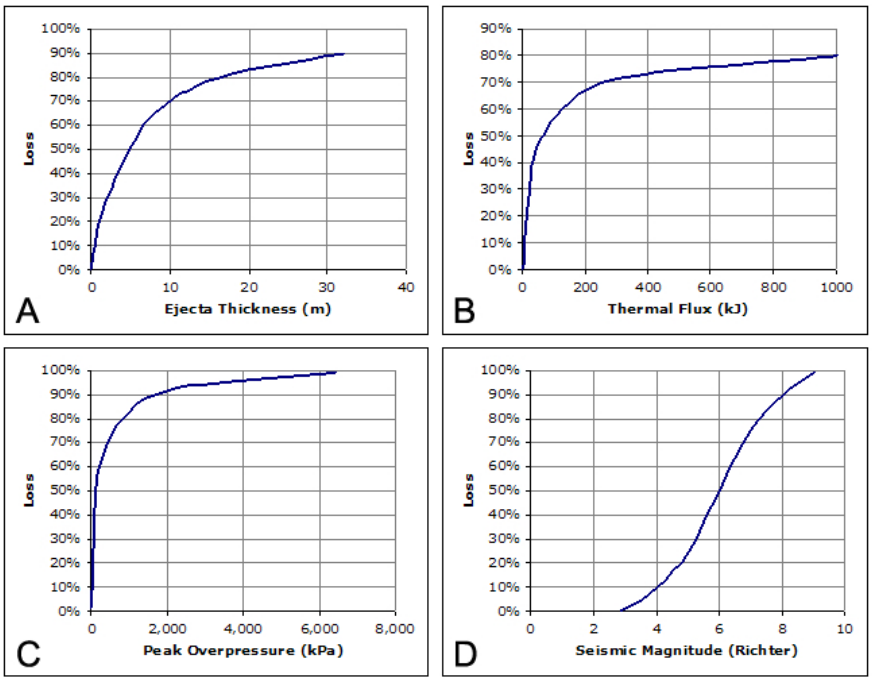

Figure 3.14: Four land IGE curves to relate the effect magnitude with the anticipated loss of population or infrastructure. These graphs show the approximate relationship implemented in the NEOimpactor interaction model. **A** - ejecta, **B** - fireball radiation, **C** - air blastwave, **D** - seismic shockwave.

characteristics by filling out dialogue boxes. Feedback to the user confirms the starting conditions before the data is stored in the 'initial conditions' vector. This vector is passed, along with the empty 'impact characteristics' vector, as arguments to the atmospheric OM. This empty array is filled by the OM and returned to the SA (as detailed in Section 3.2.2).

The impact characteristics vector contains the impact co-ordinates. At this point, the SA initiates the database system (detailed in Section 3.2.3) to build the model Earth. The impact co-ordinates then identify the impact cell within the database. Queries of this cell reveal its characteristics, principally whether it is a land or ocean cell, thus determining which OM to launch. The SA then launches the relevant OM, which processes the impact event and outputs the IGE database layers. In the final processes these IGE layers are collated with the population and infrastructure layers to derive the consequences of the simulated impact. The geographical casualty and damage distributions are then exported as bitmap images and saved to disk along with the raw casualty and damage data. Some results of the single impact simulations are provided in Section 4.3.

Global Grid Simulation

The Global Grid SA is the most complex simulation, providing more comprehensive data for analysis. The aim of the Global Grid is to investigate the relationship between the impact consequences and impact location. This is achieved by simulating an asteroid impacting the Earth at multiple, uniformly spaced locations to identify geographical regions where the consequences are most severe. This is done by dividing the globe into a series of 'grid cells' (the 'Global Grid' is a lower resolution grid than the database grid), into which the same impact event is simulated. The consequences are then recorded for each grid cell impact.

As with the single impact SA, the Boolean defaults are set and data vectors created. The UI dialogue boxes gather information about the test asteroid and define the grid cell resolution. The resolution of the Global Grid defines the number of cells, and hence the number of impact simulations. With each simulation taking time to complete, the choice of resolution is a trade-off between runtime and result data quality [3]. Figure 5.1 identifies the chosen working grid resolution.

The starting conditions are processed by the atmospheric OM to provide the impact characteristics. However, the impact co-ordinates are taken as the central co-ordinates of each grid cell. A multi-dimensional impact characteristics array is created, which contains an impact characteristics vector representing the equivalent impact into each grid cells. The database module identifies the type of impact for each grid cell. A loop in the SA cycles through this multi-dimensional array, simulating the same impact event for each grid cell using the relevant OM and recording the consequences. Two arrays representing the grid dimensions record the total casualty and damage consequence generated by each cell impact. A global map is constructed from the Global Grid by shading each grid cell according to the severity of the impact consequences. The maximum casualty and damage grid cells are identified and saved to disk as a separate text file for reference.

Line Impact Path (Line of Risk) Simulation

The linear impact path application, operates as a one dimensional version of the Global Grid model. While the Global Grid generates a two dimensional array of identical impacts, this application places impacts along a one dimensional line. Its operation is similar to the Global Grid in that the asteroid is defined by the user and the application repeatedly simulates the impact event in every cell along the path. However, rather than the whole Earth being uniformly covered, the user chooses

[3] Using a dual core 2.2 GHz AMD processor based system, the maximum Global Grid resolution simulation achievable, corresponding to the resolution of the database, would take approximately four years of processing time

either a path along a particular line of latitude or longitude, or a path between two unique locations on the Earth. The resolution of the line dictates how many impacts will be simulated along it, with the same trade off between runtime and accuracy.

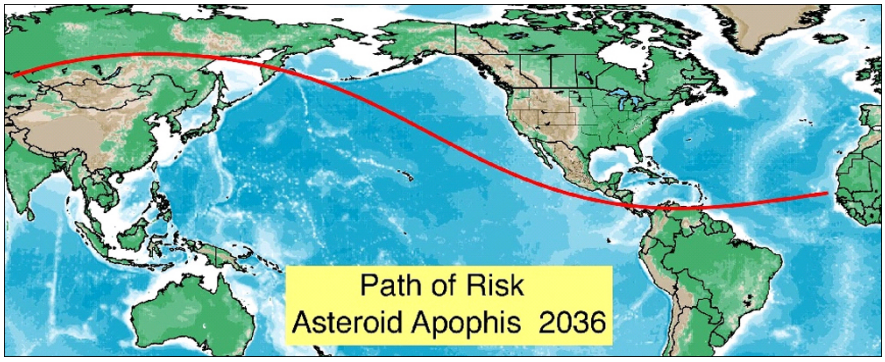

Figure 3.15: Predicted plot of the Line of Risk of the asteroid Apophis' 2036 close approach were it to pass through the keyhole during the Earth close approach in 2029. Graphic by Russell Schweickart, B612 Foundation [Durda, 2005].

The advantage of running a Line Impact simulation is that higher resolution paths are achievable. Doubling the resolution will double the runtime. This compares to the quadrupling of runtime experienced when doubling the Global Grid resolution. The output of the SA is a list of consequence figures (both casualty and damage) for impact simulated along the line. This data can then be plotted as a line graph to highlight the sections of the path which generate the most significant consequences. Section 5.2 investigates some example linear impact paths. In the event of a real threat, the object will present a Line of Risk on the Earth, such as that shown in Figure 3.15. This path can be imported into NEOimpactor as an impact path and simulated to find the associated risks along the path.

3.2.5 Data Output and Display

As introduced in Section 3.2.1, the results data generated by NEOimpactor are saved using a directory tree within a specified folder on the user's hard drive. Data output is handled independently by each SA, as the data type is dependent on the application process. Due to the potentially large disk space required to store the data produced by large multi-impact simulations, a UI message-box alerts the user of the hard disk space required for the results. With each impact simulation generating between five and ten eight-megabyte maps, this alert prevents the user unnecessarily running a simulation which may generate terabytes of stored data. Three data types are stored in the output directory. At the same time, textual information is fed back to the user via a pop-up dialogue box. This feedback informs the user of the completion of a successful simulation, including details of the impact such as its location, energy and

overall casualty and damage figures estimated.

Map outputs are generated by passing a whole database layer to the purpose-built bitmap generator algorithm. Different output map styles are available, including a choropleth style, allowing the data to be presented in a way that eases knowledge acquisition [Slocum and Egbert, 1993]. Chapter 5 presents the range of map formats available. Maps can be generated directly from a single database layer or from a combination of layers. For example, the database layer recording the coastline cells can be superimposed on the map to make it more accessible.

The data describing the impact event (or multiple events) is also stored in the output directory for later analysis. In single impact simulations, the raw data contains the IGE's magnitude experienced at every database cell as well as the cell's estimated consequence. On the other hand, in multi-run simulations (such as the Global Grid SA) each impact event is stored individually so a specific impact simulation can be investigated. Of particular importance is the recording of each affected cell's country identifier. This enables summations to be made of the consequences for a particular country. Data is provided as a comma separated variable file (.csv) which can be read by spreadsheet applications for more rigourous investigation.

3.3 Software Operation

3.3.1 User Interface Requirements

Despite the growing use of Unix based platforms and potential speed advantages this might afford, the Windows operating system remains globally dominant and was therefore chosen as the application platform. While this means that the software developed will be propitiatory rather than open source (which could be useful for potential collaboration efforts) the software tool will be self contained and user-friendly for a wide audience. Microsoft Foundation Classes (MFC) is an application framework that enables familiar Windows applications to be created within the C++ environment. Microsoft Visual Studio was chosen as the the coding environment, as it implements MFC seamlessly. All dialogue boxes are C++ objects that are derived from the MFC.

The primary requirements for the software's user interface were ease of use and intuitive data management. Ease of use is achieved through a menu-based software design, taking advantages of MFC's integration into Visual Studio. Each SA is accessed via an option in the system menu list, with clear names to guide the user to the desired simulation. When launched, the SA opens a series of dialogue boxes, which gather data from the user regarding the simulation. All dialogue boxes have built-in data checks to verify that all fields are completed and valid. If empty or invalid fields are identified, the user is notified and the dialogue box cannot be dismissed until the

error is corrected. Comprehensive instructions are provided in the dialogue boxes alongside the variable fields to help guide the user. When completed, the information is returned to the user for confirmation before the simulation commences. An estimate of the expected simulation runtime is calculated and fed back to the user, enabling them to cancel the simulation if time is unavailable.

Raw data is stored in the data repository directory. Within the repository, each simulation's data is maintained within one folder. The directory names are created based on the simulation parameters, enabling the user to locate results from any previously run simulation. Each results file is also given a unique file name to enable easy identification when Windows Explorer displays the folders in alphanumeric order. The data format itself comprises text files, comma separated variable files (for manipulation in programs such as Excel) and bitmap image files.

3.3.2 Identification of the Appropriate Usergroup

The target operator usergroup consists primarily of scientifically-minded researchers with a knowledge of the field of Near Earth Asteroids. This usergroup is relatively small in number and dispersed across the world, with only a few key people in each country. The software design assumes some prior knowledge of the potential impact scenario, so that technical details can be requested from the user such as the asteroid's characteristics and trajectory.

Of greater importance is the usergroup associated with the output data. Information concerning asteroid threats is multinational by nature and potentially of global significance. Therefore, the information is relevant to a very wide audience. However, caution is appropriate, due to the sensitivity of the information regarding particular locations at greatest risk. Logsdon [2007] raised the possible problem of land price crashes in areas that are highlighted as being particularly vulnerable to impact generated hazards. Finally, it is in the public dissemination of the simulation data that the most important indirect usergroup is located. Those investigating the natural hazard, including the global risk or the relative risk on a local or regional scale, will require data that is intelligible, firstly to themselves but also then easily understood by a wider public audience. Though all such public dissemination is potentially sensitive and must be handled with care, currently no organisation has been identified to manage this task.

3.3.3 Versatility of NEOimpactor in Application to New Problems

One key aspect of any software system is its ability to tackle new problems. Compatibility with this philosophy in the future is achieved through the modular nature of the

design. New mathematical models can replace existing models to improve accuracy, provided that the existing input and output data formats are maintained. Versatility is maximised by not heavily restricting the user in their simulation inputs. However, a trade off is sought between the capability of the system and its ease of use. Each of the simulation applications contained within NEOimpactor offers a range of configurable options to provide a myriad of possible results and investigations. Computational runtime becomes the only real limitation.

Interrogating the database following a successful impact simulation, via the database module query structure, provides an important element of versatility to the user, as it shows the impact consequences set against a number of criteria. The most useful example is using the country database layer. By selecting a particular country's identifier (the code which represents each country), the casualties can be summed for that country. Selecting a different reference layer enables a range of aspects to be investigated, such as by hemisphere, continent or economic wealth.

Future versatility is found through the addition of new SAs to the NEOimpactor system. Here, the modular nature of the system becomes important, because the SAs independently operate the OMs as internal functions. These OMs can be updated, as can the SAs, so long as the input and output data arrays are maintained. While the implementation of new SA would be beyond the skill of most usergroups, they could be developed and released as a software update at a future date, expanding the research possibilities.

Chapter 4

Validation and Testing

In a project such as this, involving the development of a software tool, the issue of validation is an important one. However, it is important to note that full validation of the results generated by NEOimpactor is beyond the data set currently available. For example, the energies involved in the impact of even a moderate-sized NEO are at least three orders of magnitude greater than those encountered in nuclear device tests. As a result, the impact generated effects (IGE) can only be extrapolated from measurements obtained during such detonations (which remain largely classified due to their high security status). With no measurements or data from real impact events, confidence in the accuracy of such extrapolations is poor. Similar comments apply to the characteristics of impact generated tsunami. Although much good work has been done on computational simulations for land-slide and other tectonic induced tsunami, the theory surrounding impact induced tsunami remains unproven. Furthermore, it is very difficult to know how these IGE will translate into casualty and damage estimates in the event of a real impact.

The reason these problems arise is due to the novel nature of the research. No-one has yet attempted to draw together all the strands of the NEO impact research to produce a tool to predict the social and economic costs of such an impact event. The current project is only the first step in this process. In doing this, we can only utilise the best data available, and have a realistic view of the limitations of the resulting software tool. It is also important to note that, as a consequence of these limitations, the results generated are best viewed as relative, rather than absolute. Thus the tool is most appropriate in performing comparative studies, for example how one geographical region is affected more than another.

Bearing in mind these comments, the following chapter focuses on aspects of validation that can be sensibly addressed. A number of testing procedures have been performed on the NEOimpactor system to provide a good measure of validation for the results generated. Firstly the database data is investigated to reveal how

accurately it represents the real-world. Secondly the dynamics of the NEOimpactor operational modules (OM) are assessed in comparison with independantly calculated data. Finally a study is presented in which two single impact event simulations are compared and contrasted.

4.1 Assessment of the Earth Model Database

Any location on the Earth can be characterised by any number of physical attributes or descriptors, from its geographical co-ordinates to elevation, terrain type, vegetation and political ownership. The Earth as a whole can therefore be described by a collection of datasets, one for each of these characteristics. The most common format in representing these characteristics is a printed map. In these datasets each data point (or pixel) represents a unique geographical region (or cell). Generally these global datasets have been constructed through field research, aerial imagery and remotely-sensed satellite data. Many are freely available on the internet in various resolutions. While one such dataset could represent the Earth accurately by assigning values to hundreds of different descriptors, the NEOimpactor model describes the Earth in terms of five physical characteristics and two human-related attributes.

While the Earth's characteristics are continuous (analogue), any dataset will be a discrete (digital) representation. Each pixel represents a small cell on the Earth with a finite area and data representing the average over that area. The cell size is determined by the dataset's resolution - increasing the resolution decreases the size of the cell. Therefore, each dataset is only an approximate model of the Earth, with an error due to digitisation of the analogue representation. Furthermore, the standard parallel cartographic projection used in this work introduces a further source of error as the pixels furthest from the equator appear the same size while actually representing an increasingly small region of the Earth. NEOimpactor imports these external dataset maps into the database as described in Section 3.2.3.

The resolution of the NEOimpactor model is optimally set to 2 million pixels[1], whereas some of the datasets are available in higher resolutions (up to 8 million pixels). Importing the data therefore reduces the data quality by up to a quarter. To import the data into the database, NEOimpactor implements a 'nearest-neighbour' sampling approach. This algorithm records the value of the central cell of a region rather than taking an average of all the cells, thus preserving actual original values of the sampled cells rather than generating a new averaged cell value. By choosing to

[1]Using a 'double' data type to construct a database layer (8 bytes per cell) requires 16 megabytes of data storage. The total database size at this resolution is 284 megabytes. Doubling the resolution would require over 1 gigabyte of data storage for the database alone. Therefore the resolution chosen provides a balance between quality and data handling requirement.

study the hazard from a global perspective, NEOimpactor must sacrifice local detail lost by this resolution re-sampling. Future advancements could be made by implementing a data compression method when storing the database layers to reduce the data transfer load. Furthermore, by developing a method of nesting higher resolution grids, the general region affected can be identified and then isolated and modelled at higher resolution. This would increase the spatial accuracy of just the small region affected (in particular coastal locations) and not require the whole earth to be modelled at the high resolution.

By summing various database characteristics for an entire country's cells, the database model can be compared to real-world estimates[2]. Four properties are compared: land area, coastline length, population and infrastructure value. The real-world data for these properties is taken from the *The World Factbook* [CIA, 2008], a widely respected source of world data maintained by the United States government and updated on a biweekly basis.

A specialist 'exterior application' within NEOimpactor interrogates the database layers, summing all the various properties for the cells related to a chosen country (see Figure 4.1 for visualisation of the User Interface and Figure 3.6 for the context). An arbitrary selection of countries are chosen for the comparison. Countries from all continents and hemispheres are represented, as well as the three country types: island, coastal and land-locked.

4.1.1 The Accuracy of the Land Area Modelled in the Database

Projection of the database's regular grid on the spherical Earth results in a rectilinear grid where the non-equatorial cells become trapezoidal in shape and eventually triangular at the poles. The area of the real-Earth that each represents is calculated using the trapezium area equation, with the various sides (along lines latitude and longitude) assumed straight. A dedicated database layer records this corrected cell area to correct the distortion caused by the original parallel cartographic projection. Cell area is critical in the process of accurately extrapolating both the population and infrastructure values for each cell because both datasets are imported as density values (see Section 4.1.3). The error associated with this method is two fold. Firstly the Earth is not a perfect sphere, rather it is an oblate spheroid. Secondly this model represents the sphere as a collection of connected flat panels, rather than truly curved panels. However, this approximation is commonly used in digital representations of the Earth,

[2]Even data taken from measurements in the field must be an approximation of the real world, based on the scale of measurement used. For example, each time a single length of coastline is measured with an increasingly fine resolution, the recorded length will grow due to the fractal characteristics of real world objects.

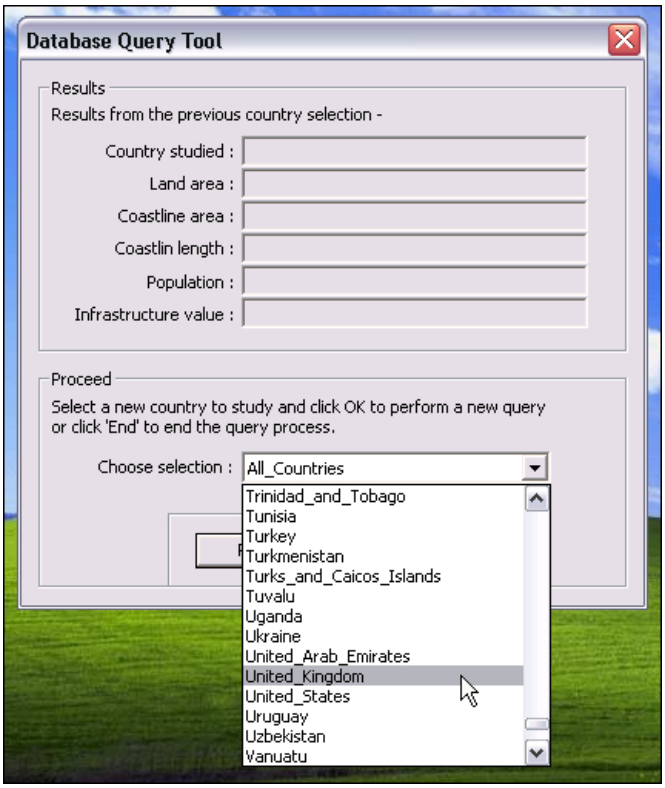

Figure 4.1: A screen capture from NEOimpactor of the database interrogation application. This application is independent of the SA and is launched through the menu-based UI.

for example, Google Earth [Google, 2008]. Figure 4.2 demonstrates the loss of accuracy in representing the Earth with a 2 million pixel database.

Table 4.1 provides a comparison of actual and modelled land area, with both the parallel projection map (Figure 4.2 **B**) and the NEOimpactor corrected cell area (Figure 4.2 **C**). The parallel projection map models the Earth as a cylinder rather than a sphere which over estimates the area of the polar regions. The table shows that this exaggerates the total land area by nearly 78% with Canada presenting the greatest discrepancy. However, using the corrected cell area slightly underestimates the global land area by just over one percent. This is a result of simplification of the coastline detail, discussed in Section 4.1.2.

In comparison with real world estimates, NEOimpactor's area corrected database values still vary somewhat, although the error is kept below 10%. The area error is largely due to pixilation during the mapping process; in other words, data quality is lost as the real world (or vector representation) is converted to a 'raster' image. The intricacies of the geographical details of coastlines and international borders is lost, being replaced with an array of simple quadrilaterals. This loss of detail is most significant in small countries such as Cambodia, which have a large coastline border

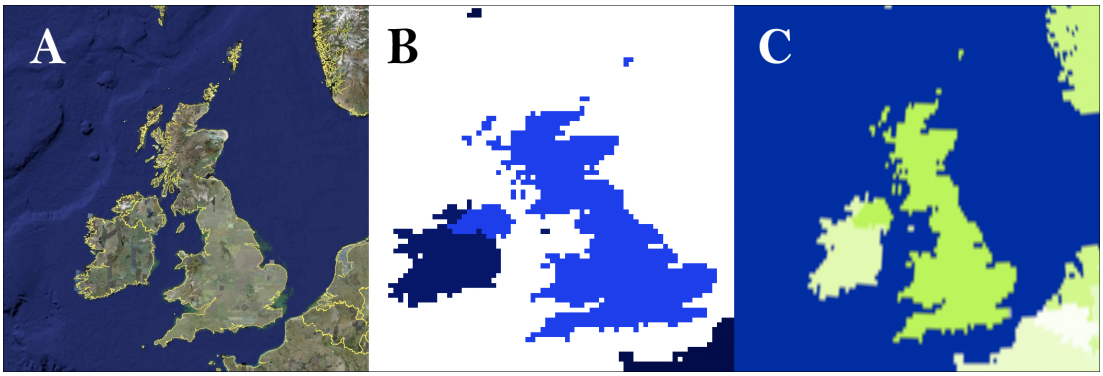

Figure 4.2: Showing the variation in area and coastline accuracy depending on image resolution and projection. Each rectangular pixel represents one cell in the system database. **A** - high resolution image presenting the real world, including intricate coastline detail [Google, 2008]; **B** - parallel projection ('typical' map) has increasingly exaggerated area at high latitudes; **C** - area corrected cells used in NEOimpactor database.

length to land area ratio. On the other hand, larger countries generally suffer from errors associated with the modelling of interconnected flat panels rather than a single curved surface. Canada, with a vast range of small islands, continues to present the greatest area error, over-predicting the real area by nearly nine percent. However, due to the low population of these island regions, the consequences of the resulting additional area is negligible. A subsequent error associated with this area discrepancy is in the calculation of a country's population. The human and economic data is based on density information which, when multiplied by the cell area, determines the total for each cell. Countries with the largest area discrepancy will see an associated error in their population and infrastructure estimates. One solution would be to increase the resolution of the database. Table 4.2 displays the accuracy difference in the area estimation of a few countries if the database resolution were doubled. While some improvement is seen, the accuracy is not uniform and as such, little overall gain is achieved at the expense of increasing the data transfer load by a factor of four.

4.1.2 The Accuracy of the Representation of Coastline Length

Error in the land area calculation is largely a result of the fine detail lost along the country's borders. Pixilation represents the coastline as a collection of straight edges, rather than as an intricate collection of coves and promontories. A dedicated algorithm has been written to calculate a chosen country's coastline by summing the length of each cell identified as bordering the ocean. The results for the ten test countries are presented in Table 4.3.

This data shows that prediction of coastline lengths vary more significantly than the land area. The greatest discrepancy again occurs for Canada, where the large

COMPARISON OF LAND AREA ESTIMATES FOR THREE PROJECTION METHODS

Country	Real	Parallel	error	Corrected	error	Count
World	148,940,000	264,677,600	+77.7%	147,198,000	-1.18%	661,694
Australia	7,617,930	8,578,000	+12.6%	7,701,070	+1.09%	21,445
Cambodia	176,520	191,200	+8.31%	186,938	+5.90%	478
Canada	9,093,507	20,900,800	+130%	9,892,270	+8.78%	52,252
Chile	748,800	957,600	+27.9%	743,065	-0.77%	2,394
China	9,324,410	11,792,800	+26.5%	9,425,070	+1.08%	29,482
India	2,973,190	3,430,400	+15.4%	3,153,670	+6.07%	8,576
Kenya	569,250	587,200	+3.15%	588,250	+3.34%	1,468
South Korea	98,190	120,800	+23.0%	97,557	-0.64%	302
Russia	16,995,800	36,232,400	+113%	16,927,900	-0.40%	90,581
Switzerland	39,770	58,000	+46.8%	39,783	+0.03%	145
UK	241,590	421,600	+74.5%	247,251	+2.34%	1,054
US	9,161,923	13,772,400	+50.3%	9,450,050	+3.14%	34,431
Estimated land area in km^2						

Table 4.1: Comparing the land area discrepancies for the three projection methods in Figure 4.2 against the real-world estimates. The columns Real, Parallel and Corrected refer to the projections A, B and C respectively in that figure. The final column entitled 'Count' records the number of database cells which make up the country.

number of small islands present a large coastline length in which error is accumulated. This property of Canada is shown by having the largest length:area ratio. For coastal regions, pixilation is a significant problem, greatly oversimplifying the real coastline detail. This coastal simplification will be a source of error when modelling coastal casualty and damage distributions. However, on the global scale being investigated only a simplified prediction of the shoaling wave is possible and the intricacies of the real coastline detail cannot be taken into account.

4.1.3 The Accuracy of the Population Estimate

The external population density dataset (Figure 4.3) is imported directly into the database as a layer of density values, $\rho_{dataset}$, for each cell. Summing the dataset density multiplied by the cell area (A_{cell}) for the entire database (N cells) gives a total population value generated by the dataset. This value is incorrect as the original dataset uses a different pixel reference area. Dividing the real-world population, P_{real}, by this summation, as in Equation 4.1, generates a density modifier, $M_{\rho_{dataset}}$. The corrected population for each cell is then given be Equation 4.2,

$$M_{\rho_{dataset}} = \frac{P_{real}}{\sum_{i=1}^{N} \rho_{dataset} A_{cell}} \tag{4.1}$$

AREA ACCURACY CHANGE WITH RESOLUTION DOUBLING

Country	Actual	Original	2 x Resolution	Error Change
World	148,940,000	147,198,000	147,172,000	-0.02%
Cambodia	176,520	186,938	184,935	1.13%
Canada	9,093,507	9,892,270	9,886,610	0.06%
Russia	16,995,800	16,927,900	16,906,900	-0.125%
Kenya	569,250	588,250	578,611	1.70%
UK	241,590	247,251	244,934	0.96%
US	9,161,923	9,450,050	9,445,160	0.05%
Land area in km^2				

Table 4.2: Change in area calculation by doubling the native resolution of the database. In this process an equatorial cell area is decreased from 20 km^2 to 10 km^2. While the area estimate of some individual countries improves, others decrease. The resolution would need to be increased considerably for a real accuracy improvement to be seen across the world.

COASTLINE LENGTH DATA FOR EXAMPLE COUNTRIES

Country	Actual	Simulated	error	Length : Area
World	356,000	666,361	+87.2%	
Australia	25,760	26,845	+4.2%	87.1
Cambodia	443	536	+21.0%	1.1
Canada	202,080	97,282	-107.7%	4490
Chile	6,435	6,378	-0.9%	55.3
China	14,500	11,440	-26.7%	22.5
India	7,000	8,368	+19.5%	16.5
Kenya	536	601	+12.1%	0.5
Korea	2,413	2,125	-11.9%	59.3
Russia	37,653	64,124	+70.3%	83.4
Switzerland	0	0	-	-
UK	12,429	7,536	-64.9%	639
US	19,924	39,364	+97.6%	43.3
Coastline length in km				

Table 4.3: Comparison of actual and simulated coastline lengths for the ten test countries. The final column presents the ratio of coastline length to land area for the country.

$$P_{cell} = \rho_{dataset} M_{\rho_{dataset}} A_{cell} \tag{4.2}$$

Table 4.4 lists a sample of countries with estimates of their actual population (using July 2007 data) and the modelled population. The modelled NEOimpactor population shows a reasonable level of accuracy, with the error ranging from -14% to +25%. The errors are of a similar magnitude to those of the area estimates, through typically slightly greater. Any error associated with the land area estimate will be factored into the population calculation. However, the greatest error will result from

the external dataset itself. Actual global population data is typically of poor quality; only rough estimates from census data can be modelled. The dataset used in this study uses only fourteen density bins ranging from from 1 to 8192 people per square kilometre (pale yellow to dark brown respectively in Figure 4.3).

On a global scale, NEOimpactor's total population estimate falls below the real-world estimate. As such any casualty estimate will tend to slightly underestimate those at risk. A greater accuracy population dataset would be desirable, especially in coastal regions, to limit the error in the system. This error reduction could again be achieved through an increase in the database resolution. However, eventually the accuracy limit of the population dataset will be reached as population models are only available as approximated region density figures.

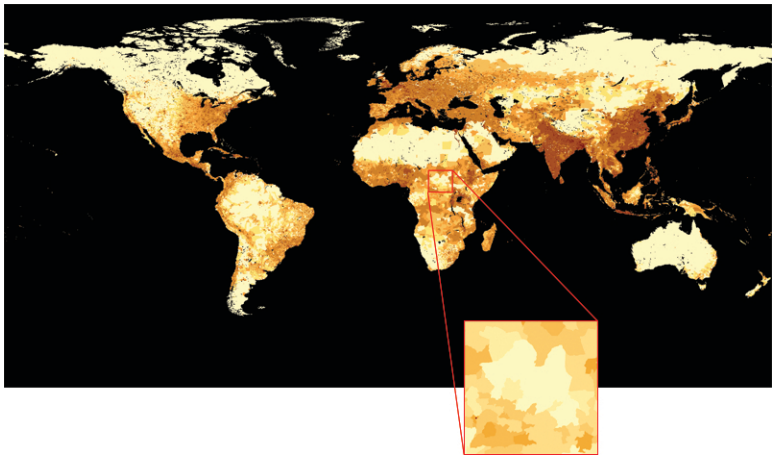

Figure 4.3: Population density map used as the dataset by the NEOimpactor system. 14 colours are used to define the population density of the entire world. Less well modelled regions such as Africa, appear 'blocky' as shown by the inset image. Generated by the Center for International Earth Science Information Network (CIESIN)

4.1.4 Validation of the Infrastructure Model

The term 'infrastructure' is a broad descriptive umbrella, encompassing industrial buildings, residential homes, road networks, electrical and gas services as well as historical monuments. Furthermore, infrastructure can include non-structural components such as communication networks. As such, an estimate of the monetary value of a geographical region is difficult to assess. Of primary concern to those involved in assessing the NEO threat will be those built structures with industrial or habitation roles. Being associated with human activity, these structures require lighting to facilitate human operation at night. It is this link which enables the use of the night-time light pollution as a proxy measurement for infrastructure density. It is assumed that the more structures there are in a region, the more lighting is required to

POPULATION COMPARISON WITH REAL WORLD DATA

Country	Actual [July 2007]	Modelled	Percentage Error
World	6,602.22	6,125.45	-7.78%
Australia	20.43	25.45	+24.6%
Cambodia	13.99	11.98	-14.4%
Canada	33.39	38.72	+16.0%
Chile	16.28	15.48	-4.91%
China	1,321.85	1,322.04	+0.01%
India	1,129.87	1,033.24	-8.55%
Kenya	36.91	35.24	-4.75%
Korea	49.04	48.20	-1.74%
Russia	141.38	151.44	+7.12%
Switzerland	7.55	8.64	+14.4%
UK	60.78	55.22	-9.15%
US	301.14	263.23	-12.6%
Country population in millions			

Table 4.4: Comparison of real world population estimates and those contained within the NEOimpactor model.

illuminate the diversity of human activity. This is then reflected to space, generating a stronger the light pollution signal.

The NASA-compiled satellite view of night-time Earth is used as the infrastructure density dataset [NASA, 2008]. This remotely sensed map portrays the intensity of light pollution across the globe. The algorithm for determining the cell infrastructure value from the imported density map is given by the equations

$$M_{\rho_{dataset}} = \frac{I_{real}}{\sum_{i=1}^{N} \rho_{dataset} A_{cell}} , \tag{4.3}$$

$$I_{cell} = \rho_{dataset} M_{\rho_{dataset}} A_{cell} . \tag{4.4}$$

The methodology is similar to that for the population density data (see Equation 4.1). Here the global reference value, I_{real}, is taken as a generic global Gross Domestic Product (GDP) value. The resultant value, I_{cell}, is a representative value for the cell's infrastructure value proportional to the world. Rather than a direct figure in dollars ($), I_{cell} represents a dimensionless measure for the total infrastructure contained within a cell. This new economic unit is termed a 'NEOimpactor Infrastructure Unit' (NIU).

It is important to note that this approach does not attempt to link human populations with infrastructure signals. While in post-industrial countries infrastructure

Figure 4.4: Night-time light pollution map used as the dataset by the NEOimpactor system. Grayscale shades are used to define the infrastructure density, with dark regions indicating high density and thus greater wealth.

and human habitation patterns will coincide due to the high standard of living, in pre-industrial nations there will not be such strong correlation due to a greater populations living in rural locations with poorly developed infrastructure. Nevertheless, cities and large conurbations in more developed countries have an associated night-time light pollution signal. Errors could be introduced by strong signals, such as gas burn-off at petrochemical works, not associated with artificial lighting.

Figure 4.5 shows GDP values plotted against the NIU for a hundred countries from the NEOimpactor database. A trend-line is fitted which shows the positive correlation between the two factors. The correlation is positive, with one NIU representing a value of approximately $ 0.2 billion. While the relationship is only approximate, it is important to note that GDP is not used as a direct indicator of the infrastructure contained in a country. Rather the NIU models the global distribution of infrastructure. Furthermore, as NEOimpactor is primarily used to compare and contrast multiple impact events, it is the global distribution of infrastructure, rather than a particular local value, which is most important.

4.2 Validation of NEOimpactor's Atmospheric Module

4.2.1 A Test of the Atmospheric Mechanics

A force propagator models the passage of the asteroid through Earth's atmosphere. Both the changing atmospheric density and gravitational acceleration are taken into account. To validate the model's mechanics, a simple simulation of a ball dropped from rest at a known altitude is performed and the results compared with standard theory. Table 4.5 provides the results of this simulation. With the atmospheric model turned off, NEOimpactor's predicted impact conditions mirror those of the constant acceleration equations. The small variation is due to the slight change in gravity

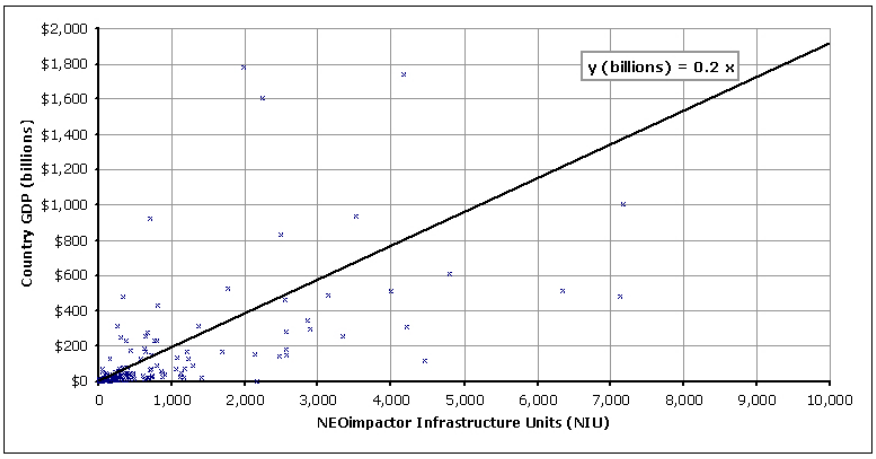

Figure 4.5: Approximate correlation between a country's GDP value and the newly defined NEOimpactor Infrastructure Unit. As an approximate relationship, one NIU accounts for 0.2 billion dollars.

with altitude modelled by NEOimpactor. With drag considered the impact speed is reduced and travel time increased as expected due to the effect of atmospheric drag.

In their analysis of small meteors and meteorites, Ceplecha et al. [1998] predict that bodies of 1 kg will impact the ground at approximately 10 m/s while those of 10 kg will impact at 100 m/s. Table 4.6 presents the predicted impact velocities of these two meteorites modelled in NEOimpactor. Although NEOimpactor is not designed to model such small objects, the force propagator predicts impact velocity values similar to those suggested in the literature. The unknown property in all meteor flight analysis remains the object's shape and its ability to generate lift during the atmospheric flight.

TEST OF NEOIMPACTOR'S NEWTONIAN MECHANICS

	Const. Acceleration	**NEOimpactor Model**	
		no drag	**inc. drag**
Travel Time (s)	14.278	14.277	14.585
Impact Velocity (m/s)	140.071	140.036	131.178

Table 4.5: Test calculation for a 20 kg ball dropped from a height of 1,000 m. The first column details the output from the constant acceleration equations (no drag). The second column presents the results as simulated by NEOimpactor, both with and without drag.

4.2.2 Analysis of the Complete Atmospheric Flight Path

In this section, the trajectory of a simple test asteroid is analysed during its passage through the Earth's atmosphere. Two entry conditions are modelled for comparison, the characteristics of which are presented in Table 4.7. These represent a vertical and oblique entry to study the difference this has on the impact conditions.

TEST OF SIMULATION'S TERMINAL VELOCITY

	Predicted Impact Velocity (m/s)	
	Ceplecha et al. [1998]	NEOimpactor Model
1 kg body	10 m/s	7.34 m/s
10 kg body	100 m/s	135 m/s

Table 4.6: Comparison of impact velocity predictions of two very small meteorites.

TEST ASTEROID'S CHARACTERISTICS AND TRAJECTORIES

Asteroid Characteristics	**At Atmospheric Entry**	
Diameter	200 m	
Radius	100 m	
Principal Length	0 m	
Shape	Sphere	
Volume	4,188,790 m^3	
Composition	Stony Iron	
Density	3,500 kg/m^3	
Mass	1.457x10^{10} kg	
Entry Conditions	**Vertical Entry**	**Oblique Entry**
Velocity	12,000 m/s	12,000 m/s
Latitude	0°	0°
Longitude	0°	0°
Bearing	-	East
Flight Path Angle	90°	45°
Kinetic Energy	1.0556x10^{18} J	1.0556x10^{18} J

Table 4.7: Physical characteristics of the test asteroid and the two example trajectories used for analysis of the atmospheric flight model. 'Principle Length' defines the length of the cylindrical segment of the asteroid body (pictured in Figure 3.1) and is zero for spherical shapes. 'Flight path angle' is the angle subtended from the local astronomical horizon.

The NEOimpactor Atmospheric Model

From the initial entry conditions and trajectory components, the NEOimpactor force propagator (using a the Runge-Kutta integrator) models each aspect of the flight path, as well as the action of the atmosphere on the object's physical characteristics. The location, force, velocity and acceleration are all calculated with the co-ordinate axes in the centre of the Earth, with the positive X-axis along the Equator at 0° Longitude, and the positive Y-axis at 90° East as pictured in Figure 4.6.

NEOimpactor models the Earth's atmosphere using the 1978 Standard Atmosphere [Minzner, 1977]. Figure 4.7 shows the characteristics of this model as simulated within NEOimpactor. The atmosphere is modelled up to an altitude of 200 km. This altitude is chosen as the starting entry point for all asteroid simulations.

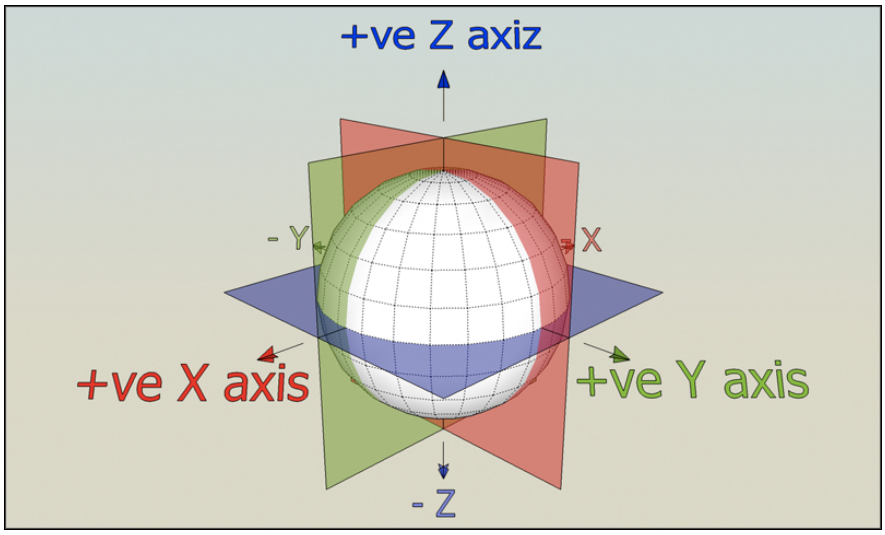

Figure 4.6: The Earth-centered Cartesian frame of reference used for all atmospheric calculations within NEOimpactor. The X-Y plane is along the equator, with the positive X-axis at the 0° longitude and the positive Y-axis at 90° East. The positive Z-axis points through the North pole at 90°N [Fortescue et al., 2003, Chapter 2]. At the point of atmospheric entry, NEOimpactor converts the incoming trajectory components (Table 4.7) into co-ordinate system for use in the Runge-Kutta force propagator.

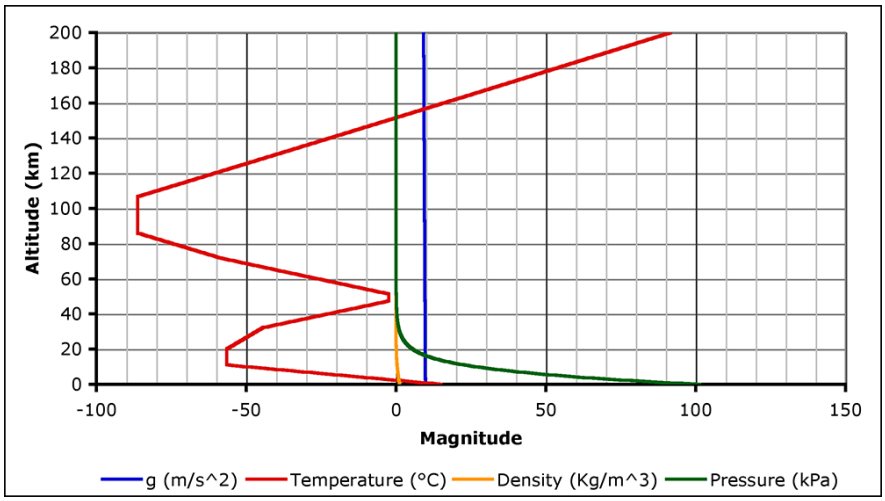

Figure 4.7: The standard atmosphere model simulated within NEOimpactor.

Entry Speed Profile Along the Trajectory

Figure 4.8 shows the speed of the object as it approaches Earth for both test trajectories. Both profiles are characterised by a steadily increasing velocity as the Earth's gravitational force attracts the body with little atmosphere present to provide a drag force. Figure 4.9 presents a diagram of the asteroid approaching the Earth along both trajectories. The velocity and acceleration axes of the system are located in the centre of the Earth, as pictured in Figure 4.6. The acceleration of the oblique entry is lower than

for the vertical entry as the gravitational acceleration is acting at 45° to the velocity vector. With no atmospheric drag both objects continue to accelerate until at 30 km altitude the atmospheric density increases such that drag begins to reduce the velocity. The vertical test clearly shows this drag affect, with the maximum speed of 12,143 m/s at an altitude of 11.66 km, reached 15.6 seconds after entry. Following this the asteroid slows to 12,131 m/s as it passes through the lower atmosphere.

The oblique speed appears not to be greatly affected by drag in the same manner. Throughout the flight path, the object's speed and acceleration remain below that of the vertical body, with the peak speed of 12,156 m/s reached at impact (23.63 seconds after entry). However, Figure 4.10 presents the separated velocity components which shows the affect of drag and gravitational acceleration on the body in the oblique trajectory. The component of acceleration of both trajectories is shown in Figure 4.11.

Comparison with the web simulation provided by Collins et al. [2004] and others are difficult because they do not specify at which altitude their simulation begins. The NEOimpactor simulation begins modelling at 200 km, as this is the maximum height of the standard atmosphere. The initial 160 km of the approach is then characterised by continuous gravitational acceleration with negligible drag, leading to a gradual increase in the asteroid's velocity. Furthermore, in the web simulation the available object densities is below that of the NEOimpactor test body.

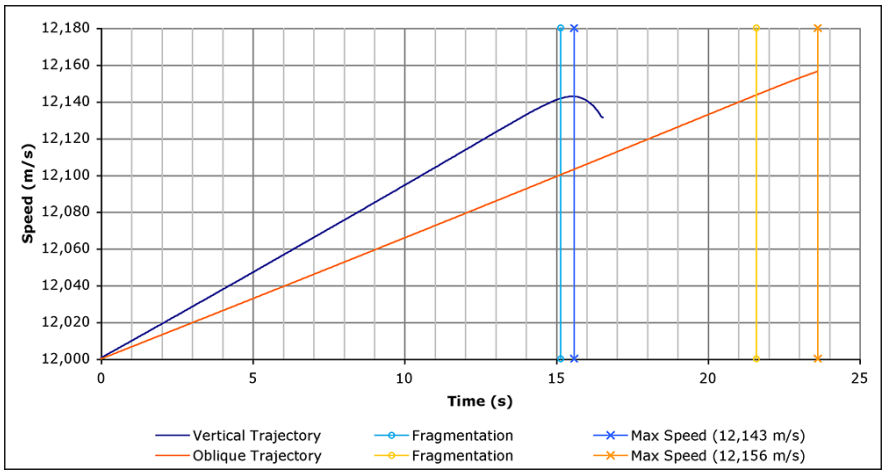

Figure 4.8: Variation in object speed (along-track velocity) with time. The blue lines represent the vertical entry test and the orange line denote the oblique test results. Velocity components of the oblique trajectory are presented in Figure 4.10.

The Affect of Ablation on the Asteroid's Flight

As the atmospheric density increases significantly below 30 km, the drag force generates frictional heating on the asteroid's surface. This has the effect of ablating the surface material and reducing the object's mass. Figure 4.12 plots the mass loss over

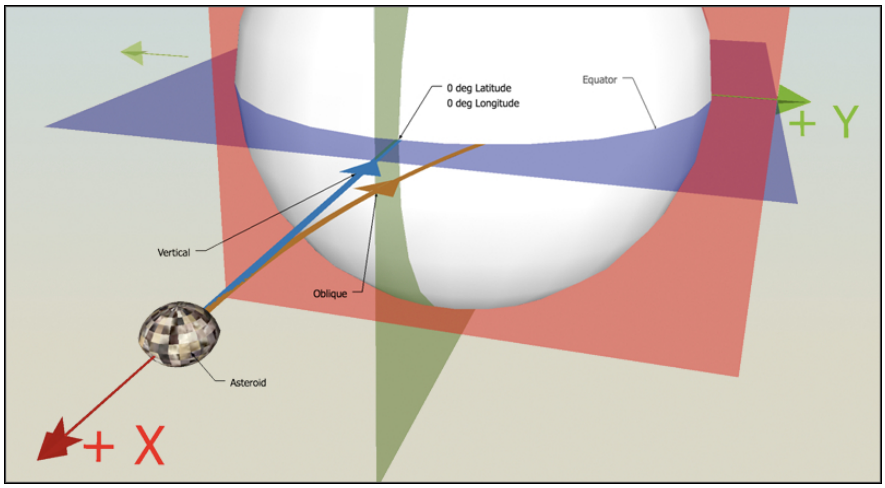

Figure 4.9: A view of the incoming asteroid along the two trajectories. The blue path represents the vertical impact case, while the orange path suggests the oblique path. Due to the co-ordinate axes from the centre of the Earth, the vertical component of both trajectories is along the negative X axis. The oblique trajectory also has a component in the positive Y axis.

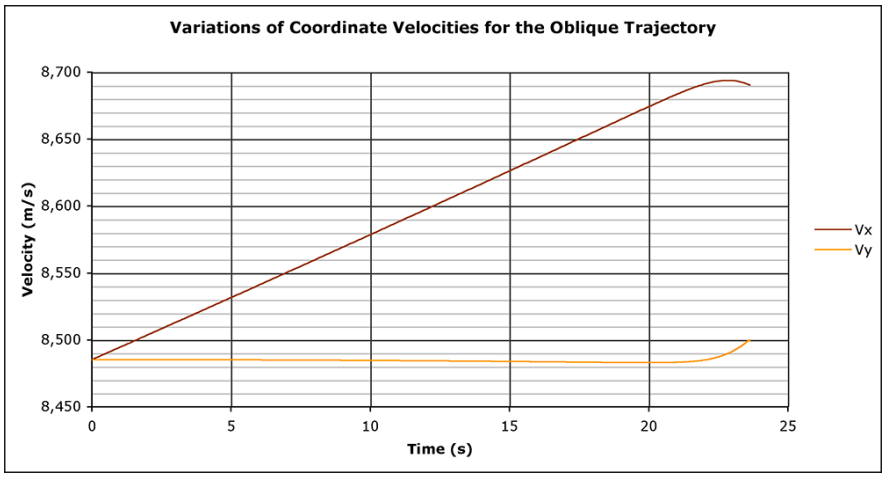

Figure 4.10: The vertical (Vx) and horizontal (Vy) velocity components for the oblique trajectory plotted in Figure 4.8.

time for both entry conditions. Also plotted is the point at which fragmentation would be expected due to the shock front pressure exceeding the internal strength of the body (discussed in Section 4.2.2). The vertical body loses 135,355 tonnes of material while the oblique trajectory body looses approximately 40% more (195,431 tonnes). This is due to the longer period of time spent travelling through the denser atmosphere. The loss of mass results in a reducing in the object size (using a direct mass-volume relationship) leading to a reduction in the opposing drag force and slight acceleration.

This ablative mass loss results in a reduction in the physical size of the object. The assumption is made that ablation is uniform over the spherical surface. At each step of the integration, the ablated mass loss is represented as a reduction in object radius,

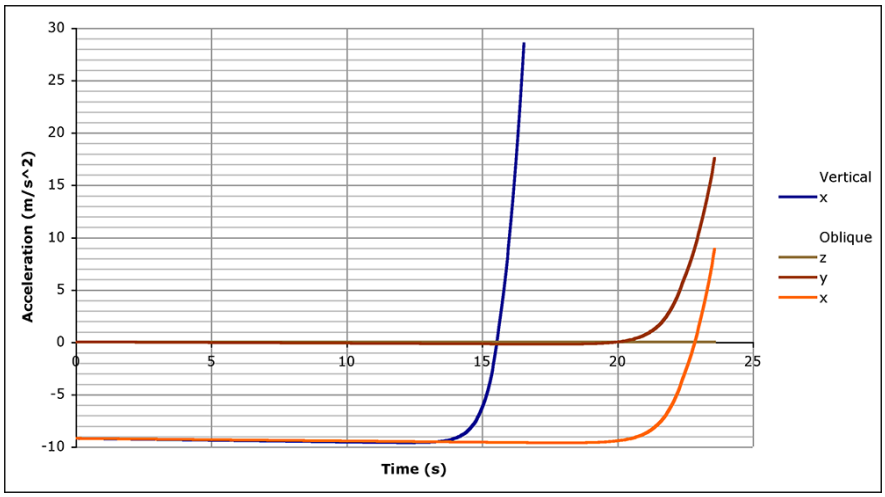

Figure 4.11: This figure presents the component acceleration over time for both asteroid trajectories. The vertical trajectory only has one component (in blue) due to the start location at 0°N, 0°E which is on the Earth's x axis. The oblique trajectory moves in the x-y (equatorial) plane.

presented in Figure 4.13. Subsequently atmospheric drag will be marginally reduced as the frontal area reduces leading to a velocity increase. The effect is small with the object's diameter being reduced by only 0.62 m for a vertical impact, and 0.90 m for the oblique trajectory. While this loss is negligible compared to the size of the test asteroid, such a loss on a small body could bring about its catastrophic break-up.

Figure 4.14 presents this information as a percentage lost over time. The mass loss is approximately one percent of the original body. While not impacting greatly on the overall kinetic energy of the impact, the ablated mass would have secondary effects on the Earth. Firstly in terms of atmospheric heating and secondly the pock-marking of ablated debris along the asteroid's ground track. However, these secondary effects are matters for separate study.

Kinetic Energy Profile Along the Trajectories

During the initial passage of the asteroid, the lack of atmospheric drag leads to a continued velocity increase. This steadily increases the kinetic energy of the body. During passage through the lower, denser part of the atmosphere, the object's velocity is attenuated, and its mass is reduced due to ablation. Both these effects combine to reduce the kinetic energy of the body, calculated as $\frac{1}{2}mV^2$. However, it is the velocity which most significantly alters the kinetic energy due its velocity-squared dependance.

Figure 4.15 presents a plot of the kinetic energy against time for both trajectories. From an initial KE of 1.0556x10^{18} J, the vertical trajectory body reaches a peak of 1.0793x10^{18} J while the oblique entry object reaches 1.0792x10^{18} J, an increase of 2.25%.

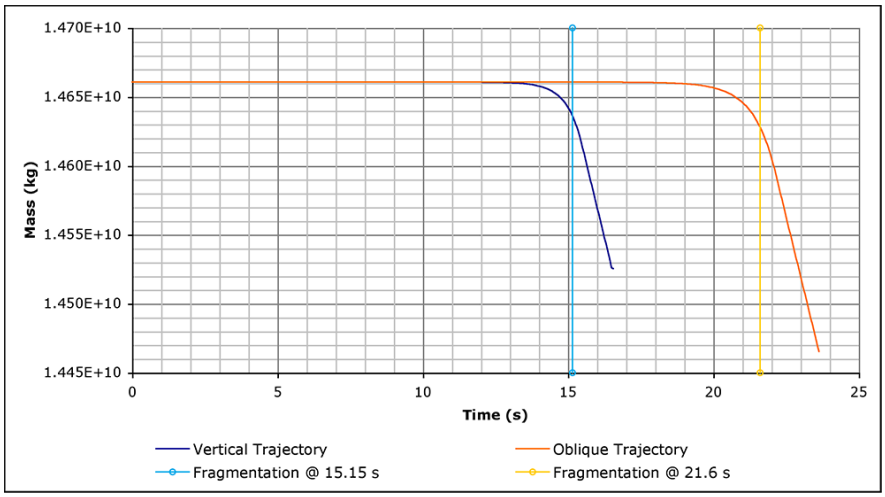

Figure 4.12: Mass lost due to ablation plotted against time. The vertical lines denote the expected point of fragmentation. This would result in a dramatically different ablation curve, but this is practically impossible to simulate accurately.

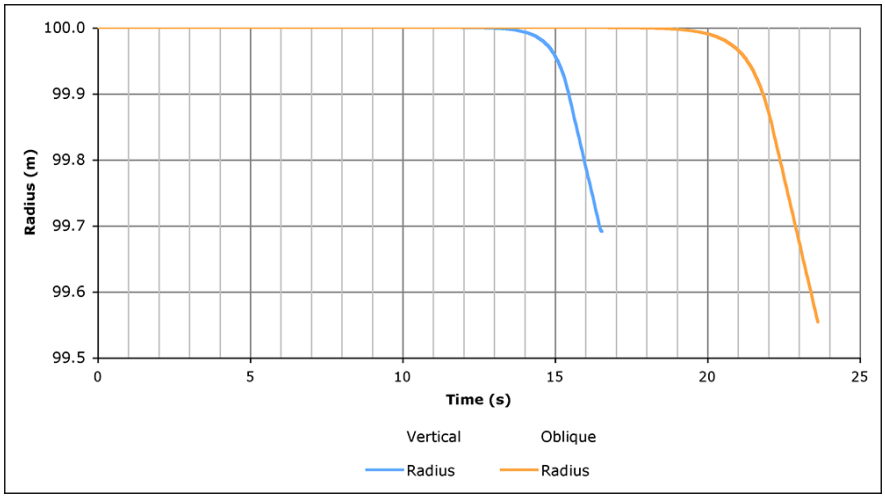

Figure 4.13: Reduction in radius over time due to the effect of ablative mass loss.

The impact energy of the vertical and oblique trajectory test objects are 1.0688x10^{18} J and 1.0686x10^{18} J respectively. Over the entire simulated flight path, NEOimpactor predicts a net increase in KE of approximately 1.2% irrespective of incoming trajectory.

The similarity between the KE profiles for both test trajectories is demonstrated in Figure 4.16. Here the KE is plotted against altitude with the secondary axis plotting the atmospheric density with altitude. This shows that it is the dense lower atmosphere that is responsible for reducing the incoming object's kinetic energy, demonstrating its role in protecting the Earth from very small objects.

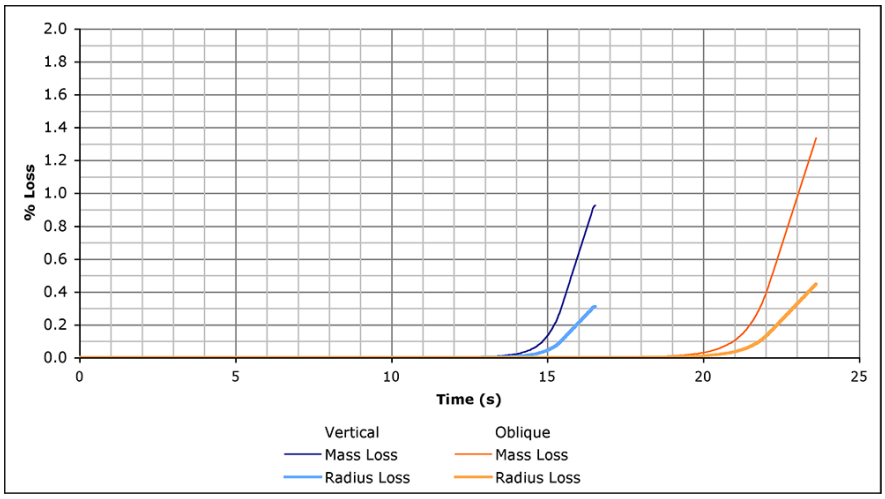

Figure 4.14: Percentage of both mass and radius lost due to atmospheric ablation for each trajectory profile.

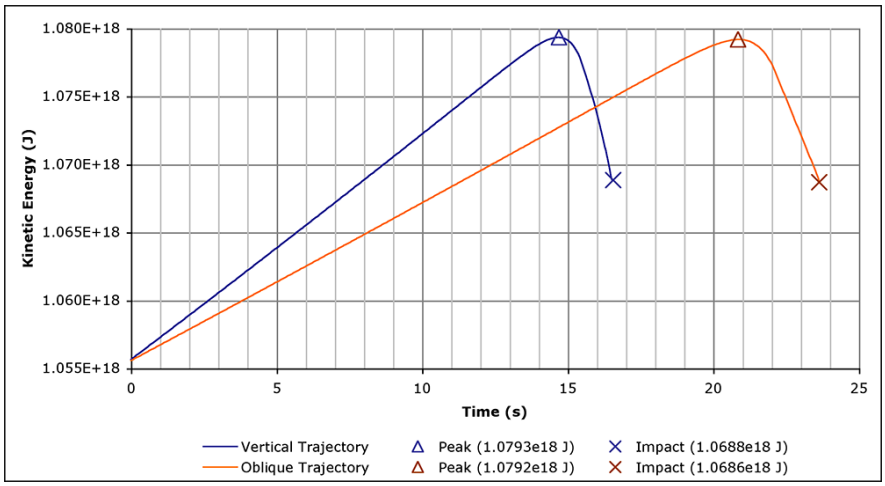

Figure 4.15: Kinetic energy profiles of the vertical (blue) and oblique (orange) trajectories plotted against time. Values for the peak energy and impact energy for both objects are given.

Comparison of the Vertical and Oblique Impact Characteristics

At the point of impact it is the object's kinetic energy that determines the extent and severity of damage generated. In reality the angle of impact does have an effect on the generation of the blast wave and ejecta distribution. This directionality of the IGE remains the focus of complex hydrocode simulations. Furthermore, complex simulations of oblique ocean impacts reveals little difference from vertical impacts [Gisler et al., 2003].

The results presented in Table 4.8 compare the asteroids' characteristics at the point of impact for both simulated trajectories. The oblique trajectory results in a marginally greater mass loss and slight velocity increase. Its passage takes it approx-

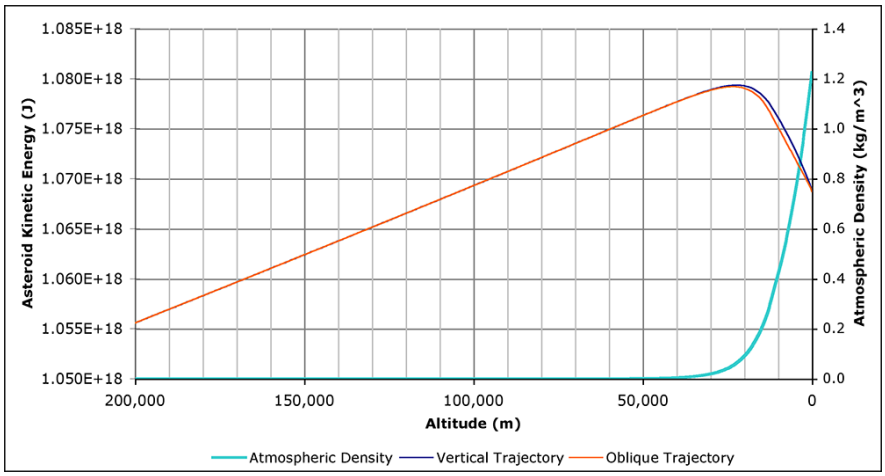

Figure 4.16: Kinetic energy of each body plotted against altitude demonstrating the negligible difference that trajectory has on the impact kinetic energy. Plotted in pale blue against the secondary Y axis is atmospheric density.

TEST ASTEROID'S CHARACTERISTICS AT POINT OF IMPACT

Impact Characteristics	**Vertical Trajectory**	**Oblique Trajectory**
Time (s)	16.56	23.63
Diameter (m)	199.38	199.11
Radius (m)	99.69	99.55
Volume (m^3)	4,150,117	4,132,953
Mass (kg)	$1.453x10^{10}$	$1.447x10^{10}$
Velocity (m/s)	12,131.3	12,155.7
Latitude	0°	0°
Longitude	0°	1.80°
Flight Path Angle	90.00°	45.64°
Kinetic Energy (J)	$1.0688x10^{18}$	$1.0687x10^{18}$

Table 4.8: Presented here are the asteroid's characteristics at the point of impact following both the vertical and oblique trajectories. Original characteristics at the point of atmospheric entry are given in Table 4.7.

imately 1.8 degrees of longitude around the Earth from the entry point and during the flight its trajectory is steepened by a small amount (0.64°). In observed meteorite falls, the object trajectory is seen to steepen as the object passes through the lower, denser atmosphere. However, the overall effect on the kinetic energy is a small reduction of 0.01% compared to the vertical trajectory. Over the full range of object radii this variation in kinetic energy could be greater. However, for simplicity oblique impacts will not be considered further, all comparison impact events will be simulated as vertical impacts. The key advantage is that the exact impact location can be chosen prior to atmospheric entry as the object will impact directly below the atmospheric entry coordinates.

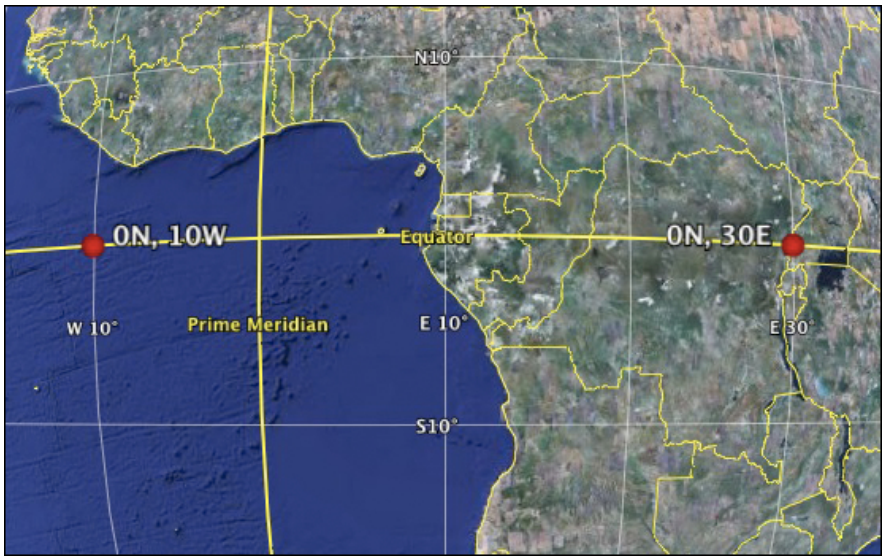

Figure 4.17: Location of the two single impact comparison sites, on land (in central Africa) and in the Atlantic Ocean.

Fragmentation Consideration

Although not a consideration for the current project, the flight-path algorithm continually tests for the possibility of asteroid break-up. The expected fragmentation point is plotted in Figure 4.12 for both the test trajectories. However, it is the energy of impact rather than the physical characteristics of the impacting body which is taken as the critical factor in determining the impact generated effects. Furthermore, recent work presented by M. Boslough at the 2009 Planetary Defence Conference suggested that despite an airburst event, the incoming momentum of the asteroid will continue to the ground causing significant damage.

LAND IMPACT CRATER DIMENSIONS

Crater	NEOimpactor	Collins et al. [2004]
Transient Crater		
Diameter	2284.9 m	2,610 m
Depth	891.2 m	922 m
Final Crater		
Diameter	2553.9 m	2,970 m
Depth	389.8 m	411 m
Rim Height	80.3 m	-

Table 4.9: Characteristics and dimensions of the land impact crater compares with those predicted by the Web-based impact model [Marcus et al., 2009]. The transient crater is initially excavated by the impact energy with the final crater form developing as the structure and debris settle.

COMPARISON OF LAND IGE MODELS

Land IGE	NEOimpactor	Collins et al.
Thermal	1.17×10^7 J	1.37×10^7 J
Ejecta	0.348 m	0.903 m
Pressure	63,729.7 Pa	59,700 Pa
Seismic	5.7	6.2

Table 4.10: Comparison of the NEOimpactor predicted land IGE and those predicted by the Web-based model [Marcus et al., 2009]. The test impact is a 500 m diameter spherical stony asteroid with an entry speed of 12,000 m/s. The IGE magnitudes are compared at a distance of 20 km from the impact point.

Figure 4.18: A closer view of the test land impact location. The site is situated in Uganda, near to the border with the Democratic Republic of the Congo and 300 km from the capital city of Kampala. Rwanda and Burundi lie to the south.

4.3 Study and Comparison of Two Example Impact Scenarios

NEOimpactor's primary data output presents the effects and consequences for an individual impact event. Impacts can be simulated anywhere on the Earth and each will generate different consequences. Events are characterised as being either land or ocean impacts. In order to demonstrate the ability of NEOimpactor to model both scenarios, two arbitrary impact locations are chosen on the Equator, equidistant from the equatorial coastline of East Africa (Figure 4.17). Both impact tests simulate the asteroid detailed in Table 4.7 using the vertical trajectory. The following present both impacts separately, and they are then compared in Section 4.3.3.

4.3.1 Land Impact Test

The test land impact is located at 0° latitude, 30° East in Uganda. Figure 4.18 shows the impact location in greater detail. At impact, the object excavates a crater in the ground. The dimensions of the impact crater are provided in Table 4.9 and show reasonable correlation with the simulation developed by Collins et al. [2004].

Study of the Land Impact Generated Effects

The four IGE maps are reproduced in Figure 4.19 at the full system resolution where one pixel represents a cell in the system database. Reproduction in print represents a challenge as each pixel along the equator represents a 20 km square on Earth (a total area of 400.3 km^2). Short range IGEs, such as ejecta, are difficult to portray as they do not cover many cells surrounding the impact site. The casualty and damage distribution maps are also reproduced in Figure 4.19.

Figure 4.19 **A** displays peak overpressure values recorded in the database. The test impact generated a peak overpressure of 452,427 Pa (56.6 psi) at the point of impact, decreasing to 9 psi over the first 20 km. From nuclear weapons research, values above 15 psi are assumed to result in total destruction of reinforced concrete structures [Glasstone and Dolan, 1977]. Nuclear weapon research data is only available up to 100 MT, but this has been extrapolated in Figure 4.20 to the simulated impact energy in MT. The extrapolated impact energy concurs with the 9 psi predicted value at 20 km. It is this pressure difference across the shock front which generates the characteristic blast wave 'wind'. Damage is sustained as a result of direct action, for example knocking over objects or exploding windows, or indirectly by the high velocity debris carried in the wind. However, relating damage to more familiar atmospheric natural hazards is difficult as damage is usually generated by sustained wind velocities.

Seismic shock waves are distributed efficiently through the Earth's crust as vibrational energy resulting in their wide spread appearance in Figure 4.19 **B**. Here, each shade contour (visible clearly at full resolution) represents a 0.1 magnitude drop on the Richter Scale. The peak magnitude at the point of impact is M 6.02 which is just below the Egion earthquake of 15 June 1995 [Tselentis et al., 1996] which claimed 26 lives. Magnitude 6 earthquakes are not rare, occurring on an approximately daily basis world-wide. The seismic magnitude of this event is not special and would need to be above 6.5 to have real significance [USGS, 2008b].

The radius of the fireball at the critical temperature (peak radiation flux) is 2 km which is similar in magnitude to that predicted by Glasstone and Dolan [1977]. The flux is attenuated by distance from source as $\frac{1}{R^2}$ and limited by the curvature of the Earth (i.e. the visibility of the fireball above the horizon). In Figure 4.19 **C** the extent of the irradiation is shown as a small circle of affected cells surrounding the impact site. Studies concerning the survivors of the Japanese nuclear detonations on Hiroshima and Nagasaki demonstrate the potential catastrophe that irradiation can generate [Sublette, 2007]. The Radiation Effects Research Foundation [RERF, 2008] continues to monitor the health of those that survived the bombs.

The majority of the ejected material is deposited within the excavated crater, forming the crater rim. Any ejecta falling outside the crater will be impacting a

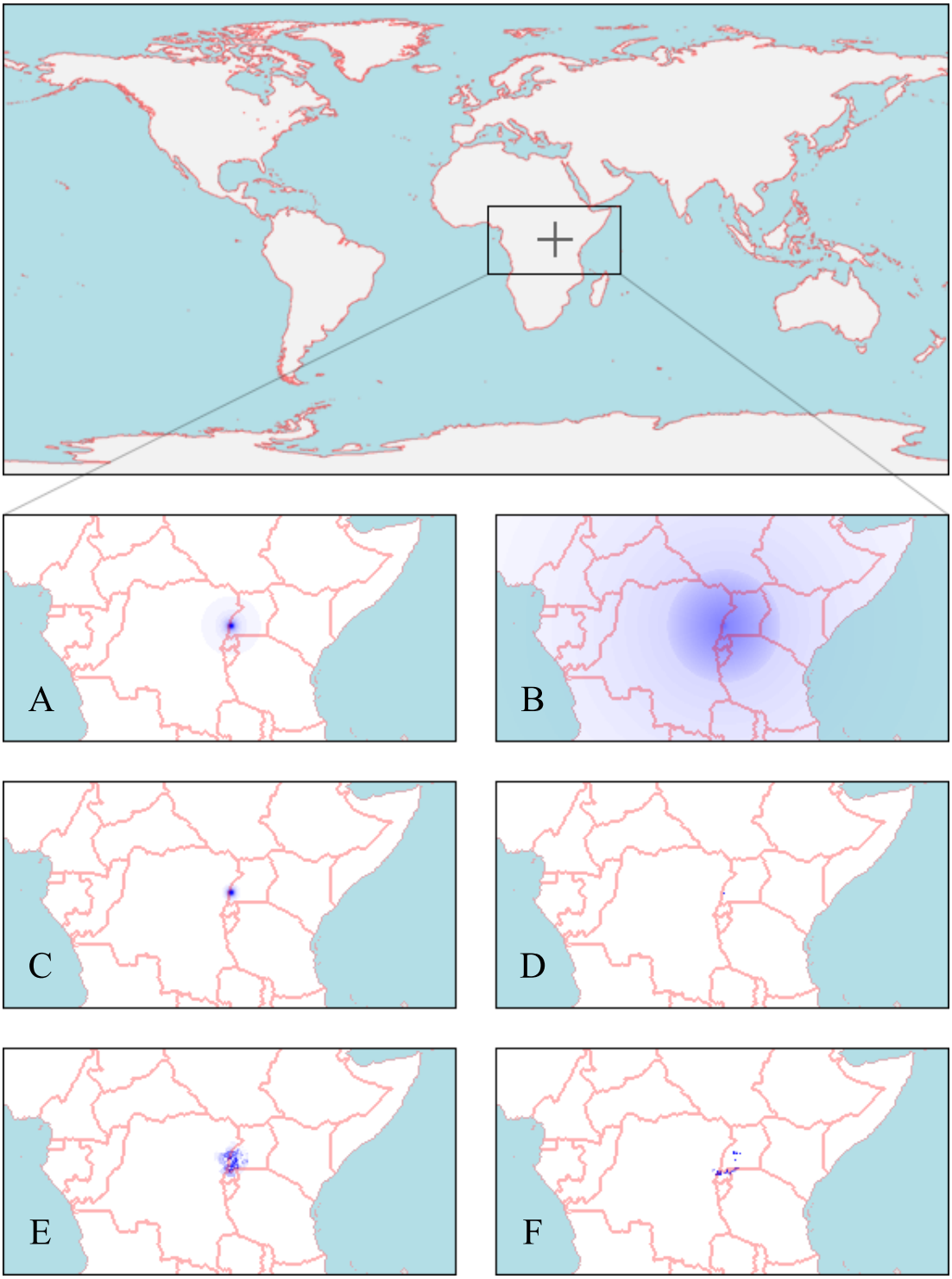

Figure 4.19: Land IGEs and consequences from the test land impact. The main map displays the location of the test impact with the sub figures as follows. **A** - peak blastwave overpressure, **B** - seismic shock magnitude, **C** - thermal radiation, **D** - ejecta (negligible), **E** - casualty distribution, **F** - damage sustained.

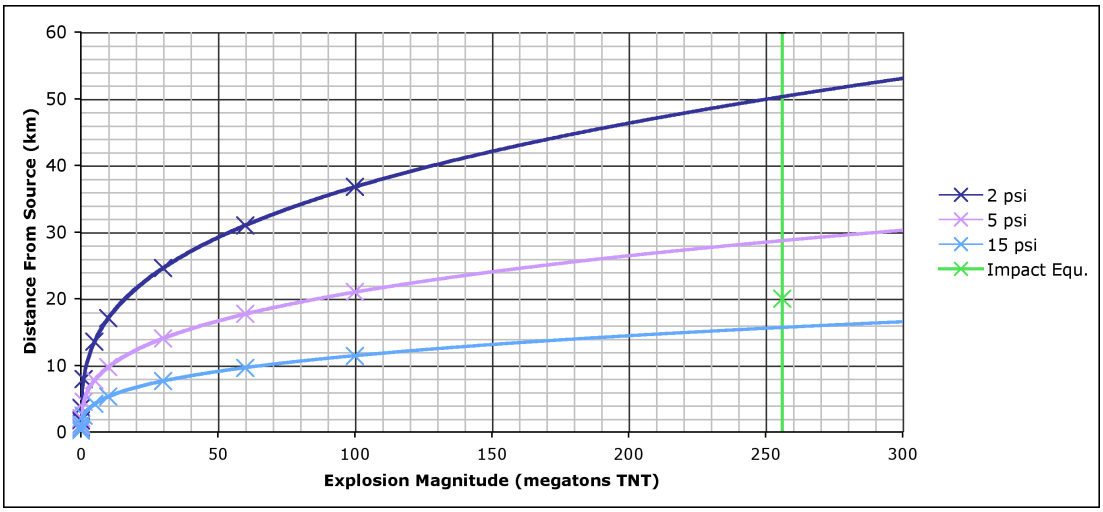

Figure 4.20: Plot of the range of peak overpressure resulting from various explosive detonations. Power law extrapolation lines have been added to reach the 256 MT of the test asteroid impact. The vertical green line represents the test impact energy equivalent in MT. The cross indicates the 9 psi point for the test imapact. Data points extracted from Meyer and Meyer [2005].

region already devastated by the IGEs and therefore will have limited additional effect. Furthermore, refuge from falling debris is possible by finding cover, whereas the other IGEs are able to penetrate such shelters. Ejecta is therefore the least significant of the four IGEs modelled. Nevertheless, the possibility of damaged sections from buildings falling on people is obvious. Comparisons can be made with the experience of Pompeii and Herculaneum during the eruption of Vesuvius. Evidence of casualties and damage caused by tephra[3] prior to the pyroclastic flows reaching the city is found in the stratigraphy of the deposits [Spence et al., 2005].

External Validation of the Land IGE

The Arizona State University's *Earth Impact Effects Program* developed by Collins et al. [2004] provides the external verification for NEOimpactor's land IGE model. Table 4.10 compares the NEOimpactor predicted IGE magnitudes for the test land impact, with those from the web application. The reference distance is set to 20 km from the impact site. The table shows good correlation of the data. The variation between the two models is largely due to the impact event calculation where the impact energy develops the crater. Differences in the computational approach used by both programs will result in a difference in the predictions. However, it is important to note that no real-life external comparison data is available to validate either of the models.

[3] Air-fall material emanating from a volcanic explosion. Volcanic bombs are an example of tephra and have been found to have killed many of the inhabitants of Pompeii.

CONSEQUENCES OF THE TEST LAND IMPACT

	Casualties	**Damage (NIU)**
	Uganda (1,546,570) Congo [DRC] (812,549) Rwanda (216,000) Tanzania (33,600)	Uganda (8.75) Rwanda (7.90) Congo [DRC] (3.75) Tanzania (2.69)
Total:	2.91 million	23.1
No. of affected countries:	4	4
% of world affected:	0.046 %	0.036 %

Table 4.11: Casualty and damage estimates from the test land impact into Uganda at 0° latitude, 30° East. Damage values are given in NEOimpactor Infrastructure Units.

Human and Economic Consequences from the Test Land Impact

Figure 4.19 **E** and **F** present the predicted casualty and damage distribution maps respectively. Table 4.11 presents the details of the consequence data for each country affected. While the absolute values of people killed or infrastructure destroyed is difficult to verify without a real-world comparison event, the relative consequences for each country is important. Uganda, having the impact site within its borders, is the most affected country, suffering the greatest casualty and damage loss. However, the relative casualties and damage per country suggest that while the Democratic Republic of the Congo will suffer a greater casualty loss, Rwanda has greater infrastructure vulnerability. Such information would be valuable in providing aid agencies with prior knowledge as to where to focus particular aid efforts.

4.3.2 Ocean Impact Test

The ocean impact site was chosen at 0° latitude, 10° West in the Atlantic Ocean and the same asteroid as described in Table 4.7 is impacted, assuming a vertical trajectory. The transient ocean cavity generated by the asteroid is specified in Table 4.12. This cavity is over twice the size of the land impact crater due to the lower density of sea water compared to rock strata.

Ocean Impact Generated Effects

Due to the nature of wave transmission, the kinetic energy of impact is efficiently propagated across the ocean. This results in a large number of countries being affected by the single event. However, it is only a small coastal region of each country which is affected. Figure 4.21 presents five of the output maps generated by NEOimpactor's ocean impact model. Similar difficulties exist in mapping the ocean IGEs as with the

DEEP WATER WAVE CHARACTERISTICS

Cavity Characteristic	NEOimpactor	Collins et al. [2004]
Diameter	4,888 m	4,780 m
Depth	1,617 m	
Volume	$30.6x10^9$ m^3	
Ocean Depth	2,345 m	
Bottom Out ?	No	
Initial Tsunami Characteristics		
Wave Speed	234.3 m/s	
Wave Period	23.5 min	
Amplitude	153.9 m (deep water)	

Table 4.12: Dimensions of the transient ocean cavity and the initial tsunami characteristics following the test ocean impact. (Only the cavity diameter is predicted by the web simulator.)

land IGE discussed previously. Tables 4.13 and 4.14 provide examples of detailed data available to the NEOimpactor user.

Figure **B** displays the full geographical region influenced by the tsunami propagator. The data plotted is the wave travel time, shading from white to blue with increasing time. The fact that the whole ocean is shaded indicates that the wave has, eventually, inundated every coastline unlike simple ray tracing methods. This is seen with real tsunami, though the attenuation is such that the eventual tsunami magnitude is negligible. Simulations of the Boxing Day Tsunami by NOAA [2008] show the eventual global coverage of that particular tsunami wave.

Subfigure **C** displays information about the radiating wave pattern. The tsunami algorithm uses an orthogonal propagation methodology (detailed in Section 3.2.3) which is represented by the concentric diamond pattern. The critical amplitude at each stage is affected by the ocean depth, which is seen in the 'rough' edges of the tsunami diamond. Although mapping this information is of limited use, it can be used to identify the order in which coastlines are inundated. Table 4.13 displays data about the location in Liberia which is affected first.

Tsunami Decay Model Validation

NEOimpactor's tsunami model is primarily based on the models produced by Ward [2000]. Comparison of the tsunami amplitude attenuation has been made using a later study by Ward and Asphaug [2002]. Figure 4.22 overlays the NEOimpactor predicted amplitude attenuation on Figure 3 from their paper. The curve predicts the decay of peak amplitude with distance from source for a particular depth of ocean. The impact site used in the NEOimpactor simulation is 3.5 km deep rather than 3 km,

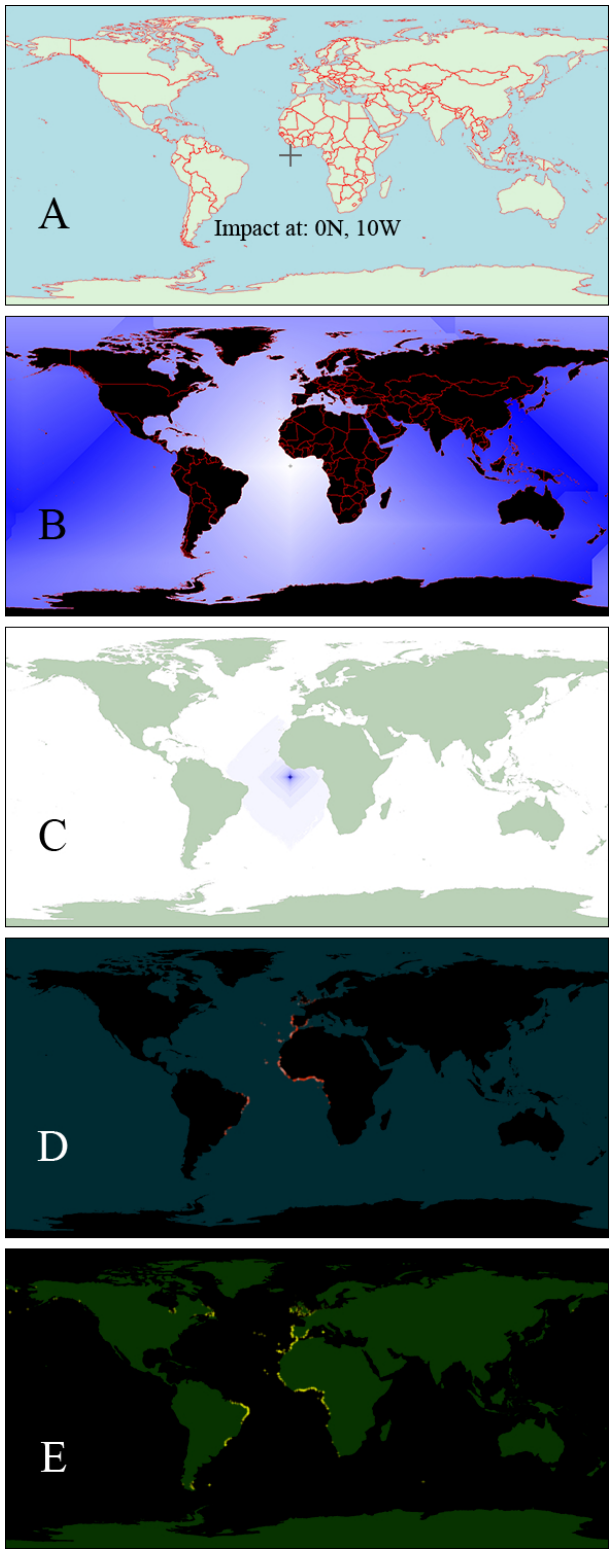

Figure 4.21: Compiled presentation of the various data types generated by NEOimpactor following an ocean impact simulation. **A** - impact site identification, **B** - wave travel time, **C** - decay of the peak wave amplitude, shaded from blue to white, **D** - casualty distribution along the coastline (shaded red), **E** - damage distribution along the coastline (shaded yellow).

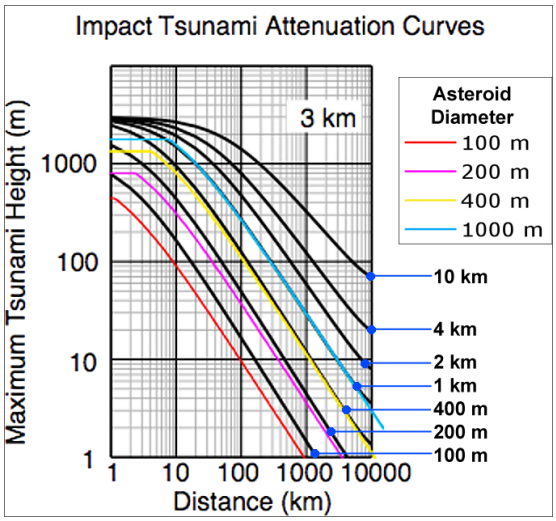

Figure 4.22: Comparison of the NEOimpactor tsunami attenuation with that predicted by Ward and Asphaug [2002] in a uniform ocean depth of 3 km (Figure 4 in their paper). The coloured overlays present the NEOimpactor predicted amplitude decay curves for four of the object sizes modelled. NEOimpactor

SHOALING WAVE MAGNITUDE

Shoaling Characteristics	Magnitude
First Landfall	Liberia
Distance	662 km
Traveltime	47.1 min
Run Up	15.0 m
Run In	2.26 km

Table 4.13: Data concerning the shoaling characteristics of the wave as it first reaches landfall on the coast of Liberia.

so some degree of difference is to be expected. The shape of the curve is accurate for the 1,000 m and 400 m diameter objects, but the smaller diameters fall below Ward's estimates. Therefore the tsunami conditions in NEOimpactor can be taken as a conservative approximation.

Ocean Impact Consequences

Figure 4.21 **D** and **E** present the casualty and damage data stored in the coastal pixels of the database. Table 4.14 collates the consequence data from all the coastal pixels, and details those countries most affected. Of particular interest is that, in terms of casualties, those countries nearest the impact site are most severely affected, whilst in terms of infrastructure damage it is more remote countries which appear top of the list. This is largely because they have more developed infrastructure in coastal regions, such as large trading ports. Brazil is especially vulnerable, despite being on the far

side of the Atlantic Ocean, because it presents a large length of populated coastline to inundation by the ensuing wave.

CONSEQUENCES OF THE TEST OCEAN IMPACT

	Casualty	**Damage (NIU)**
	Ivory Coast (1,129,500) Brazil (949,433) Liberia (501,405) Ghana (455,660) Nigeria (426,461)	Brazil (30.6) Ivory Coast (16.6) Ghana (14.1) Portugal (8.90) Morocco (7.90)
Total	8.08 million	103
Number of affected countries	55	50
% of world affected	0.13 %	0.16 %

Table 4.14: Casualty and damage consequence estimates from the test asteroid impact into the Atlantic Ocean at 0° latitude, 10° West.

LAND AND OCEAN IMPACT CONSEQUENCE COMPARISON

Consequence	**Land Impact**	**Ocean Impact**
Total Casualty Figure	2,910,000	8,080,000
Total Damage Figure (NIU)	23.1	103
Number of Affected Countries	4	55

Table 4.15: Comparison of the predicted consequences from the test land and ocean impact simulations.

Validation of the Ocean Impact Consequences

To validate NEOimpactor's ocean impact consequence model, a simulation comparison was made with the Indian Ocean Tsunami of the 26^{th} December 2004. This tsunami was generated by the lifting of a fault-line under the Indian Ocean by a 8.5 m earthquake releasing $1.17 \text{x} 10^{17}$ Joules of energy [USGS, 2008a]. Within NEOimpactor an asteroid of equivalent energy ($\approx$ 95 m diameter stony asteroid, with other characteristics set to those in Table 4.7) was impacted at the earthquake's epicentre coordinates: 3° North, 96° East. The simulation predicted 223,621 casualties as a result of the generated tsunami while the most recent casualty estimate from the Sumatra earthquake suggest this figure is 227,898. This figure accounts for both those known to have died and those missing, presumed dead. The extremely close correlation of these two casualty figures is somewhat accidental as the casualty distribution will have been different for each event due to the different forms of the tsunami. However, it suggests that the results are in the right ball park.

4.3.3 Comparison of Consequences from Land and Ocean Impact Events

Although the study of individual impact events is important, the associated errors in the specific consequence figures are difficult to determine. Therefore, the results of NEOimpactor become most useful when presented as a comparison of two or more events. Table 4.15 contrasts the consequences for the example land and ocean impact events. The most significant factor is the number of countries affected. Land impacts are local events characterised by a low number of affected countries, typically just one, or a few if the impact is close to borders. On the other hand, ocean impacts have the ability to affect several tens of counties across the world. Such differences between land and ocean impact are clearly significant in understanding Earth's vulnerability to the NEO hazard.

Chapter 5

Results

Chapter 4 demonstrates the ability of the NEOimpactor system to model the global threat of asteroid impacts. This provides a means of assessing the consequences for both humans and the economies of the world. This represents a significant step forward in our ability to model and analyse the global NEO threat faced by any country. However, the limitation of studying individual impact events is the inability to accurately quantify the absolute error associated with the simulation and the consequence prediction. The validation appears to suggest that NEOimpactor provides slightly conservative estimates when compared with the existing models. Both NEOimpactor and the models of other researchers are predominantly limited by the lack of comparison data from a real-world impact event. All models are therefore only extended extrapolations from known phenomena.

In order to counteract the effects of this limitation, the results presented in what follows focus on studying the relative consequences of multiple impact events. The Global Grid and Line Impact Simulation Applications (SA) provide the results studied in the present chapter. The first of these models an asteroid impacting the Earth uniformly over its entire surface and then maps the relative consequence of each event. These results, presented in Section 5.1, highlight which regions of the Earth are most vulnerable to an impact event in terms of population or infrastructure loss. The raw data extracted from the database is correlated to identify which countries are at greatest risk from an impact event.

In Section 5.2 the results of the Line Impact SA studies are presented. Being one-dimensional, the resolution of the line can be greatly increased at little cost to the simulation runtime, since the line of impact represents only a minute percentage of the Earth. These results again focus on the comparative consequences of land and ocean impact events.

5.1 Global Grid Simulation Data

The portrayal of the Global Grid results uses shaded cell mapping, choropleth mapping and country ranking. Choropleth mapping is a technique used to display complex range data using only a limited number of colours, discussed in Section 5.1.4. During the multi-impact simulation, each individual impact event is recorded independently, as well as being compiled into the multi-impact grid output. The two mapping processes implemented (gridded cell in Section 5.1.1, and choropleth in Section 5.1.4) construct a global map by shading in the grid cells, or by colouring the individual countries. The colour shade used is proportional to the relative consequence value recorded for that cell or country. Data is also presented in Section 5.1.6 in tabular form. These are generated by summing the consequence recorded over the entire country and then ranking each country according to this severity scale. The severity scale can then be referenced to various physical, socio-economic, or global indices. For example, referencing the casualty ranking against each country's total land area generates a ranking based on 'casualty density'. These referenced rankings reveal further insights into the global risk and vulnerability assessment. Probabilistic risk assessments for various countries, as well as the world as a whole, are presented in Section 5.1.5.

5.1.1 Grid Celled Mapping Technique

The graphical output maps are presented using two shading techniques. The first uses a single colour, where the 'brightest' (or 'strongest') colour shade represents the impact cell which generated the greatest consequences. This format provides 256 colour shade variations from white (or black) to full colour. Any colour can be chosen for the scale, or grayscale can be used. The shading is linear making each shade variation a 255^{th} increment of the peak consequence value.

The second shading format improves on this by using shading through three consecutive colour ranges. This provides 768 colour variations and consequently a clearer distinction between regions of high and low vulnerability. While any colour range is possible, NEOimpactor adopts three ranges, each used to display a different data set. Casualty results are presented using a ⟨⟨ `white` – `yellow` – `red` – `black` ⟩⟩ range (Figure 5.5); damage maps use the ⟨⟨ `white` – `green` – `yellow` – `red` ⟩⟩ range (Figure 5.6); and comparisons of casualty and damage implement a ⟨⟨ `black` – `blue` – `cyan` – `white` ⟩⟩ scaling (Figure 5.3).

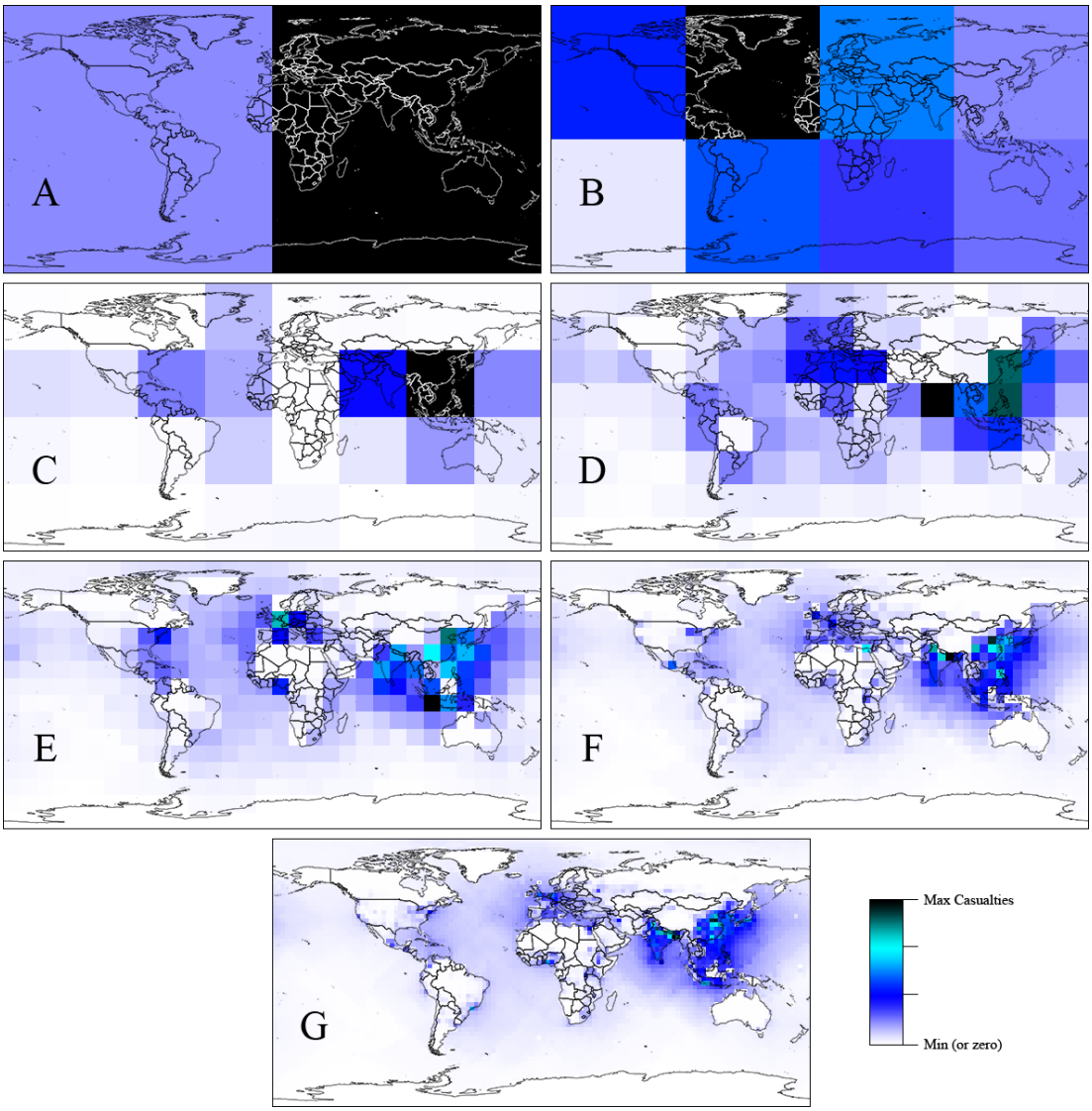

Figure 5.1: Variation of the NEOimpactor Global Grid simulation resolution setting. Resolutions displayed, with the runtime given in brackets, are as follows: **A** - 2x1 (3 mins), **B** - 4x2 (12 mins), **C** - 8x4 (48 mins), **D** - 16x8 (3.2 hours), **E** - 32x16 (12.8 hours), **F** - 64x32 (2.1 days), **G** - 128x64 (8.5 days).

Investigation to Determine the Optimum Global Grid Resolution

Each cell in the Global Grid represents the results of one impact event simulation (taking approximately 1.5 minutes to run). Grid resolution is therefore a balance between data quality and computational time. Low resolution grids do not provide enough comparison impacts to deliver a clear picture of the global vulnerability. On the other hand, the difference in data quality between two high resolution grids may be negligible but incur a significant runtime cost. Figure 5.1 presents seven resolution grids simulated using the impact event. NEOimpactor has the ability to perform a study as fine as 2048x1024 cells. However, at current processing speeds this would

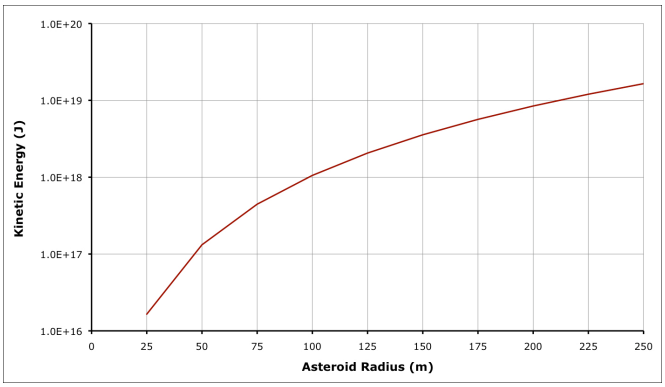

Figure 5.2: Variation of object kinetic energy over the range of radius studied in NEOimpactor for a spherical asteroid. The density is fixed to 3,500 kg/m^3 and the velocity is 12,000 m/s.

take nearly six years to complete. After due deliberation the 64x32 grid (giving a total of 2048 impacts) was adopted as the optimum resolution and this is used in all the following simulations.

Study of the Effect of Impact Kinetic Energy Variation

Up to this point all simulations have modelled the same 'standard' test asteroid. As discussed in Section 2.2.3, asteroids come in a range of sizes, shapes and compositions. This presents a potentially infinite range of asteroids to simulate and study. In order to limit this range, all but one of the asteroid's characteristics were fixed. Its radius is allowed to vary to assess the effects of increasing kinetic energy. The asteroid's other characteristics are constrained to that of the vertical trajectory test object, detailed in Table 4.7).

Principal papers in the field, such as NASA's Science Definition Team report [Stokes and Yeomans, 2003], as well as the community at large loosely use asteroid 'diameter' as a replacement for asteroid energy. With the assumption that the asteroid is spherical, it is easy to show that the object's kinetic energy is given by

$$E_{ke} = \frac{1}{3}\pi\rho_{neo}R_{neo}^3V_{neo}^2 \,. \tag{5.1}$$

This thesis will adopt 'radius' as a measure of kinetic energy, assuming particular values for the object's density and speed. Figure 5.2 displays this implied dependance of energy on the radius of the object, taking reference values of ρ_{neo} = 3,500 kg/m^3 and V_{neo} = 12,000 m/s from Table 4.7.

From the literature review (see Chapter 2), the range of asteroid sizes considered for NEOimpactor simulation have been constrained to the radius values of 25 to 250 m (50 to 500 m in diameter). This range falls outside the current Spaceguard survey

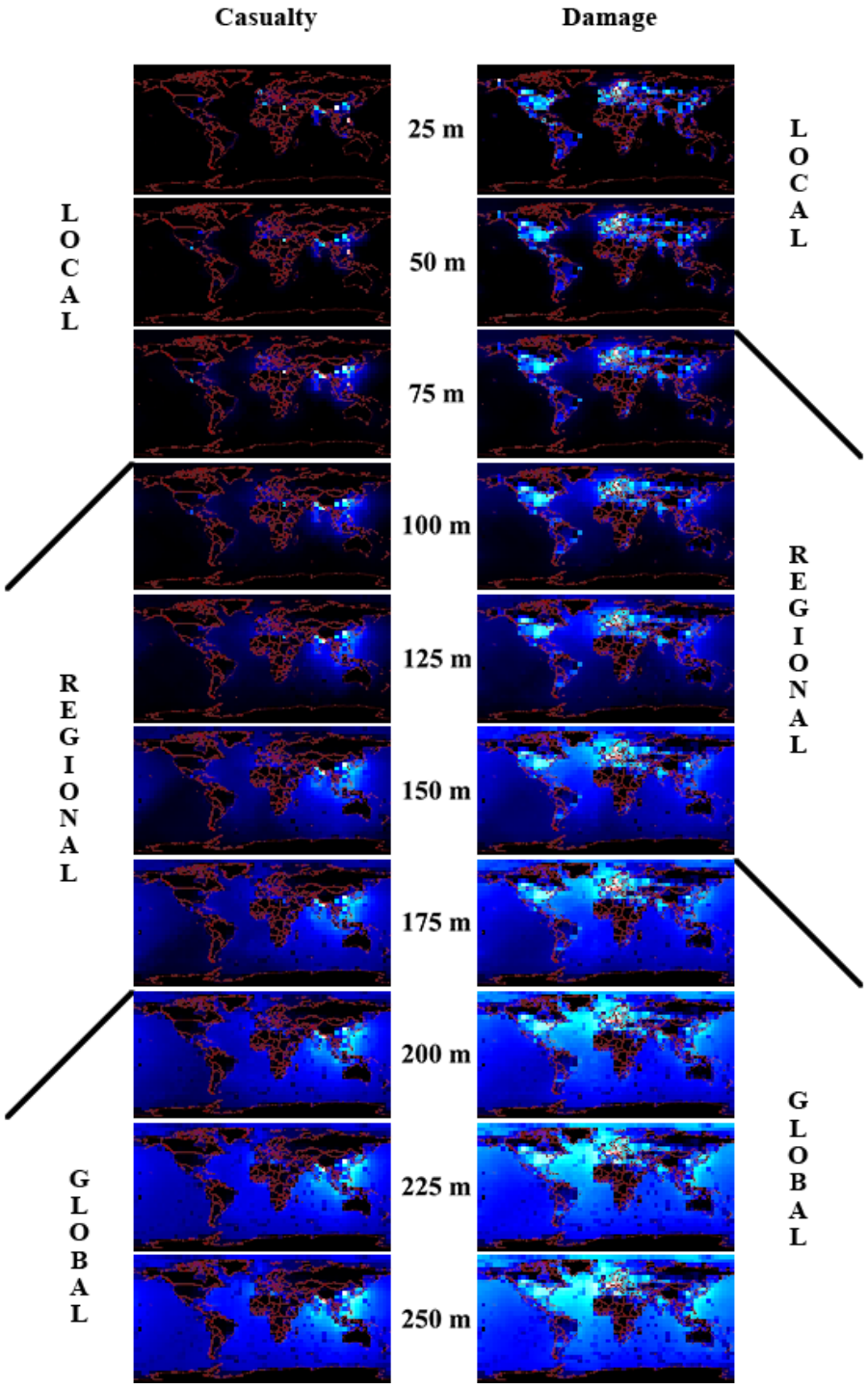

Figure 5.3: Casualty and damage consequence maps from the Global Grid SA for the complete radius range modelled. The severity of each cell is denoted by its colour, using the ⟨⟨ black – blue – cyan – white ⟩⟩ shading, where black is least significant and white most significant. Each map is normalised relative to its own peak cell value. The local, regional and global designations given on each side are further discussed in Section 6.1.

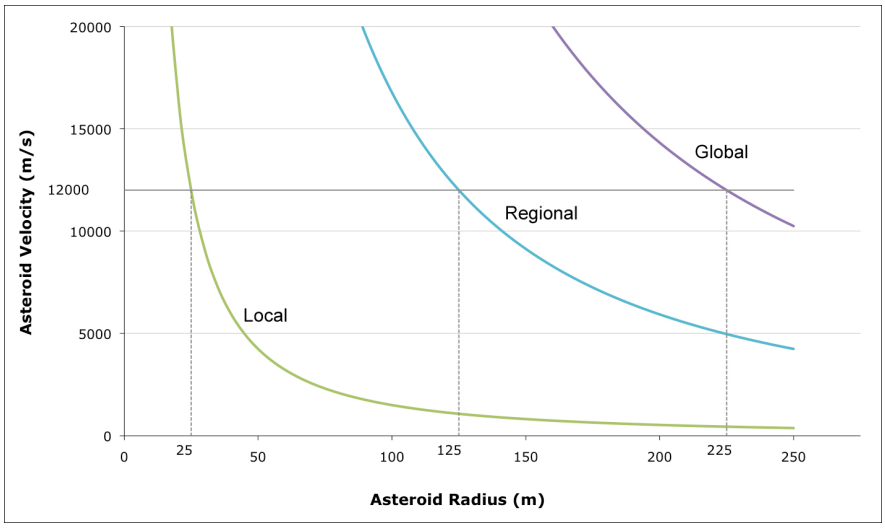

Figure 5.4: The relationship between object radius R_{neo} and impact speed for asteroids with Local (1.649x10^{16} J), Regional (2.062x10^{18} J) and Global (1.202x10^{19} J) scale event impact energy (with density set to 3,500 kg/m^3). The default speed of 12,000 m/s indicates the radii of objects used in the analysis.

and covers the lower size limit where objects may or may not reach the ground intact. This debate over the nature of atmospheric disruption and the ability for small bodies to penetrate the atmosphere intact remains unresolved. No existing atmosphere models yet have the ability to accurately model this important phase in the impact process. The atmospheric flight model contained within NEOimpactor is not sophisticated enough to accurately predict the impact characteristics from the given entry characteristics. As a result, the following results focus on the impact characteristics of the asteroid, i.e. the radius and kinetic energy of the asteroid at impact.

A Global Grid simulation was run over the full size range in 25 m increments of radius. Figure 5.3 presents the results of these ten simulations. From a visual study of these images, three severity categories are identified (local, regional and global) and marked alongside the result maps. These categories form a descriptive catastrophe scale, and from each category a single representative radius value is selected. This reduces the extent of the analysis from ten result sets to three, which is more practical. 'Local' events are simulated by a 25 m radius body which is approximately comparable to the tunguska object. 'Regional' events will be modelled by a 125 m radius body, while 'global' scale events are assumed to be produced by a 225 m radius body.

In this process, we are adopting object radius as a convenient proxy for impact energy, which is a common practice. However, it is important to emphasise that it is actually the impact energy that is the principal driver in determining the impact consequences (see Chapter 3). The impact energy associated with the local scale event

(a 25 m radius sphere with a speed of 12,000 m/s and density of 3,500 kg/m^3) is in the order of 1.65x10^{16} J. It is easily seen from Equation 5.1 that this energy can be achieved by objects of various sizes and speeds. Figure 5.4 shows the line of constant energy for the local scale impact event in radius-speed space. Similar curves for the regional and global scale events are also plotted. This is useful in showing the combination of object size and speed which can give rise to the impact consequences discussed in the impact simulations that follow. However, for ease of understanding, we will continue to discuss the results in terms of the default values of object radius.

GLOBAL GRID CASUALTY DATA

	Local	**Regional**	**Global**
Peak Impact			
Type	Land	Land	Land
Country	China	India (Bangladesh, Nepal)	China
Latitude	30.9° N	25.3° N	36.6° N
Longitude	104.1° E	87.2° E	115.3° E
Casualty Estimate	1,688,450	16,981,700	34,741,700
Most Affected Country			
Averaged over Grid	China	China	China
Casualties per impact	4,042	139,567	814,085
No. of Countries Suffering Casualties			
$>$ 1,000 (%)	2 (0.8)	82 (32.8)	142 (56.8)
$>$ 10,000 (%)	0 (0.0)	19 (7.6)	71 (28.4)
$>$ 100,000 (%)	0 (0.0)	2 (0.8)	14 (5.6)
No. of Impacts Generating Casualties			
$>$ 100,000 (%)	69 (3.91)	1,577 (77.0)	1,665 (81.3)
$>$ 500,000 (%)	11 (0.54)	1,034 (50.5)	1,571 (76.7)
$>$ 1,000,000 (%)	7 (0.34)	648 (31.6)	1,521 (74.3)
Averaged Casualties Over Grid			
Ocean Impacts	3,518	849,732	616,7927
Land Impacts	13,725	207,760	438,703
Grid Mean	17,243	1,057,492	6,606,630
Grid Median	0	506,891	7,321,055

Table 5.1: Analysis of the casualty data drawn from the three Global Grid simulations depicted in Figure 5.5

5.1.2 Global Grid Casualty Results

Figure 5.5 displays the casualty result maps for the three object sizes. The shading for each cell represents the number of casualties generated by the impact in the centre of that cell. Each figure includes a key denoting the casualty values represented by the

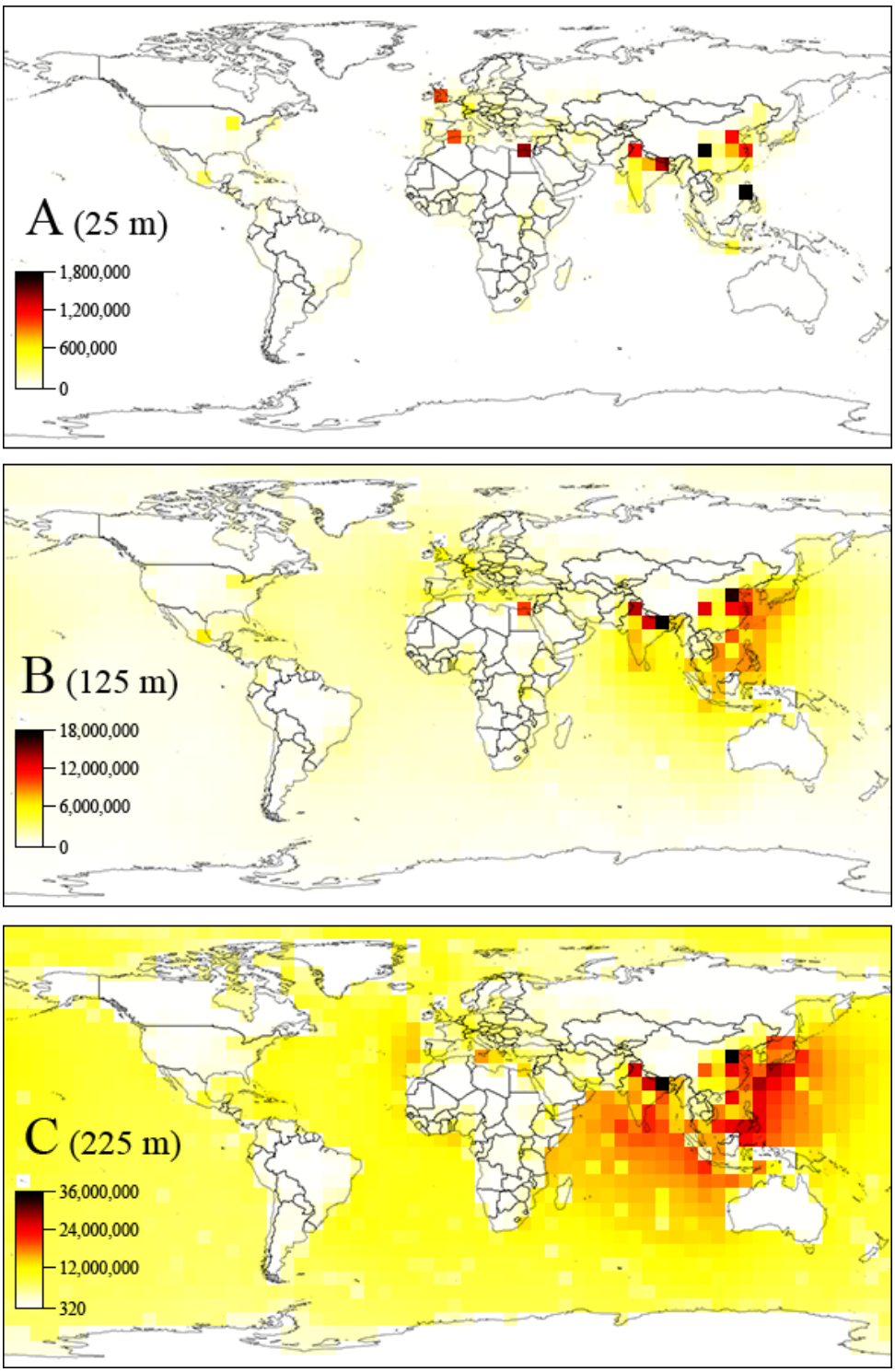

Figure 5.5: Presentation of the casualty maps from the three representative scale Global Grid simulations. The results are shaded according to the ⟨⟨ `white` – `yellow` – `red` – `black` ⟩⟩ shading, with peak impact cells coloured black. The length specifier in parenthesise denotes the impacting object's radius. The three representatives of the scale are marked: **A** - Local; **B** - Regional; **C** - Global.

⟨⟨ white – yellow – red – black ⟩⟩ colour range. For the local data, two peak cell are identified, one in central China and the other in the Philippines. A few other cells are highlighted across India, North Africa and Europe. Most of the ocean cells appear white, indicating the low potential these impacts have for generating casualties. Comparatively the regional data image presents a concentration of highlighted land cells in India and Southeast Asia, as well as a significant increase in the danger from ocean impacts. The global result map clearly demonstrates the significance of ocean impacts to the casualty generations, with all ocean impacts generating significant casualty figures.

Data extracted from the simulation, recording the impact consequences for each cell, is summarised in Table 5.1. The data records the individual impact consequences for the 250 countries in the NEOimpactor database. We see the peak value for each simulation is either in China or India. However, in all three cases summing the casualty figures over the entire grid reveals that the most affected country per impact is China. The three country casualty threshold rows indicate the multi-national nature of the event. While only 0.8% of countries will be affected by the local event, the global event has the potential to generate over one hundred thousand casualties in 14 countries. Whereas, the three impact casualty threshold rows give an indication of the likelihood of some level of global injury. For example, 50% the regional event's impacts generate over 500,000 casualties. Finally the Table provides some grid-average values to compare each size event. The ocean and land impacts show a transition from land-dominance to ocean-dominance over the size range. The mean values show the combined average casualty figure per-impact, while the median value is that most frequently occurring and therefore the most likely expected figure.

5.1.3 Global Grid Infrastructure Damage Results

Presented in Figure 5.6 are the equivalent damage distribution maps generated during the simulation. Three maps are presented representing the three catastrophe scales. The colour shading scheme uses the white to red scale chosen for infrastructure damage data with individual scales provided for each image. In comparison to the casualty data maps, these results predominantly highlight regions in Europe and North America as being most at risk. This is expected due to the larger regions of high infrastructure density indicated by the light pollution map. The local event map indicates that land impacts are most significant, with impacts into anywhere except Canada, Africa, Russia and Australia being likely to generate infrastructure damage. A similar story is seen as the asteroid size increases, with the increasing dominance of ocean impacts. However, the two peak land impact regions remain dominant, with the Eastern seaboard of the US increasing its risk.

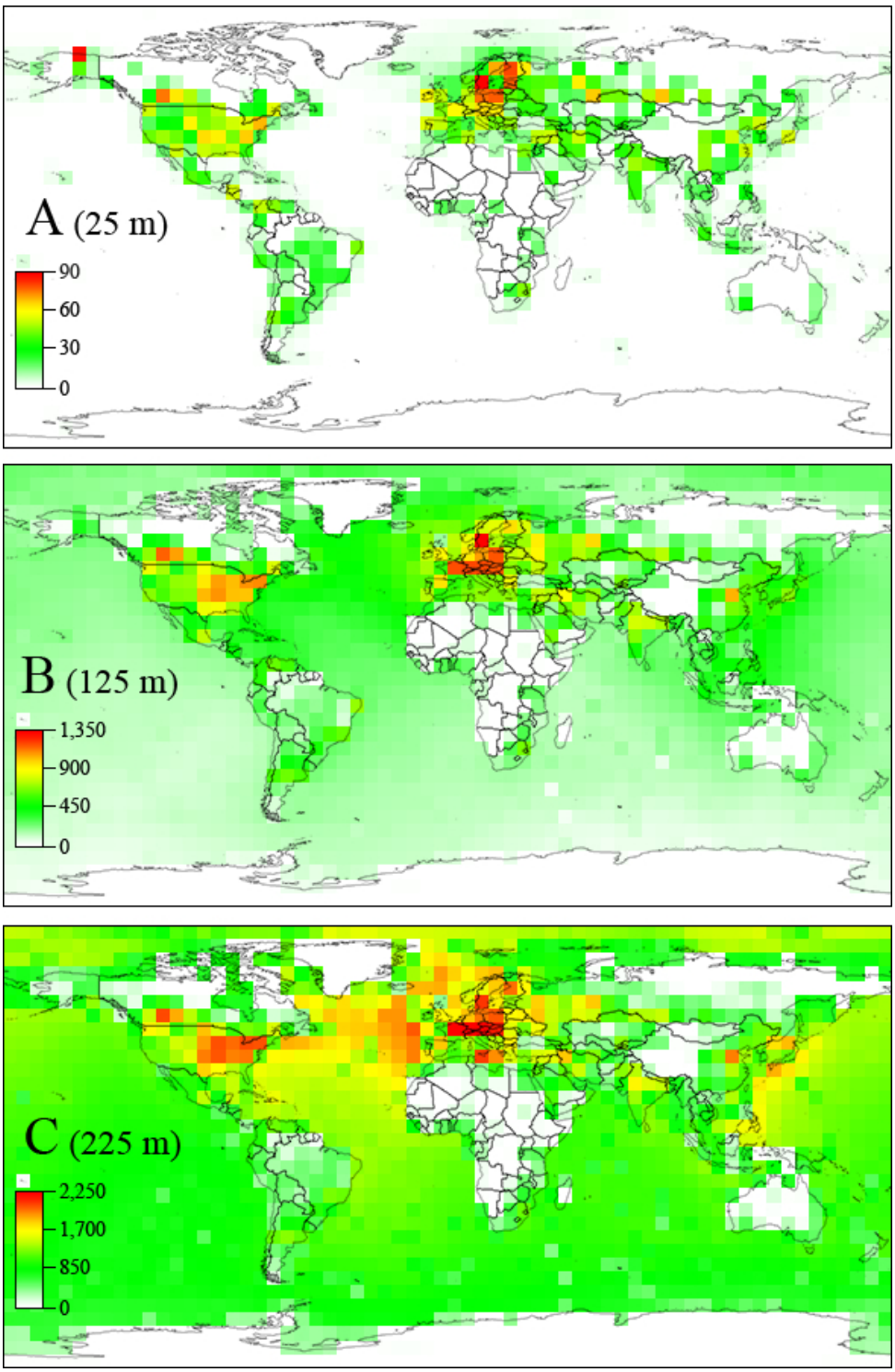

Figure 5.6: Presentation of the NEOimpactor Global Grid simulations damage distribution maps. The colour shading uses the ⟨⟨ `white` – `green` – `yellow` – `red` ⟩⟩ range with peak impacy cells coloured red. The scale values are given in NIUs. The length specifier in parenthesise denotes the impacting object's radius. The three representatives of the scale are marked: **A** - Local; **B** - Regional; **C** - Global.

GLOBAL GRID DAMAGE DATA

	Local	Regional	Global
Peak Impact			
Value (NIU)	92.5	1,325	2,556
Type	Land	Land	Land
Country	Sweden	Sweden	Germany, Austria, Czech Rep.
Latitude	59.1° N	59.1° N	47.8° N
Longitude	14.1° E	14.1° E	14.1° E
Most Affected Country			
Grid Average	US	US	US
Average Damage (NIU)	4	22	79.5
No. of Countries Suffering Damage			
$>$ 0.5 NIU (%)	2 (0.8)	49 (19.6)	116 (46.4)
$>$ 5 NIU (%)	0 (0.0)	10 (4.0)	36 (14.4)
$>$ 50 NIU (%)	0 (0.0)	0 (0.0)	1 (0.4)
No. of Impacts Generating Damage			
$>$ 5 NIU (%)	301 (14.7)	1,711 (83.5)	1,753 (85.6)
$>$ 50 NIU (%)	50 (2.4)	1,583 (77.3)	1,694 (82.7)
$>$ 500 NIU (%)	0 (0)	160 (7.8)	1,516 (74.0)
Averaged Damage Over Grid			
Ocean Impacts (NIU)	0.5	125	692
Land Impacts (NIU)	4	65.5	138
Grid Mean (NIU)	4.5	190	830
Grid Median (NIU)	0	138.5	878

Table 5.2: Analysis of data from the three damage simulations depicted in Figure 5.6. NIU stands for the NEOimpactor Infrastructure Unit (see Section 4.1.4).

Table 5.2 provides some analysis of the recorded simulation data. Again the peak value for all three events is located on land. However, this demonstrates the ability for land impacts to affect more than one country, with the global peak impact affecting Germany, Austria and the Czech Republic. Overall, however, the United States suffer the greatest infrastructure loss. This is due to their greater level of infrastructure already at risk along the Eastern seaboard. The comparison of all ocean and land averaged impacts shows the same transition from land to ocean-dominance over the size range. The median damage values correlate more closely with the mean values than was seen in the casualty data.

5.1.4 Global Grid Data Using Choropleth Mapping Techniques

The technique of 'choropleth' mapping enables the display of complex range of data using only a few colour shades to simplify the process of interpretation. The data presented in Figures 5.5 and 5.6 uses 768 colour shades to contrast between individual

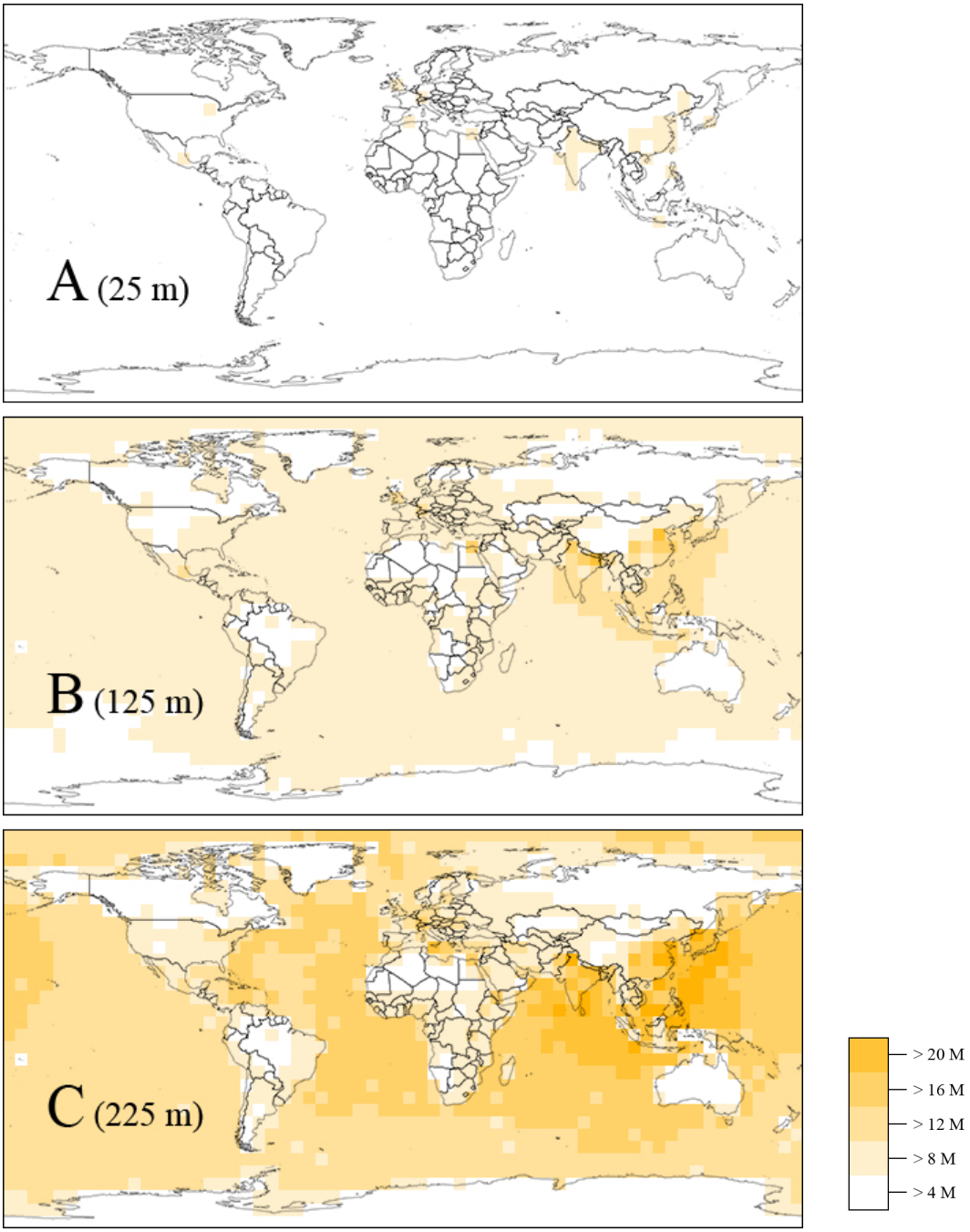

Figure 5.7: Choropleth representation of the casualty data maps presented in Figure 5.5, with the shading set to a pre determined maximum casualty estimate of 35 million (peak impact value of the global data). Each map is shaded to the same scale as shown on the right. **A** - Local, **B** - Regional, **C** - Global

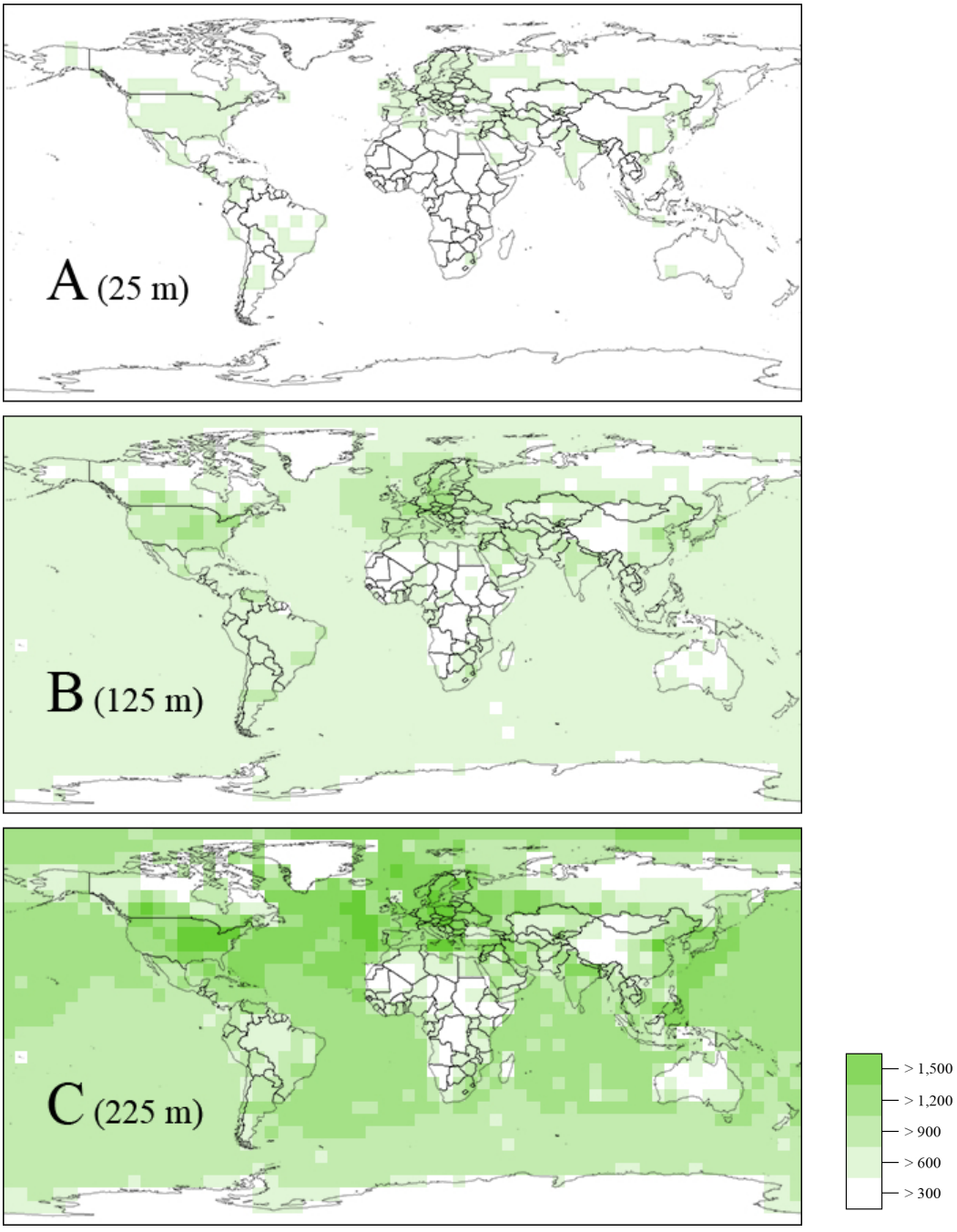

Figure 5.8: Choropleth representation of the damage data maps presented in Figure 5.6, with the shading set to fixed maximum estimate of 2,500 NIU (each map is shaded according to the same scale given on the right). **A** - Local, **B** - Regional, **C** - Global

cells. By reducing the number of shades to between five and eight (found to be the optimum range [Brewer et al., 1997]), the data is presented as regions of equal severity.

Figures 5.7 and 5.8 present casualty and damage choropleth maps respectively for the three radius simulations. One colour range is used (yellow for casualty and green for damage) with each of the five shades covering a range of consequence values. While no new data is portrayed in the map, the clarity is improved. All three maps are shaded using the same scale so that the colour regions in each map are comparable.

The result is a clearer representation of the size of region within which a particular level of devastation would be expected for various impacting bodies. The severity of an impact around Southeast Asia and the North Atlantic, in terms of casualty and damage potential respectively, is more clearly revealed in the choropleth versions.

5.1.5 Histogram Plots and Probability Density Analysis

The simulation output data detailing the impact consequence value for each of the 2048 Global Grid impact runs can be analysed further as a histogram. Due to the large range of possible casualty figures (from zero to nearly 40 million) a logarithmic scale of casualty bins is required to plot the data clearly. Figure 5.9 plots the histograms of the three severity scale event simulations. The cumulative percentage is also plotted as three curves on the second vertical axis. These plots demonstrate the increasing casualty expectation as impact energy is increased. For each plot a large number of 'zero' casualty impacts are recorded. For the Local events, over half the impacts generate zero casualties (1038 grid cells), whereas, for the Regional and Global events, this number is reduced to under 200. In fact, studying the full range of grid simulations, the number of zero-casualty impacts reaches 197 by the 150 m object radius simulation and remains constant. Further investigation of these data points reveals that they are all land impact cells, suggesting that they are so remote from human populations that no casualties are possible at any scale studied here. The most frequent response, the modal value, of the Regional and Global events are 2 million and 20 million respectively.

The same data has been plotted as histogram probability density functions, shown in Figure 5.10. This data format enables the user to predict the probability that a specified object will generated a particular casualty estimate. So for Local events there is a 50% chance the impact will generate no casualties. Furthermore, taking the inverse of the cumulative frequency percentage curve generates Figure 5.11. This plot allows the user to assess the probability that an impacting asteroid will generate consequences up to a particular threshold value. For example, the probability of a 25 m radius asteroid generating up to 100,000 casualties is approximately 0.04, whereas the probability for a 125 m radius asteroid generating this level is 0.77. While these

plots have been produced for the complete Global Grid dataset and concern only the casualty results, they can be produced for damage data as well as for an individual country in the database.

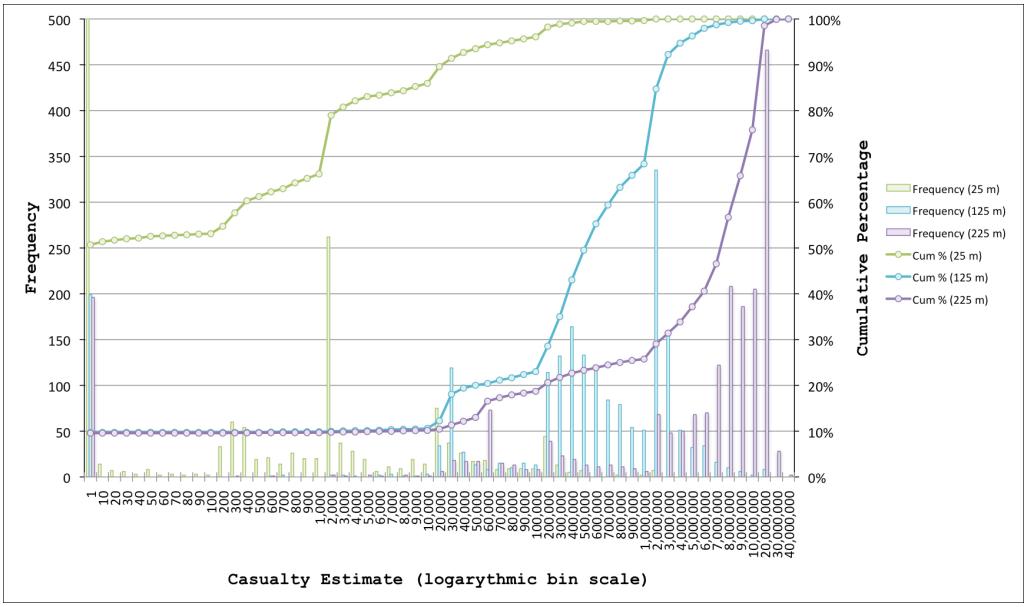

Figure 5.9: Histogram plots of the casualty data for the three Global Grid simulations. The frequency figures are related to the number of individual impact events which generated consequences in a particular casualty range. The range is specified by a logarithmic scale up to a maximum of 40 million casualties. The cumulative percentage distribution lines are plotted on the second axis for the three histogram plots. Colour shading denotes the three simulation results as: green - **Local** [25 m radius]; blue - **Regional** [125 m radius]; purple - **Global** [225 m radius].

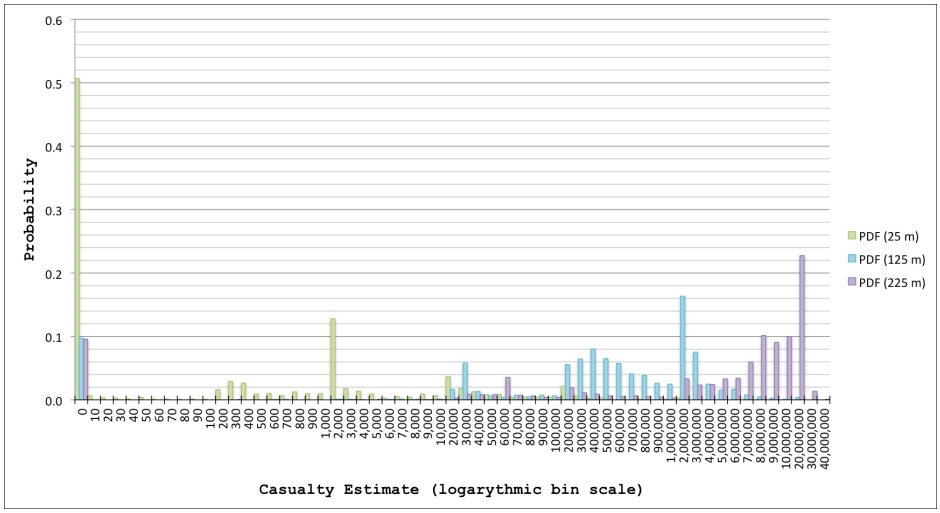

Figure 5.10: A histogram plot of the three event scale probability density functions for the Global Grid casualty data. Colour shading denotes the three scale simulation results as: green - **Local** [25 m radius]; blue - **Regional** [125 m radius]; purple - **Global** [225 m radius].

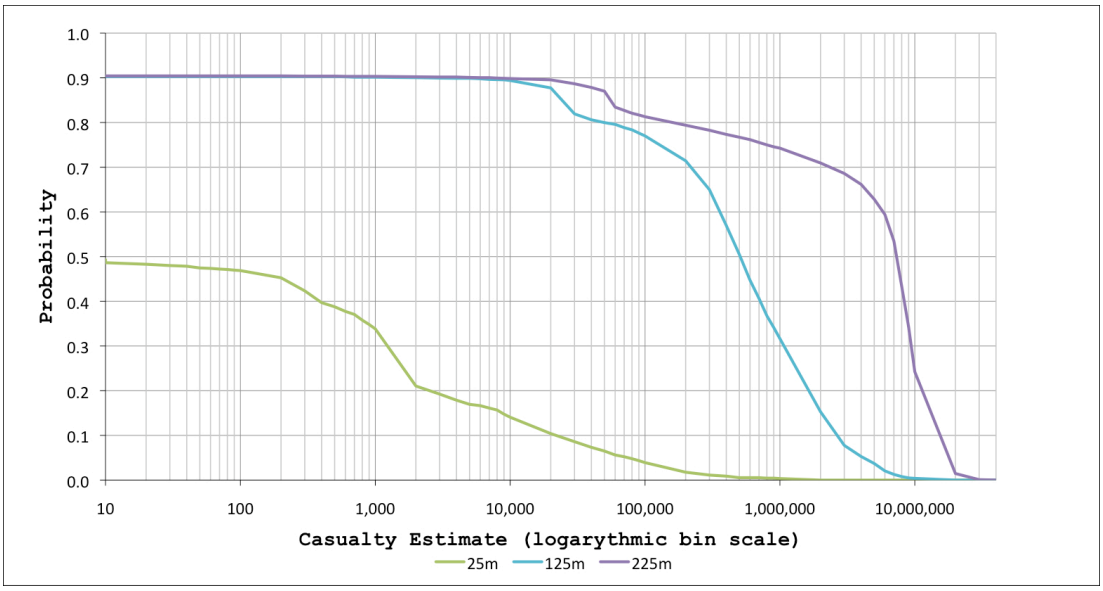

Figure 5.11: Inverse probability functions from the cumulative frequency data in Figure 5.9. Colour shading denotes the three scale simulation results as: green - **Local** [25 m radius]; blue - **Regional** [125 m radius]; purple - **Global** [225 m radius].

5.1.6 Country-By-Country Summated Data Presentation

NEOimpactor records the consequence attributed to each country in the database. Thus for every simulation, the severity of the consequences for every country can be determined. NEOimpactor automatically develops an output map using this data, shading each country depending on its cumulative consequence estimate. While each of the 250 modelled countries could be shaded separately (using one of the one or three colour ranges), a five-colour choropleth map format is adopted. This groups countries based on their expected consequence severity levels, allowing a clearer interpretation of the image. A representative of this output map format is given in Figure 5.12 using data from the 125 m radius object simulation. The advantage of this format is that, in one single image, the data for every country is presented (see Figure 7.1).

Summated Country Consequence Data in Tabular Form

The country-by-country consequence data can be exported in tabular form direct from the NEOimpactor results. The limitation with this format is that NEOimpactor records data for 250 countries and, as such, the complete table would be excessively long and cumbersome. The tabulated data in the following rankings list the top ten countries ranked in descending order. These top-ten lists are provided based on the casualty and damage data summated for each country. This raw consequence data can then be referenced against the various physical and socio-economic factors of each country to provide further insight into the risk and vulnerability of the global community.

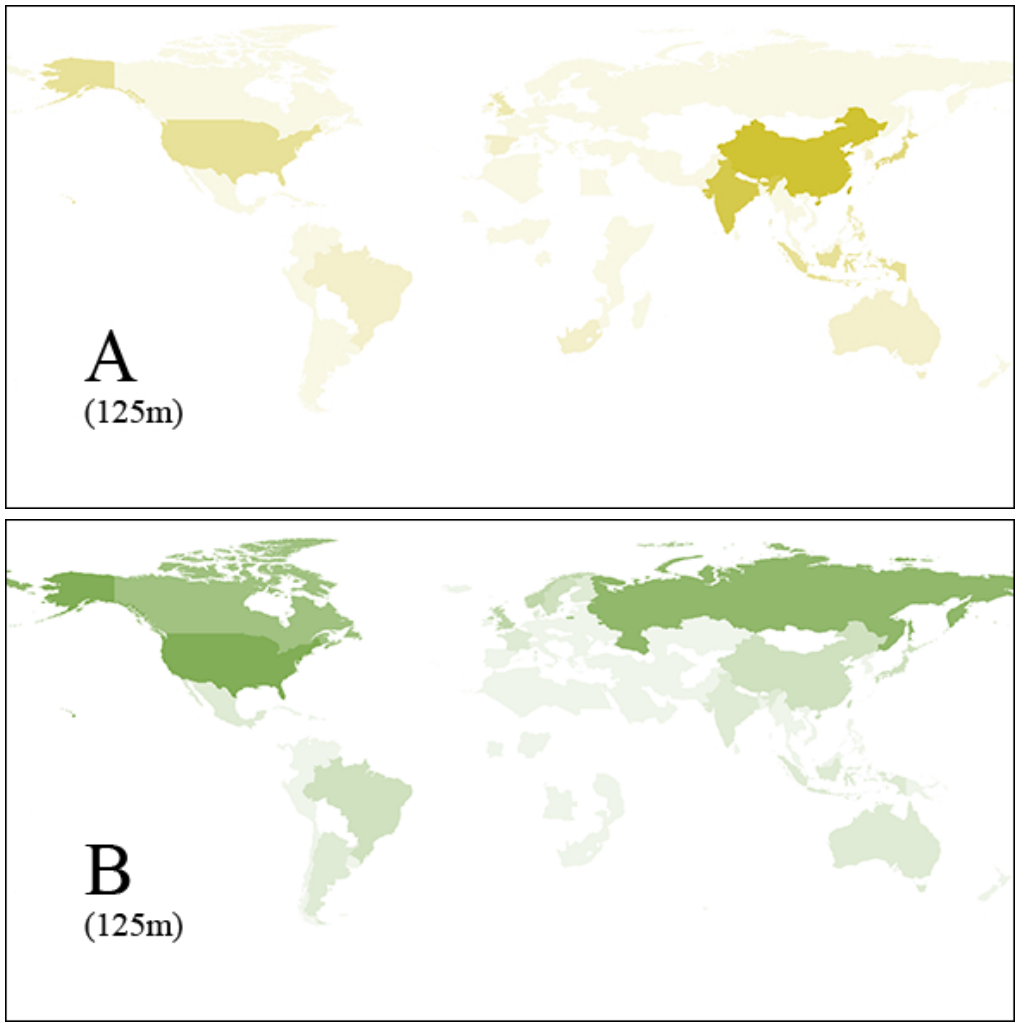

Figure 5.12: The cumulative country consequence data for the Regional event (125 m radius object) simulation as a choropleth map. This result map format is useful for a non-scientific audience and can be imported in to Google Earth as demonstrated in Figure 7.1. **A** represents the casualty dataset, with countries in Southeast Asia highlights, while **B** presents the damage data, with the US highlighted as the most affected country. These results graphically display the data given in the middle column of Table 5.3.

Global Ranking Based on Overall Casualty and Damage Sustained In Table 5.3 the cumulative casualty and damage data for the three scale simulations are presented. These results show those countries that face the greatest overall risk on a global scale. These countries are therefore those most likely to suffer loss in the event of an asteroid impact event. The high correlation across the rankings is an indication of the stability of this ranking system. China faces the greatest risk to its population, while the USA's infrastructure is most at risk.

COUNTRY RANKING BY CASUALTY TOTAL

	Local Event	(%)	Regional Event	(%)	Global Event	(%)
1	**China**	(23.4)	**China**	(13.2)	**China**	(12.3)
2	**India**	(39.6)	**India**	(23.3)	**Indonesia**	(22.1)
3	**Philippines**	(45.4)	Japan	(30.8)	**India**	(31.1)
4	**Indonesia**	(49.3)	**Indonesia**	(37.2)	Japan	(39.4)
5	Egypt	(53.2)	**United States**	(42.5)	**United States**	(44.0)
6	**United States**	(56.9)	**United Kingdom**	(47.4)	**Philippines**	(48.6)
7	American Samoa	(60.1)	**Philippines**	(51.2)	**Brazil**	(52.1)
8	**United Kingdom**	(63.1)	**Brazil**	(54.5)	South Korea	(54.8)
9	Russia	(65.3)	South Korea	(57.0)	Italy	(57.2)
10	**Brazil**	(67.2)	South Africa	(59.0)	**United Kingdom**	(59.4)

COUNTRY RANKING BY DAMAGE TOTAL

	Local Event	(%)	Regional Event	(%)	Global Event	(%)
1	**United States**	(17.1)	**United States**	(11.7)	**United States**	(9.6)
2	**Russia**	(29.1)	**Russia**	(20.7)	**Canada**	(15.5)
3	**China**	(35.6)	**Canada**	(28.8)	**Russia**	(21.0)
4	**Canada**	(41.7)	**Norway**	(33.6)	Japan	(25.8)
5	**Brazil**	(45.8)	United Kingdom	(38.0)	**China**	(30.7)
6	India	(48.8)	**China**	(42.2)	**Norway**	(34.6)
7	**Norway**	(51.8)	Japan	(45.6)	**Brazil**	(38.0)
8	Mexico	(54.1)	Sweden	(48.8)	Indonesia	(41.5)
9	Kazakhstan	(56.2)	**Brazil**	(52.0)	United Kingdom	(44.8)
10	Sweden	(58.4)	Australia	(54.7)	Australia	(47.8)

Table 5.3: Ranking based on the summated casualty and damage consequence values for each country. The summated consequence value is calculated (but not shown) as a percentage of the total casualty or damage figure sustained globally over the Global Grid simulations. The figures in brackets denote the cumulative percentage affected. The countries marked in bold appear in all three ranking lists.

ISLAND NATION RANKING USING REGIONAL DATA

	by Casualty Figure	by Damage Potential
1	**Japan**	**UK**
2	**Indonesia**	**Japan**
3	**UK**	**Australia**
4	**Philippines**	**Indonesia**
5	**Australia**	**New Zealand**
6	**American Samoa**	**Ireland**
7	**Malaysia**	**Philippines**
8	Sri Lanka	Iceland
9	**New Zealand**	**American Samoa**
10	**Ireland**	**Malaysia**

Table 5.4: Extraction of the ranking for the most affected island nations, using the Regional Event (125 m radius object) simulation consequence data.

COUNTRY RANKING BY % POPULATION LOSS

	Local Event	(%)	Regional Event	(%)	Global Event	(%)
1	Svalbard	(.006)	St. Pierre	(.62)	**Faroe Islands**	(1.33)
2	Samoa	(.006)	**Faroe Islands**	(.42)	Cook Islands	(1.27)
3	Iceland	(.003)	Iceland	(.39)	St. Pierre	(1.26)
4	**Faroe Islands**	(.002)	Wallis & Futuna	(.30)	Wallis & Futuna	(1.23)
5	Greenland	(.002)	Cook Islands	(.30)	Tonga	(1.21)
6	Georgia	(.002)	Tonga	(.29)	Kiribati	(1.18)
7	Barbados	(.002)	Svalbard	(.28)	Samoa	(1.17)
8	The Bahamas	(.002)	Falkland Islands	(.27)	French Polynesia	(1.14)
9	American Samoa	(.002)	Isle of Man	(.27)	Micronesia	(1.13)
10	Estonia	(.002)	Guam	(.23)	Isle of Man	(1.07)

COUNTRY RANKING BY % INFRASTRUCTURE LOSS

	Local Event	(%)	Regional Event	(%)	Global Event	(%)
1	**Samoa**	(.009)	St. Pierre	(.63)	**Faroe Islands**	(1.34)
2	Estonia	(.003)	**Faroe Islands**	(.42)	St. Pierre	(1.28)
3	Albania	(.003)	French S&A Lands	(.34)	French Polynesia	(1.18)
4	Honduras	(.003)	Vanuatu	(.30)	**Samoa**	(1.16)
5	**Faroe Islands**	(.002)	Falkland Islands	(.26)	Vanuatu	(1.12)
6	C. African Rep.	(.002)	French Polynesia	(.25)	French S&A Lands	(1.11)
7	Iceland	(.002)	Guam	(.24)	Palau	(1.01)
8	Timor L'este	(.002)	**Samoa**	(.24)	Guam	(1.01)
9	Barbados	(.002)	Barbados	(.21)	Cape Verde	(1.00)
10	Georgia	(.002)	Antigua & Barbuda	(.21)	Isle of Man	(0.99)

Table 5.5: Top ranked countries based on the percentage of their total population and infrastructure lost. Fgures in parenthesise are the estimated percentage lost suffered by each country. This value has been averaged over each impact in the grid, to give the average impact value. The countries highlighted in bold type are those appearing in all three lists. 'St. Pierre' is used in short for St. Pierre & Miquelon

Specific Risk Faced By Island Nations Table 5.3 highlights the island nations of the Philippines, Indonesia and the United Kingdom in all three rankings, together with Japan. Their presence in the global lists, alongside far larger and more populated countries, suggests that island nations face an acute risk from the NEO threat. Table 5.4 extracts only the island nations from the complete dataset for the regional (125 m radius object) simulation and presents them as a separate ranking.

Ranking of Casualty and Damage Percentage Loss Table 5.5 ranks the countries based on the percentage of the total population and infrastructure lost. The average consequence figure for each country for any grid impact is calculated and then taken as a percentage of the each country's population. When ranked by percentage lost, this list reveals those most vulnerable to the impact threat. These are the countries most likely to lose a significant proportion of their entire population. Of particular note again is the high number of island nations or archipelagos appearing in the list.

RANKING BY CASUALTY 'DENSITY'

	Local Event	Regional Event	Global Event
1	**Barbados**	**Barbados**	**Barbados**
2	**Aruba**	**Aruba**	**Aruba**
3	**Guam**	**Guam**	**Guam**
4	**Martinique**	Tonga	**Reunion**
5	**Mayotte**	**Comoros**	**Martinique**
6	Philippines	**Martinique**	**Mayotte**
7	**Comoros**	**Mayotte**	**Comoros**
8	**Reunion**	Cook Islands	Seychelles
9	Mauritius	**Reunion**	Tonga
10	St. Lucia	Guadeloupe	Puerto Rico

RANKING BY DAMAGE 'DENSITY'

	Local Event	Regional Event	Global Event
1	**Faroe Islands**	St. Pierre & Miquelon	**Faroe Islands**
2	Estonia	**Faroe Islands**	Isle of Man
3	Samoa	Isle of Man	St. Pierre & Miquelon
4	Albania	French S&A Lands	Singapore
5	Ireland	Denmark	Reunion
6	**Mauritius**	**Mauritius**	**Mauritius**
7	Norway	St. Lucia	Palau
8	Virgin Islands	Antigua & Barbuda	French S&A Lands
9	St. Lucia	Guadeloupe	Sao Tome & Principe
10	Austria	Reunion	Guadeloupe

Table 5.6: Global Grid casualty and damage consequence results divided by total land area per country. This ranking provides information relating to high vulnerability members of the global community (see Section 6.4.1).

These countries often only have a small but vulnerable population concentrated on the coast. The vulnerability of low-lying small islands to tsunami inundation rends them at greatest risk of total loss or destruction. However, due to the small size of the countries concerned the results are subject to a high degree of variation, leading to little correlation across the three object simulaitons.

Casualty and Damage 'Density' Rating Dividing the grid-averaged consequence value for each country by its land area produces a ranking scale for the 'consequence density risk'. Table 5.6 lists the top countries for both casualty and damage density. This ranking provides information on those countries that suffer the greatest loss per square kilometre of land. Naturally again, island nations are expected to appear high in the list. This density ranking is important in assessing which countries will be affected to such an extent that they would be unable to respond to the disaster

RANKING BY CASUALTY PER UNITY LENGTH OF COASTLINE

	Local Event	Regional Event	Global Event
1	Congo (DRC)	Jordan	**Benin**
2	Iraq	**Benin**	Togo
3	American Samoa	Togo	South Korea
4	**China**	Congo (DRC)	Kenya
5	**India**	**India**	**China**
6	**Syria**	South Korea	**India**
7	Georgia	**China**	Pakistan
8	Germany	Netherlands	Israel
9	**Benin**	Iraq	American Samoa
10	Egypt	**Syria**	**Syria**

RANKING BY DAMAGE PER UNITY LENGTH OF COASTLINE

	Local Event	Regional Event	Global Event
1	**Jordan**	**Jordan**	**Jordan**
2	**Iraq**	**Iraq**	**Iraq**
3	**Syria**	Lithuania	**Syria**
4	Bulgaria	**Germany**	**Germany**
5	**Poland**	**Serbia & Montenegro**	**Serbia & Montenegro**
6	**Germany**	**Syria**	**Poland**
7	**Serbia & Montenegro**	Faroe Islands	Lithuania
8	Georgia	**Poland**	Finland
9	Albania	Sweden	Faroe Islands
10	Iran	Finland	Bosnia & Herzegovina

Table 5.7: The top ten casualty and damage rankings for the three Global Grid simulation results referenced against coastline length. The combined casualty and damage estimate was divided by the country's coastline length and listed in order. The entries in bold are those countries appearing in all three lists.

themselves. These countries are therefore most vulnerable to significant destruction and will be in greatest need of external aid following an asteroid impact.

Country Ranking Taken Against Coastline Length By referencing the data against each country's coastline length, a picture of which countries face the greatest tsunami risk is developed. This data is given in Table 5.7 which highlights countries with long coastlines as being at risk. However the results are skewed in favour of those countries with a large area and relatively small coastline, for example Jordan. Despite this skewing, this ranking is similar to the original ranking in Table 5.3, indicating that coastline length is already a dominant factor in the global risk assessment. Table 5.8 presents the data for those countries with no coastline. These countries cannot be affected by ocean impacts, which represent 75 % of all impacts, and will therefore

LAND-LOCKED COUNTRY RANKING

	Casualty	Damage
1	Ethiopia	**Kazakhstan**
2	**Uzbekistan**	Belarus
3	**Kazakhstan**	**Austria**
4	**Hungary**	**Hungary**
5	Afghanistan	Turkmenistan
6	Niger	Bolivia
7	Switzerland	**Uzbekistan**
8	**Austria**	Mongolia
9	Burundi	Slovakia
10	Uganda	Zimbabwe

Table 5.8: Top ten ranking for land-locked countries based on the Regional event simulation data. These are countries with no coastline and therefore excluded from appearing in Table 5.7. Bold entries are those countries appearing in both the casualty and damage lists. These four countries are the most vulnerable land-locked countries.

experience a significantly reduced vulnerability.

Ranking Against the Ratio of Land Area to Coastline Length Finally, in addition to the ranking by coastline length, the ratio of a country's land area to length of coastline is investigated. Extracting these two data for each country in the NEOimpactor database and dividing them provides the land area:coastline length ratio for comparison. The simulated casualty and damage consequence figures for each country is then divided by this ratio. Table 5.9 presents this final ranking. The importance of this ratio for determining a country's risk will be investigated further in Chapter 6.

5.2 Linear Impact Path Investigations

The importance of being able to study a linear impact path comes from the nature of real asteroid threats to Earth. Due to the inherent uncertainties in orbit prediction, if an object is located with a finite probability of impact, the projection of this probability onto the Earth (by a procedure of orbit intersection) derives a 'line of risk'. This is a probability region in which the asteroid would fall. Only with 100% accurate orbit determination would this line resolve to a single impact point (a level of accuracy unlikely to be attained before a mitigation mission is launched). An example of such a line of risk is shown in Figure 3.15.

NEOimpactor's Linear Impact SA enables a line of risk to be modelled and impacted along. This enables a more detailed study of the relative effects from land and ocean impacts. While no known asteroid threat exists, the three lines simulated here

CASUALTY RANKING BY AREA:LENGTH RATIO

	Local Event	Regional Event	Global Event
1	**Philippines**	**Japan**	**Japan**
2	**United Kingdom**	**Philippines**	**Philippines**
3	**Indonesia**	**United Kingdom**	**Indonesia**
4	**Japan**	**Indonesia**	**United Kingdom**
5	**India**	**South Korea**	**South Korea**
6	China	Denmark	**Italy**
7	**Italy**	**Italy**	Greece
8	United States	**India**	**India**
9	**South Korea**	Puerto Rico	Denmark
10	Egypt	United States	Puerto Rico

DAMAGE RANKING BY AREA:LENGTH RATIO

	Local Event	Regional Event	Global Event
1	**Norway**	**Norway**	**Japan**
2	United States	**United Kingdom**	**Norway**
3	**Canada**	**Japan**	**United Kingdom**
4	Russia	Denmark	**Philippines**
5	**Japan**	**Canada**	**Indonesia**
6	United Kingdom	**Philippines**	Denmark
7	**Indonesia**	United States	Greece
8	**Philippines**	Faroe Islands	**Canada**
9	Estonia	French S&A Lands	Italy
10	Ireland	**Indonesia**	New Zealand

Table 5.9: Ranking table giving the casualty and damage figures referenced against the calculated land area:coastline length ratio for each country.

are chosen as illustrative examples to demonstrate the software's capabilities. The SA defines the line of risk between two latitude/longitude locations. Any number of unique pathways could be investigated, but this study here limits the focus to three particular lines interest. The first two lines are the Tropics of Cancer, 23.5° North, and Capricorn, 23.5° South (pictured in Figure 5.13). These two geographically defined parallel lines of latitude emphasise the contrast between northern and southern hemisphere impacts. A third, more detailed, study is made of a segment of the 40° North line of latitude. This intersects Europe and the Mediterranean, and passes directly through Madrid, the capital city of Spain.

5.2.1 Impacts Along the Tropic of Cancer (23.5° North)

The Northern hemisphere is characterised by large land-masses (North America and Asia) and a non-permanent polar ice cap. Land accounts for approximately 39% of

Figure 5.13: Map of the Earth's equatorial region depicting the lines of the Tropic of Cancer and Capricorn in red.

CASUALTY ESTIMATES ALONG THE TROPIC OF CANCER

	Local Event		Regional Event		Global Event	
Path Average	72,323	(0)	2,561,061	(47)	9,498,751	(162)
Land Impacts	169,656	(1)	2,797,100	(2)	5,859,990	(2)
Ocean Impacts	17,309	(1)	2,427,648	(58)	11,555,442	(147)

DAMAGE ESTIMATES ALONG THE TROPIC OF CANCER

	Local Event		Regional Event		Global Event	
Path Average (NIU)	7.25	(0)	282.3	(42)	1,016.0	(142)
Land Impacts (NIU)	18.0	(1)	283.9	(1)	594.2	(2)
Ocean Impacts (NIU)	1.15	(1)	281.4	(52)	1,254.3	(129)

Table 5.10: Data breakdown from the Tropic of Cancer impact path simulation. The figures in parenthesise denote the average number of countries affected along the impact path. Damage values are given in NEOimpactor Infrastructure Units.

the hemisphere, with 61% ocean coverage. However, other than via the North Pole, there is no circumpolar ocean route. The majority of the industrialised countries are situated in the Northern hemisphere (focused around Europe and the coastal regions of North America), while the combined population of China and India accounts for approximately half the total global population. The third largest population is the United States. The impact path taken along the Tropic of Cancer (23.5° North) cuts a line which is 36% land and 64% ocean passing through 26 countries. Impact data for the path is plotted eastwards from the 180^{th} meridian in the Pacific Ocean.

The results shown in Figure 5.14 present the casualty and damage plots along the Tropic of Cancer. There is a large degree of variation in both consequence figures along the line and between the three object sizes plotted. Of particular importance is the 25 m radius plot (turquoise) which is characterised by a largely negligible response across the ocean, only appearing to generate casualties when impacting the land. This suggests that for small local scale events, the land impacts are expected to be of most significance, and mitigation may be possible by causing the asteroid to impact the ocean. Table 5.10 presents some results from both data sets which characterises

CASUALTY ESTIMATES ALONG THE TROPIC OF CAPRICORN

	Local Event		Regional Event		Global Event	
Path Average	15,376	(1)	977,881	(39)	7,631,218	(116)
Land Impacts	48,976	(1)	455,254	(2)	908,675	(2)
Ocean Impacts	4,669	(0)	1,144,433	(51)	9,773,567	(152)

DAMAGE ESTIMATES ALONG THE TROPIC OF CAPRICORN

	Local Event		Regional Event		Global Event	
Path Average (NIU)	2.95	(0)	144.5	(33)	810.4	(102)
Land Impacts (NIU)	11.1	(1)	171.5	(1)	361.3	(2)
Ocean Impacts (NIU)	3.5	(0)	135.9	(43)	953.5	(134)

Table 5.11: Data extracted from the Tropic of Capricorn Impact Line simulation. The figures in parenthesise denote the average number of countries affected by the line of impacts. Damage values are given in NEOimpactor Infrastructure Units.

the impact path. These results are discussed further in Section 6.2 to develop out understanding of the different characteristics of land and ocean impacts.

5.2.2 Impacts Along the Tropic of Capricorn (23.5° South)

The southern hemisphere is characterised by a larger percentage of ocean coverage, 72% compared with 28% land. The southern ocean is also circumpolar enabling tsunami to pass easily between the Pacific, Atlantic and Indian Oceans. The hemisphere contains two complete continents - Antarctica and Australia. Antarctica prevents tsunami passing over the south pole. The Tropic of Capricorn passes through only ten countries. Plotted from the antemeridian eastward, the Tropic is predominantly ocean (76%), and only 24% land.

Figure 5.15 presents a graphical view of the casualty and damage consequence estimates along the 23.5° South parallel. A full discussion of the results is provided in Chapter 6. Of particular note are the similarities in the overall pattern of the casualty and damage plots, with land impact regions typically showing lower consequence estimates. Table 5.11 provides a summary of the data.

5.2.3 40° North Impact Path (Between 30° West and 30° East)

Covering only 60°'s of longitude (Figure 5.17), this segment of the 40° North line of latitude passes from the Portuguese islands in the Atlantic through the Mediterranean Sea to Turkey. This path was arbitrarily chosen due to its interest of passing over ocean, land and sea. Figure 5.16 present a graphical representation of both consequence plots for the three test objects, together with a reference map. Of note is

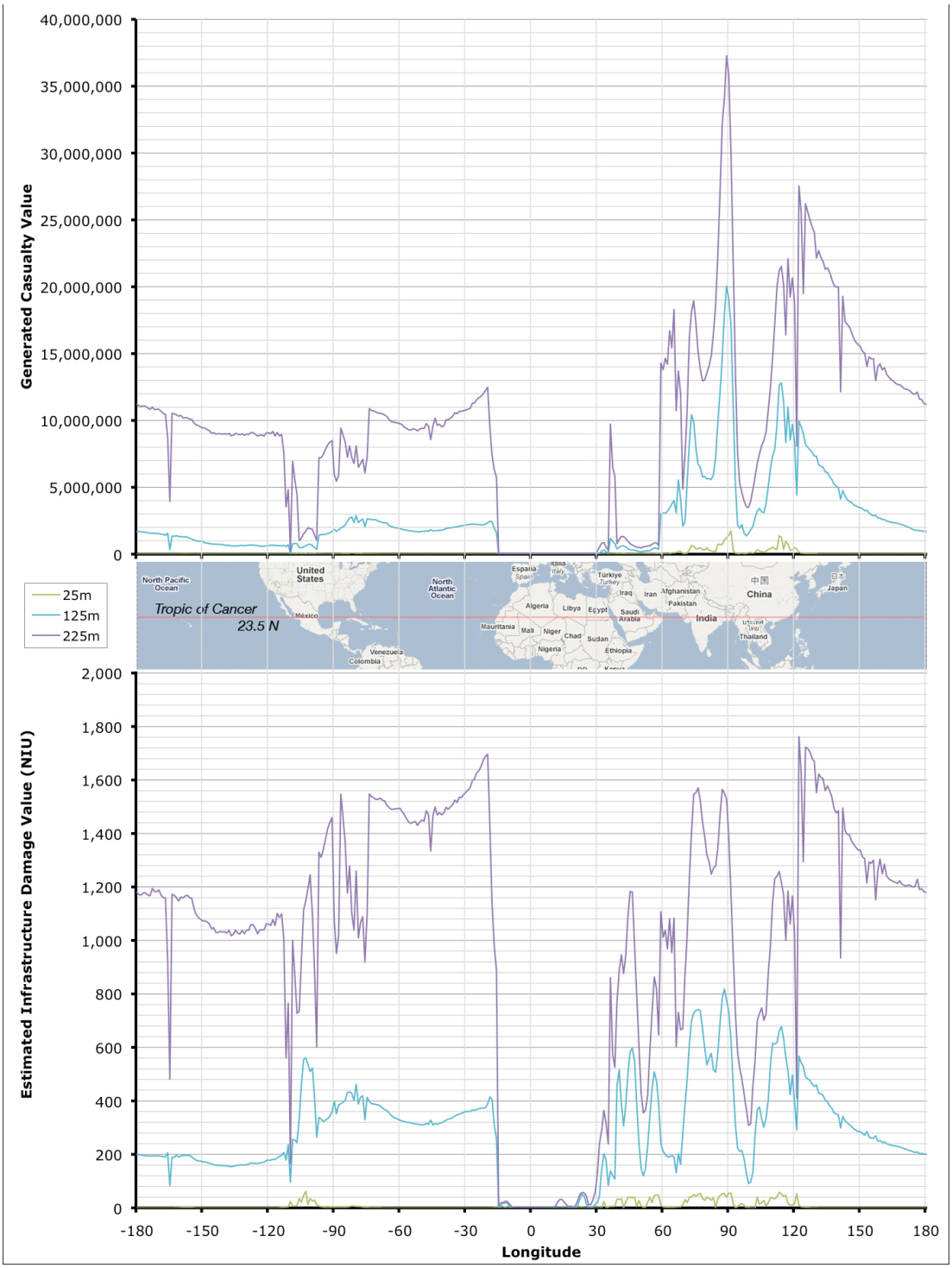

Figure 5.14: Casualty and damage estimates values along the Tropic of Cancer, 23.5° North. The inset map is aligned to distinguish between land and ocean impacts. Colour shading denotes the three scale simulation results as: green - **Local** [25 m radius]; blue - **Regional** [125 m radius]; purple - **Global** [225 m radius].

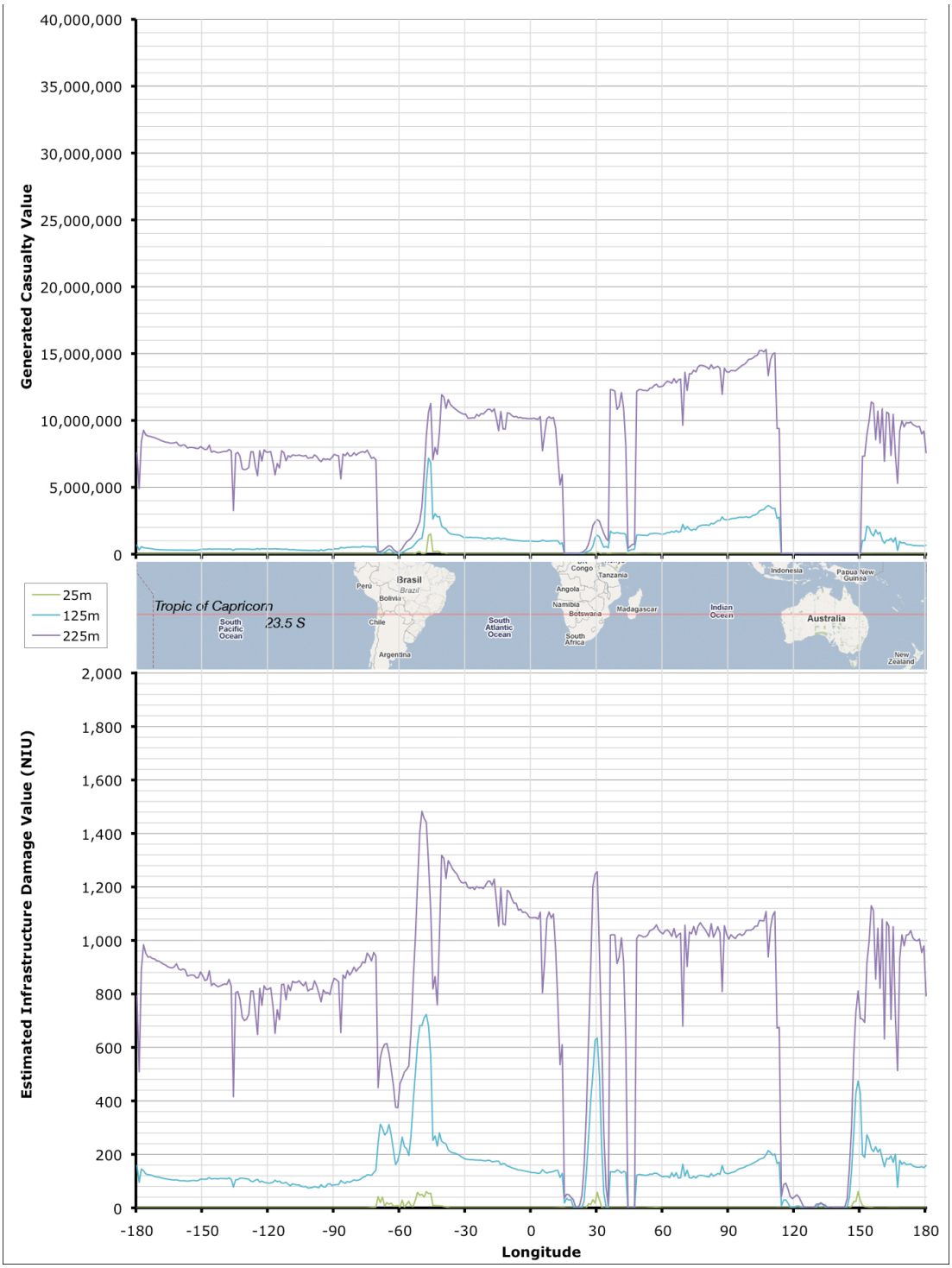

Figure 5.15: Casualty and damage estimated values along the Tropic of Capricorn, 23.5° South. The inset map shows the land and ocean path of the Tropic. Colour shading denotes the three scale simulation results as: green - **Local** [25 m radius]; blue - **Regional** [125 m radius]; purple - **Global** [225 m radius].

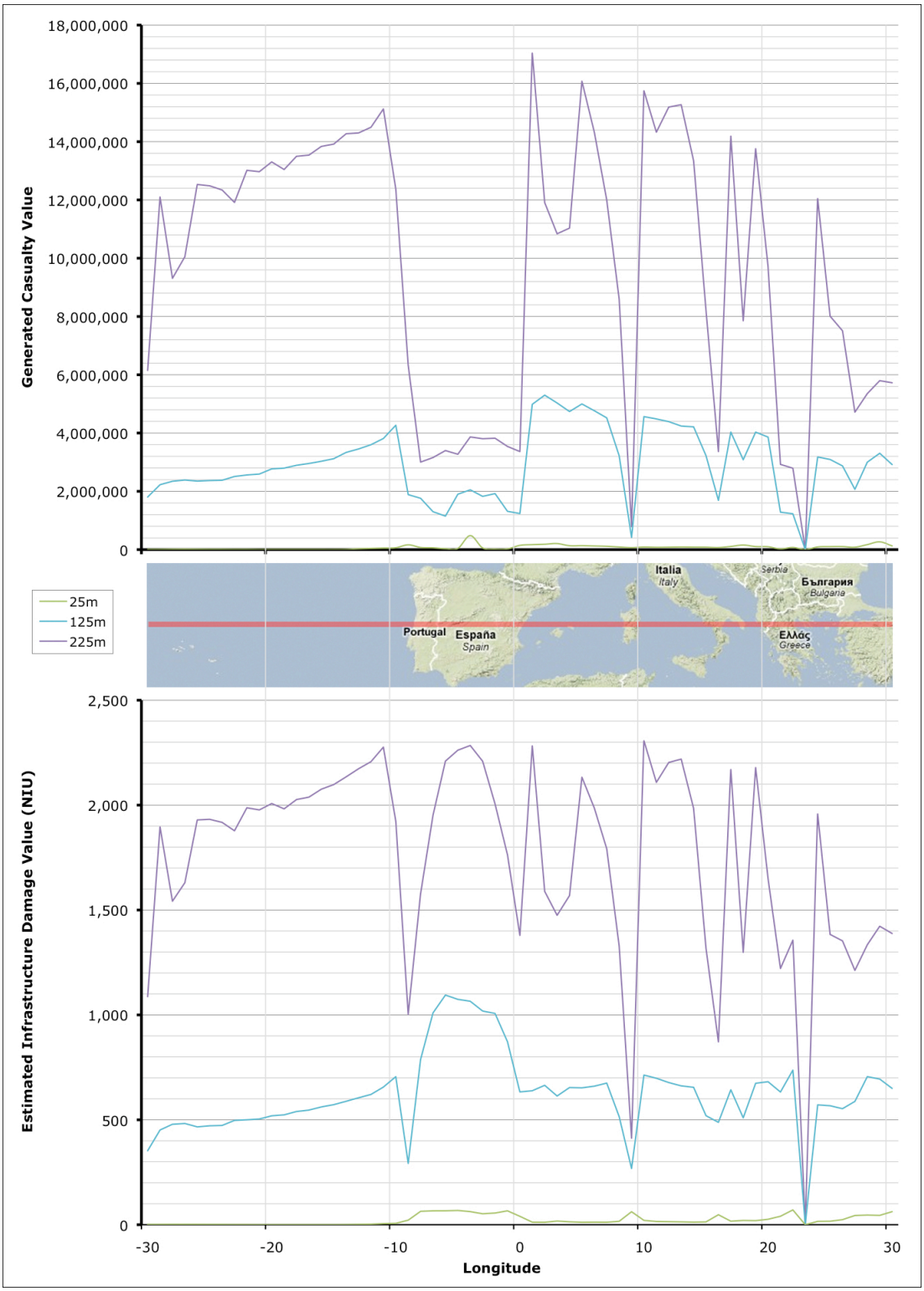

Figure 5.16: Results of the three test impacts along the segment of the 40° North line of latitude. The top graph presents the estimated casualty results while the bottom graph depicts the infrastructure damage figures. The inset map plots the path on a map of the Mediterranean.

CASUALTY ESTIMATES ALONG 40° NORTH

	Local Event		Regional Event		Global Event	
All Impact	76,067	(2)	2,928,513	(52)	9,680,870	(102)
Land Impacts	100,225	(1)	1,687,177	(2)	3,482,829	(3)
Ocean Impacts	65,955	(2)	3,448,141	(73)	12,275,399	(144)

DAMAGE ESTIMATES ALONG 40° NORTH

	Local Event		Regional Event		Global Event	
All Impact	22.0	(2)	621.9	(48)	1,752	(89)
Land Impacts	53.2	(1)	740.3	(2)	1,492	(3)
Ocean Impacts	9.0	(2)	572.3	(67)	1,861	(126)

Table 5.12: Data for a segment of the 40° North line of latitude. Figures in parenthesise are the average number of countries affected by impacts along the line.

the higher average consequences for those objects impacting the Mediterranean Sea compared to the surrounding land impacts. Furthermore, the coastal point on the line are clearly identified by sharp changes in both the casualty and damage consequence estimates. However, the peak infrastructure damage data across Spain is greater than the surrounding ocean impact estimates. Table 5.12 provides a summary of the data for this segment highlighting the difference in the potential for ocean impacts to influence significantly more countries than land impacts. However, the impact of asteroids directly into the capital city of Madrid out-weights the ocean impact consequences for both the local and regional impacts. Only for global scale events, in this small region, do ocean impacts out-weight the consequences of land impacts. This is further discussed in Section 6.2.2.

Figure 5.17: Map of the segment of the 40° North line of latitude impacted along.

Chapter 6

Discussion

The results chapter has demonstrated the capability of NEOimpactor to model the effects of both land and ocean impacts and to provide a means for assessing the potential consequences for both human population and global infrastructure. This fulfils the overall project aim described in Section 1.2.3 and is a novel addition to the field of NEO hazard studies. In addition, the project has investigated the risk faced by individual countries. Section 5.1.6 provides a number of different ranking systems for assessing the various vulnerability factors that countries face. This indicates the difficulty associated with determining an overall vulnerability scale. This chapter provides a discussion of these different risk parameters and attempts to unify them into a single cohesive vulnerability analysis. When studied on a global scale (i.e. ignoring political borders and treating the world as one), the NEO threat is understood in relation to the difference between ocean and land impact events. Section 6.2 investigates the differences between these two impact scenarios and proposes a set of rules for determining their potential impact consequences.

6.1 Determination of the Asteroid Impact Severity Scale

In Section 5.1.1, a first glance at the complete range of consequence maps, corresponding to the different object radii (Figure 5.3), provides a working guide to the classification of Local, Regional and Global scale events. This definition of the classification is subjective, and thus is corroborated in Section 6.1.2. The transition between each classification is continuous, and represented by the slanted angle of the separators. Local events are visually characterised by individually highlighted cells. The local to regional transition is placed when the ocean regions indicate an increased impact severity. In the Regional phase contrast is seen between ocean and land impacts, with the ocean impacts presenting a more significant overall threat. The Global scale designator is applied when ocean impact cells appear dominant.

SELECTION OF THE THREE REPRESENTATIVE RADII

Severity Scale	Casualty Results	Damage Results	Selected Radius
Local	25 m - 100 m	25 m - 75 m	25 m
Regional	100 m - 200 m	75 m - 175 m	125 m
Global	200+ m	175+ m	225 m

Table 6.1: Selection of the three representative object radii to model the severity scale classifications. The radii ranges shown are taken from the designators in Figure 5.3. The final column indicates the radii chosen to represent both casualty and damage ranges, termed the 'scale representative'.

6.1.1 Possible Problems with the Scale Representatives Used

The range of asteroid radii studied by NEOimpactor is limited to between 25 and 250 m. This range only accounts for a small range of the orbital asteroid population. It falls below the Spaceguard Survey study range of $>$ 500 m radius - a size at which the impact consequences become catastrophic [Stokes and Yeomans, 2003]). Objects in NEOimpactor's study range remain both largely undetected and frequently unconsidered in the literature. Very small bodies ($\ll$ 25 m) are expected to be easily attenuated by the Earth's atmosphere, and thus present little risk to the ground. In all the studies investigated in this thesis, the asteroid's other parameters, such as velocity, density and shape (spherical), have been fixed allowing radius to be used as a proxy for kinetic energy. The velocity adopted, 12,000 m/s, is at the lower range of impact speeds and, as such, the results will represent conservative estimates. The asteroid composition used throughout is a stony iron (density of 3,500 kg/m^3). Denser than the more numerous soft-stone asteroids, they are more likely to reach the Earth's surface intact (see Section 5.1.1).

6.1.2 Local-Regional-Global Scale Designators

In this project, three descriptive catastrophe classifications are chosen to simplify the analysis of results. The original scale descriptors from Figure 5.3 offer a range of object sizes associated with each scale of catastrophe, as detailed in Table 6.1. From these ranges the 25 m, 125 m and 225 m radius representative asteroids are selected, bearing in mind that radius is being used as a proxy for kinetic energy of impact. The scale classification can be summarised as:

Local: Events that affect an area typically smaller than a country.

Regional: Events that affect one country severely and possibly its neighbours.

Global: Events that have a significant effect on many countries.

However, this summary is restricted by the difference characteristics of land and ocean impacts. Typically regional scale ocean impacts will easily effect multiple countries, with global scale impacts generating world-wide consequences.

In terms of kinetic energy, the 125 m object is two orders of magnitude greater than that of the 25 m object, while being only one order below the 225 m body. This uneven impact energy distribution is seen in the peak impact consequence values recorded in the keys of Figures 5.5 and 5.6. An order of magnitude step is seen between the local and regional consequence peak values, but only a doubling between the regional and global scale. The radius distribution itself is also uneven, with a factor of five separation between the local and regional object radii, while a factor of less than two separates the regional and global representative radii.

Analysis of the Global Grid result datasets reveals the number of affected countries for each simulation averaged over the entire grid. This value, rather than the specific casualty or damage values, is useful for assessing the potential scale of an average impact and is provided in Table 6.2. Counting the number of countries affected by each grid impact and dividing by the number of grid cells produces the average number of countries affected. Taking the whole grid, an average local, regional or global scale event would be expected to affect 1, 30 and 90 countries respectively. Similarly, averaging the consequence figures over the number of grid cells, a local impact would be expected to produce in the order of ten thousand casualties, while a global impact would produce in excess of six million.

Considering only the land impacts, the average number of affected countries is just one (here the peak number of affected countries are listed to demonstrate the potential of land impacts to affect more than one country). Whereas, considering just the ocean impacts demonstrates their ability to affect a multitude of countries, up to 146 recorded. This large dependence on the differing characteristics of land and ocean impacts is discussed in detail in Section 6.2.

In summary:

> *Three classifications of severity stand up to testing, these being the Local, Regional and Global scale events. Studying the number of affected countries is an effective way of assessing the scale of a potential disaster. However, this will depend on the type of impact event, with ocean impacts easily affecting a larger number of countries per impact.*

AVERAGE NUMBER OF COUNTRIES AFFECTED

Severity Scale	Casualty	Simulation	Damage	Simulation
Local	1	(17,243)	0	(4.4 NIU)
Regional	32	(1,057,492)	28	(190.1 NIU)
Global	98	(6,606,630)	86	(830.0 NIU)
Countries Affected by Land Impact Events				**[Max.]**
Local	1		0	[4]
Regional	1		1	[9]
Global	1		1	[11]
Countries Affected by Ocean Impact Events				
Local	1		0	
Regional	47		41	
Global	146		129	

Table 6.2: The values given in this table represent the average number of countries affected (i.e. that suffer casualties or damage) by an impact in the Global Grid. The values in parentheses are the grid averaged casualty and damage values. The land and ocean impacts are separated, and their country averages shown. The *Max.* column records the number of counties affected by the peak peak event.

6.1.3 Consequence Predictions Using Inverse Probability Functions

Figure 6.1 presents the inverse probability functions for the complete range of object radii simulated by NEOimpactor, expanding on the three scale representatives shown in Figure 5.11. This plot gives a clear distinction between the casualty probability estimate curves of the lower range of objects. By shading the curves according to the object radius ranges, given in Table 6.1, an understanding of the confidence in the probability calculations is gained. Figure 6.2 provides this shaded version of the inverse probability functions. The size of the shaded probability region indicates the uncertainty range in the probability prediction. While the logarithmic plot aids understanding of the probability certainty for Local scale events, the data for Regional and Global scale events is compressed giving the impression that the certainty of these results is higher.

This, however, is not the case, as the linear scale plot in Figure 6.3 reveals. In this plot, the Local scale events exhibit an exponential decay in probability as the casualty estimate increases. This is due to the hit-and-miss characteristics of small impacts, which require a direct hit of a populated region to generate high casualty numbers (or damage). Whereas, the large scale events present the greatest variation in consequence estimates, from zero over unpopulated regions of Australia (see Figure 5.15) to very high casualty and damage consequence figures from both land and ocean impacts. This high variation is indicated by the increasingly dispersed nature of the Regional (blue) and Global (purple) curves.

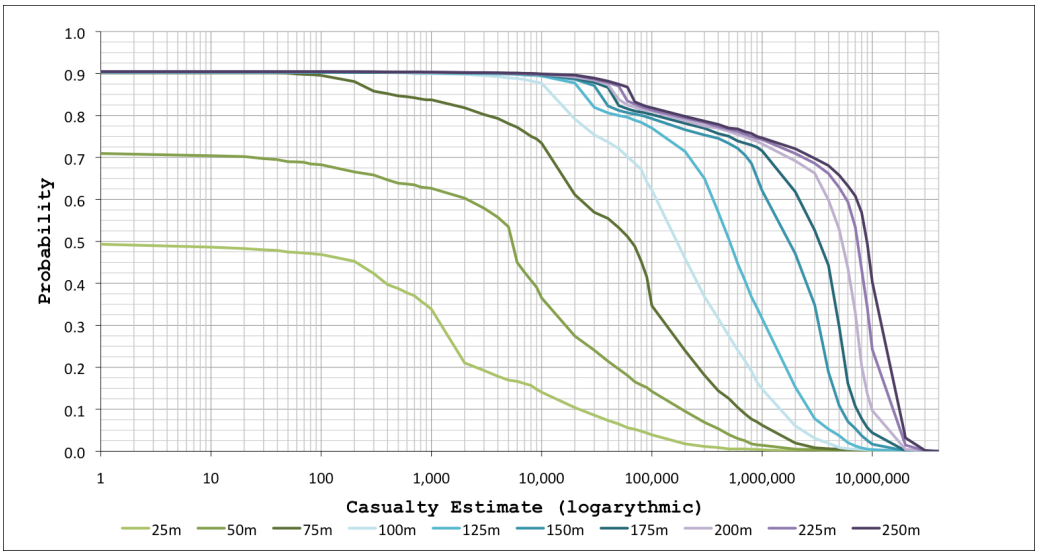

Figure 6.1: Inverse probability functions for each of the ten radius objects simulated in the NEOimpactor Global Grid (shown in Figure 5.3). The green curves represent the Local scale objects, blue represents Regional scale objects and purple the global scale events.

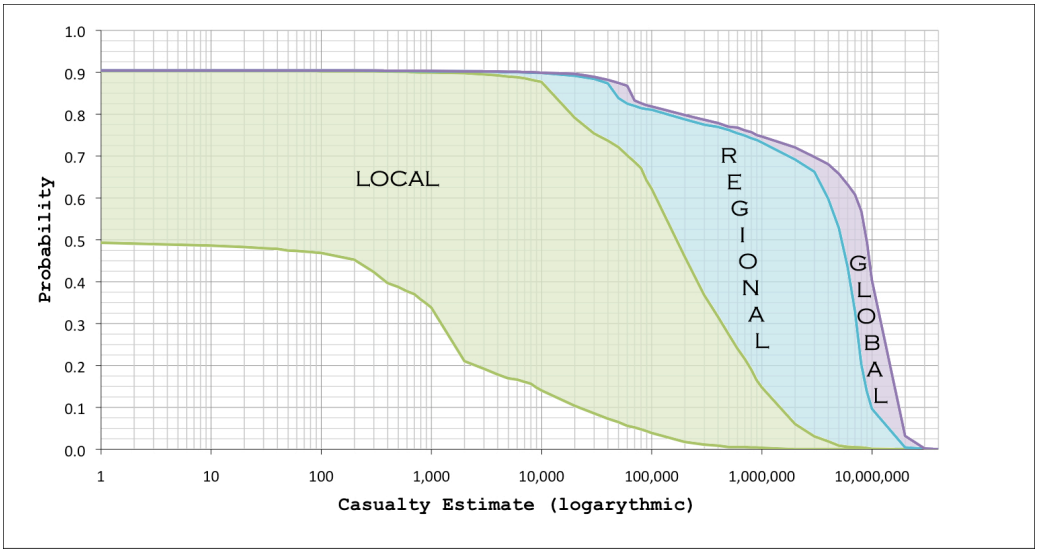

Figure 6.2: Shading the Global Grid casualty data inverse probability functions in Figure 6.1 according to the Local, Regional and Global range in Table 6.1.

Both plot formats allow the user or decision maker to two important assessments. Given an acceptable probability that a maximum casualty (or damage) threshold is not exceeded, the user can identify the radius threshold above which the impact risk becomes too great. Alternatively, given a known asteroid threat, the generated curve enables the user to analyse the probability of exceeding a casualty threshold. If the probability of exceeding that threshold is too high, the decision to act can be informed.

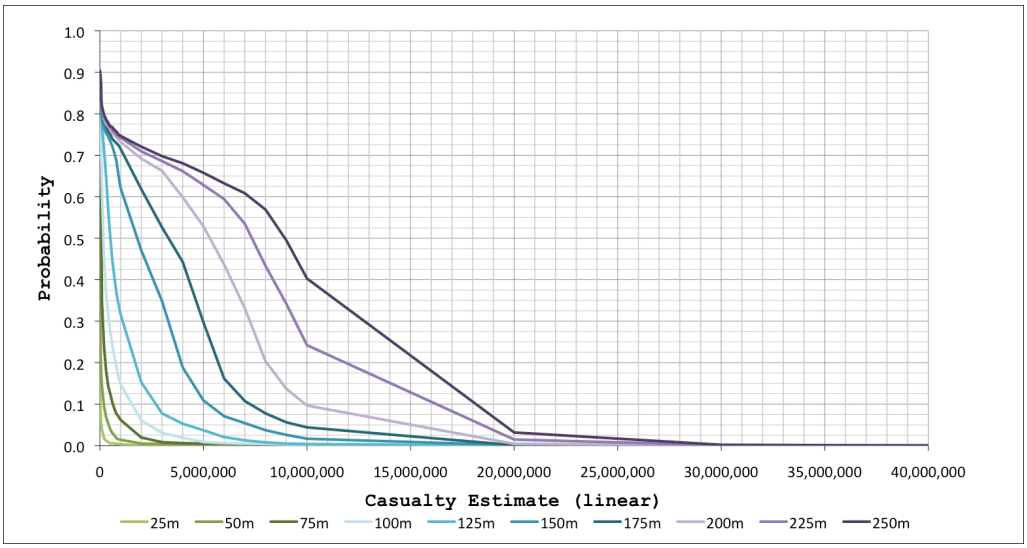

Figure 6.3: The ten casualty inverse probability function curves plotted against a linear x-axis to highlight the variability in the large radius impact events. The scale is equivalent to that in Figure 6.1.

In summary:

> *Using the probability plots from a generic simulation, or the simulation of a particular threatening asteroid, enables an instant assessment of the risk faced either globally or by a particular country. Due to the large range of consequences possible, both logarithmic and linear plots are required to study the low and high energy impacts respectivly. The tool is important for informing the decision making process by predicting the probability that an event will exceed a particular consequence threshold.*

6.2 A Comparison Study of Land and Ocean Impacts

Section 5.2 presented the linear impact path results for three test pathways. These were the Tropics of Cancer and Capricorn and a small segment along the 40° North line of latitude. Each plot demonstrates a great degree of variation in expected consequences from impacts along the path. Each of the graphical results (Figures 5.14, 5.15 and 5.16) present a line for each of the three scale simulations.

6.2.1 Study of the Linear Path Results for the Global Scale Object

For the 225 m radius results, the most striking characteristic of each graph is the contrast between the land and ocean segments of the path. Particularly prominent in the casualty plots are the sections of near-zero casualties as the path crosses Saharan Africa

and Australia. Here, the very low population density results in almost no casualties. This is in stark contrast to the ocean segments, where the casualty estimate barely drops below five million. Variation is also seen along the ocean impact segments of the paths which are a result of three key factors:

Distance from coastlines - increased distance from coastline attenuates the potential destructive power. This is most clearly demonstrated by the path between -75° W and -15° W along the Tropic of Cancer (Figure 5.14), which exhibits a dip in the consequence estimate towards the middle of the Atlantic Ocean.

Proximity to islands - impacts close to islands or archipelagos add significant variation to the results. This is most obvious across the Caribbean (Figure 5.14).

Ocean Bathymetry - submerged volcanoes (called sea mounts) and other ocean floor anomalies, where the ocean depth changes significantly, has a pronounced affect on the tsunami strength. The deep trough in the consequence estimate at -165° W on the Tropic of Cancer (Figure 5.14), is caused by an impact on a sea mount part of the Hawaii island chain.

Ocean impacts are therefore characterised by nearly uniform high damage and casualty potential with occasional local anomalies, whereas even large land impacts can generate negligible casualties and damage.

Along both Tropics, the peak casualty and damage estimate is generated from a land impact event. The most significant peak is at 90° East on the Tropic of Cancer (Figure 5.14), just south of the Bangladesh capital, Dhaka. On the Tropic of Capricorn (Figure 5.15), the peak infrastructure damage estimate results from an impact on the city of São Paulo in Brazil (46° W). Therefore, despite the potential for land impacts to generate almost zero casualties, they can also be extremely destructive.

In summary:

A series of ocean impacts will typically produce a higher average consequence figure compared with the same number of land impacts. The consequences of two identical ocean impacts a small distance apart will vary only slightly. On the other hand, land impact consequences vary significantly with only a small displacement.

6.2.2 Comparison Of Severity Scale Plots

The contrast between the three radius simulation results for each individual linear path, further defines the three catastrophe scales. As discussed previously, the global scale asteroid (225 m radius) generates casualties and damage largely from ocean

AVERAGE CONSEQUENCE VALUES FOR THE LINEAR PATHS

Tropic of Cancer	**Casualty Average**		**Damage Average**	
	Land	**Ocean**	**Land**	**Ocean**
Local	169,656	17,309	18.0	1.2
Regional	2,797,100	2,427,648	283.9	281.4
Global	5,859,990	11,555,442	594.2	1,254.3
Tropic of Capricorn	**Casualty Average**		**Damage Average**	
	Land	**Ocean**	**Land**	**Ocean**
Local	48,976	4,669	11.1	0.4
Regional	455,254	1,144,433	171.5	135.9
Global	908,675	9,773,567	361.3	953.5
Segment of 40 ° North	**Casualty Average**		**Damage Average**	
	Land	**Ocean**	**Land**	**Ocean**
Local	100,225	65,955	53.2	8.95
Regional	1,687,177	3,448,141	740.3	572.23
Global	3,482,829	12,275,399	1,492.4	1,860.7

Table 6.3: Consequence data averaged along each linear path for the three scale simulations. Damage values are given in NEOimpactor Infrastructure Units.

impacts. When averaged over length of the path, the casualties generated by ocean impacts account for just over half the total, while the southern path has ten times the land impact value. In terms of infrastructure loss the ocean impacts account for over twice the land impact averages for both Tropic paths (data from Tables 5.10 and 5.11).

The 125 m radius, regional scale data, shows a more even distribution between land and ocean impacts along the Tropic of Cancer. However, the tropic of Capricorn with its larger expanse of ocean, exhibits mixed results. Here the casualty results are predominantly associated with ocean impacts, and the damage estimates are dominated by the two peak land impacts. These are near São Paulo in Brazil and in South Africa (near the conurbation of Johannesburg and Pretoria).

Studying the smallest object size reveals a different picture entirely. Figure 6.4 reproduces the 25 m radius object casualty consequence plot along the Tropic of Cancer. There is a clear distinction between this dataset and those for the 125 m and 225 m plots, in that it is the land impact events that generate casualties, while ocean impacts largely record negligible casualties. Of note is the section across the Sahara where, again, the land impacts likewise produce negligible casualties. This suggests that for small bodies, land impacts present the greatest hazard. This conclusion is confirmed by the choropleth representations in Figures 5.7 and 5.8, which show only land cells shaded on the 25 m results map. This apparent transition between the severity of land impacts compared to ocean impacts is discussed further in Section 6.2.3.

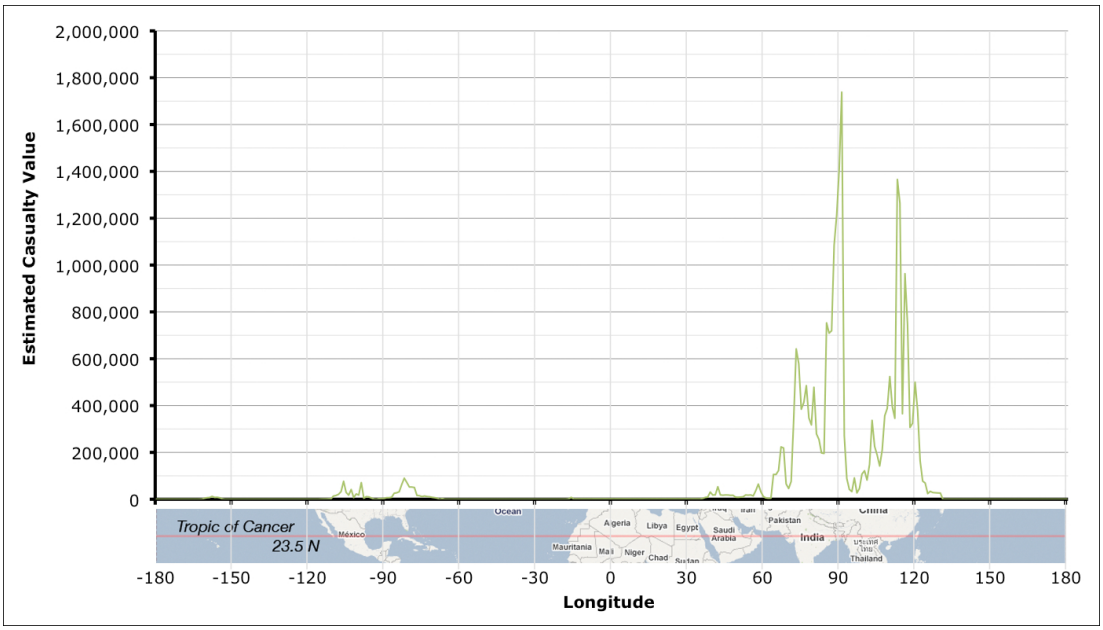

Figure 6.4: Reproduction of the casualty plot of the 25 m radius body along the tropic of Cancer with inset map of the tropics.

In summary:

> *Small asteroids present the greatest hazard when impacting the land and principally threaten only the country where the impact takes place. However, large asteroids present the greatest threat when impacting the ocean with the consequences shared by many countries globally.*

6.2.3 Land-Ocean Impact Severity Transition Radius

This shift in the magnitude of the consequence from land impacts to ocean impacts is an important factor in understanding the NEO hazard. The size of object at which this switch in the severity of the consequences occurs is termed the transition radius. This transitional behaviour is clearly exhibited in Figure 5.16 as the impact path crosses Portugal and Spain. The casualty plot shows a land impact dominance for the 25 m curve, but ocean impact dominance is evident at 125 m. For damage data, the peak land value is still dominant at 125 m and only equivalent to ocean impacts at 225 m. To investigate this further, the path across Portugal and Spain is investigated further.

A Detailed Transect Across Portugal and Spain

Figure 6.5 and 6.6 show the casualty and damage values along a small segment of the 40° North line of latitude. Results of all ten radius objects are plotted to locate the radius at which the land consequence peak is exceeded by the ocean impact

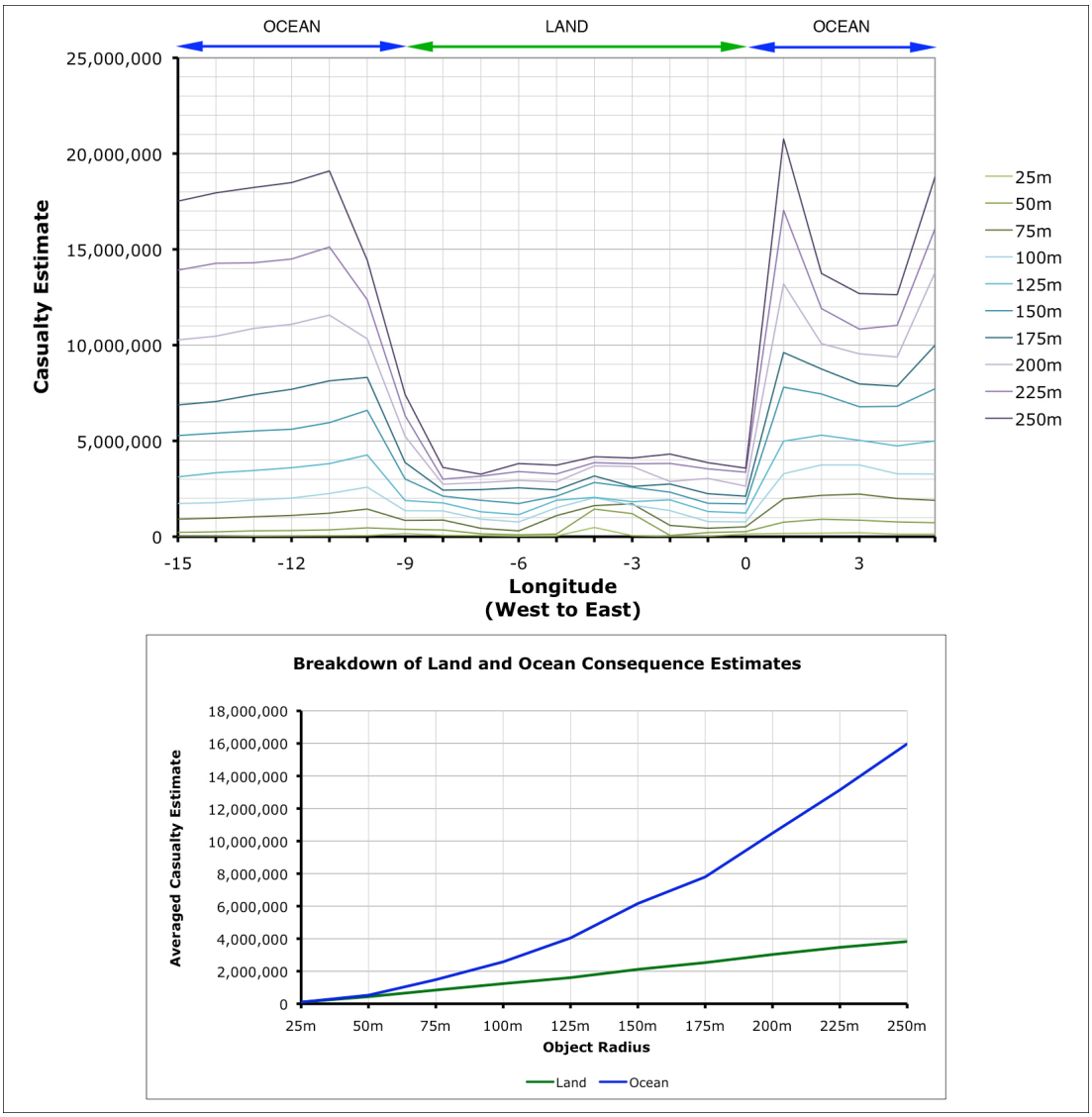

Figure 6.5: Casualty plots for impacts along the 40° North line of latitude from 15° West to 5° East. All ten radius objects are plotted. Inset figure presents the casualty average over both the land and ocean segment (green and blue respectively) for each impactor.

values. There is a distinct contrast between the casualty and damage plots due to the relative consequence of impacts into the land and ocean. Concerning casualty potential, the impact consequences are dominated ocean impacts, while the damage plot demonstrates similar consequences for both impact types. The inset in each figure plots the combined land impact and ocean impact consequences for each radius of object. Both land impact consequence plots appears to show an approximately linear relationship to impact energy, while the ocean plot follows an approximate x^2 trend. The land-ocean transition radius is found at the intersection of these two lines and is given in Table 6.4.

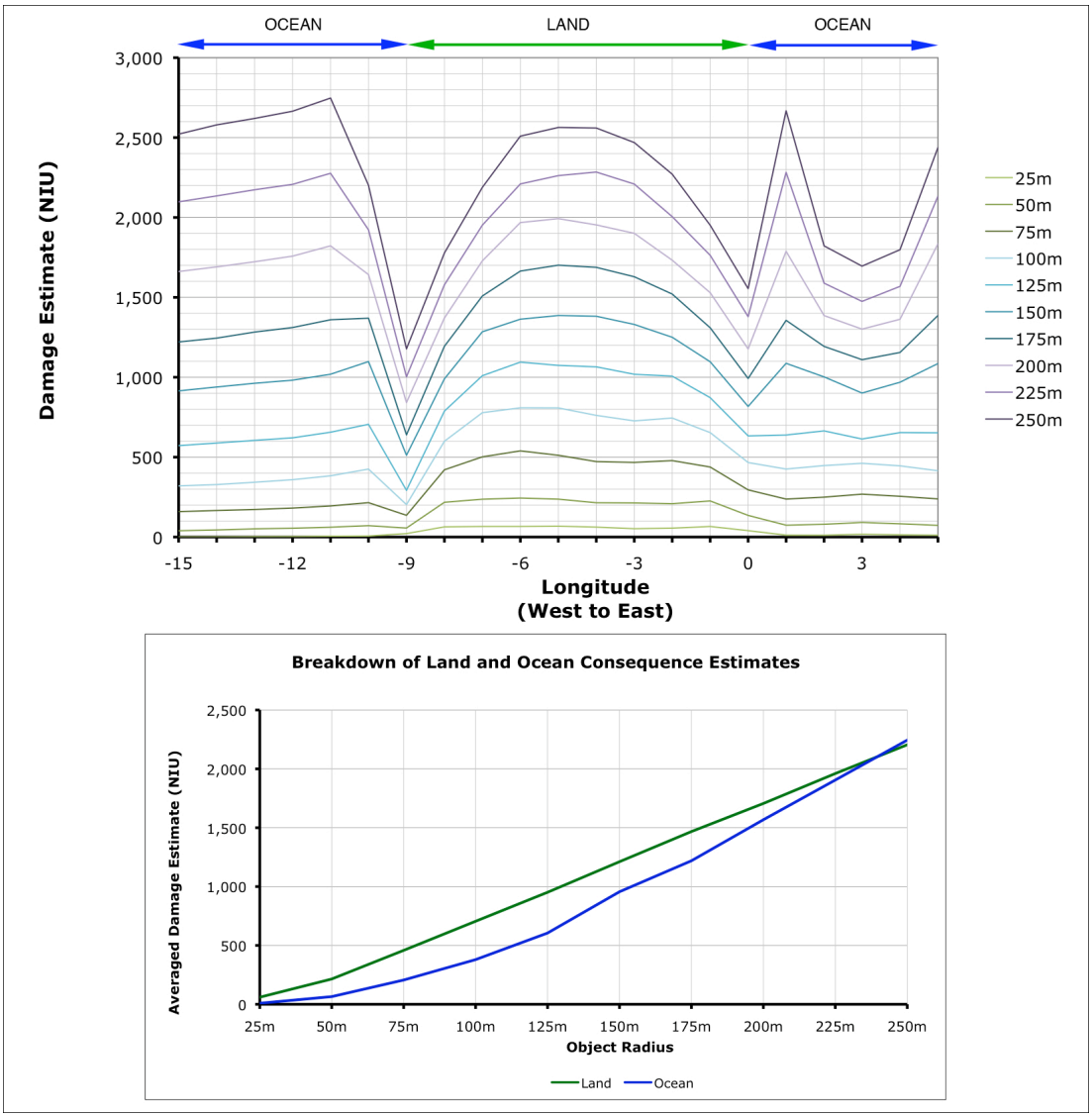

Figure 6.6: Damage plots for impacts along the 40° North line of latitude from 15° West to 5° East. All ten radius objects are plotted. Inset figure presents the damage average over both the land and ocean segment (green and blue respectively) for each impactor.

Transition Radius Investigation Using the Tropics Data

Averaging ocean and land impact consequence values along the more extensive Tropic paths (as shown in Tables 5.10 and 5.11) increases the robustness of the investigation due to the increased number of data points available. The land-ocean transition along the Tropic of Capricorn appears between 25 m and 125 m based on casualty estimates, but between 125 m and 225 m for damage predictions. Conversely the Tropic of Cancer data presents an opposing view with the casualty transition radius above the damage transition radius. Table 6.4 presents the transition radii calculated by plotting the land and ocean data graphically (not shown).

TRANSITION RADII CALCULATIONS

	Casualty Data	Damage Data
40° North	26 m	240 m
Tropic of Cancer	131 m	125 m
Tropic of Capricorn	31 m	131 m
Global Grid:	31 m	32 m

Table 6.4: Transition radii found from the intersection of the cumulative land and ocean consequence plots. Figures 6.5 and 6.6 show the radius determination procedure for the 40° North segment.

Both Tropics, however, have a pronounced land impact peak value which will act to skew the results. The Bangladesh casualty peak on the Tropic of Cancer is between 4 and 24 times the average of the entire path for the 25 m and 225 m data respectively. While damage generated by the Brazilian impact on the Tropic of Capricorn is between 1.5 and 98 the path average over the simulated radius range. This large difference is an indicator of the differing land and ocean impact characteristics noted.

Transition Radius from Global Grid Results

The difference between land and ocean impacts is a global phenomenon. Therefore, the Global Grid datasets can be interrogated to provide the average land and ocean consequences values over the entire world. Figure 6.7 displays the land and ocean data plotted against object radius, with inset figures locating the transition point. By averaging data over the entire grid, the skewing affect of particular peak impact values is further reduced. Increasing the grid cell resolution would further refine this transition point. These plots reveal far greater similarity in the transition radius based on casualty and damage data, 31 m and 32 m respectively, as given in Table 6.4. These two values for the transition radii are significantly lower than those based on the linear paths. Furthermore, unlike the linear path data, the close correlation between the casualty and damage transition radii indicates that the two consequence models are comparable.

The plots in Figure 6.7 reveal that the 125 m radius on both the casualty and damage plot is a point of inflection for the combined data. This allows the relationship to be simplified into a two regime approximation for the NEO consequence estimation. The combined data curve can be approximated by two line segments represented by Equations 6.1 and 6.2, where R_{neo} is the asteroid radius, in metres, as:

$$\text{Casualty Estimate} = \begin{cases} 10{,}000\ R_{neo} - 250{,}000 & \text{for} \quad 25 < R_{neo} < 125 \\ 56{,}000\ R_{neo} - 6{,}000{,}000 & \text{for} \quad 125 < R_{neo} < 225 \end{cases} \tag{6.1}$$

$$\text{Damage Estimate (NIU)} = \begin{cases} 2.0\ R_{neo} - 50 & \text{for} \quad 25 < R_{neo} < 125 \\ 6.4\ R_{neo} - 600 & \text{for} \quad 125 < R_{neo} < 225 \end{cases} \tag{6.2}$$

In summary:

> *Line impact simulations form a useful tool for investigating the difference in consequence generation between land and ocean impacts. Small asteroids are shown to present the greatest threat when impacting land, while large bodies produce the greater consequences from ocean impacts. By studying the Global Grid data, a transition radius is found at approximately 31.5 m (63 m diameter) for the chosen asteroid characteristics. This equates to an kinetic energy transition of 3.3x10^{16} J.*

6.3 Factors Contributing to the NEO Hazard

6.3.1 The Influence of Asteroid Composition on the NEO Hazard

Table 2.4 presented a summary of the compositional details of the NEA population. The results analysed here all concern the stony-iron S-Type, which has a density of 3,500 g/m^3, detailed in Table 4.7. Taking the population as a whole, an 'average' object density would be 2,965 g/m^3. With the test object's density above this average, the results here will suggest above average consequence figures. Table 6.5 reveals the effect density has on the consequence estimates from a single ocean impact. These results show the limited effect object composition has on the overall threat. However, of greater significance is the increased likelihood for low-density, C-type asteroids to fragment.

In summary:

> *Increasing the density of the incoming asteroid has the expected effect of increasing the potential casualty and damage generation. This is due to the increase in kinetic energy of the impact. Composition will have a more significant affect on the nature of the asteroids flight through the atmosphere in terms of its fragmentation potential, with more dense bodies less likely to fragment.*

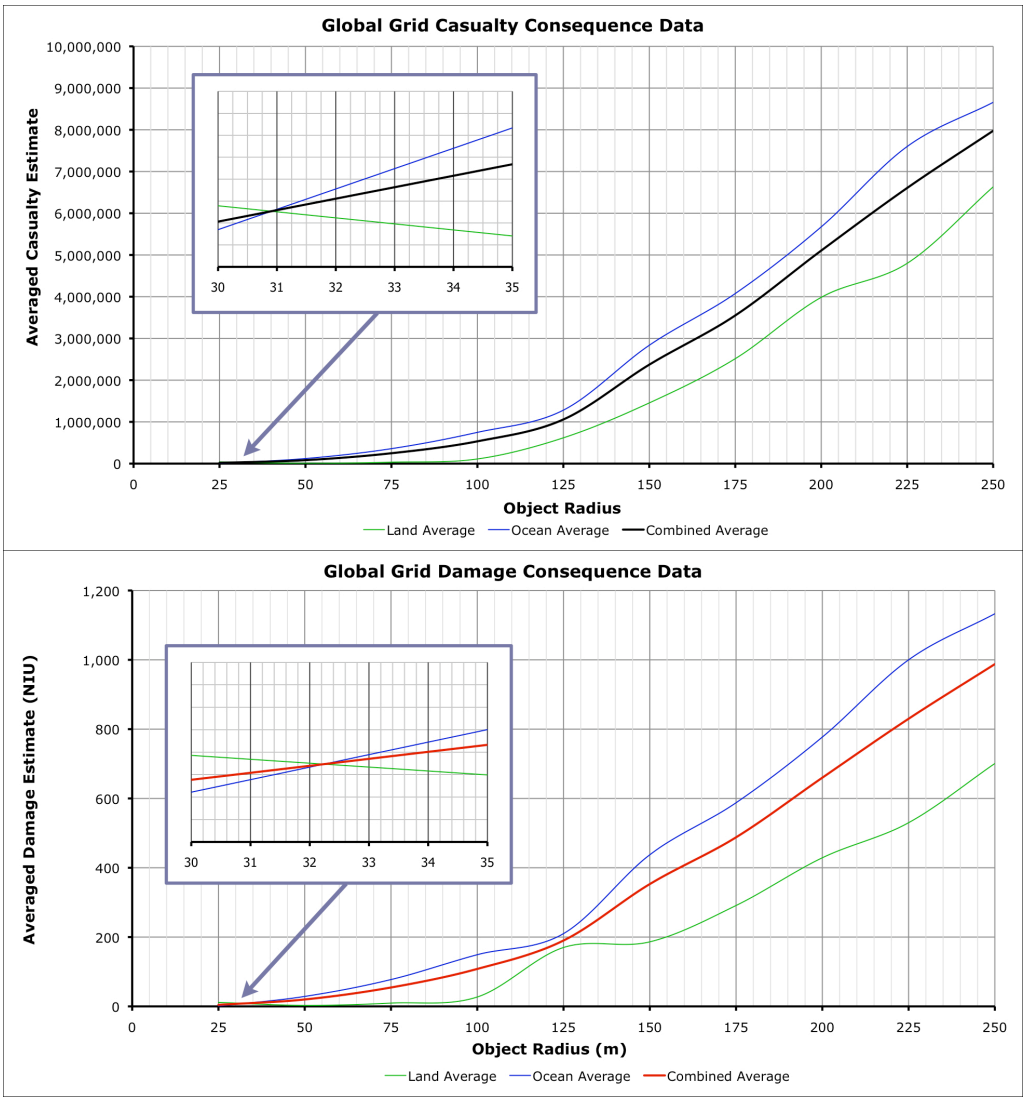

Figure 6.7: Land and ocean casualty (top) and damage (bottom) data plotted against object radius, showing the Global Grid transition radius as inset figures.

6.3.2 The Influence of Fragmentation on the NEO Threat to Earth

The NEOimpactor results presented so far concern the impact of only monolithic asteroids, making the assumption that the body reaches ground intact. Pravec and Harris [2000] suggest that this assumption is acceptable for small bodies, whereas large bodies (of the order of 1 km in diameter, 500 m radius) are more likely to be loosely cohered rubble piles. However, Boslough and Crawford [2008] suggest that it is the smaller objects which will fragment most easily.

Fragmentation is an important issue due to the likelihood for real bodies to fragment, as well as the various mitigation proposals focussed on pre-fragmenting the asteroid while in orbit. The NEOimpactor fragmentation model has not been implemented in the studies made in this thesis due to the high level of uncertainty

TEST IMPACT AT 0° LATITUDE, 0° LONGITUDE

Density	Casualty Figure	Damage Estimate (NIU)
C-Type (2,200g/m^3)	1,872,332	201.2
S-Type (3,500 g/m^3)	1,933,930	210.8
M-Type (7,900 g/m^3)	2,200,342	229.0

Table 6.5: Analysis of the effect asteroid density has on the impact consequences for a single 125 m radius spherical asteroid with an impact velocity of 12,000 m/s.

surrounding modelling the fragmentation processes. However, a simple study is possible by comparing the potential consequences from multiple single impacts. Here, the consequences from a 250 m radius asteroid impact is contrasted with the impact of a number of small bodies of equivalent total mass. One thousand 25 m radius bodies represent an equivalent impacting mass and, using the same impact velocity, therefore equal kinetic energy impacting Earth. Table 6.6 presents this comparison based on Global Grid averages. As such, the variation in consequence estimate with impact location is removed. Demonstrated clearly is the doubling of the average casualty estimate and the five-fold increase in damage potential from the multiple fragment impacts.

The conclusion is that fragmented bodies have the potential to dramatically increase the casualty and damage potential of a large body. This is particularly relevant for mitigation mission proposals which aim to remove the threat of an approaching asteroid by disrupting the asteroid catastrophically. The aim of such missions would be to reduce the asteroid to fragments small enough to ensure complete attenuation in the atmosphere. However, if the mission fails to achieve this and instead generates a number of bodies just large enough to reach the ground, the impact threat might be dramatically increased. This should be sobering reading for proponents of mitigation missions using nuclear detonation techniques.

Furthermore by taking the fragmentation results and considering land and ocean impact events separately, a second insight is revealed. Table 6.6 shows significant increases in casualty and damage potential when an object fragmented over land. On the other hand, if the fragments impact only the ocean, the consequences are reduced. This conclusion has particular relevance for understanding a particular asteroid's threat if it is expected to fragment. If the predicted impact is over the ocean, then one might be tempted to leave it on course, whereas if the target is land (particularly if that region is populated), then the risk to Earth will be dramatically increased and every attempt must be made to deflect the object's trajectory. This analysis does not take into account the possibility that the smaller fragments might become further fragmented during atmospheric entry.

ASTEROID FRAGMENTATION TEST

Impact Type	Single 250 m Radius Body Casualty	Damage	1000 Fragments of 25 m Radius Casualty	Damage
Global Average	7,976,483	987.5	17,243,000	4,425
Land Impacts	6,632,036	701.0	40,796,000	11,451
Ocean Impacts	8,658,105	1,133	5,302,000	862.5

Table 6.6: Analysis of the average impact consequences of a single impact event compared to multiple smaller impacts. Damage values are given in NIUs.

In summary:

> *On average, the results of NEOimpactor suggest that the consequences resulting from a fragmented asteroid are more severe than from a monolithic body of equivalent mass and kinetic energy. This is particularly the case if the region where the fragments fall is populated land. However, if the impact region is entirely mid-ocean, the impact effects would be less severe.*

6.4 Consequences for Mitigation Mission Proposals

Of the three mitigation mission proposals (gravity tractors, kinetic impacts and nuclear explosion), the proponents of the nuclear detonation missions have the loudest voice. At the recent Planetary Defence Conference [IAA, 2007], a worryingly large number of delegates focused on 'nuking' asteroids. The outcome of that conference by Ailor [2007b], gave the recommendation that such missions would only be adopted as a last resort when either all else had failed, or the lead-in time was too short to mount a mission using a more gradual deflection technique. The results discussed in Section 6.3.2 substantiate this argument by demonstrating the possible disastrous consequences of a partially successful nuclear mission. Fragmentation into bodies smaller than the transition radius will increase the impact consequences. However, if the object's predicted impact location is mid-ocean, then pre-entry fragmentation could potentially decrease the object's threat.

Chodas [2007] predicts the average time period between detection and impact to be around 10 to 20 years for large objects. For small bodies this will be lower, however, until adequate detection techniques are able to catalogue the sub-kilometre population. When a future impact event is predicted, this takes the form of a line of risk across the Earth. This line is due to uncertainties in the object's orbit characteristics and position in space (the line represents the probable intersection of the asteroid's orbit with Earth's). Figure 3.15 displays a map showing the line of risk of

the asteroid 99942 Apophis which, briefly, posed an impact risk. A risk analysis along this particular line of risk has been investigated in depth in a previous publication by Bailey et al. [2006]. NEOimpactor can be used to predict the consequences along any real line of risk. Figure 6.8 presents the plot for the Apophis path. While this particular line of risk is no longer relevant, the results of a real impact threat path can be used to aid the decision regarding the method of mitigation.

Gravity tractor-type missions, such as that proposed by Lu and Love [2005], provide the most accurate means of controlling an asteroid's deflection by gradually moving it along its orbit path resulting in the asteroid crossing Earth's orbit before or after the Earth reaches the predicted impact point. The inherent error in orbit determination results in a probability of impact. Therefore there exists a probability that the object is not on a collision course and would naturally miss the Earth. Thus any attempt to alter this non-threatening situation could potentially result in the object being moved onto a collision course. This is largely a problem for those responsible for the orbit determination. However, it raises the issue that any attempt to alter an object's orbit will alter the impact threat and change the hazard classification from natural to man-made.

Furthermore, even if the object is certain to impact the Earth, the decision to alter the orbit (and thus move the predicted impact location) will immediately raise the risk of one region above another. Here both types of NEOimpactor outputs can be of value - firstly the Global Grid can locate the region of lowest impact consequence, and secondly impacts along the specific line of risk will highlight which parts of the line face the greatest threat. Figure 6.8 suggests that an impact at the centre point of the path (North of Hawaii) results in significantly fewer casualties than impacts at either end of the path. It also reveals that the region of highest vulnerability is around Central America. From this analysis it could be concluded that the impact site be moved in a westward direction. However, this will raise the threat to Japan and central Asia. Furthermore, if the mitigation is not entirely successful the eventual impact consequences may have been increased, compared to the original impact point. Therefore, the decision to mitigate a threat is both a political and international one, as well as being highly complex. However, this example shows the potential of NEOimpactor as an aid in the decision making process.

6.4.1 Responsibility for the Mitigation of the Asteroid Threat

Put simply, the responsibility for making a decision on whether, or how, to mitigate the threat of a particular NEO impact lies squarely with the international community. However, clearly not all countries have the available infrastructure to mount a mitigation mission (indeed most have no space program). Therefore, it will only be the

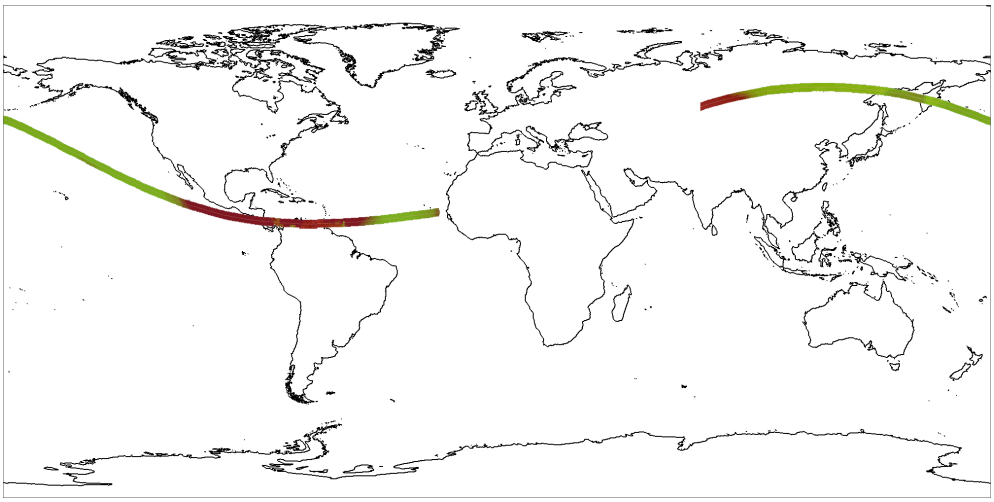

Figure 6.8: Simulation of impacts along the 99942 Apophis' line of risk for the 2036 close approach. Red and green denotes the high and low casualty estimates for impacts along the line.

few space-faring nations, and their associated space agencies, who can take action. This leads to problems of self-interest, where these advantaged countries may want to protect their own interests above others. For example, if NASA took responsibility of deflecting Apophis, would it decide to deflect the body East and away from the USA, thereby increasing the risk to Japan?

Such questions are not easy to answer and much debate continues amongst the international community [Schweickart, 2007]. Certainly organisations such as the UN would be a venue to provide unbiassed decision making. Also organisations such as the European Space Agency, with its foundation of international co-operation, would reduce the influence of single countries. A number of questions arise from this discussion, related to the vulnerability of the different members of the global community to the NEO hazard. These will be the focus of the following section.

In summary:

> *Of the three proposed mitigation mission types, the gravity tractor is favoured due to the gradual and controlled manner in which the orbit deflection is achieved, thus limiting the probability of on-orbit asteroid break up. However, any deflection procedure will turn a natural hazard into a man-made hazard. Therefore modelling of the impact line of risk using NEOimpactor will aid the mission planning by indicating in which direction the deflection would most effectively limit the impact consequences.*

6.5 Analysis of the Factors Affecting a Country's Vulnerability

The analysis of the countries most at risk from the NEO threat involves consideration of many factors. It is difficult to identify any one country that faces the greatest overall threat. In this section the various risk factors are discussed, along with the associated ranked lists presented previously in Section 5.1.6. The aim is to provide an overall assessment of those countries most vulnerable to the NEO hazard. The world's countries can be divided into three categories based on their morphology: land-locked, coastal, and islands. These three categories are studied independently.

6.5.1 The Risk to Land-Locked Countries

Impacting asteroids with radii above the 31 m transition threshold (i.e. the majority of objects studied) present the greatest average threat when impacting the ocean. This is due to the ability of tsunami to reach any coastline worldwide. Therefore, for any given ocean impact, only the totally land-locked countries will be 'safe'. There are 39 land-locked countries (of the 250 countries in the NEOimpactor database); they represent 11.5% of the world's land area, and 3.3% of the global surface area. Assuming that asteroids have a uniform probability of impact across the globe, these countries will only be directly affected by 3.3% of asteroid impacts [Grieve, 1990]. Their only other source of risk is from asteroid impacts into neighbouring countries close to their borders. Assuming that the 'casualty reach' of a 25 m impact is 10 km, and 120 km for a 250 m body, each country's region of risk can be calculated. Totalling these combined areas, we find that these 39 countries have between a 3.4% and a 4.4% share of the total NEO risk.

Table 5.8 presented the top ten land-locked countries ranked by their total recorded consequence levels over the entire grid. Only Austria and Kazakhstan in this table appear in another of the rankings. Austria is ranked tenth by the damage per unit area, as shown in Table 5.6. It can be said, therefore, Austria's infrastructure is particularly vulnerable. This high level of ranking is due to the high infrastructure density of this relatively small country, which is a characteristic of the Western European nations. Kazakhstan appears ranked ninth in the overall global damage risk (see Table 5.3). Of particular interest is the fact that both these occurrences appear in the 25 m datasets, which further confirms the suggestion that small bodies are most dangerous when impacting land rather than the ocean (that is, those below the transition radius).

In summary:

> *Land locked countries face the lowest overall risk due to their isolation from ocean impacts. They can only be affected by impacts within, or close to their borders.*

6.5.2 Risk Assessment of Island Nations

Unlike land-locked countries, island nations appear dotted throughout the five rankings presented in Chapter 5. In particular, they dominate the ranking by percentage population and infrastructure lost. While the total global area of these nations is also small, only 9.61% of the global surface area, the overall risk to island nations is significant. The reason is due to the coastlines which surround them entirely. As shown in Section 6.2.3, ocean impacts present the biggest threat to the global community for the majority of asteroid radii. Therefore it follows that those countries with the largest coastal regions will face the most frequent impact threat. NEOimpactor models a total of 64 island nations. Table 5.4 displays the top ten island nations in terms of casualty estimates and damage potential.

Table 5.3 show the global ranking for all countries based on the raw casualty and damage estimates respectively. In these two rankings, island nations appear five times. This is a critical observation as these countries do not have the largest coastline length, nor the greatest populations. However, their island morphology means that they are particularly vulnerable to ocean impact tsunami. Being surrounded by coastlines, they face a tsunami threat from all directions. Another contributing factor will be dependency of island peoples on coastal regions for fishing and trade. Thus these countries will naturally have a high density of coastal communities. Local geography - such as mountainous central regions - can also act to limit populations to flat coastal regions, as in Japan. The combination of need and necessity places a large population, and the associated infrastructure, at high vulnerability to tsunami inundation.

This is particularly prominent for any nation which is an archipelago. Here the small size of each island will mean that even the centre of the island is potentially at risk from tsunami (unless mountainous geography provides safe higher ground). This effect is particularly pronounced in Indonesia, which suffered disastrous consequences following the Boxing Day Tsunami of 2004. Along with the Philippines and Japan, Indonesia is ranked highly in the global casualty data (see Table 5.3). Table 5.9 demonstrates this effect of the concentration of populations along coastal regions. This presents the casualty data ranked according to each countries area:coastline length ratio. In this ranking these three countries, together with the United Kingdom, are ranked highest, suggesting their greater vulnerability. These countries also have relatively large populations, which also contributes to their high risk factor.

In terms of damage, Australia and New Zealand can be added to the high vunerability list. These countries are both classed as 'developed' and have significant infrastructure. New Zealand's geography is similar to that of Japan resulting in settlements limited to flat coastal regions. Australia on the other hand is very large and predominantly flat. However, here it is the desert climate of the central regions, rather

than geography, which confines most urban conurbations to coastal regions. In both examples these industrialised countries present a large urban environment within reach of tsunami inundation.

In summary:

> *By combining the casualty and damage rankings in Table 5.4, together with the above analysis, we find that the five island nations most at risk are (in order): Japan, the United Kingdom, Indonesia, Australia and the Philippines.*

Casualty and Damage Density Ranking

When the casualty and damage potential of each country is divided by its land area, a new ranking is found which represents a consequence density value, as shown in Table 5.6. This ranking takes into account all countries within the NEOimpactor database but is again dominated by island nations. The countries in the casualty density ranking are predominantly small island nations (with the Philippines as the exception, although this is an archipelago of relatively small islands) grouped into three global regions: the Caribbean, Madagascar and the South Pacific Islands. This ranking appears fairly stable across the range of object radii, with seven countries being common to each of the three casualty density rankings. However, the damage density ranking contains a number of non-island European countries and their island dependancies. Singapore also appears in the damage list, as expected, due to its very high infrastructure density on such a small island. However, it only appears in the top ten for the 225 m results, which is due to the large number of surrounding islands and land masses offering protection from most small local impacts. Here again the land-ocean transition is visible with large non-island countries represented in the 25 m list (Estonia, Albania, Norway and Austria), but only islands in the 225 m list.

The density rankings provided in Table 5.6 gives information relating specifically to the vulnerability of countries. The ranking indicates a value of casualty and damage 'density' which does not relate to the global peak figures (those found by impacting a built up city), but rather to the most casualties or destruction per square kilometre over the entire country. this implies that these countries face the risk of being decimated over their entire area rather than simply at one particular location. This indicates that these countries will have few regions that remain unaffected, from which to mount rescue and recovery efforts. The fact that the countries within these rankings are predominantly island nations presents an additional serious risk factor - the isolation of island nations. While evacuation and recovery is not assessed by NEOimpactor, both are critical for islands which have no inland 'safe zones' where coastal population can

re-locate. Nor are there any land borders across which evacuees can flow. Following the event, these small islands highlighted will face widespread devastation with the only means of external aid arriving again by air or sea.

The ranking for casualty and damage densities are quite distinct from each other and therefore cannot be combined. The top five countries by casualty and damage are therefore:

Vulnerability by Human Populations: Barbados, Aruba, Guam, Martinique and Mayotte.

Vulnerability by Infrastructure: Faroe Islands, Mauritius, Saint Piere and Miquelon, French Southern & Antarctic Lands and St. Lucia.

In summary:

> *By normalising casualty and damage estimates with respect to area, a density ranking is derived. This highlights those countries most at risk of large scale devastation in proportion to their overall size, and therefore those vulnerable to total devastation.*

6.5.3 Risk Assessment of Coastal Countries

Of those countries with some length of coastline, Table 5.7 provides an analysis of the threat per kilometre of coastline. This provides some useful indicators of risk. The ranking uses the Global Grid averaged consequence figures for each country, divided by its recorded coastline length. This highlights countries that have a large area:coastline length ratio, combined with a high population or infrastructure density. The Democratic Republic of the Congo and Iraq are two examples of countries with very short coastlines (between 80 and 90 km) but the country itself occupies a large area. Despite this skew in favour of countries with large areas and short coastlines, two countries with very long coastlines are found: India and China. The shear population density along these country's extremely long coastlines makes them stand out as being particularly at risk.

In summary:

> *While ranking by coastline length highlights those countries with large areas and small coastlines, India and China are identified as being at particularly high risk due to their extremely long yet highly populated coastlines.*

6.5.4 Overall Country Based Risk Analysis

With reference to the Global Grid result maps (Figures 5.5 and 5.6), two different impact hazard regions are identified. Impacts around Southeast Asia are dramatically highlighted, generating the highest casualty potential. On the other hand, it is the North Atlantic, together with land impacts across Europe and the Eastern seaboard of the United States which clearly present the most significant consequences for infrastructure. These results are largely to be expected - Europe and the US are the most industrialised regions on Earth, while South East Asia contains the two most populated countries, China and India.

It is in the tabulated ranking of each country, based on their casualty and damage potential (see Table 5.3), that information is gained about each country's vulnerability. The degree of variation in the counties for each object radius ranking indicates that the relative vulnerability of a country is highly dependant on impact kinetic energy. For example, while Indonesia's population is more resilient to a small energy impacts, they are extremely vulnerable to largest asteroids (due to the risk of tsunami inundation from ocean impacts). This variation must therefore be taken into account in the development of a combined vulnerability table.

Looking at the casualty rankings for the three different radii, we find that seven countries appear consistently in each list (see Table 5.3). Table 6.7 collates these rankings into a collective top ranking. The position of each county is based on its collective position in all three ranking lists. The first point to note is that the top three countries, China, India and Indonesia, are all situated in South and South East Asia, previously indicated as at risk by the grid output map. These countries have the first, second and fourth largest human populations in the database, and so present the largest populations at risk. The USA has the third highest population which contributes to its high ranking. The Philippines has a relatively small population despite appearing fourth in the Table.

Two different factors are therefore at work in determining the vulnerability of a country's population: the size of population at risk, and the exposure of the country to tsunami inundation. Both China and India have a long coastal region and a high proportion of coastal dwellers. China has many highly populated port conurbation's, most notably Shanghai, while India has a huge dependence on many small coastal fishing communities. The island nations of Indonesia and the Philippines suffer from the 'archipelago effect', where all population's are located close to the littoral, and thus at high risk from tsunami inundation by impacts in the surrounding ocean. This risk to Indonesia was demonstrated disastrously during the 2004 Boxing Day tsunami, for which the greatest casualty figure was that of Sumatra island in Indonesia, Titov et al. [2005]. The Philippines have also witnessed a devastating tsunami when the volcano

COLLATED TOP COUNTRY RISK RANKING

Casualty Rank	Damage Rank	Combined
China^{+5}	United States$^{\odot,G8}$	China^{+5}
India^{+5}	Russia^{G8}	United States$^{\odot,G8}$
Indonesia	Canada$^{\odot,G8}$	India^{+5}
United States$^{\odot,G8}$	China^{+5}	Japan$^{\odot,G8}$
Philippines	Norway$^{\odot}$	Brazil^{+5}
Japan$^{\odot,G8}$	Brazil^{+5}	
United Kingdom$^{\odot,G8}$	Japan$^{\odot,G8}$	
Brazil^{+5}	Sweden$^{\odot}$	
South Korea$^{\odot}$	Mexico^{+5}	
Spain$^{\odot}$	India^{+5}	

Table 6.7: The collated top-ten ranking by casualty and damage based on the three rankings given in Table 5.3. From these two lists, the top five countries facing the greatest overall risk are identified (right hand column). Countries indicated by a $^{\odot}$ are part of the Organisation for Economic Co-operation and Development (OECD). Those indicated by ^{G8} are part of the Group of Eight (G8) countries, while those denoted by $^{+5}$ are pare of the additional five countries added to the G8.

Pinatubo erupted and partially collapsed into the sea [Rantucci, 1995].

The remainder of the countries listed display a varied range of vulnerability factors. The dominating factor is their coastal properties. Japan and the United Kingdom appear highly ranked due to the 'island effect', where many populations are located in coastal communities. Being islands, they are exposed to tsunami from every direction, although their proximity to the Eurasia land mass results in the primary threat coming from the Pacific Ocean to Japan's Southeast and the North Atlantic Ocean to the UK's West. South Korea, while not an island, is surrounded by ocean on three sides and faces a similar risk to that of Japan. Its geography is also similar to Japan, and has two major ports of Busan and Pohang on its Southeast coastline, exposed to the Pacific Ocean.

The USA, ranked fourth, is part of the North American continental land mass. Its high risk is a result of three key factors. The USA's population is the third highest in the world meaning there are more people at risk. Secondly, its large land area (6.4% of the world's land area) leads to a higher probability of receiving a direct land impact. Thirdly, and most significantly, the USA is exposed on both its East and West coast to two large oceans - the Atlantic and the Pacific. Mexico, which shares a similar geographical situation, is highlighted in the infrastructure damage ranking due to its exposure to the Pacific and the Gulf of Mexico. The Gulf itself is shallow, which reduces the peak wave height, thereby mitigating some of the tsunami risk. However, evidence presented by Maurrasse and Sen [1991] and Smit [1999] reveals that the Yucatan impact, 65 million years ago, generated a significant tsunami

in the Gulf which inundated the surrounding coastlines and physically altered the littoral. Furthermore, as indicated by the Mexico earthquake of 1985 in which 10,000 people died, Mexico City is particularly vulnerable to earthquake destruction due to its construction on a dry lake-bed [Seed et al., 1988].

Brazil is the only Southern Hemisphere country represented in either list. Its appearance is indicative of its long Atlantic coastline and high coastal population focused around São Paulo and Rio de Janeiro (see Section 6.2.2). This population is heavily urbanised leading to a significant infrastructure risk as seen in Figure 5.15.

Understanding the damage ranking follows the same underlying rules. The USA is ranked number one, and is presently the leading industrialised nation of the world. Russia is placed second, despite not having appeared in the casualty list. Its extensive land mass results in the accumulation of many land impacts, which collectively raise its risk level. Canada is present for much the same reason, though it has the additional contributing effect of its many islands, increasing the coastline length. It also has a historical dependence on the water for trade and industry.

These three countries displace India, Indonesia and the Philippines, primarily due to the lower state of industrialisation of the latter, so lowering their overall infrastructure vulnerability. A warning must be given to the affect that the lack of infrastructure loss here does not equate to a lack of suffering. Although the total value of the infrastructure lost is low on a global scale, the infrastructure that is lost will be the most vital local amenities, such as shelter and fresh water supplies. This is a limitation of the NEOimpactor system, as it values industrialised infrastructure above basic housing (due to the increased light pollution signature produced). Three years after the Boxing Day tsunami, Robinson and Jarvie [2008] reports that coastal populations along Sri Lanka's Eastern seaboard have still yet to return to full function. Likewise, three years on from hurricane Katrina, large sections of New Orleans remain destroyed and deserted [Paxson and Rouse, 2008].

While China is demoted to fourth place, two new entries in the damage ranking are Norway and Sweden. Though not leading superpowers, these are two highly developed countries with strong infrastructure networks. One indication of this is the percentage of the population with access to broadband internet, 85% compared with only 19% in the US [Savage and Waldman, 2005]. This high-tech infrastructure is put at risk due to both countries award winning crinkly edges and mountainous interior, which tends to force communities to the coastline [Adams, 1979].

Table 6.7 also highlights which countries in the list are members of the Organisation for Economic Co-operation and Development [OECD, 2009], the G8 (*Group of Eight* and the extended G8+5). Half of the G8 along with four of the five G8+5 countries are highlighted in the ranking, while nearly a third of the OECD countries

are listed. Critically, only two countries listed are not members of either body, Indonesia and the Philippines. However, these countries do not appear in the final top five ranking. These international co-ordination organisations are in place to improve communication between the most developed countries in the world. The fact that so many are shown to be most vulnerable to asteroid impacts may not be surprising, but is important. These counties collectively account for the majority of scientific and economic power in the world and are therefore best placed to tackle the hazard. These two organisations perhaps also provide a forum for decision making policies to be discussed. However, with two countries not represented in either organisation, it would be important to include their voice if such a forum was used for mitigation discussions.

In summary:

> *By using the collated country rankings, a total of 15 countries are identified as being most vulnerable to a general asteroid impact based on either casualty or damage potential. From these, the top five are highlighted as (in order): China, the United Stated, India, Japan and Brazil. This is for a combined casualty and damage potential. All of these countries have been highlighted in the previous ranking lists and all are part of the G8+5.*

6.5.5 Implications for Global Vulnerability and the Decision Making Processes

The third column of Table 6.7 highlights the five countries that face the the greatest combined socio-economic risk. Together, these five countries represent 41.4% of the casualty risk and 27.3% of the damage risk to Earth while representing only 6.1% of the global surface area (21.0% of the world's land area) thus receiving 6% of impacts directly. The implication again is that ocean impact tsunami are the most significant threat. Combined, this small group of countries account for over a third of all damage and casualties generated on average by an 'average' impactor.

There are implications for such a small number of countries representing a significant proportion of the overall risk. These five countries collectively have the most to lose in the event of an impact. Their proximity to all the major oceans (except the Southern Ocean), means that any ocean impact will strongly effect one or more of these countries. Having the most to lose would suggest that these countries should be instrumental in any action tackling the threat. Currently the USA is leading efforts to catalogue threatening objects through the Spaceguard Survey, as well as having a high level of asteroid mitigation research activity. Japan and Brazil both have long

established space agencies and therefore potentially have the resources to plan and execute a mitigation mission. JAXA has proved its capabilities though the Hayabusa mission [JAXA, 2006]. China has a rapidly developing space agency, reviewed by Harvey [2004], having developed from first flight to first manned flight in a period of four years. Therefore it could no doubt easily develop and launch a mitigation mission in a short timeframe. India's space research is growing steadily with the recent launch of its first unmanned moon mission [ISRO, 2008].

These five countries are identified as having the greatest risk. However, it is those countries facing the greatest percentage of population or infrastructure loss, detailed in Table 5.5, which are most vulnerable to total devastation. These are the countries that do not possess adequate resources to rebuild following an impact and thus need the greatest protection. This protection will take the form of the development of adequate evacuation procedures and other procedures for improving resilience. Furthermore, these countries mostly have small populations and as such are not well represented at an international level. Nor do they have the ability to provide assistance in the development of an international mitigation mission.

Finally it is of utmost importance that the decision making processes take place at an open international forum. This will allow each nation an equal voice and prevent the possibility that mitigation missions could be planned based on the sole participant's vested interests. Furthermore, it is of critical importance that the decision making processes be informed by reliable data regarding each country's relative vulnerability, in order to accurately understand the factors associated with a particular asteroid threat. In the event that mitigation fails, such information would become vital in assessing which countries require particular assistance.

In summary:

> *The five highlighted countries that face the greatest risk are, thankfully, well placed to take a leading role in co-ordinating NEO research and mitigation efforts. All have well developed space agencies and are members of the G8, providing a good forum for discussion. While these five countries face the greatest risk, their combined objective should be the protection of those countries most vulnerable to an asteroid impact.*

6.6 Sources of Uncertainty and Error

As mentioned previously in this report, the very nature of the NEO threat is an uncertain one. Principally the probability of an Earth-impact event can only be estimated from asteroid population estimates drawn from incomplete observations [D'Abramo

et al., 2001]. This leaves a large section of the NEO family undetected and thus an unknown threat. Furthermore, while repeat observations of catalogued asteroids continually refine the orbit characteristics, there remains a residual uncertainty due to error in the observing techniques (both optical and radar ranging [Giorgini et al., 2002]). Orbital perturbations such as the Yarkovsky effect [Farinella et al., 1998] and gravitational forces will continually act to change the orbit.

These sources of error have the greatest consequences when disseminating the hazard warning to the international political community and subsequently the public. The Torino Scale was established to provide a means for assessing the threat of an asteroid and informing the public [Binzel, 2000]. However, without a precisely accurate set of observations, the probability of impact and, therefore, the threat posed will continue to alter. It is difficult for those outside the scientific community to grapple with the notion of a probable risk. With this risk rising and then falling (as is usually the case [Chapman, 2004]) the public may experience a 'crying wolf' syndrome. This is especially true when they are faced with much more tangible risks, such as hurricanes and flooding. While statistically speaking the British public face a greater risk of death due to an asteroid impact than from flooding, according to Crowther [2004], the average citizen will call for greater flood defences rather than asteroid defences as it is a tangible threat to their own life.

It is the uncertainty in the asteroid's physical characteristics and impact dynamics that pose the greatest challenge for this research. It is the inherent structural weaknesses rather than aerodynamic drag that will likely determine whether the asteroid fragments, and what break-up pattern occurs. This will dictate the impact characteristics - a single monolithic event or multiple fragment impacts - and thus the impact generated effects and their consequences for humanity.

Within the model itself a number of sources of error are identified. The greatest source of error will be as a result of the simplification in the overall modelling of such a complex sequence of events combined with the global nature of the investigation. At each stage of the dynamic modelling, the models used are approximations of the real conditions. While complex hydrocode simulations can model the complex behaviour with a greater degree of accuracy, their long processing times make them unfeasible for application to the global problem. Therefore it is only possible to use the simplified models available. Furthermore, investigating the threat to Earth as a whole prevents any detailed study of the consequences for specific local regions. Therefore the simplification of the Earth data model will naturally be a large source of error. So while the specific outputs can not be taken as accurate predictions of the real consequences, it is the overall global vulnerability that can be studied.

In summary:

> *The NEO hazard is largely neglected in favour of more tangible and frequent natural disasters. However, the catastrophic nature of a single impact should highlight the need for long term investment in research. Due to natural limitations in modelling both the entire impact sequence and the global threat, the error in within the specific consequence predictions will be large. However, by performing a relative study a picture of the global vulnerability emerges with implications for the international decision makers.*

Chapter 7

Conclusions

This thesis presents a novel software model for evaluating the consequences of an asteroid impact on Earth. The software architecture implements existing models for atmospheric entry (including ablation and fragmentation), land impact (cratering, seismic shock wave, pressure blast, thermal radiation and ejecta) and ocean impact (cavitation and tsunami inundation). Unlike existing models, these impact generated effects are combined with global models for human population and infrastructure to provide an assessment for the destructive potential of an impact. The results focus on the relative consequences for impacts over an area or along a single path to determine the regions and countries most at risk from the NEO hazard.

With reference to work by Friedland et al. [2006], the NEOimpactor model defines a new study level for disaster monitoring - 'Level Zero'. This is the global-level modelling approach; analysing an event which could cause fatalities across the globe. The role of a Level Zero study is to quickly pinpoint the regions most likely affected so they can be further investigated in depth. It is in this context that the results from NEOimpactor make the most sense. Their strength is to highlight where the risk and vulnerability is greatest, rather than giving an absolute quantification of the risk.

7.1 Summary and Conclusions Drawn

Current impact research is typically focussed on individual topics (atmospheric flight, land impact or ocean impact) and, as such, there is generally no integration of these specialist topics to give an cohesive view of the consequences of an impact. Some systems, such as the Collins et al. [2005] web-based simulator, provide public access to this research, but is limited to determining an individual's personal risk from an event. NEOimpactor attempts to bridge the gap between the three specialist fields, combining many research areas into an accessible tool capable of assessing the overall vulnerability of the Earth. Data output formats of the system have been designed

with a non-specialist audience in mind to aid the dissemination of information. The primary data outputs are in the form of global casualty and damage consequence maps. Further analysis requires the simple manipulation of datasets using a spreadsheet package, such as Microsoft's Excel.

NEOimpactor has been constructed in a way which aids future development of the software. The software architecture is modular, with pre-defined data transfer mechanisms between operational modules which ensures the necessary information flow through the software. It has also been designed with a simple and familiar menu-based user interface to improve ease of use. This user-interface operates a number of applications which utilise the internal modular system architecture. Throughout development of the project, the number of applications has increased proving the ability for the system to be updated.

Simulations performed by NEOimpactor have provided insight on a number of aspects of the NEO hazard. A summary of these is given below.

Impact Severity Scale. While kinetic energy of impact, rather than object 'size', determines the magnitude of impact generated effects, the radius of the object is a commonly used proxy for this kinetic energy. Radius is also a reasonably familiar term in the non-scientific community (although confusion with diameter could occur). The asteroid size range studied covers objects from those which might be just large enough to survive entry, up to those with potentially catastrophic consequences. From this range, three classifications of catastrophe are defined - Local, Regional and Global. These designators are based on a combination of casualty and damage estimates, together with the geographical spread of affected people groups. While all loss of life could be described as a catastrophe on a personal scale, at an international level defining the scale of an event is important in determining the response needed.

Local events will primarily influence only one country, with casualties in the tens of thousands and damage in the order of one NIU. Regional events principally effect more than one country with casualties in hundreds of thousands and damage in tens of NIU. Global scale events are predominantly ocean impacts of large objects, with the possibility of affecting over a hundred nations, generating millions of casualties and thousands of NIU (hundreds of billions of dollars).

Land and Ocean Impact Characteristics. The different characteristics of land and ocean impact consequences cause difficulty when estimating the severity of a 'typical' impact event. In one location an impact may generate many thousands of casualties, while in another, virtually none are produced.

Land impacts are shown to exhibit this extreme range of consequences. This is

due to the clustered distribution of human populations across a country's interior regions related to the distribution of natural resources. A direct hit on a conurbation may destroy everything, while the same impact 100 km away may have relatively minor consequences. Ocean impacts, however, are characterised by a gradual change in consequence potential with distance. On average, for larger bodies above the transition radius, the consequences resulting from an ocean impact will outweigh those from a land event.

Impact Severity Transition Radius. All results demonstrate that very small objects present the greatest risk when impacting land, while for very large asteroids ocean impacts become the main threat. Therefore there exists a transition radius at which the severity switches from land to ocean impacts. When studying only a small region of the Earth, the transition radius is found to vary. However, when averaging impact data across the entire global, the casualty and damage results agree on a transition radius of approximately 30 m. This is based on a spherical stony-iron asteroid with a velocity of 12,000 m/s, or an impact energy of $2.85 \text{x} 10^{16}$ J.

Approximate Casualty and Damage Estimate Equations. The Global Grid simulations reveal a two phase model for predicting a rough casualty and damage estimate based on the radius of the body (for the particular composition and trajectory chosen). The inflection point between the two phases is at 125 m radius, representing a 'Regional' scale event. Equations 6.1 and 6.2 provide an approximate analysis based on global average casualty and damage potential - the actual impact consequences will vary depending on the type of asteroid and the impact location.

The Consequences of Fragmentation. The fragmentation model within the NEOimpactor system has not been used extensively in this thesis. However, a fragmentation study in Section 6.3.2 shows that multiple fragment impacts present a combined hazard typically greater than that of an equivalent energy, single impact event.

This conclusion is of vital significance for the proponents of asteroid mitigation by nuclear detonation such as Gertsch et al. [2007] and Patenaud [2007]. While their aim is to obliterate the asteroid to the dust-grain size level, failure to do this will result in the disruption of the body into multiple medium size fragments, with potentially an increased threat to Earth. Due to the low variation in expected consequences with displacement of ocean impacts, the affect of many tsunami is not cumulative and the effect is equivilent to just one small impact. This results in a casualty reduction. However, on land, increasing the number of impact events increases the probability that one (or more) will directly hit a populated region, which would immediately raise

the casualty and damage potential.

The Risk to Individual Countries There are five principle factors which determine any particular country's vulnerability. These are are:

- Total land mass area
- Size of human population
- Total infrastructure value
- Proximity to large oceans
- Length of coastline

These can be expanded to include the population density of coastal regions, the number of large sprawling urban conurbations, the land area : coastline length ratio, and country's geographical morphology (land-locked or island). Five countries have been highlighted as having the greatest combined human and infrastructure exposure to the risk. They are: China, the USA, India, Japan and Brazil. However, the most vulnerable countries are those small island nations which face potential devastation in the event of a nearby impact. Land-locked countries present the lowest exposure to the hazard, as well as affording likely evacuation pathways, and can therefore be considered 'safest'.

Informing the Decision Making Process A number of conclusions are drawn concerning the decision making process. Firstly regarding the nature of land and ocean impacts, the conformation of the general consensus that ocean impacts are the most significant impact threat. Secondly the capability is provided, through NEOimpactor, to model an asteroid's impact consequences along its predicted line of risk. This helps inform the mitigation strategists when selecting the lowest risk mitigation manoeuvre. Thirdly the international community is informed regarding the nature of each country's vulnerability. The research presented here provides an indication of those counties that face the greatest risk. It could be argued that these nations should, therefore, be called on as leading makers of policy.

7.2 Future Work

Despite the extensive capabilities of the NEOimpactor system, this is only a first attempt at the analysis of the global threat. The limiting factor hindering progress is the lack of data from real asteroid impact events. While obviously it would not be desirable to witness one, it would be an invaluable aid to our understanding of the processes involved. Until then, advancements in the various process models will be

ongoing; these can be implemented directly into the modular architecture. Such future refinement will continue to improve the robustness of the impact model and reduce the associated errors (or enable them to be quantified). Furthermore, by incorporating the different, and sometimes conflicting models, from the NEO hazard community (such as the two contrasting tsunami models by Ward and Boslough) into the single NEOimpactor tool the estimated consequences from each can be compared to derive an error range for the consequence prediction.

In parallel with these external advances in impact modelling, a number of improvements can be made to the NEOimpactor system. Refining the data-handling capabilities will allow an increased database resolution to be used and reduce simulation time to model higher resolution Global Grids. Advances in computing power and distributed computing networks will also improve such capabilities. Better resolution will allow the modelling of subtle coastline morphologies more accurately, as well as some very small island nations, which are currently lost by the resolution resampling. As highlighted in this thesis, the length of a country's coastline is a critical factor in determining its vulnerability and thus this parameter is of prime importance. Eventually, advancing the database model from its current 'raster' format into a vector based system would improve the defining characteristics of coastline dramatically. To help with this, collaboration with digital software systems such as Google Earth, will greatly improve the quality of the raw datasets. Figure 7.1 demonstrates the ability to import NEOimpactor result maps into Google Earth. Making this feature integral to the system would open avenues which would allow the research to be increasingly disseminated. However, the system will remain limited by the low quality bathymetric and infrastructure datasets. These two factors are a matter for external research agencies outside the NEO field to resolve.

The final research area where improvements can be made is in determining the impact consequences. Presently, the system outputs an estimated casualty and damage figure. However, this figure is derived using a relatively simple relationship between the IGE magnitude and the resultant casualty/damage percentage lost. This does not take into account exterior factors, such as early-warning systems and evacuation time. These two factors will mitigate the casualty level by reducing the size of population left behind, an exposed to the IGEs. Evacuation will come at a cost, either in terms of expensive evacuation logistics, or through the risk of evacuation failure generating more casualties. These factors will require enhanced understanding of the various types of infrastructure, in particular for communication and transportation. Furthermore, the complex social aspects related to vulnerability, which include public perception of the risk, morale, and community cohesiveness, will have a large effect on the population's resilience and speed of recovery following the event. An example

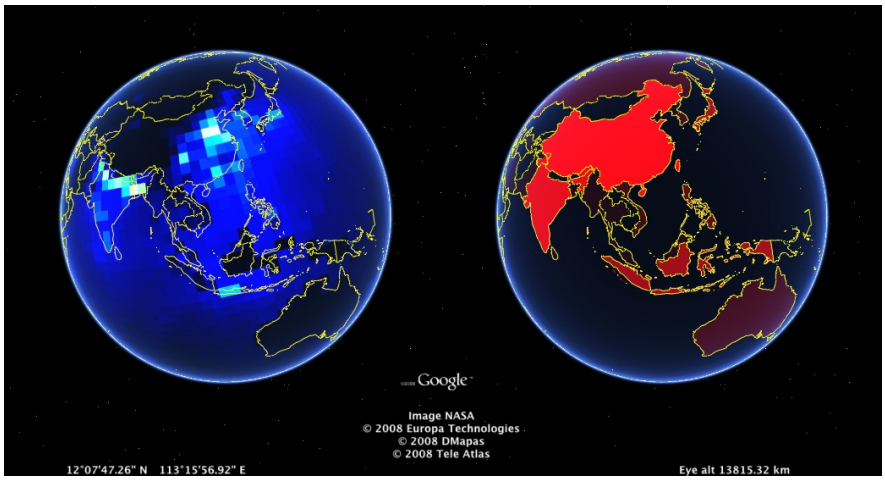

Figure 7.1: Presenting some sample NEOimpactor result maps in the virtual environment of Google Earth. This freely available and intuitive software package is a good means of disseminating data.

of this was reported by the Bhaumik [2005] following the Boxing Day Tsunami, where native islanders climbed to higher ground after the earthquake was felt, following the advice of their traditional folklore.

7.3 The Future of NEO Hazard Research

NEO research will continue primarily to map out the existing population of asteroids in and around the Earth's orbit. The focus will extend to increasingly smaller bodies as detection networks become more powerful. Of particular importance is to catalogue the Atens population which lie within the Earth's orbit. These asteroids are difficult to observe due to their low solar aspect. Cataloguing the population will reduce the unknown population to the target 10% and thus reduce the unknown risk also to that percentage. If a body is eventually discovered on a future collision course, the survey will have been successful if it affords mitigation missions the time to launch and remove the threat. The closure of the Aricibo radio telescope facility in Puerto Rico would present a significant loss to the cataloguing efforts due to its high asteroid ranging precision (and hence accurate orbit determination and prediction).

Mitigation missions will continue to be proposed [Walker et al., 2004], and in time, more 'rehearsal' missions will be launched ahead of time to gain experience. It is the particular goal of the B612 Foundation to launch just such a rehearsal mitigation mission by 2020 using their proposed gravity tractor [Lu and Love, 2005]. It is the view of the author that the tractor-type mitigation strategies represent the best means of mitigating a known asteroid threat and that any suggestion of a strategy involving a nuclear detonation should be ruled out. Nevertheless, all proposed missions to

visit asteroids will help to increase our knowledge of their dynamical characteristics, chemical composition, and structural integrity. Such missions are of great value, and should obviously be encouraged.

The potential destructive capacity of a single NEO impact event, even from a relatively small body, greatly outweighs that of any other natural disaster. While the infrequency of impact is often taken as a reason for ignoring the threat, this is a mistake. The relative lack of NEO research funding, compared to flood defences for example, indicates this oversight. Asteroid impacts are unique amongst natural disasters in being the only one that uniformly threatens every country on Earth and the only one that can be predicted and mitigated. Countries that are most vulnerable should, therefore, take a leading role in funding a global planetary defence programme, and defining the policy of such a programme.

References

Adams, D. N. (1979). *The Hitch Hiker's Guide to the Galaxy*. Pan Macmillan, England.

Ailor, W. H., editor (2007a). *Tsunamis from asteroid impacts in deep water*. Retrieved 26 January, 2009, from http://www.aero.org/conferences/planetarydefense/2007papers.html.

Ailor, W. H. (2007b). White paper: Summary and recommendations. Technical report, 2007 Planetary Defence Conference, Washington, DC, 58 March 2007. Retrieved from http://www.aero.org/conferences/planetarydefense/2007papers/WhitePaperFinal.pdf.

Alexander, D. (1997). The study of natural disasters, 1977 – 1997: Some reflections on a changing field of knowledge. *Disasters*, 21(4):284 – 304.

APL (2002). *Near Earth Asteroid Rendezvous Mission*. Retrieved 19 July, 2006, from http://near.jhuapl.edu/.

Bailey, N. J. (2005). Near Earth object literature review. Technical report, University of Southampton.

Bailey, N. J., Swinerd, G. G., Morley, A. D., and Lewis, H. G. (2006). Near Earth object impact simulation tool for supporting the NEO mitigation decision making process. In *International Astronomical Union*, volume 2, pages 477 – 486. Cambridge University Press.

Baillie, M. (2007). The case for significant numbers of extraterrestrial impacts through the late Holocene. *Journal of Quaternary Science*, 22:101 – 109.

Bay, M. (1998). (Director), Pool, R. R. and Hensleigh, J. (Writers). *Armageddon* [Motion picture] Burbank, California, USA : Touchstone Pictures.

Bhaumik, S. (2005). *Tsunami Folklore Saved Islanders*. Retrieved 16 March, 2005, from http://news.bbc.co.uk/2/hi/south_asia/4181855.stm.

Binzel, R. P. (2000). Torino impact hazard scale. *Planetary and Space Science*, 48(4):297 – 303.

Bland, P. A. and Artemieva, N. A. (2003). Efficient disruption of small asteroids by Earth's atmosphere. *Nature*, 424(6946):288 – 291.

Bland, P. A., Smith, T. B., Jull, A. J. T., Berry, F. J., Bevan, A. W. R., Cloudt, S., and Pillinger, C. T. (1996). The flux of meteorites to the Earth over the last 50,000 years. *Monthly Notices of the Royal Astronomical Society*, 283:551.

Boerner, D. E., Milkereit, B., and Davidson, A. (2000). Geoscience impact: A synthesis of studies of the Sudbury Structure. *Canadian Journal of Earth Sciences*, 37(2):477 – 501.

Borovijcka, J., Popova, O. P., Nemtchinov, I. V., Spurny, P., and Ceplecha, Z. (1998). Bolides produced by impacts of large meteoroids into the Earth's atmosphere: Comparison of theory with observations: I. Benesov bolide dynamics and fragmentation. *Astronomy and Astrophysics*, 334:713 – 728.

Boslough, M. B. E. and Crawford, D. A. (2008). Low-altitude airbursts and the impact threat. Retrieved 30 November, 2008, from `10.1016/j.ijimpeng.2008.07.053`.

Brewer, C. A., MacEachren, A. M., Pickle, L. W., and Herrmann, D. (1997). Mapping mortality: Evaluating color schemes for choropleth maps. *Annals of the Association of American Geographers*, 87(3):411 – 438.

Bronshten, V. A. (1983). *Physics of Meteoric Phenomena*. Reidel Publishing Company, Dordrecht, The Netherlands.

Bronshten, V. A. (1995). Fragmentation and crushing of large meteoric bodies in an atmosphere. *Solar System Research*, 29:392 – 399.

Bronshten, V. A. (2000). Nature and destruction of the Tunguska cosmical body. *Planetary and Space Science*, 48(9):855 – 870.

Cartlidge, E. (2006). The threat from above. *Physics World*, 19(3):27 – 29.

Carusi, A., Valsecchi, G. B., DAbramo, G., and Boattini, B. (2002). Deflecting NEOs in route of collision with the Earth. *Icarus*, 159:417 – 422.

Ceplecha, Z., Borovicka, J., Elford, W. G., ReVelle, D. O., Hawkes, R. L., Porubcan, V., and Simek, M. (1998). Meteor phenomena and bodies. *Space Science Reviews*, 84(3-4):327 – 471.

Chapman, C. R. (2004). The hazard of near Earth asteroid impacts on Earth. *Earth and Planetary Science Letters*, 222(1):1 – 15.

Chapman, C. R., Durda, D. D., and Gold, R. E. (2001). The comet/asteroid impact hazard: A systems approach. White paper, Southwest Research Institute.

Chapman, C. R. and Morrison, D. (1994). Impacts on the Earth by asteroids and comets: Assessing the hazard. *Nature*, 367(6458):33 – 40.

Chesley, S. (2007). NEO alert frequency, the evolution of impact probabilities, and keyhole dynamics. In *Planetary Defense Conference, Washington, DC, 58 March 2007*. Retrieved 28 October, 2008, from `http://www.aero.org/conferences/planetarydefense/2007papers/S1-5--ChesleyBrief.pdf`.

Chesley, S. R. and Ward, S. N. (2003). Assessing the human hazard from impact-generated tsunami. *AAS/Division for Planetary Sciences Meeting Abstracts*, 35.

Chester, D. K. (2001). The 1755 Lisbon earthquake. *Progress in Physical Geography*, 25(3):363 – 383.

Chodas, P. (2007). NEO warning times for NEAs and comets. In *Planetary Defense Conference, Washington, DC, 58 March 2007*. Retrieved 28 October, 2008, from `http://www.aero.org/conferences/planetarydefense/2007papers/S1-4--Chodas-Brief.pdf`.

Chyba, C. F. (1993). Explosions of small Spacewatch objects in the Earth's atmosphere. *Nature*, 363(6431):701 – 703.

Chyba, C. F., Thomas, P. J., and Zahnle, K. J. (1993). 1908 Tunguska explosion: Atmospheric disruption of a stony asteroid. *Nature*, 361(6407):40 – 44.

CIA (2008). *World Factbook*. Retrieved 25 March, 2008, from `https://www.cia.gov/library/publications/the-world-factbook/`.

Collins, G. S., Melosh, H. J., and Marcus, R. (2004). Earth impact effects program: A web-based computer program for calculating the regional environmental consequences of a meteoroid impact on Earth. Technical report, LPL, University of Arizona, USA.

Collins, G. S., Melosh, H. J., and Marcus, R. A. (2005). Earth impact effects program: A web-based computer program for calculating the regional environmental consequences of a meteoroid impact on Earth. *Meteoritics and Planetary Science*, 40(6):817 – 40.

Collins, G. S., Melosh, H. J., Morgan, J. V., and Warner, M. R. (2002). Hydrocode simulations of Chicxulub crater collapse and peak-ring formation. *Icarus*, 157(1):24 – 33.

Courtillot, V. and McClinton, J. (2002). *Evolutionary Catastrophes: The Science of Mass Extinction*. Cambridge University Press, 1st edition.

Crowther, R., Tremayne-Smith, R., Swinerd, G. G., and Bailey, N. J. (2005). Societal risk evaluation of the near Earth object impact hazard. *Geophysical Research Abstracts*, 7(09175).

D'Abramo, G., Harris, A. W., Boattini, A., Werner, S. C., and Valsecchi, G. B. (2001). A simple probabilistic model to estimate the population of near Earth asteroids. *Icarus*, 153:214 – 217.

Dietz, R. S. (1964). Sudbury structure as an astrobleme. *Journal of Geology*, 72:412 – 424.

Durda, D. (2005). *B612 Foundation*. Retrieved from `http://www.b612foundation.org/` [1 February 2005].

Farinella, P., Vokrouhlick, D., and Hartmann, W. K. (1998). Meteorite delivery via yarkovsky orbital drift. *Icaruasts*, 132:378 – 387.

Foderà Serio, G., Manara, A., and Sicoli, P. (2002). *Giuseppe Piazzi and the Discovery of Ceres*. University of Arizona Press, Tucson, USA.

Fortescue, P., Stark, J., and Swinerd, G. G., editors (2003). *Spacecraft Systems Engineering*. Wiley, 3rd edition.

Friedland, C. J., Adams, B. J., and Levitan, M. L. (2006). Deployment of remote sensing technology for multi-hazard post-Katrina damage assessment within a spatially-tiered reconnaissance framework. In 4th *International Workshop on Remote Sensing for Post-Disaster Response*. Retrieved 30 October, 2008, from `http://www.arct.cam.ac.uk/curbe/aahill\_etal.pdf`.

Fritz, H. M., Hager, W. H., and Minor, H. E. (2004). Near field characteristics of landslide generated impulse waves. *Journal of Waterway, Port, Coastal and Ocean Engineering*, 130(6):287 – 302.

Fujiwara, A., Kawaguchi, J., Yeomans, D. K., Abe, M., Mukai, I., Okada, T., Saito, J., Yano, H., Yoshikawa, M., Scheeres, D., Barnouin-Jha, O., Cheng, A. F., Demura, H., Gaskett, R. W., Hirata, N., Ikeda, H., Kominato, T., Miyamoto, H., Nakamura, A. M., Nakamura, R., Sasakj, S., and Uesugil, K. (2006). The rubble-pile asteroid Itokawa as observed by Hayabusa. *Science*, 312(5778):1330 – 4.

Gálvez, A. and Carnelli, I. (2005). ESA studies on the Don Quijote NEO mission: Dealing with impact uncertainties. In 56th *International Astronautical Congress, 2005*, volume IAC-05-Q.P.21, Fukuoka, Japan. Re-

trieved 5 January, 2008, from http://www.esa.int/gsp/ACT/doc/MAD/pub/ACT-RPR-MAD-2006-DQdealingImpactUncertainties.pdf.

Gálvez, A., Coradini, M., and Ongaro, F. (2003). The role of space missions in the assessment of the NEO impact hazard. In *54th International Astronautical Congress, 2003*, Bremen, Germany. Retrieved 8 January, 2008, from http://www.esa.int/gsp/ACT/doc/MAD/pub/ACT-RPR-MAD-2003-THEROLEOFSPACEMISSIONSINTHEASSESSMENTOFTHENEOIMPACT.pdf.

Gerrard, M. B. (2000). Risks of hazardous waste sites versus asteroid and comet impacts: Accounting for the discrepancies in US resource allocation. *Risk Analysis*, 20(6):895 – 904.

Gertsch, L., Baird, J., and Worsey, P. (2007). Blast designs for NEO destruction. In *Planetary Defense Conference, 5 – 8 March 2007*, Washington, DC. Retrieved 30 October, 2008, from http://www.aero.org/conferences/planetarydefense/2007papers/P2-2--Gertsch-Paper.pdf.

Giorgini, J. D., Ostro, S. J., Benner, L. A. M., Chodas, P. W., Chesley, S. R., Hudson, R. S., Nolan, M. C., Klemola, A. R., Standish, E. M., Jurgens, R. F., Rose, R., Chamberlin, A. B., Yeomans, D. K., and Margot, J. L. (2002). Asteroid 1950 DA's encounter with earth in 2880: Physical limits of collision probabitity prediction. *Science*, 296(5565):132 – 136.

Gisler, G. R., Weaver, R. P., Gittings, M. L., and Mader, C. L. (2003). Two- and three-dimensional asteroid ocean impact simulations. *International Journal of Impact Engineering*, 29(1-10):283 – 291.

Glasstone, S. and Dolan, P. J. (1977). *The Effects of Nuclear Weapons*. Dept of Defense (US), Washington DC.

Glikson, A. (2005). Asteroid/comet impact clusters, flood basalts and mass extinctions: Significance of isotopic age overlaps. *Earth and Planetary Science Letters*, 236(3-4):933 – 7.

Glikson, A. Y. (1999). Oceanic mega-impacts and crustal evolution. *Geology*, 27(5):387 – 390.

González, J. A., Belló, M., Martín-Albo, J. F., and Gálvez, A. (2004). Don Quijote: An asteroid deflection technological demonstrator. In *55th International Astronautical Congress, 2004*, volume IAC-04-Q.P.21, Vancouver, BC, Canada.

Google (2008). *Google Earth: Explore, Search, and Discover*. Retrieved 25 March, 2008, from http://earth.google.com/.

Grieve, R. A. F. (1990). Impact cratering on the Earth. *Scientific American*, 262:44 – 51.

Grigorian, S. S. (1976). On the question of Tunguska meteorite nature. *Doklady Akad. Sci. USSR*, 231:57 – 60.

Grigorian, S. S. (1979). Motion and disintegration of meteorites in planetary atmospheres. *Cosmological Research*, 17:875 – 893.

Grigorian, S. S. (1998). The cometary nature of the Tunguska meteorite: On the predictive possibilities of mathematical models. *Planetary and Space Science*, 46(2-3):213 – 217.

Grokhovsky, V. I., Kozlov, E. A., Karkina, L. E., and Teplov, V. A. (2001). Structural signs of impact deformation of the Sikhote Alin iron meteorite. *Fizika Metallov i Metallovedenie*, 91(3):72 – 80.

Harvey, B. (2004). *China's space program: From conception to manned spaceflight*. Springer, New York.

Haslett, S. K. and Bryant, E. A. (2007). Evidence for historic coastal high-energy wave impact (tsunami?) in North Wales, United Kingdom. *Atlantic Geology*, 43:137 – 147.

Haslett, S. K. and Bryant, E. A. (2008). Historic tsunami in Britain since AD 1000: A review. *Natural Hazards and Earth System Sciences*, 8(3):587 – 601.

Head, J. N., Melosh, H. J., and Ivanov, B. A. (2002). Martian meteorite launch: High-speed ejecta from small craters. *Science*, 298(5599):1752 – 1756.

Hecht, J. (2007). *New Scientist*. Retrieved 15 April, 2008, from `http :// space. newscientist.com/ article/ dn12704- report- clarifies- some-- but- not- all-- details- of- peru- impact.html`.

Hills, J. G. and Goda, M. P. (1993). The fragmentation of small asteroids in the atmosphere. *The Astronomical Journal*, 105(3):1114 – 1144.

Hills, J. G. and Goda, M. P. (1998). Damage from the impacts of small asteroids. *Planetary and Space Science*, 46(2-3):219 – 229.

Hodge, P. W. (1965). The Henbury meteorite craters. In *Smithsonian Contributions to Astrophysics*, volume 8, pages 199 – 213. Smithsonian Institution, Washington D.C.

Hodge, P. W. (1994). *Meteorite Craters and Impact Structures of the Earth*. University Press, Cambridge.

Holdstock, D. and Barnaby, F. (1995). *Hiroshima and Nagasaki: Retrospect and Prospect*. Routledge, UK.

Hoyt, W. (1987). *Coon Mountain Controversies*. University Arizona Press, Tucson, USA.

Hughes, D. W. (1976). Giordano Bruno, the Moon's latest large crater. *Nature*, 264:212 – 213.

Hutchinson, I., Guilbault, J. P., Clague, J. J., and Bobrowsky, P. T. (2000). Tsunamis and tectonic deformation at the northern Cascadia margin: A 3000-year record from Deserted Lake, Vancouver Island, British Columbia, Canada. *The Holocene*, 10(4):429 – 439.

IAA (2007). *1st IAA Planetary Defence Conference*. Retrieved 26 January, 2009, from `http://www.aero.org/conferences/planetarydefense/`.

IAU (2006). Resolutions 5 and 6. In *26th International Astronomical Union General Assembly, 2004*, Cambridge University Press, UK. Retrieved 11 September, 2008, from `http://www.iau.org/static/resolutions/Resolution\_GA26-5-6.pdf/`.

IAU (2008). *Minor Planet Center*. Retrieved 28 October, 2008, from `http://www.cfa.harvard.edu/iau/mpc.html/`.

ISRO (2008). *Indian Space Research Organisation*. Retrieved 1 December, 2008, from `http://www.isro.org/`.

Ivanov, A. G. and Ryzhanski, V. A. (1997). Splitting process of Sikhote Alin meteorite in the content of modern fracture mechanics. *Journal De Physique. IV*, 7(3):975 – 980.

Ivanov, B. A., Deniem, D., and Neukum, G. (1997). Implementation of dynamic strength models into 2D hydrocodes: Applications for atmospheric breakup and impact cratering. *International Journal of Impact Engineering*, 20:411 – 430.

JAXA (2006). *Institute of Space and Astronautical Science - Hayabusa Mission*. Retrieved 19 July, 2006, from `http://www.isas.ac.jp/e/enterp/missions/hayabusa/index.shtml`.

Jensen, N., editor (1998). *The NEO Impact Hazard and Options for Mitigation*, Cagliari, Italy. Retrieved 13 May, 2005, from `http://www.estec.esa.nl/conferences/98b02/`.

Kahle, R., Hahn, G., and Kuhrt, E. (2006). Optimal deflection of NEOs en route of collision with the Earth. *Icarus*, 182:482 – 488.

Kalashnikova, O., Horanyi, M., Thomas, G. E., and Toon, O. B. (2000). Meteoric smoke production in the atmosphere. *Geophysical Research Letters*, 27(20):3293 – 3296.

Kerr, A. C. (1997). Asteroid impact and mass extinction at the K-T Boundary: An extinct red herring. *Geology Today*, 13(4):157 – 159.

Korycansky, D. G. and Zahnle, K. J. (2004). Atmospheric impacts, fragmentation, and small craters on Venus. *Icarus*, 169(2):287 – 99.

Langewiesche, W. (2003). Columbia's last flight: The inside story of the investigation-and the catastrophe it laid bare. *Atlantic Monthly*, 292:58 – 88.

Leder, M. (1998). (Director), Rubin, B. J. and Tolkin, M. (Writers). *Deep Impact* [Motion picture] Hollywood, Los Angeles, CA, US : Paramount Pictures.

Logsdon, J. (2007). The domestic politics of planetary protection. In *Planetary Defense Conference, Washington, DC, 58 March 2007*. Retrieved 17 November, 2008, from `http://www.aero.org/conferences/planetarydefense/2007papers.html`.

Lu, E. T. and Love, S. G. (2005). Gravitational tractor for towing asteroids. *Nature*, 438:177 – 178.

Lyne, J. E., Tauber, M. E., and Fought, R. M. (1996). An analytical model of the atmospheric entry of large meteors and its application to the Tunguska event. *Journal of Geophysical Research*, 101(E10):23207 – 23212.

Marcus, R., Melosh, H. J., and Collins, G. (2009). *Earth Impact Effects Program*. Retrieved 22 January, 2009, from `www.lpl.arizona.edu/impacteffects`.

Matsuyama, M., Walsh, J. P., and Yeh, H. (1999). Effect of bathymetry on tsunami characteristics at Sisano Lagoon, Papua New Guinea. *Geophysical Research Letters*, 26(23):3513 – 3516.

Maurrasse, F. J. M. R. and Sen, G. (1991). Impacts, tsunamis, and the Haitian Cretaceous-Tertiary boundary layer. *Science*, 252(5013):1690.

McCall, G. J. H., editor (1977). *Meteorite Craters*, volume 36 of *Benchmark Papers in Geology*. Dowden, Hutchinson and Ross, Inc.

Melosh, H. J. and Ivanov, B. A. (1999). Impact crater collapse. *Annual Review of Earth and Planetary Sciences*, 27:385 – 415.

Meyer, E. A. and Meyer, K. S. (2005). *HYDESim*. Retrieved 3 July, 2008, from `http://meyerweb.com/eric/tools/gmap/hydesim.html`.

Milani, A. (2005). *Near Earth Objects Dynamic Site*. Retrieved 9 May, 2005 from `http://131.114.72.13/cgi-bin/neodys/neoibo`.

Milani, A., Chesley, S. R., Chodas, P. W., and Valsecchi, G. B. (2002). *Asteroid Close Approaches: Analysis and Potential Impact Detection*. University of Arizona Press, Tucson, USA.

Miller, J. K., Konopliv, A. S., Antreasian, P. G., Bordi, J. J., Chesley, S., Helfrich, C. E., Owen, W. M., Wang, T. C., Williams, B. G., Yeomans, D. K., and Scheeres, D. J. (2002). Determination of shape, gravity, and rotational state of asteroid 433 Eros. *Icarus*, 155:3 – 17.

Minzner, R. A. (1977). The 1976 Standard Atmosphere and its relationship to earlier standards. *Reviews of Geophysics and Space Physics*, 15(3):375 – 84.

Morris, W. A. (2002). The Sudbury Structure: A circular impact crater? *Geophysical Research Letters*, 29(20):63 – 1.

Morrison, D. (1992). The Spaceguard Survey: Report of the NASA international near Earth object detection workshop. Technical report, NASA.

NASA (2008). *Visible Earth: A Catalog of NASA Images and Animations of Our Home Planet*. Retrieved 21 November, 2008, from `http://visibleearth.nasa.gov/`.

NASA - JPL (2008a). *Near Earth Asteroid Discovery Statistics*. Retrieved 28 October, 2008, from `http://neo.jpl.nasa.gov/stats/`.

NASA - JPL (2008b). *Small Asteroid Predicted to Cause Brilliant Fireball over Northern Sudan*. Retrieved 27 October, 2008, from `http://neo.jpl.nasa.gov/news/news159.html/`.

Nemtchinov, I., Shuvalov, V., Artem'eva, N. A., Ivanov, B., Kosarev, I., and Trubetskaya, I. A. (1998). Light flashes caused by meteoroid impacts on the lunar surface. *Solar System Research*, 32:99.

Nicholls, R. J., Hoozemans, F. M. J., and Marchand, M. (1999). Increasing flood risk and wetland losses due to global sea-level rise: Regional and global analyses. *Global Environmental Change*, 9:69 – 87.

NOAA (2005). *Home Page*. Retrieved 13 May, 2005, from `http://www.noaa.gov/`.

NOAA (2008). *Center for Tsunami Research*. Retrieved 7 July, 2008, from `http://nctr.pmel.noaa.gov/indo\_1204.html`.

Nordt, L., Atchley, S., and Dworkin, S. I. (2002). Paleosol barometer indicates extreme fluctuations in atmospheric CO_2 across the Cretaceous-Tertiary boundary. *Geology*, 30(8):703 – 706.

OECD (2009). *Home Page*. Retrieved 17 January, 2009, from `http://www.oecd.org/home/`.

Patenaud, S. (2007). Nuclear deflection. In *Planetary Defense Conference, Washington, DC, 58 March 2007*. Retrieved 30 October, 2008, from `http://www.aero.org/conferences/planetarydefense/2007papers/S2-2--Patenaud-Brief.pdf`.

Paxson, C. and Rouse, C. E. (2008). Returning to New Orleans after hurricane Katrina. *American Economic Review*, 98:38 – 42.

Peter, N., Robinson, D., A., B. J., and Salotti, J. M. (2004). Global responses options for threatening near Earth objects. In 55^{th} *International Astronautical Congress, 2004*, volume IAC-04-C.2.07, Vancouver, BC, Canada.

Pierazzo, E. and Collins, G. (2003). *A Brief Introduction to Hydrocode Modeling of Impact Cratering*. Submarine Craters and Ejecta-Crater Correlation. Planetary Science Institute, Springe, New York.

Pope, K. O. (2002). Impact dust not the cause of Cretaceous-Tertiary mass extinction. *Geology*, 30(2):99 – 102.

Pravec, P. (2006). NEA rotations and binaries. Retrieved 29 October, 2008, from `http://www.astronomy2006.com/symposia-archive.php?symposium=236`.

Pravec, P. and Harris, A. W. (2000). Fast and slow rotation of asteroids. *Icarus*, 148(1):12 – 20.

Rantucci, G. (1995). *Geological Disasters in the Philippines: The July 1990 Earthquake and the June 1991 Eruption of Mount Pinatubo*. DIANE Publishing, 1^{st} edition.

Raup, D. M. (1986). Biological extinction in Earth history. *Science*, 231(4745):1528 – 1533.

RERF (2008). *Radiation Effects Research Foundation*. Retrieved 3 July, 2008, from `http://www.rerf.or.jp/`.

Robinson, L. and Jarvie, J. K. (2008). Post-disaster community tourism recovery: The tsunami and Arugam Bay, Sri Lanka. *Disasters*, 32(4):631 – 645.

Rountree-Brown, M. (2005). *JPL: Deep Impact Mission*. Retrieved 13 May, 2005, from `http://deepimpact.jpl.nasa.gov/`.

Sagy, A., Reches, Z., and Fineberg, J. (2002). Dynamic fracture by large extraterrestrial impacts as the origin of shatter cones. *Nature*, 418(6895):310 – 313.

Savage, S. J. and Waldman, D. (2005). Broadband internet access, awareness, and use: Analysis of United States household data. *Telecommunications Policy*, 29:615 – 633.

Schweickart, R. (2006). NEO deflection: An international challenge. Retrieved 20 July, 2006, from `http://www.unoosa.org/oosa/COPUOS/stsc/2006/presentations.html`.

Schweickart, R. (2007). The NEO threat: International policy issues. In *Planetary Defense Conference, Washington, DC, 58 March 2007*. Retrieved 30 November, 2008, from `http://www.aero.org/conferences/planetarydefense/2007papers/S6-1--Schweickart-Paper.pdf`.

Scotti, J. V., Rabinowitz, D. L., and Marsden, B. G. (1991). Near miss of the Earth by a small asteroid. *Nature*, 354:287 – 289.

Seed, H. B., Romo, M. P., Sun, J. I., Jaime, A., and Lysmer, J. (1988). The Mexico earthquake of September 19, 1985: Relationships between soil conditions and earthquake ground motions. *Earthquake Spectra*, 4(4):687 – 729.

Shoemaker, E. M. (1995). Report of the near Earth objects survey working group. Technical report, NEO Survey Science Working Group. Retrieved from `http://www.impact.arc.nasa.gov/news\_detail.cfm?ID=94`.

Shoemaker, E. M. and Eggleton, R. E. (196l). Terrestrial features of impact origin. Technical Report 1, Geophysical Laboratory: Lawrence Radiation Lab.

Siripong, A. (2006). Andaman seacoast of Thailand field survey after the December 2004 Indian Ocean tsunami. *Earthquake Spectra*, 22(S3):S187 – S202.

Slocum, T. A. and Egbert, S. L. (1993). Knowledge acquisition from choropleth maps. *Cartography and Geographic Information Society*, 20(2):83 – 95.

Smit, J. (1999). Global stratigraphy of the Cretaceous-Tertiary boundary impact ejecta. *Annual Review of Earth and Planetary Sciences*, 27:75 – 113.

Smit, J., Simonson, B. M., Hassler, S., and Sumner, D. (2002). Large-impact triggered tsunami deposits in the deep sea: Examples from the 65 m.a. Chicxulub crater and 2.5 – 2.6 g.a. Hamersley Basin. *Geological Society of America Cordilleran Meeting Symposium*, pages 178 – 181.

Smith, D. E., Shi, S., Cullingford, R. A., Dawson, A. G., Dawson, S., Firth, C. R., Foster, I. D. L., Fretwell, P. T., Haggart, B. A., Holloway, L. K., and Long, D. (2004). The Holocene Storegga slide tsunami in the United Kingdom. *Quaternary Science Reviews*, 23(23-24):2291 – 2321.

Spence, R. J. S., Kelman, I., Baxter, P. J., Zuccaro, G., and Petrazzuoli, S. (2005). Residential building and occupant vulnerability to tephra fall. *Natural Hazards and Earth System Sciences*, 5:477 – 494.

Spray, J. (2008). *Earth Impact Database*. Retrieved 28 October, 2008, from `http://www.unb.ca/passc/ImpactDatabase/index.html`.

Spray, J. G., Kelley, S. P., and Rowley, D. B. (1998). Evidence for a late Triassic multiple impact event on Earth. *Nature*, 392(6672):171 – 173.

Stokes, G. H. and Yeomans, D. K. (2003). A study to determine the feasibility of extending the search for NEOs to smaller limiting diameters: Report of a NASA science definition team. Technical report, NASA Office of Space Science, Solar System Exploration Division. Retrieved from `http://neo.jpl.nasa.gov/neo/neoreport030825.pdf`.

Stuart, J. S. (2003). *Observational Constraints on the Number, Albedos, Sizes, and Impact Hazards of the Near-Earth Asteroids*. PhD thesis, Massachusetts Institute of Technology.

Stuart, J. S. and Binzel, R. P. (2004). Bias-corrected population, size distribution, and impact hazard for the near Earth objects. *Icarus*, 170(2):295 – 311.

Stulov, V. P. (2004). Asymptotic theory of the motion of celestial bodies in the atmosphere. *Planetary and Space Science*, 52(5-6):459 – 463.

Sublette, C. (2007). *Nuclear Weapons Frequently Asked Questions*. Retrieved 3 July, 2008, from `http://nuclearweaponarchive.org/`.

Svetsov, V. V., Nemtchinov, L. V., and Teterev, A. V. (1995). Disintergration of large meteoroids in Earth's atmosphere: Theoretical models. *Icarus*, 116:131 – 153.

Titov, V., Rabinovich, A. B., Mofjeld, H. O., Thomson, R. E., and Gonzalez, F. I. (2005). Ocean science: The global reach of the 26 December 2004 Sumatra tsunami. *Science*, 309(5743):2045 – 2048.

Tselentis, G. A., Melis, N. S., Sokos, E., and Papatsimpa, K. (1996). The Egion June 15, 1995 (6.2 M_L) earthquake, western Greece. *Pure and Applied Geophysics*, 147:83 – 98.

Urrutia-Fucugauchi, J., Marin, L., and Trejo-Garcia, A. (1996). UNAM scientific drilling program of Chicxulub impact structure-evidence for a 300 kilometer crater diameter. *Geophysical Research Letters*, 23(13):1565 – 1568.

USGS (2008a). *Earthquakes Hazard Program: Magnitude 9.1 - off the West Coast of Northern Sumatra*. Retrieved 23 November, 2008, from `http://earthquake.usgs.gov/eqcenter/eqinthenews/2004/usslav/`.

USGS (2008b). *Earthquakes Hazards Program: Latest Earthquakes M5.0+ in the World - Past 7 days*. Retrieved 2 July, 2008, from `http://earthquake.usgs.gov/eqcenter/recenteqsww/Quakes/quakes\_big.php`.

USGS (2008c). *Historic Earthquakes: Chile, 1960 May 22*. Retrieved 1 December, 2008, from `http://earthquake.usgs.gov/regional/world/events/1960_05_22.php`.

Walker, R., Summerer, L., and Izzo, D. (2004). Concepts for near Earth asteroid deflection using spacecraft with advanced nuclear and solar electric propulsion systems. In *55*$^{\text{th}}$ *International Astronautical Congress, 2004*, volume IAC-04-Q.5.08, Vancouver, BC, Canada.

Wallis, D. and McBride, N. (2002). Planetary impact crater analysis with eigenfunction expansion. *Monthly Notes of the Royal Astronomical Society*, 330:458 – 472.

Ward, S. N. (2000). Tsunamis. In Meyers, R. A., editor, *Encyclopaedia of Physical Science and Technology*, volume 17. Academic Press, New York, USA.

Ward, S. N. (2001). Landslide tsunami. *Journal of Geophysical Research*, 106(B6):11201 – 11215.

Ward, S. N. and Asphaug, E. (2000). Asteroid impact tsunami: A probabilistic hazard assessment. *Icarus*, 145(1):64 – 78.

Ward, S. N. and Asphaug, E. (2002). Impact tsunami — Eltanin. *Deep-Sea Research Part II: Topical Studies in Oceanography*, 49(6):1073 – 1079.

Ward, S. N. and Asphaug, E. (2003). Asteroid impact tsunami of March 16^{th}, 2880. *Geophysical Journal International*, 153(3):6 – 10.

Ward, S. N. and Day, S. (2001). Cumbre Vieja volcano – potential collapse and tsunami at La Palma, Canary Islands. *Geophysical Research Letters*, 28(17):3397 – 3400.

Wells, N., Walker, R., Green, S., and Ball, A. (2006). SIMONE: Interplanetary microsatellites for NEO rendezvous missions. *Acta Astronautica*, 59(8-11):700 – 709.

Whipple, F. J. W. (1934). On phenomena related to the Great Siberian meteor. *Quarterly Journal of the Royal Meteorological Society*, 60:505 – 513.

Yau, K., Weissman, P., and Yeomans, D. (1994). Meteorite falls in China and some related human casualty events. *Meteoritics*, 29:864 – 871.

Zotkin, I. T. (1966). Trajectory and orbit of the Tunguska meteorite. *Meteoritika*, 27:109 – 118.